

Rock & Roll

Turbulence-induced damage to granular bed protections

Rock & Roll

Turbulence-induced damage to granular bed protections

Proefschrift

ter verkrijging van de graad van doctor
aan de Technische Universiteit Delft,
op gezag van de Rector Magnificus prof.dr.ir. J.T. Fokkema,
voorzitter van het College voor Promoties,
in het openbaar te verdedigen

op dinsdag 6 december 2005 om 15.30 uur

door

Bastiaan HOFLAND

civiel ingenieur
geboren te Alphen aan den Rijn.

Dit proefschrift is goedgekeurd door de promotoren:

prof. dr. ir. J.A. Battjes
prof. ir. K. d'Angremond

Samenstelling promotiecommissie:

Rector Magnificus	voorzitter
prof. dr. ir. J.A. Battjes	Technische Universiteit Delft, promotor
prof. ir. K. d'Angremond	Technische Universiteit Delft, promotor
prof. dr. ir. J. de Rouck	Universiteit Gent
prof. J.J.R. Williams PhD.	University of London
prof. dr. ir. M.J.F. Stive	Technische Universiteit Delft
ir. G.J. Schiereck	Rijkswaterstaat
dr. ir. G.J.C.M. Hoffmans	Rijkswaterstaat

drs. R. Booij en dr. ir. H.L. Fontijn hebben als begeleiders in belangrijke mate aan de totstandkoming van het proefschrift bijgedragen.

This research has been supported by the Road and Hydraulic Engineering Division of the Ministry of Transport, Public Works and Water Management (contract DWW-1700), and by the first Delft Cluster programme, under the theme Coast and River. A four month extension of the project has been supported by Royal Boskalis Westminster and Van Oord.

ISBN-10: 90-9020122-X
ISBN-13: 9789090201221

Copyright © 2005, B. Hofland.
Printed by Febodruk b.v., The Netherlands.

All rights reserved. No part of this publication may be reproduced in any form, by print or photo print, microfilm or any other means, without written permission by the publisher.

This thesis is also published in the series 'Communications on Hydraulic and Geotechnical Engineering' of the Faculty of Civil Engineering and Geosciences, Delft University of Technology, as Report # 05-4. ISSN 0169-6548.

Contents

Samenvatting	xi
Summary	xv
1 Introduction	1
1.1 Background	1
1.2 Aim and approach	5
1.3 Outline	6
2 Governing Processes and Parameters	9
2.1 Introduction	9
2.2 Turbulence and flow properties	10
2.2.1 Open-channel flow over a rough bed	10
2.2.2 Backward-facing step	16
2.2.3 Roughness transition	17
2.3 Forces on a single stone	17
2.3.1 Basics	17
2.3.2 Drag force	19
2.3.3 Lift force	21
2.4 Entrainment mechanism	22
2.5 Stability of a granular bed	25
2.5.1 Initiation of motion	25
2.5.2 Bed load transport	27
2.6 Size, shape, position, and orientation of stones	30
2.7 Engineering approach	35
2.8 Concluding remarks	37
3 Stone Positions	41
3.1 Introduction	41

3.2	Previous use of Discrete Particle Models for determination of bed surface characteristics	42
3.3	Features of present DPM	43
3.4	Configurations	44
3.5	Water-working	45
3.6	Characteristics of the modelled water-worked bed	47
3.6.1	Time dependence	50
3.7	Summary and discussion	52
4	Experimental Arrangement	55
4.1	Introduction	55
4.2	Pressure transducers	55
4.3	Particle Image Velocimetry	57
4.3.1	General technique	57
4.3.2	Equipment	58
4.4	First experimental series	60
4.4.1	Equipment	60
4.4.2	Configurations	63
4.4.3	Mean flow characteristics	65
4.5	Second experimental series	66
4.5.1	Equipment	67
4.5.2	Artificial stones	67
4.5.3	Timing	69
4.5.4	Configurations	70
4.5.5	Mean flow characteristics	71
4.5.6	Position of the target stone	74
4.6	Reattachment length	76
5	Quasi-Steady Forces	77
5.1	Introduction	77
5.2	Probability density function (PDF) for quasi-steady drag force	78
5.2.1	PDF for u_b^2	78
5.2.2	PDF for $u_b u_b $	79
5.2.3	Drag force distribution	80
5.3	Uniform flow	82
5.3.1	Influence of exposure	83
5.3.2	Vortex shedding	87
5.4	Roughness transition	89
5.5	Summary and discussion	89

6	Turbulence Wall Pressures (TWP)	93
6.1	Introduction	93
6.2	Theoretical considerations	94
6.2.1	Mechanisms	94
6.2.2	Model vortex	94
6.2.3	Transfer functions	96
6.2.4	Estimation of magnitude of TWP-forces	98
6.2.5	Behaviour of TWP forces in time	100
6.3	Analysis of measurements	101
6.3.1	Cross-correlation drag and lift	101
6.3.2	Probability density of lift force	103
6.3.3	Pressure spectra	105
6.4	Summary and discussion	107
7	Flow Structures and Stone Movement	109
7.1	Introduction	109
7.2	Data processing	110
7.2.1	Inspection of vector plots	110
7.2.2	Indicators for force mechanisms	111
7.2.3	Splicing	112
7.3	Uniform flow	114
7.3.1	Classification	114
7.3.2	Conditional averages	115
7.3.3	Small-scale instantaneous flow structure	118
7.3.4	Large-scale flow structure during individual movements	120
7.3.5	Sensitivity of results	121
7.4	Backward-facing step	124
7.4.1	Classification	125
7.4.2	Conditionally averaged flow structure	126
7.4.3	Quasi-periodic structures	126
7.5	Evaluation of quadrant analysis	130
7.6	Pressures	131
7.7	Conclusions	133
8	Modelling Damage to Bed Protections	135
8.1	Introduction	135
8.2	Governing parameters	136
8.2.1	Shields parameter including Quasi-Steady and TWP forces	136
8.2.2	Damage criterion: Entrainment	137
8.2.3	Aim	138

8.3	Assessment of possible modelling approaches	139
8.3.1	(Very) Large Eddy Simulation	139
8.3.2	RANS simulation with $k-\varepsilon$ turbulence closure	139
8.4	New model for using RANS output	141
8.4.1	Incorporating the length-scale of the turbulence	141
8.4.2	Determination of the length scale	143
8.4.3	Inclusion of Turbulence Wall Pressures	144
8.4.4	The new stability parameter	145
8.5	Performance of the methods	146
8.5.1	Data used	146
8.5.2	Comparing measured and calculated flow fields	150
8.5.3	Entrainment under uniform flow	155
8.5.4	Entrainment under non-uniform flow	156
8.6	Evaluation of new approach	159
8.6.1	Influence of the relative depth	160
8.7	Conclusions	163
9	Conclusions and Recommendations	165
9.1	Conclusions	165
9.2	Recommendations	168
9.2.1	Experimental research	168
9.2.2	Modelling	169
9.2.3	Design of bed protections in practice	170
	Acknowledgements	171
	List of Symbols	173
	List of Figures	178
	References	187
A	Techniques for Filtering Spurious Pressures	197
A.1	Introduction	197
A.2	High-pass filtering	197
A.3	Difference filter	198
A.3.1	Performance of the filter	199
A.4	Optimal filter	200
A.4.1	Performance of the filter	200
A.4.2	Implementation	202

B Rolling Stones	203
C PDF of bed shear stress	207
D Estimating entrainment from conventional measurements	209
D.1 Introduction	209
D.2 Definitions and assumptions	210
D.3 Using the technique	212
E Measurements used for evaluation of modelling approach	215
F Geometrical characteristics of prototype bed protections	219

Samenvatting

Rondom waterbouwkundige kunstwerken worden vaak lagen breuksteen aangebracht om ontgroning te voorkomen. De stenen in deze bodembeschermingen dienen groot genoeg te zijn om de krachten van het water te kunnen weerstaan. De bepaling van de benodigde grootte wordt bemoeilijkt door het feit dat de stroming rond kunstwerken niet uniform is. Voor deze niet-uniforme stromingen bestaan geen fysisch correcte formules om de stabiliteit van de stenen te bepalen. De meeste stabiliteitsvoorspellers zijn ontwikkeld voor uniforme stromingen. Ze gebruiken de gemiddelde stroomsnelheid om de kracht van het water op de stenen te bepalen. De fluctuaties van de krachten die door de turbulentie in het water ontstaan worden impliciet verdisconteerd in empirische factoren. Bij niet-uniforme stromingen verandert de verhouding tussen de gemiddelde en de fluctuerende krachten, waardoor de formules niet meer te gebruiken zijn. De grootte van stenen in een steenbestorting is dan niet meer goed te voorspellen.

Schade aan bodembeschermingen is mede moeilijk te voorspellen doordat zowel de posities van de stenen – die de sterkte van de laag beïnvloeden – als de turbulente stroming nabij de bodem – die de kracht van het water op de stenen beïnvloedt – een willekeurig karakter hebben. Verder zijn er tegenstrijdige opvattingen over de manier waarop een steen wordt meegenomen door het water.

In dit project is vooral experimenteel werk verricht. Het doel was te achterhalen hoe een turbulente stroming stenen van de bodem verplaatst. Dit werd gedaan op een kleine schaal: een enkele steen werd beschouwd. Voordat dit soort experimenten gedaan kon worden moest eerst bekend zijn wat een karakteristieke positie van die enkele steen in een (willekeurig gestorte) laag stenen is. Daartoe is een mathematisch model gemaakt dat bollen één voor één op een willekeurige plaats liet vallen. Met de bodem die zo ontstond kon een schatting worden gemaakt van de karakteristieke positie van een steen. Ook kon getoond worden hoe de vorm van het oppervlak van de steenlaag naar een evenwicht tendert onder invloed van de stroming.

Twee series experimenten zijn uitgevoerd. De eerste richtte zich op de relatie tussen (instantane) stroomsnelheden nabij de bodem en krachten op een steen. De

tweede richtte zich op de relatie tussen structuren in de stroming (wervels) en de eerste beweging van een steen. Bij deze experimenten zijn miniatuur drukmeters gebruikt, alsmede de zogenaamde *Particle Image Velocimetry* (PIV) techniek waarmee momentopnames van snelheidsvelden gemaakt kunnen worden. Een uniforme stroming, de stroming benedenstrooms van een plotselinge toename van de bodemruwheid (begin van een bodembescherming) en de stroming benedenstrooms van een afstap (modelconstructie) werden beschouwd. In de eerste serie was de modelsteen kubusvormig, in de tweede serie werd een realistisch gevormde steen gebruikt.

Over het algemeen wordt gedacht dat de fluctuerende krachten op een steen worden veroorzaakt door hetzelfde mechanisme als de gemiddelde krachten. Deze krachten worden daarom aangeduid als quasi-stationair. De kansdichtheidsverdeling van deze krachten is afgeleid en kon worden gebruikt om te verifiëren of de quasi-stationaire krachten verantwoordelijk zijn voor de krachten op de stenen. Het bleek dat de quasi-stationaire krachten voornamelijk corresponderen met de horizontaal gerichte krachten op stenen die hoog boven de bodembescherming uitsteken. Ook de vorm van de kansdichtheidsverdeling bij de stroming benedenstrooms van het begin van een ruwe laag was goed voorspeld. Echter, voor beschutte stenen kunnen niet alle krachtsfluctuaties verklaard worden met het quasi-stationaire mechanisme.

De quasi-stationaire krachtsfluctuaties hebben een lange duur, lang genoeg om de steen te laten wegrollen.

De quasi-stationaire krachten worden veroorzaakt door drukverschillen die ontstaan door de stroomlijnkromming die door de uitstekende steen zelf wordt geïnduceerd. Echter, een turbulente stroming bevat altijd allerlei wervels en fluctuaties die drukverschillen veroorzaken – zelfs op een vlakke wand. Deze turbulente wanddrukken, geïntegreerd over het steenoppervlak, geven fluctuerende krachten op de steen. In een verdere analyse van de eerste serie metingen is onderzocht in hoeverre deze krachten significant kunnen zijn voor het verplaatsen van een steen. Op basis van de volgende aanwijzingen werd geconcludeerd dat deze krachten inderdaad een significante bijdrage leveren aan de totale kracht op de steen. Ten eerste heeft de kruiscorrelatie tussen de horizontale en verticale kracht de vorm die behoort bij door turbulente wanddrukken veroorzaakte krachten – vooral bij de steen die het minste uitstak. Ten tweede vallen de dimensieloze spectra van de drukken op de steen benedenstrooms van een afstap samen met die van de wanddrukken op een gladde wand benedenstrooms van een afstap.

De wervels die de wanddrukken veroorzaken zijn klein, zodat de krachtsfluctuaties een korte duur hebben. Daardoor zal deze kracht de steen over het algemeen niet doen wegrollen, maar alleen laten trillen.

De turbulente wanddrukken veroorzaken significante krachtsfluctuaties bij lagere uitsteelingen en hogere turbulentieïntensiteiten. Daarom is dit krachtsmechanisme belangrijk voor de verplaatsing van granulair bodemmateriaal, vooral voor stenen die

beschut zijn door andere stenen. Bij een bodem die door de stroming is uitgevlakt zullen dit de kleinere stenen zijn, omdat die over het algemeen een lagere ligging hebben. Voor stenen die minder beschut liggen lijken de turbulente wanddrukken meer invloed te hebben op de verticale kracht dan op de horizontale kracht.

Tijdens de tweede meetserie zijn met behulp van de PIV meettechniek de georganiseerde structuren in de stroming onderzocht die steenbeweging veroorzaken. Instantane stromingsvelden in het verticale vlak parallel aan de stroomrichting zijn gemeten voor, tijdens en na het bewegen van de steen. Omdat de steen in sommige gevallen maar eens per uur beweegt, werden de metingen volledig geautomatiseerd. De structuren die leidden tot steenbeweging bleken kwalitatief gelijk te zijn voor de uniforme stroming en de stroming achter een afstap. De steen beweegt tijdens de aanwezigheid van grootschalige gebieden met een verhoogde longitudinale, en een kleine naar beneden gerichte, snelheid. Dit komt overeen met een verhoogde horizontale quasi-stationaire kracht. Vaak krijgt de steen een eerste zetje door een intense, kleine fluctuatie in de verticale snelheid. Deze fluctuatie is een teken van de aanwezigheid van een dwars georiënteerde wervel die met de gemiddelde afschuiving in de stroming meedraait, en die waarschijnlijk een doorsnede is van de kop van een hoefijzerwervel. De kleine wervel veroorzaakt turbulente wanddrukken. Het eerste zetje zorgt ervoor dat het blootgestelde oppervlak van de steen groter wordt, zodat de stroming meer vat krijgt op de steen. Ook verandert de hoek van de steen ten opzichte van het rotatiepunt. Dit alles zorgt ervoor dat de steen makkelijker beweegt.

Tenslotte is een methode geformuleerd om de stabiliteit van bodembeschermingen onder niet-uniforme stromingen te evalueren. De methode gebruikt parameters die berekend kunnen worden met een Reynolds-gemiddeld stromingsmodel. De profielen van de gemiddelde snelheid en van de turbulentie-energie in de waterkolom boven een bepaalde plek van een bodembescherming worden gebruikt om een lokale stabiliteitsparameter te formuleren. Dit is een aangepaste Shieldsparameter, waarin alleen de quasi-stationaire krachten expliciet worden gemodelleerd. De verplaatste hoeveelheid steen per eenheid van tijd en oppervlak (*entrainment rate*) wordt gebruikt als een maat voor de schade. Uit conventionele metingen – met stroken van stenen met verschillende kleuren – kan deze *entrainment rate* bepaald worden na correctie voor het transport van steen binnen een strook. Een methode voor het bepalen van deze correctie wordt gepresenteerd. Gemeten waarden van de nieuwe stabiliteitsparameter zijn gecorreleerd met de dimensieloze *entrainment rate*. De relatief grote invloed van de turbulentie in deze parameter geeft aan dat de turbulente wanddrukken een extra invloed op de steenstabiliteit hebben.

Summary

Layers of stone or rock are often applied around hydraulic structures to protect the sand bed from scouring. The stones in the top layer of these bed protections must be large enough to withstand the hydraulic loads exerted on them. Determining this size is complicated by the fact that the flow over a bed protection usually is non-uniform, and no physically sound (design) formulae exist for estimating the stability of stones under non-uniform flow. The stability parameters that are the basis of most design formulae were developed for uniform flows. They use the mean velocity or shear velocity to quantify the flow attack on the bed. The (force) fluctuations due to turbulence are accounted for in empirical factors. Therefore, when the ratio of the magnitude of the mean to the fluctuating forces changes (i.e. non-uniform flow), the damage level cannot be predicted well.

Damage to bed protections is difficult to quantify objectively in consequence of the random character of the problem. The positions of the stones – that determine the strength of the bed protection – and the turbulent flow – which determines the load – both have a random nature. An exact definition of damage is lacking as well. Moreover, there are still conflicting notions about the exact entrainment mechanism of bed material.

Experimental work was the core of this project. The aim was to determine which kind of flow events remove a stone from the bed at a micro level. A single stone at a characteristic position was considered. Before this could be undertaken the position of the stone in the bed had to be known. To this end a mathematical model was developed. This is a so-called discrete particle model for randomly and sequentially deposited spheres. This model was used to obtain a first estimate of the position of the most unstable stone on a flat bed. It was also used to illustrate how a bed can reach an equilibrium state as a result of the attack by the flow, and it can give some qualitative information about the structure of a bed. It was seen that even though the bed is stochastic in nature, there exists a maximum protrusion of the stones.

Two experimental series were conducted. The first focussed on the relation between the velocity near and the pressure fluctuations on the bed material. The sec-

ond focussed on the relation between flow structures and initial stone movement. For these experiments two measurement techniques were deployed. One was the use of miniature pressure sensors, used in both experimental series. The second was two-dimensional digital Particle Image Velocimetry (PIV), used in the second experimental series. In the first measurement series, pressures on a bed-mounted cubical model stone were measured. The cases of a uniform flow, a developing uniform flow just downstream of an increase in bed roughness, and the flow behind a backward-facing step were studied. In the second series the movement of stones with a realistic shape was measured for the same flow conditions, except the developing flow.

It is generally thought that the fluctuating forces on bed material are generated by the same mechanism as the mean forces. We will refer to these as quasi-steady forces. The probability density function for the forces on bed material, based on the quasi-steady force-generating mechanism, has been derived. This function was used to check whether the quasi-steady mechanism is responsible for the forces on bed material. From the measurements of the first series it was deduced that the quasi-steady mechanism can account for the drag forces on exposed stones under uniform flow. Also the influence of a sudden increase of bed roughness on the fluctuating drag forces can be explained well by it. However, for shielded particles and flow behind a backward-facing step the quasi-steady mechanism cannot explain all fluctuations anymore. The largest quasi-steady forces have a long duration, long enough to make the stone roll away.

The quasi-steady forces are caused by pressure differences due to the streamline curvature that is caused by the presence of a stone protruding in the flow, hence the name ‘form drag’. In a turbulent flow, however, acceleration of water parcels and streamline curvature are always present, also without the presence of a stone that forces this curvature. Therefore, turbulence near a wall creates fluctuating pressures on the bed, even when it is smooth. These turbulence wall pressure fluctuations (TWP), when integrated over a stone, will result in net forces on the stone and therefore contribute to the fluctuating forces on a stone.

In a further analysis of the first measurement series this different force-generating mechanism is considered. TWP give a significant contribution to the fluctuating forces under certain circumstances. This is deduced from the following evidence. First of all, the cross-covariance of drag and lift has the shape predicted on the basis of convecting TWP, especially for the lowest exposure. Further, the dimensionless spectra of the pressures on top of the stone downstream of a backward-facing step coincide with the spectra of pressures on a smooth wall downstream of a backward-facing step, which clearly illustrates that the quasi-steady mechanism is not applicable here. Even the spectra of the drag force coincide with the smooth wall data, especially for a low exposure of the model stone and high relative turbulence intensity.

The flow structures causing TWP are small, so these forces have a short duration.

Therefore these forces by themselves will merely lead to a rocking motion of the stone.

The conclusion can be drawn that the TWP give a significant contribution to the force fluctuations for lower exposures and higher turbulence levels. Therefore, the TWP are of importance for the entrainment of granular material, especially for stones that are shielded by other stones. In a granular bed that has been water-worked this would be the smaller stones, as they generally have small exposures. For higher exposures the relative influence of the TWP on the lift force seems larger than it is on the drag force.

In the second experimental series the flow structures that initiate stone movement are obtained from PIV measurements. Streamwise-vertical flow fields were measured around the time of movement of a single stone. The frequency of movement of the stone could be as low as one time per hour, therefore the measurements had to be fully automated. It was seen that the flow structures that lead to stone movement are similar for a uniform flow and a flow downstream of a backward-facing step. The stone is entrained during the presence of large-scale areas with increased streamwise and downward velocity. This coincides with the presence of an increased quasi-steady force. Often the stone gets an initial lift (or rotation) by an intense, small-scale fluctuation of vertical velocity. This fluctuation of the vertical velocity is usually connected to the presence of a spanwise vortex, rotating in the direction of the mean shear, which probably is a cross-section of a hairpin vortex. The initial lift of short duration increases the exposed area and angle of repose such that the stone is moved more easily by the increased streamwise velocity reaching the stone after the fluctuation in vertical velocity. The small-scale force is related to the TWP. One can state that in general the stone is moved by an exceptional combination of two normal structures, at least one of which has an exceptionally high magnitude. If both flow structures work together they can make a stone rock and roll.

A method for evaluating the stability of bed protections under non-uniform flows, using output of a three dimensional (Reynolds-averaged) numerical flow model has been formulated. The profiles of the mean velocity and turbulence kinetic energy in the water column above the bed are used to formulate a local stability parameter, which basically is an adapted Shields parameter. Only the quasi-steady forces are explicitly modelled. The (dimensionless) entrainment rate is used as a measure of damage. It can be determined from conventional measurements (using strips with coloured stones) when a correction is made for the transport within a strip. A method for this is presented. Measured values of the new stability parameter are correlated to the entrainment parameter. A relation between the stability parameter and the entrainment parameter is given. The relatively large influence of the turbulence in the stability parameter compared to the mean forces, indicates that the turbulence wall pressures aid in the entrainment of stones.

Chapter 1

Introduction

1.1 Background

Layers of stone or rock are often applied around hydraulic structures like weirs, spillways, groins, revetments and breakwaters to protect the sand bed from scouring (Schierack, 2001). As the total surface area that has to be covered by these bed protections is large, and the stones are not always readily available, the total cost of these bed protections is considerable.

The stones in the top layer of these bed protections must be large enough to withstand the hydraulic loads exerted on them. Determining this size is complicated by the fact that the flow over the bed protections is – almost per definition – non-uniform. However, no physically sound (design) formulae exist for estimating the stability of stones under non-uniform flow. Granular bed protections can further be characterised by:

- hydraulically rough flow regime ($Re_* \gtrsim 500$)¹,
- low-mobility transport ($\Psi \lesssim 0.05$)², which implies:
 - bed load transport,
 - sliding or pivoting motion of particles,
 - no active bed forms, and
 - flow as over a fixed bed,
- non-cohesive stones,
- narrow grading of sizes,
- angular stones, and
- non-equilibrium transport.

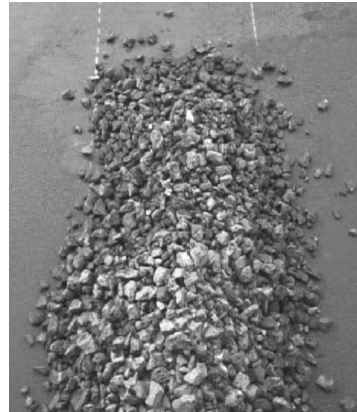


Figure 1.1: Left: laboratory model of a granular bed protection (present tests). Right: trial bed protection with 10-60 kg rock (Meulepas *et al.*, 1999).

¹ Re_* is the particle Reynolds number $\equiv u_*d/\nu$, where u_* is the shear velocity, d the stone diameter, and ν the kinematic viscosity.

² Ψ is the Shields number $\equiv u_*^2/(\rho_s/\rho - 1)gd$, where ρ_s is the density of the stones, ρ the density of water and g the gravitational acceleration.

Turbulence

Turbulence fluctuations³ of velocity and pressure are a key factor in the entrainment of bed material, as the mean forces alone are often not large enough to displace the particles (McLean *et al.*, 1994; Kleinhans & Van Rijn, 2002; Schmeeckle & Nelson, 2003, among others). However, the stability parameters that are the basis of most design formulae were developed for uniform flows. They use the mean velocity (Isbash, 1932) or shear velocity (Shields, 1936) to quantify the flow attack on the bed. The (force) fluctuations due to turbulence are accounted for in empirical factors. Therefore, when the ratio of the magnitude of the mean to the fluctuating forces changes (i.e. non-uniform flow), the damage level cannot be predicted well. A very clear example is the flow at a reattachment point behind a backward-facing step. Here the mean velocity is zero, so zero damage is predicted by conventional formulae, while in reality the damage is nearly maximal at this position. For existing geometries, ad-hoc design formulae and empirical correction factors do exist, but these lack general validity. Because of this, physical modelling is still necessary for the design of bed protections in new configurations. Otherwise large safety factors have to be used. Contrary to this lack of knowledge, the ability to compute the hydrodynamics has increased immensely over the last decades.

Fluctuating forces can have several origins. They can be caused by vortices that are shed from stones upstream, by turbulence that originates from the outer flow, or by vortices shedding from the stone under consideration itself (Kalinske, 1947). These origins are difficult to distinguish. Moreover the position of a stone determines the flow around it, and the force to which it is susceptible. As the movement of a stone is a sporadic event, the generation of extreme pressures by extreme flow events becomes important.

Random character

Damage to bed protections is difficult to quantify objectively in consequence of the random character of the problem (see figure 1.1). Both the positions of the stones (which determine the strength of the bed protection) as well as the turbulent flow (which determines the load on the structure) have a random nature. These two important stochastic elements determine the average entrainment rate of bed material. Hence damage to bed protections can be described by two probability distributions. Key works on this notion were by Einstein & El-Samni (1949) and Kalinske (1947) who studied the turbulence fluctuations in the context of sediment motion, and by Grass (1970) who also included the randomness of the bed material. Some approaches

³For simplicity a broad definition of turbulence is used during this project. We will call all flow structures that cause the velocity to fluctuate – except surface waves – to be turbulence. This is valid as we do not treat the origin of the fluctuations, but only how these cause damage.

exist that use probabilistic theory to evaluate damage, but many assumptions have to be made in order to obtain the final estimate of damage. These are therefore not yet better than other approaches.

Damage

The random character of the bed complicates things even further. Even a general, consistent definition of ‘damage’ is not available. Damage usually builds up gradually, which makes the formulation of a clear definition of it difficult. If a stone has moved it is not clear whether this was a single stone in an awkward position, or whether it represents the onset of ongoing damage. The fact that the value of the critical Shields parameter can be chosen by the designer somewhere in the range of 0.02–0.05 is exemplary for this uncertainty. As the stone size is estimated on the basis of the experience of an engineer, objective choices about failure probability and maintenance frequency of bed protections are not possible.

Entrainment mechanism

Even if one were able to determine the statistics of the flow and of the bed arrangement, another problem remains. The exact manner in which a stone is entrained by the flow is not well understood either. There are still conflicting notions about the exact mechanism of entrainment of bed material. For hydraulically rough beds, like gravel bed rivers, the drag and lift force are usually assumed to be proportional to the streamwise velocity squared, so that extreme values of this velocity component will cause most transport of bed material. However, detailed measurements of both the velocity near and the force on a stone do not substantiate this theory completely. For instance, drag and lift coefficients fitted to the results differ for the instantaneous and the mean force. In particular the extreme values cannot be predicted. This indicates that other factors like the spatial variability of the flow near the bed and accelerations also influence the forces on the stone (Schmeeckle & Nelson, 2003). For hydraulically smooth beds, for instance, it has been stated that the pressure gradients under streamwise vortices create forces on the grains, which are thereby displaced (Gyr & Schmid, 1997). In this project it is examined which force-generating mechanisms significantly influence the entrainment of stones.

Previous work

In the engineering field much practical experience on the design of bed protections has been accumulated over the years. This has yielded a large amount of design rules and of rules-of-thumb. For instance, in The Netherlands many physical model studies on bed protections have been executed during the creation of the Delta Works. However,

the physical concepts on which all the practical knowledge is based, are still the same as a century ago. The aspects of the turbulence and the random bed have hardly been incorporated.

Further, on a more detailed and fundamental level, there has been much research as well. For example, the forces on single stones on a bed, the origin of pressure fluctuations on smooth walls under turbulent flows, and the origin of coherent flow structures in various turbulent flows have been studied. These studies usually deal with schematised geometries that are difficult to compare to practical situations. Moreover, transport of gravel in rivers and seas is a field with intensive research. Here mostly rounded gravel and uniform flow is dealt with. This has yielded a large variety of literature in different fields, which could all be of importance to the present work.

1.2 Aim and approach

In this project the physical mechanisms governing the entrainment of coarse particles from hydraulically rough beds under low-mobility conditions are investigated. The exact way in which turbulence affects the stability of stones under various flow types is to be determined. Ultimately this knowledge is to be used to improve the present stability or damage formulations for granular bed protections. This aim is reached in the following steps.

First it is inspected how the extreme forces on the stones come about. Hence the relation between the velocity field near the bed and the forces on the stone needs to be understood. This relation is examined by regarding the relation between velocity or acceleration components near the bed and pressures on the stones. Furthermore it has to be determined which flow structures create these near-bed velocities and accelerations, and can thus move the stones. This should reveal which length or time scales of the velocity fluctuations displace the stone. This can give information that is of importance to the modelling of damage. An example is whether the flow structures that create the largest forces originate from the outer flow or from the bed.

The research is predominantly conducted on a micro-scale. A single stone is considered. This is rarely done. Most research focusses on an integrated number of displaced or transported stones. Under low-mobility transport conditions only a few stones will move during such an experiment. This leads to a large uncertainty in the experimental results. Moreover, the results are influenced by a number of factors with an unknown influence, which are also difficult to distinguish and describe precisely, like the shape of the bed material, the thickness of the granular layer, and the nature of the near-bed turbulence. All of the above makes that the empirical results exhibit

a large scatter. When regarding a single stone it is clear that the variability in the movement of this single stone is due to the turbulence, while the stone itself remains the same.

It is still difficult to fully resolve turbulent flows over a rough bed in a computation. Therefore mainly experimental work was conducted. Measurements of pressures on a bed-mounted cube were the focus of a first experimental series. Particle Image Velocimetry (PIV) measurements – where entire flow fields are measured instantaneously – were the focus of a second experimental series.

In the experiments various degrees of turbulence were realised. The canonical flow configurations of the uniform flow (normal turbulence intensity) and flow downstream of a backward-facing step (increased turbulence intensity) were investigated in both experimental series. In addition the flow just downstream of a smooth-bed-to-rough-bed transition was investigated in the first series (deficient turbulence intensity).

As the position of the single stone that is studied is crucial for the way it is entrained, a numerical model was developed and applied to investigate the distribution of the stone positions in a randomly deposited bed. From these results new information became available about a typical position for an unstable stone, and the way that damage can be defined. This was used, together with results from literature, to determine the position for the single stone in the experiments.

In order to model damage to bed protections it is necessary to determine damage from calculated flow fields. In most practical calculations only averaged or large-scale flow parameters are obtained. Therefore a model was developed that determines the flow attack on the bed protection from flow parameters that can be obtained from numerical calculations. This model is compared to measurements of the (bulk) entrainment of bed material.

1.3 Outline

The next chapter gives an overview of the current state of knowledge of flow and turbulence, stone characteristics, forces on stones, coarse-sediment transport, and existing design formulae. Then, in chapter 3, a numerical model is used to gain more insight in the positions of stones in a granular bed. This was needed to choose a suitable position for the moving stone in the experiments. Two measurement series were carried out. The experimental arrangements of these measurement series are described in chapter 4. In chapter 5 a first analysis of the first experimental series is given, focussing on the generally used quasi-steady forces, whereafter chapter 6 deals with the turbulence-induced forces due to accelerations in the flow that are caused by turbulence vortices. In chapter 7 the results of the second experimental series are used to see which flow structures actually move stones from a bed under various flow

conditions.

In the first seven chapters a bottom-up approach is used, where the processes are studied rather fundamentally. In contrast, in chapter 8 an improved practical approach is developed to evaluate the stability of bed material under non-uniform flows. This approach is based on several notions that were treated in the preceding chapters. Here it is evaluated how well a calculated flow field can be used to predict damage to bed protections.

Chapter 9 summarises the conclusions and ends with recommendations.

Chapter 2

Governing Processes and Parameters

2.1 Introduction

This chapter deals with literature that is useful as a background for the present detailed examination of stone stability. As detailed studies on granular beds and turbulence specifically aimed at bed protections are rare, other fields of research are also used, like research on gravel-bed rivers, research on turbulence wall pressures and research on coherent structures.

First, flow and turbulence characteristics in general are discussed, which are of importance to the present experiments. Besides the classical statistical turbulence theory, coherent flow structures in uniform, open-channel, rough-wall flows are described. Then some features of turbulence wall pressures – which might influence stone stability – are presented. The flow configurations used in the present experiments are the uniform flow, the backward-facing step flow and a transition from a smooth bed to a rough bed. Some characteristics of these flow configurations are described as well.

In order to understand the processes causing damage to granular bed protections, the stability of the separate particles must be evaluated. The hydrodynamic forces on the particles are very important for understanding this stability. Section 2.3 deals with these forces.

The next section gives a description of research on the processes of entrainment of particles. The research discussed is quite diverse, and deals with aspects like: the influence coherent structures on the initiation of motion of bed material, and the influence of a non-uniform turbulence structure on the initiation of motion.

Section 2.5 focuses on the stability of an entire bed. A description of some bed load transport formulas is given. Some parameters that can be used for the determination of ‘damage’ are defined and their relation is discussed. Several basic aspects of the influence of turbulence on stone stability and transport are treated as well. The stochastic approach of treating transport and entrainment is also discussed.

The characteristics of stones in a granular bed which can influence stone stability – like position, shape, size and orientation – are treated in section 2.6, both for single stones and for an entire bed.

The present day engineering approach for designing stable bed protections, which is largely based on the formulae treated in section 2.5, is explained in section 2.7.

2.2 Turbulence and flow properties

In this section some characteristics of the flow configurations used during the present experiments (see chapter 4) are discussed. Mainly research on turbulence in rough-bed flows is described. In the following x , y , and z denote the streamwise, upward, and transverse coordinate respectively, and u , v , w the velocity components in the respective directions. Variables can be split in a stationary mean part (e.g. \bar{u}) and a fluctuating part with zero mean (e.g. u').

Hydraulically rough flow is characterised by a large particle Reynolds number $Re_* \equiv u_* d / \nu \gtrsim 70$ where $u_* \equiv \sqrt{\tau_b / \rho}$ is the shear velocity, τ_b the bed shear stress, ρ the density of water and ν the kinematic viscosity.

2.2.1 Open-channel flow over a rough bed

For uniform flow over a rough bed, the mean velocity profile is given by the law-of-the-wall:

$$\bar{u} = \frac{u_*}{\kappa} \ln \frac{y}{y_0} \quad , \quad (2.1)$$

where κ is the Von Karman constant and y_0 the roughness length. Eq. (2.1) is only valid for a part of the depth, h : $150y_0 \lesssim y \lesssim 0.2h$. The roughness length is proportional to the diameter of the roughness elements, d . For flow over sand glued to a flat bed, Nikuradse (1933) found $y_0 = d/30$. However, for a bed with randomly placed stones, this value can increase up to values of $y_0 \approx d/10$. In addition to the constants κ and y_0 , eq. (2.1) has a third unknown empirical constant: the position of the theoretical bed, $y = 0$. In contrast to a smooth bed, this is not clearly defined for a granular bed. Estimates for the level of the theoretical bed vary from $0.35d$ to $0.15d$ under the tops of the roughness elements (Nikora *et al.*, 2002). The flow – and especially the turbulence fluctuations – near the rough bed ($y \lesssim 150y_0$) is still influenced considerably by the shape of the bed and represents the so-called

roughness sublayer. Between the roughness elements the average velocity profile is approximately linear (Nikora *et al.*, 2001b).

The standard deviation of the velocity components, $\sigma(u_i)$, is approximated by Nezu & Nakagawa (1993), as:

$$\frac{\sigma(u_i)}{u_*} \approx \alpha_i e^{-y/h} \quad , \quad (2.2)$$

The values given for the empirical factor α_i are: $\alpha_x = 2.30$, $\alpha_y = 1.27$, and $\alpha_z = 1.67$. The values of $\sigma(u_i)/u_*$ near the bed differ from eq. (2.2), especially for smooth beds. Flow near a rough bed is more isotropic: the peak value of $\sigma(u)/u_*$ is about 2.8 for a smooth bed compared to 2.0 for a rough bed. Outside the roughness sublayer most turbulence statistics are rather similar for smooth and rough beds. This is called wall similarity. A difference is that the integral time scale (i.e. the time lag for which the autocorrelation of u becomes zero) is somewhat shorter for a rough bed. For beds with a large relative roughness ($y_0/h \gtrsim 150$) the fluctuating velocities deviate from eq. (2.2) (Wang *et al.*, 1993).

In an equilibrium flow the Reynolds stress (outside the roughness sublayer) is given by:

$$-\overline{u'v'} = (1 - y/h) u_*^2 \quad . \quad (2.3)$$

When secondary currents due to sidewalls or an acceleration of the flow are present the terms $-\int_y^h \bar{v} \frac{\partial \bar{\pi}}{\partial \tilde{y}} d\tilde{y} - \int_y^h \frac{\partial \overline{u'w'}}{\partial z} d\tilde{y}$ should be added to the right hand side of eq. (2.3) (Nezu & Nakagawa, 1993).

Coherent structures

Turbulent flows are highly variable and chaotic. Still certain similar flow patterns can be observed repeatedly, the so-called ‘coherent structures’. Transport of stones at low hydraulic loads is mainly determined by the extreme values of the fluctuating forces. If these extreme forces can be linked to a certain kind of flow structure then a model for damage to bed protections can be based on characteristics of this structure (e.g. size, intensity, frequency of occurrence).

The well-known bursting process is the turbulence generation mechanism near smooth walls (Robinson, 1991, gives a review). Undulations of the laminar sublayer grow into hairpin vortices which become unstable, and intermittently fluid is injected into the outer flow, the ‘burst’. Between the legs of the hairpin – which form counter-rotating, streamwise vortices near the wall – elongated low momentum streaks are formed, with a typical spanwise spacing of $\lambda_z \approx 100\nu/u_*$. This process has a smaller scale than the stones on a rough bed, so it has to be different for rough walls. The larger isotropy of the turbulence above rough beds reflects this difference. In the following we focus on coherent structures over rough beds with high Reynolds numbers.

Raupach (1981) applied a quadrant analysis to point velocity measurements of a rough-bed flow. Near smooth beds the quadrant where the (u', v') -vector is present (Q_i , $i = 1, 2, 3, 4$) has been shown to be linked to the kind of coherent structure present. These quadrants are also linked to the sign of the instantaneous Reynolds stress, $-u'v'$. Therefore Q_4 ($u' > 0$, $v' < 0$) and Q_2 ($u' < 0$, $v' > 0$) events occur most frequently, as in these quadrants $-u'v' > 0$. So a quadrant analysis gives information on how the average Reynolds stress is generated as well. Q_4 events were seen to become the most important contributions to the Reynolds stress near rough walls ($y/h \lesssim 0.1$), in contrast to smooth wall flows where Q_2 events are most important. Further from the wall the contributions of Q_2 and Q_4 events are similar to those over the smooth wall surfaces (i.e. wall similarity). The names that are often given to the various events are taken from the research over smooth walls: outward interaction, ejection, inward interaction, and sweep for quadrants 1 to 4 respectively. As for rough-bed and non-uniform flow the link between a certain structure and the quadrant of the velocity vector is less clear, we will refer for instance to a Q_4 event instead of a sweep.

The smooth-wall bursting process is usually regarded as a near-wall phenomenon. However, the outer flow is also seen to contain coherent structures, roughly consisting of wedge-shaped areas with uniform momentum bordered by small-scale vortices (Grass, 1971; Nezu & Nakagawa, 1993; Buffin-Bélanger *et al.*, 2000). These structures have also been described as large ‘rollers’ (spanwise vortices), covering the water depth, and with average longitudinal dimensions of 4 to 5 times the water depth (Tamburrino & Gulliver, 1999; Shvidchenko & Pender, 2001). The largest structures are influenced by the upper boundary of the flow, so differences are expected between pressurised flow, open-channel flow, and developing boundary layers, more so than for the near-bed flow structures.

Adrian *et al.* (2000b) proposed a model for the structure of the outer flow (see fig. 2.1) based on smooth-wall boundary layer experiments with $Re_\delta \equiv u_0\delta/\nu \approx 7000$ (δ is the boundary layer thickness and u_0 the free stream velocity.) Hairpin vortices originating from the bed align with their heads on straight lines, forming ‘hairpin vortex packages’ (HVP). The induced flow under these vortices causes the fluid under them to retard uniformly. The structures can grow well into the outer flow, where they become broader, weaker, and are advected faster. They can also be nested inside each other. The HVP-model does not include a description of flow structures with increased velocities. HVPs are also observed in high Reynolds number atmospheric boundary layers (Hommema & Adrian, 2003). In a gravel-bed river with $Re \equiv \langle \bar{u} \rangle_h h/\nu \approx 1.4 \cdot 10^5$ ($\langle \bar{u} \rangle_h$ is the depth-averaged \bar{u}) Buffin-Bélanger *et al.* (2000) measured velocities simultaneously at three (varying) positions over the depth. Large-scale wedge-like flow structures with either increased or decreased velocity over most of the depth were present, with a front tilted in the streamwise direction with an

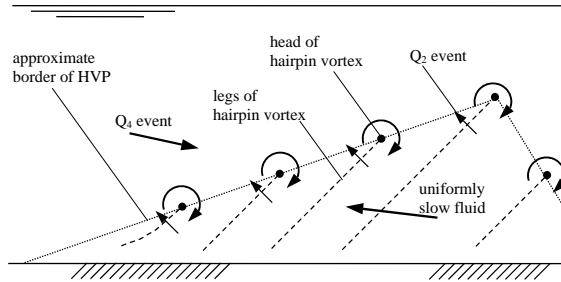


Figure 2.1: Model of HVP, viewed from the side. Flow is from left to right.

average angle of 36° with the bed, and length scales¹ of $2\text{--}5h$ (on average $2\text{--}3h$). Flow structures can become very large. In pipe flow, energy was measured at wavelengths of fourteen pipe radii (Kim & Adrian, 1999). This was thought to be caused by the alignment of several HVPS.

Tomkins (2001) measured HVPS in boundary layer flow over a rough wall consisting of hemispheres placed with a low density with $Re_* \equiv u_*d/\nu = 200$ and 400 (d is the sphere diameter). The packets had upstream slopes with angles to the wall in the range of $10\text{--}20^\circ$. The maximum length scale in the streamwise correlation for $Re_* = 400$ was 0.6δ compared to 0.74δ for the smooth wall. It was conjectured that this was due to the disturbance of the organisation of the vortices by the roughness elements. Near the roughness elements (for $Re_* = 400$) Q_2 events were observed at $y^+ \approx 100$ that were much larger than the average Q_2 event over a smooth wall. It was conjectured that the strong hairpin vortices that create these events are introduced into the layer by the roughness elements, and adopt the scale of the elements.

Hairpin or horseshoe vortices are a common flow structure in wall flow. They can be created by various mechanisms. In the standard mechanism the hairpin vortices are created by the instability of the near-bed laminar sublayer. A second mechanism is the shedding of hairpin vortices from roughness elements on the bed (Arcalar & Smith, 1987). Hairpin vortices can also be created by strong, existing hairpin vortices (Zhou *et al.*, 1999). In the $x\text{--}y$ plane the heads of these vortices appear as a vortex with a Q_2 event near it, which is caused by the presence of the legs of the vortex, see fig. 2.1.

The low-speed streaks that are bordered by elongated counter rotating streamwise vortices are visible in rough-wall experiments as well (Grass & Mansour-Tehrani,

¹Only the time scales were given. The length scale is simply estimated here as $(\bar{u})_h T$, where T is the duration of the increased velocity

1996; Defina, 1999). Grass & Mansour-Tehrani (1996) found that the spanwise spacing of these structures near rough walls is $\lambda_z \approx 100\nu_t/u_*$ instead of $\lambda_z \approx 100\nu/u_*$ (ν_t is the turbulence viscosity). Away from the wall $\lambda_z \approx 4y$ (Defina, 1999).

Turbulence Wall pressure fluctuations

Booij (1998) states that pressure fluctuations caused by turbulent eddies could contribute considerably to the forces that initiate motion of bed particles. These pressures also act on a smooth wall and are known as turbulence wall pressures (TWP). They have mainly been studied in other fields of application (e.g. naval and acoustical); yet numerous aspects are of interest to the present research.

Pressure fluctuations on the bed can be obtained by solving the Poisson equation for fluctuating pressures, p' (Chang *et al.*, 1999):

$$\nabla^2 p' = -2\rho \frac{\partial \bar{u}_i}{\partial x_j} \frac{\partial u'_j}{\partial x_i} - \rho \frac{\partial^2 (u'_i u'_j - \overline{u'_i u'_j})}{\partial x_i \partial x_j}, \quad (2.4)$$

where $i, j = x, y, z$. It follows from the Poisson equation that TWP in an incompressible fluid are caused by the velocity fluctuation gradients in the entire fluid domain at a certain moment, although the contribution of a single source decreases with its distance from the wall. Different regions of the pressure spectrum are influenced by sources from different regions. In general, lower-frequency TWP are caused by larger-scale fluctuations further away.

A number of power-laws have been predicted for the power spectrum of the TWP under an equilibrium boundary layer flow, which is examined most often. Some power laws have also been measured (Gravante *et al.*, 1998; Farabee & Casarella, 1991). In the low-frequency range ($2\pi f\delta/u_* < 5$, f is frequency) the spectra collapse on the outer variables δ , and u_* , although other variables are possible (\bar{u} is proportional to u_* , for instance). Farabee & Casarella (1991) state that the scaling behaviour in the low-frequency range will be different in pressurised flow, due to the different upper boundary. The length scale h will be more appropriate than δ . In the mid region ($5 < 2\pi f\delta/u_* < 100$) the spectrum is quite flat. The scaling variables used for the high-frequency range are ν and u_* . A frequency range exists where the spectrum scales on both inner and outer variables ($100 < 2\pi f\delta/u_*$ and $2\pi f\nu/u_*^2 < 0.3$). Here the spectrum would decrease as f^{-1} . The velocity sources of these pressures are thought to be situated in the log-region of the boundary layer. The width of this range increases with increasing Reynolds number. In the high-frequency range ($0.3 < 2\pi f\nu/u_*^2$), a power law according to $f^{-7/3}$ is predicted, but it has not clearly been measured in an equilibrium boundary layer flow. For the highest, viscosity dominated, frequencies, a power law of f^{-5} is predicted.

Based on these scaling laws Farabee & Casarella (1991) proposed the following relation for the variance of the TWP for $Re_\delta > 333$:

$$\frac{\sigma(p')^2}{\tau_w^2} = 6.5 + 1.86 \ln \left(\frac{Re_\delta}{333} \right) \quad . \quad (2.5)$$

Only one paper was found which presented measurements of TWP on a rough wall (Blake, 1970). Measurements were done under an equilibrium boundary layer on both smooth and rough walls. The scaling and shape of the spectrum appeared to be similar for both walls, with the distinction that the length scale that can be used to collapse the high-frequency part of the rough wall spectrum is the roughness height, d , instead of the viscous length scale (ν/u_*). The dimensionless frequency and spectral density, G_{pp} , for which the high frequency part of the pressure spectra collapse, are now: $f^+ = fd/u_*$ and $G_{pp}^+(f^+) = G_{pp}(f)u_*/\tau_b^2 d$. For the low frequencies the wall pressures under a rough boundary layer flow show the same scaling behaviour as for the smooth wall. Also the influence of various spatial densities of roughness-elements was investigated. The spacing between the roughness elements is of influence to a lesser extent than their height. The r.m.s. value of the pressure fluctuations (scaled by the dynamic pressure) was found to be roughly equal to that on smooth walls, although the value was different than found in later research.

Pressure fluctuations with a value of four times the standard deviation of the TWP have been found in windtunnels (Schewe, 1983). This implies that the TWP can become very large, and possibly influence the stability of stones. Correlation of pressures with velocities did give clear origins for positive pressures. They appear to be located near shear layers with a velocity deficit, followed by fast moving flow. However, no clear velocity sources have been found for the negative pressures.

Uittenbogaard *et al.* (1998) developed a model, based on eq. (2.4), that derives the fluctuating pressures on the bed from calculations with a k - ε model. The calculated turbulence kinetic energy k and the dissipation ε are integrated via weighting functions to obtain an estimate of the standard deviation of the TWP. The assumption of $u'/\bar{u} \ll 1$ is made, so it is not generally applicable. Moreover, the model is derived from the first (mean-shear) term in eq. (2.4). The second (turbulence-turbulence) term is neglected. This term was proven to account for only a little over 50% of the pressure fluctuations under a channel flow by (Chang *et al.*, 1999), so the model is far from perfect. It might be used to obtain an indication of the relative change of TWP under a non-uniform channel flow (under the assumption that the magnitudes of the mean-shear and turbulence-turbulence term are correlated). The model has not been calibrated or validated extensively by measurements until now.

2.2.2 Backward-facing step

A characteristic of flow passing hydraulic structures is the separation of the flow. In a separated flow the turbulence intensity is increased, which can cause an increased attack on bed protections. A basic example of a separating flow is the flow over a backward-facing step. This configuration is used to model a flow with increased turbulence intensity in the measurements described later.

Also for flow downstream of a backward-facing step the Reynolds number(s) must be high enough to represent environmental flows. Behind a backward-facing step a recirculating eddy develops. Between this eddy and the upper (faster) flow a mixing layer is present where turbulence is generated. In open-channel smooth-bed flows the upper flow was seen to reattach to the bed at about 5 to 6 step heights, h_s , downstream of the step, for $Re \approx 1-4 \cdot 10^4$ and $Fr \equiv \langle u \rangle_h / \sqrt{gh} = 0.12-0.33$. The flow reattached further from the step for lower Re , and a higher Fr seemed to increase the reattachment length (Nakagawa & Nezu, 1987). Xingkui & Fontijn (1993) measured negative drag forces on a bed element at ten step heights behind a BFS with a high Fr and a rough bed downstream of the step.

Downstream from the reattachment point a new boundary layer starts to develop, and the turbulence intensity originating from the mixing layer decays to the value for a uniform flow. The following relation is proposed for the depth-averaged normalised turbulence intensity $\langle r_u \rangle_h$ ($\equiv \langle \sigma(u) \rangle_h / \langle \bar{u} \rangle_h$) behind a BFS (Schierreck, 2001):

$$\langle r_u \rangle_h = \sqrt{0.5k_0 \left[1 - \frac{h_s}{h}\right]^{-2} \left[\frac{x}{6.67h} + 1\right]^{-1.08} + 1.45 c_f} \quad , \quad (2.6)$$

where $k_0 = k_{\max}/u_0^2$ in the centre of the mixing layer (≈ 0.045), u_0 is the average velocity on the step, c_f the friction coefficient $u_*^2/\langle u \rangle_h^2$, and $x = 0$ at the reattachment point.

A large number of flow processes occur in this complicated flow. Downstream from the separation point a mixing layer is present where Kelvin-Helmholtz instabilities are generated. These instabilities roll up and form spanwise vortices. These vortices pair to form larger structures. They also become unstable over their rotational axis and develop into three-dimensional turbulence. At the reattachment point flow structures with a size of the order of the step height are observed. Also a low-frequency flapping motion of the separation bubble is reported, with frequencies about eight times lower than the large scales arising from the mixing layer. This is thought to be caused by the entrainment of fluid by the mixing layer, which is released periodically from the recirculation area (Lee & Sung, 2002). Downstream of the reattachment point in the relaxation zone, both large-scale, two-dimensional structures from the mixing layer are observed, as well as vortex packages with higher intensities than for a uniform flow (Kostas *et al.*, 2002).

2.2.3 Roughness transition

Bed protections are usually placed on a sand bed, which has a smaller hydraulic roughness than the stones of the protection layer. The mean velocity and turbulence of the flow reaching the increased roughness are not immediately adapted to it. This sudden increase in roughness gives rise to another non-uniform flow that is characteristic for bed-protections. It is also studied in the present experiments.

Flow over a transition from a smooth bed to a rough bed is characterised by a newly developing internal boundary layer, on the basis of the increased roughness. Nezu & Tominaga (1994) found that in the very first part the bed shear stress was highly increased. This can be explained by the large near-bed velocity of the smooth-wall velocity profile that ‘hits’ the first bed elements. The bed shear stress decreases very rapidly, over a length of one to two times the depths, to the equilibrium value for the rough bed. Conversely, Chen & Chiew (2003) found a more gradual change of the bed shear stress from the low magnitude of the smooth bed to the large magnitude of the rough bed over about $10h$. The second-order moments of the velocity fluctuations take a longer distance to adapt (Chen & Chiew, 2003).

2.3 Forces on a single stone

Drag and Lift, the two components of the hydrodynamic force that acts on a stone, are discussed in this section. The drag and lift force are defined here as the streamwise and vertical force components respectively. Basic knowledge about these forces is treated briefly. Subsequently the various definitions used for drag and lift forces on stones are discussed. Then the more empirical results on drag and lift on particles that are part of a rough bed are given.

2.3.1 Basics

Steady drag. The classic example of a drag force on a body is the case of a sphere in an infinite, uniform flow field of an incompressible fluid with velocity u . The parameter that determines the magnitude of the drag force on this sphere is the Reynolds number, $Re \equiv ud/\nu$ where d is the diameter of the sphere. For low Reynolds numbers ($Re \lesssim 1$, the Stokes regime) the resistance is dominated by viscous stresses (skin drag). For higher Reynolds numbers the laminar flow separates from the sphere and the stagnation pressure starts to influence the drag force (form drag). For still higher Reynolds numbers the wake becomes unstable, first with periodic oscillations ($Re \approx 10^2$), later with a turbulent wake ($Re \gtrsim 10^3$). At these high Reynolds numbers the skin drag becomes negligible and the drag force is given by:

$$F_D = \frac{1}{2}C_D\rho Au|u| \quad , \quad (2.7)$$

where C_D is the drag coefficient and A is the project area of the particle. At even higher Reynolds numbers ($Re \approx 2.5 \times 10^5$) the drag coefficient for the sphere decreases (the ‘drag crisis’) due to the transition of the boundary layer on the sphere from laminar to turbulent, which causes the wake to decrease in size. When the sphere is rough, the Reynolds number at which the drag crisis occurs becomes lower. For objects with sharp edges C_D remains constant for high Reynolds numbers.

Dynamic drag. A pressure gradient also gives a net force on a particle. An example is the buoyancy force due to the hydrostatic pressure gradient. When the sphere is accelerating relative to the flow, an extra force is exerted on the sphere in consequence of the acceleration of the fluid surrounding the sphere – the added mass. These two forces combined are given by (Maxey & Riley, 1983):

$$\vec{F} = \rho V \frac{D\vec{u}}{Dt} + \rho V C_m \left(\frac{D\vec{u}}{Dt} - \frac{d\vec{v}_p}{dt} \right) \quad , \quad (2.8)$$

where C_m is the added mass coefficient, and \vec{v}_p the velocity of the particle.

Booij (1998) states that turbulent eddies could contribute considerably to the forces that initiate motion of bed particles via eq. (2.8). He estimates that eddies twice the size of a stone give the most effective pressure gradient for moving a stone. Larger eddies have a smaller gradient, and the net forces due to pressure fluctuations created by smaller eddies is negligible due to phase cancellations when integrated over the surface of the stone. In places like a stagnation point, with negligible flow velocity, these forces could be a major contribution to the force.

Lift. When a sphere is surrounded by a flow with a velocity gradient normal to the flow direction, the velocity difference over the sphere results in a lift force. Asymmetrical and rotating bodies can also produce an asymmetrical pressure distribution, and therefore a lift component.

An estimation of the lift force on a particle can be obtained from potential flow theory. Auton (1987) determined an equation for the lift force on a sphere in inviscid, rotational flow. It reads:

$$\vec{F} = \rho C'_L V \vec{u} \times \vec{\omega} \quad , \quad (2.9)$$

where C'_L is a lift coefficient, V the volume of the sphere, and $\vec{\omega}$ the vorticity. For a particle on a flat bed the following approximations can be made: $V \approx d^3$, $\vec{u} \times \vec{\omega} \approx u \partial u / \partial y \vec{e}_y$, $\partial u / \partial y \approx u/d$, and $A \approx d^2$, which – when substituted – transform eq. (2.9) into almost the same form as eq. (2.7):

$$F_L = \frac{1}{2} C_L \rho A u^2 \quad . \quad (2.10)$$

Vortex shedding from an object in free shear flow can also give rise to large lift force fluctuations, resulting in a mean lift force in the opposite direction to that given

by eq. (2.9) (Moraga *et al.*, 1999). The exact interaction of these two mechanisms, the influence of a wall, and the importance for non-spherical particles on a bed is not yet understood.

Near-wall particles. Determining the value of the forces on particles near or on a (rough) wall becomes more difficult. One complicating factor is the random character of the rough wall. Both the near-bed flow profile and the exact shape of the rough wall are difficult to define, which makes quantification of the forces hard. Generally the drag force follows eq. (2.7), but the lift force can deviate from eq. (2.10).

Many different definitions are used for the parameters in eqs. (2.7) and (2.10). Therefore mutual comparison of C_D and C_L values is difficult. Only rough estimates can be made. For instance, Benedict & Christensen (1972) compared their calculated lift forces with the experimental results of Einstein & El-Samni (1949) and Chepil (1958). To this end many assumptions about the experimental works had to be made. The calculated lift forces resembled those measured. Nevertheless, doubt remains about the validity of the comparison.

Different definitions lead to different values of C . For example, the drag coefficients $C_{D,0.15}$, $C_{D,0}$, and $C_{D,*}$, which are defined using \bar{u} at $0.15d$ above the top of the sphere, \bar{u} measured at the height of the centre of the sphere, and u_* , respectively, can differ by an order of magnitude. The flow velocity near the bed has a large vertical gradient, making the values of C_D and C_L very sensitive to the choice of the y -coordinate. The area A can be the entire projected area or the exposed part of it. In the equation for the lift force, A can be the plan area of the stone, or a representative area around the protruding stone. These differences make mutual comparison of C_D - or C_L -values from literature difficult. For a sphere the area used in eqs. (2.7) and (2.10) usually is $\pi d^2/4$. The various definitions are discussed in Hofland (2000).

The main results found on lift and drag forces are presented below. Especially experiments dealing with uniform flow over rough boundaries are treated. The roughness elements generally used are spheres.

2.3.2 Drag force

In the previous section some basic features of the drag force were already mentioned. Usually eq. (2.7) is assumed to describe the mean drag force. The drag coefficient becomes fairly constant for high particle Reynolds numbers, but most authors still find a small dependency of C_D on the particle Reynolds number.

Spheres in a closely packed arrangement all give an equal contribution to the bottom friction, consisting of the drag force on the sphere divided by its surrounding (hexagonal) area. Therefore the value of the drag coefficient can be determined exactly

at $C_{D,*} = 4\sqrt{3}/\pi \approx 2.2$ (Watters & Rao, 1971). This corresponds to² $C_{D,0.15} \approx 0.3 \pm 0.05$. Xingkui & Fontijn (1993) measured the drag on a naturally formed stone between other natural stones placed on a flat bed, so with approximately the same protrusion of the top of the particle above the mean bed level, Π . They found a comparable $C_{D,0.15} = 0.36$.

For more complicated geometries of the bed, every element is subject to a different drag force. Chepil (1958) did measurements on hemispheres spaced three diameters apart in a hexagonal arrangement, resembling a ‘natural’ spacing of the upper stones, which are moved most easily. For these hemispheres $\Pi/d \approx 0.5$. A linear regression through his data points of friction velocity versus lift force yields $C_{D,*} \approx 5$ and $C_{D,0.15} \approx 0.26$. In another paper Chepil (1959) concluded that these upper grains take up two thirds of the drag on the bed.

For single spheres on top of other spheres values were found that closely resemble the values of the drag on a sphere in free fall where $C_{D,0} \approx 0.4$ (Coleman, 1967; Coleman, 1972; Patnaik *et al.*, 1992). The reference velocity now is the velocity at the centre of the sphere, without the sphere present. Extrapolating the velocity yields $C_{D,0.15} \approx 0.23$ and $C_{D,*} \approx 18.3$.

It can be concluded that using $u_{0.15}$ as the reference velocity in eq. (2.7) leads to a rather constant drag coefficient for all protrusions, $C_{D,0.15} \approx 0.23$ – 0.3 . The velocity measured at this height was found to have more special meanings. First, the correlation between the instantaneous velocity at this height and the drag force was maximum (Xingkui & Fontijn, 1993). Secondly, Einstein & El-Samni (1949) found a constant C_L for different flow velocities at this height.

Fluctuations. Kalinske (1947) gave two possible sources for fluctuating (drag) forces on a particle. The first was the unsteady separation of the flow from the particle. The second was the larger-scale turbulence fluctuations from the main stream. If the ambient flow velocity is rather uniform, does not change too rapidly in time, and $|u'| \ll \bar{u}$, then the fluctuating drag force changes according to eq. (2.7) for the steady force, so the quasi-steady fluctuating force – without contributions of eq. (2.8) – becomes proportional to:

$$F'_D \propto \bar{u}u' \quad . \quad (2.11)$$

However, close to the bed the extreme values of $|u'|$ can have the same order of magnitude as \bar{u} . Generally $|u'| < \bar{u}$ still holds for a uniform flow. Then $u|u| = u^2$ and the quasi-steady force will be:

$$F'_D \propto \bar{u}u' + \frac{1}{2}u'^2 - \frac{1}{2}\sigma(u)^2 \quad . \quad (2.12)$$

²The velocity is extrapolated using the logarithmic velocity profile [eq. (2.1)] with $y_0 = d/30$ and the theoretical zero level at $\approx 0.2d$ under the top of the sphere.

Not many direct simultaneous measurements of \bar{u}' and \bar{F}' have been made to validate eqs. (2.11) and (2.12). Examples are Radecke & Schulz-DuBois (1988), Xingkui & Fontijn (1993) and Schmeckle & Nelson (2003). Schmeckle & Nelson (2003) tried to predict the fluctuating and mean drag on a particle for a constant C_D but the fluctuations were overpredicted by about 30%. They attribute the difference to the influence of the added mass and pressure gradient, eq. (2.8). For stones with a low protrusion, experimentally determined values for the ratio $\sigma(F_D)/\overline{F_D}$ are in the range of 0.4–0.8 (Chepil, 1959; Cheng & Clyde, 1972; Xingkui & Fontijn, 1993). This means that the fluctuating part of the drag force is of the same order of magnitude as the time-averaged force, and should be taken into account when examining stone stability.

2.3.3 Lift force

The lift coefficient also becomes fairly constant for high Re_* . Pressures around the particle are then proportional to the stagnation pressure. But the variation of this force with varying particle orientation is less predictable. The force is negative (directed towards the boundary) for certain positions at low Re_* . When $Re_* > 100$ the lift is mostly found to be positive. At high Re_* , values of 0.15 to 0.22 are found for $C_{L,0.15}$, when the particle is placed between other particles (Einstein & El-Samni, 1949; Xingkui & Fontijn, 1993; Benedict & Christensen, 1972). The measurements of Chepil (1958) indicate that $C_{L,0.15} \approx 0.23$ for the configuration with hemispheres spaced three diameters apart. Based on the same data Wiberg & Smith (1985) find $C_{L,t} \approx 0.2$ where $C_{L,t}$ is based on the velocity at the level of the top of the spheres.

A sphere located on, or just above a boundary clearly has different lift characteristics. For a sphere just above a smooth wall Willets & Murray (1981) found a negative lift when a small gap, G , is present between the sphere and the wall: $G/d = 0.05$ – 0.1 . On rough surfaces, it is well possible that no negative lift will occur, as the gap between the particle and the bottom has an entirely different shape. Patnaik *et al.* (1994) measured lift on a sphere on a rough bottom in a windtunnel with high Re_* and a high ratio of particle size to boundary-layer thickness, $d/\delta = 0.2$ – 0.5 , which does not seem realistic for bed protections. They found $C_{L,0} \approx 0.1$ – 0.4 . $C_{L,0}$ was decreasing for increasing Reynolds number and increasing d/δ . Coleman (1967) found higher values for $C_{L,0}$, but as he determined the lift force from a force balance using the critical flow velocity and the measured drag force, this was more an indication of the maximum force occurring during the measurement.

Fluctuations. For the fluctuating part of the lift force the following relation is proposed by Radecke & Schulz-DuBois (1988):

$$F'_L \propto a\bar{u}u' + b\bar{w}w' \quad . \quad (2.13)$$

The first term on the right-hand side is caused by the Bernoulli-effect. Like the fluctuating drag force, it is the linear expansion of eq. (2.10). The second term is due to the fact that the instantaneous flow direction does not have to be horizontal like the mean flow. Therefore, the instantaneous force in line with the velocity can have a vertical component. Radecke & Schulz-DuBois (1988) used eq. (2.13) to determine the gain function from the velocity spectrum to the force spectrum for a sphere on a smooth wall. Using these gain functions they could predict 20–70% of the power spectrum of the forces based on point measurements of the velocity. The spectrum for the lowest frequencies was almost exactly predicted from the measured gain functions. Most of the variance originated from the u fluctuations [first term on the right hand side of eq. (2.13)]. The second term caused a small part of the variance in a frequency band corresponding to the Strouhal number of the eddies shed from the sphere.

The fluctuating part of the lift force was found to be normally distributed over the interval of 1–97% exceedance probability (Einstein & El-Samni, 1949). However, Xingkui & Fontijn (1993) found for a naturally shaped bed element that the distribution outside this range deviated in such a way that the larger fluctuations of the lift force occurred more frequently. Reported values for the normalised standard deviation of the lift force, $\sigma(F_L)/\overline{F}_L$, are 0.36 (Einstein & El-Samni, 1949), 0.49 (Chepil, 1959), and 1.00 (Xingkui & Fontijn, 1993, natural stone), so also these fluctuations are of the same order of magnitude as the mean force.

Willems & Murray (1981) studied the lift on a sphere near a smooth boundary for $G/d = 0-2$. They saw that the position of the flow separation line varied randomly, thereby changing the direction of the force on the sphere often and abruptly. They suspected that this was due to turbulent eddies from the main flow. This effect will probably be less pronounced on natural stones with sharp edges that fix the flow separation locations.

2.4 Entrainment mechanism

The force magnitudes mentioned in the previous section do not give all information needed to determine when a stone will be entrained. First, additional information is needed on the duration of the fluctuations: a force should last long enough to displace a particle. Also the mean and standard deviation of the forces alone do not give all information about the chance of occurrence of extreme fluctuations. Further the correlation between the drag and lift force is of importance. Also the point of application of the forces determines the moment that is exerted on the stone. Finally, the movement of the particle itself will influence the forces on it. All these influences together can be defined as the entrainment mechanism. The entrainment mechanism is possibly connected to the occurrence of certain coherent flow structures.

A review of previous research on this topic is given in this section. As hardly any research is available about the exact configuration studied presently, research is also discussed dealing with sediment transport instead of entrainment, smooth beds instead of rough beds, and higher mobility instead of low-mobility transport.

Smooth bed. Sutherland (1967) visualised the flow during the entrainment of sand from a plane, hydraulically smooth bed and from a dune bed by means of dye injection. For the plane bed case, it was observed that the entrainment of grains was correlated to ejections of parts of unstable low speed streaks near the bed (i.e. Q_2 events). Always several grains moved at the same time, indicating that the size of the eddies responsible for movement was larger than the grain size. In the case with the dune bed, which is comparable to a series of backward-facing steps, grains were displaced first at the reattachment point, although mean flow velocities are low at that position. They were moving in a random, jerky manner. Sometimes small ‘craters’ were visible, indicating the impingement of eddies with a large downward velocity. Next to the shear stress a possible minor role in the entrainment process was attributed to the hydrodynamic lift, pressure gradients in the eddy, vertical forces due to contacts with other grains, and upward flow through the porous bed. In general Q_2 events are seen to influence (suspended) sediment transport for hydraulically smooth beds and high-mobility flow (Sutherland, 1967; Niño & Garcia, 1996).

Grass (1970) used high-speed hydrogen bubble photographs to measure the instantaneous (u,v) flow profile near a hydraulically smooth sand bed at low-mobility conditions. The instantaneous bed shear stress, τ_b , could be determined from the slope of the velocity profile in the viscous sublayer. Grains started to move during events with an increased shear stress; the quantities $d\tau_b/dt$ and v' were correlated less to the initiation of movement. However, the value of the critical shear stress τ_c varied for different grains.

Gyr & Schmid (1997) also studied the incipient motion of grains from a smooth sand bed, and linked this to the so-called bursting cycle. Based on the pattern of the displaced sand they concluded: “When a sweep consisting of a patch of spanwise limited fast outer fluid hits the bed, the fast fluid from the outer flow regions is decelerated and produces very concentrated vorticity at its edges. These vortex cores have a high under-pressure which is the motor for the sediment transport. The resulting transport is directed mainly sideways from the impact area and produces a sand stripe on each side of the sweep”. This can be seen as a direct influence of turbulence wall pressures on entrainment: a vortex-induced pressure gradient is dislodging the grains instead of a shear stress or a drag force. Based on a comparison of the sizes of the coherent structures and the grain sizes they conclude that always several grains will move at once, and that: “The study of incipient motion of single grains (...) only makes sense for fairly large grains”. The viscosity-dominated bursting cycle does not

exist over rough walls, so this idea cannot be applied directly to the present case.

Rough bed. Drake *et al.* (1988) filmed transport of gravel with a 4 mm median diameter in a natural stream where $Re \approx 2 \cdot 10^5$ and $\Psi \approx 2\Psi_c$. They observed that transport of gravel took place in what they called sweep-events, inferred to have an increased streamwise, and downward velocity (i.e. Q_4 events). These events were characterised by a localised roughly circular area on the bed where particles were entrained. These areas became larger and travelled downstream faster than the particles that were entrained, causing an elongated area where transport occurred. These sweep-events occupied 9% of the bed area at any given time and accounted for about 70% of the total transport.

Thorne *et al.* (1989) did measurements of flow velocity and gravel transport on a flat sea bed and saw that mainly u' was correlated to the transport of the gravel. The instantaneous transport rate differed significantly between two locations, for the same instantaneous near-bed flow velocity.

Non-uniform flows. Xingkui & Fontijn (1993) did research on lift and drag forces on a large, naturally shaped stone near a backward-facing step (BFS). The turbulence structure of the flow near the stone varied strongly with distance from the stone to the step. The time-averaged drag coefficient was determined by varying the flow velocity, and relating the drag force linearly to the square of the average velocity. The (average) drag coefficient was found to be increasing with increasing distance downstream of the step (until at least $20h_s$), tending to a constant value as the flow became uniform. It can be expected that a drag coefficient defined using the mean velocity, $C_{D,\text{mean}}$, changes for a changing turbulence intensity if the coefficient based in the instantaneous velocity [defined in eq. (2.7)] is constant: $C_{D,\text{mean}} = C_D (1 + \sigma(u)^2/\bar{u}^2)$ for $|u'| < \bar{u} \forall u'$. However, this does not explain the increasing value for the drag coefficient with increasing distance from the BFS. Apparently the quasi-steady mechanism does not explain all fluctuations. The lift coefficient could not be determined at all in the same way near the step. The lift force was positive at all locations behind the BFS.

Nelson *et al.* (1995) undertook experiments on the entrainment of coarse sand at $Re_* \approx 22.5$, so the bed was transitionally rough. Flow velocity (u and v) and sediment transport rate were measured instantaneously at various positions behind a BFS. Quite some transport occurred, as the dimensionless shear stress far behind the step was twice the critical value. The maximum near-bed $\sigma(u)$ was measured at $10h_s$ from the step, but the highest transport was measured at $20h_s$ from the step. Velocity and transport were correlated in order to find out which turbulence events cause transport. Especially the longitudinal velocity fluctuations, u' , were found to be correlated to transport of grains. Instantaneous values of $-u'v'$ and $-v'$

were both positively correlated to the transport as well, only less clearly. They also concluded that both low-frequency fluctuations, caused by eddies shedding from the step, and higher-frequency fluctuations contributed to the transport. However, for different positions behind the step equal (u,v) combinations gave different transport rates. It was proposed that the magnitude of the transport for a certain value of u' is frequency-dependent.

De Gunst (1999) studied stone stability behind a BFS. The flow had a rigid lid. Critical conditions were reached when the flow velocity was about 20% lower than the critical flow conditions under uniform flow. Most damage occurred in an area beginning at the reattachment point ($6.5h_s$) to $9h_s$ downstream of the step. Significantly increased damage was seen to occur to roughly $18h_s$ downstream of the step, but the entrainment rate decreased asymptotically. Around the reattachment point transport of stones occurred in both upstream and downstream direction.

2.5 Stability of a granular bed

In this section expressions for stability of a granular beds are treated. These expressions are derived using many assumptions and simplifications, so the focus now shifts from science to engineering.

The words ‘stability’ and ‘damage’ are rather arbitrary. There are always some particles that have an unstable position, so an arbitrary state of the bed has to be defined as being unstable. Also damage has to be quantified. Transport, entrainment, mobility and displacement length are parameters that can be quantified better. These quantities are defined and compared, and some ways in which they are used to determine the stability of bed protections are discussed. One way of dealing with the random nature of bed protections is to use distributions of values of certain parameters, leading to stochastic approaches of evaluating bed stability. These are discussed last.

2.5.1 Initiation of motion

Granular bed protections can be designed using various criteria. Defining a critical dimensionless shear stress is one of the oldest and most basic methods. A certain low dimensionless shear stress is chosen as being the critical shear stress, τ_c , at which the bed material will initiate motion. Bed protections must be able to withstand this load. In this way bed protections are designed without any significant transport of stones.

The thesis of Shields (1936) is the best-known research on initiation of motion in uniform turbulent flow. He defined ‘initiation of motion’ as the state of the bed in which some particles can be seen displacing at each moment at each part of the bed.

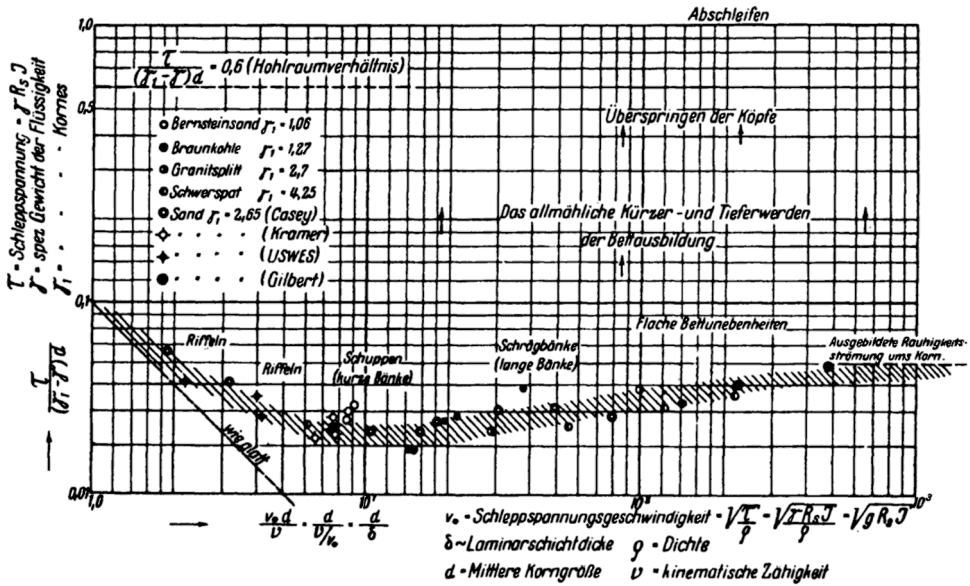


Figure 2.2: Original Shields curve (1936). The hatched area depicts the critical shear stress as a function of the particle Reynolds number.

This state occurs when the (dimensionless) shear stress has a certain critical value. For a lower shear stress particles will only move occasionally, or not at all. For a higher shear stress the whole top layer will start to move, and bed forms will emerge. The dimensionless shear stress or Shields parameter is defined by:

$$\Psi \equiv \frac{u_*^2}{\Delta g d} = \frac{\tau_b}{\rho \Delta g d} \quad , \quad (2.14)$$

where Ψ is the Shields parameter, $\Delta = \rho_s/\rho - 1$, ρ_s is the stone density, and g the gravitational acceleration. This is roughly the ratio of the load on the particle ($\propto \rho u^2 d^2$) to the gravitational force on the particle that resists movement ($\propto g(\rho_s - \rho)d^3$). The critical value of Ψ where motion starts is called the critical Shields parameter, Ψ_c . This parameter is a function of the particle Reynolds number, Re_* . Figure 2.2 shows this relation, also known as the Shields curve. Shields used particles of different densities and was able to cover a large range of particle Reynolds numbers. The value of the critical Shields parameter for high Re_* is a constant value of about 0.055.

Later researchers defined several states of mobility – described qualitatively as the observed number of particles moving and or rocking per area of bed – and it was

found that for every state a graph like figure 2.2 could be established (Breusers & Schukking, 1971, for example).

Bed protections are characterised by a very low mobility of the bed material and by fully rough flow, i.e. $Re_* \gtrsim 500$. The value of the critical Shields parameter which is used as a safe limit for bed protections is: $\Psi_c = 0.03\text{--}0.04$. Therefore the flows regarded in the present research are located in figure 2.2 in the bottom right corner, under the hatched line (low-mobility flow) and extending right of the graph (hydraulically rough flow). Note that the critical Shields parameter only represents uniform flow, whereas here non-uniform flows are studied.

2.5.2 Bed load transport

Designing bed protections using the stability approach could lead to conservative designs. Sometimes a small amount of movement of the bed material (i.e. damage) can be allowed. Therefore it is useful to obtain an estimate of the amount of damage. To quantify the amount of damage, the balance equation for sediment can be used (Mosselman *et al.*, 2000):

$$\frac{\partial y_b}{\partial t} = -\frac{1}{(1-\epsilon)} \frac{\partial q_s}{\partial x} \quad , \quad (2.15)$$

where y_b is the bed level, t is time, q_s the bed load transport rate (i.e. the volume of particles passing a cross section per unit time and width), and ϵ porosity. According to eq. (2.15) a positive transport gradient causes the bed to lower. Now the lowering of the bed (divided by d) can be used as an indication of the amount of damage in a more flexible approach for designing bed protections. In this way more explicit choices can be made about maintenance frequency and safety, and protection layers could be designed that are economically more viable.

In order to make this method work, a suitable transport equation – including turbulence effects – is needed. There are many bed load transport formulae available, which have limited predictive capabilities. This is due to the fact that transport is dependent on many uncertain parameters and mechanisms. Therefore they should not be used outside the parameter range for which they were calibrated. In the following the specific processes that determine the transport rate are discussed. This could be used to link measurements on a single stone to the bulk transport rate.

Transport equations

Based on assumptions for the different processes in bed load transport, Einstein (1950) derived a transport parameter from combined physical and dimensional analysis and linked it to the Shields parameter. This parameter is used in most transport functions and can be written as:

$$\Phi \equiv q_s / \sqrt{\Delta g d^3} \quad . \quad (2.16)$$

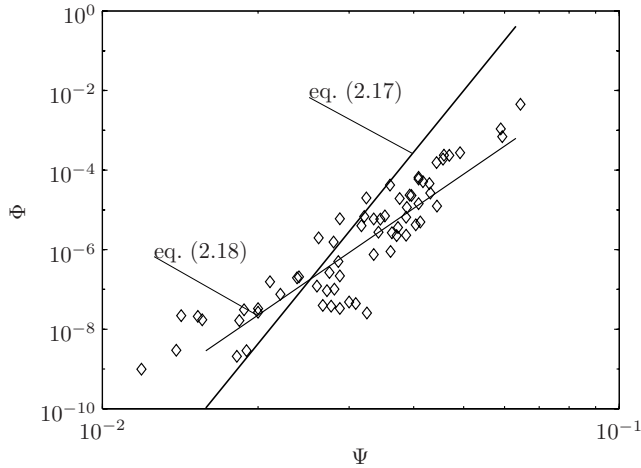


Figure 2.3: Dimensionless transport for low Ψ values after Paintal (large particles only).

Most bed load formulae are written in the form: $\Phi \propto (\Psi - \Psi_c)^n$, or $\Phi \propto \Psi^n$ (Mosselman & Akkerman, 1998) and were developed for higher transports. This makes them useless for the present purpose.

Paintal (1969) did the most elaborate and best-documented measurements on transport under low hydraulic loads, with dimensionless shear stresses below the ‘critical’ value of 0.05, as found by Shields. He fitted the following transport formula:

$$\Phi = 6.56 \cdot 10^{18} \Psi^{16}, \quad \text{for } 0.02 < \Psi < 0.05 \quad . \quad (2.17)$$

He used particles of 2.5, 7.95 and 22.2 mm (sieve diameter). The flow over the smallest material was not completely hydraulically rough. Therefore Mosselman & Akkerman (1998) discarded the data of the 2.5 mm particles and corrected some small calculus errors. The resulting graph is shown in figure 2.3. The resulting equation is:

$$\Phi = 3 \cdot 10^7 \Psi^{8.9}, \quad \text{for } 0.02 < \Psi < 0.05 \quad . \quad (2.18)$$

Processes in transport of coarse material

Einstein (1942) divided sediment transport into the processes of pick-ups and steps of the particles, which led to the formulation of the parameters Ψ and Φ . The pick-up can be related to several other parameters. This is discussed next. Often one or more of the parameters is assumed to be random, leading to stochastic approaches.

In many experiments on stone stability the number of stones that are displaced from a certain bed area are counted. This leads to the measurement of the volume entrainment rate, E , which is the volume of particles that is entrained (entrainment is usually defined as a displacement of at least $1d$) per unit of time and bed area ($[E]=LT^{-1}$). Expressed in terms of the number of entrained particles, it is often called the pick-up rate. The entrainment is linked to the bed load transport by:

$$q_s \approx E L \quad , \quad (2.19)$$

where L is the displacement or step length. As entrainment and step length could be correlated, this step length is not exactly the average displacement length. When the displacement length is assumed to be proportional to d , one can also make a dimensionless parameter for the entrainment:

$$\Phi_E \equiv E/\sqrt{\Delta g d} \quad . \quad (2.20)$$

An expression used for E is:

$$E \propto \frac{dp(\tau_b > \tau_c)}{T_p} \quad , \quad (2.21)$$

where T_p is the typical pick-up duration of a particle, for which d/w_s (Einstein, 1942) or d/u_* (Paintal, 1969) are proposed (w_s is the settling velocity). An assumption in this approach is that the length scale of the flow structures that cause the entrainment is much larger than the particle.

In order to determine the entrainment of a single particle many researchers use a force or moment balance. When the displacing force on the particle exceeds the resisting (gravitational) force the particle will start to move (White, 1940; Wiberg & Smith, 1987; Bridge & Bennet, 1992; Andrews & Smith, 1992; Ling, 1995, for example). The hydrodynamic forces acting on a particle used in these models are usually those according to the quasi-steady forces in eqs. (2.7) and (2.10). The influence of turbulence is rarely regarded. When turbulence is included in the models it usually is by introducing a fluctuating velocity in the quasi-steady equations (2.7) and (2.10), which is equivalent to using a fluctuating u_* .

Mosselman & Akkerman (1998) state that the variability of the displacement lengths – as measured by De Boer (1998) – is high at low hydraulic loads, so a model based on these processes cannot be accurate. However, the varying displacement lengths are consistent with an exponential distribution of the displacement length as found by Nakagawa & Tsujimoto (1980). Under low-mobility conditions the stones move by rolling, which will make the displacement length a function of the bed topography and not only of the flow velocities.

This way of regarding transport seems realistic for low-transport conditions, as stones are seen to be moving for a short amount of time – the step – after which they

rest for a long time. A different way of decomposing transport in different processes is to regard the number of particles that is moving per unit of area at an instant (the mobility) and their velocity. This also gives a (dimensionally) correct expression for the transport rate (Andrews & Smith, 1992).

Stochastic methods

The probability that $\tau_b > \tau_c$ was linked to the mobility of the bed via eqs. (2.19) and (2.21). This probability can be calculated by the following convolution (McEwan *et al.*, 2003):

$$p(\tau_b > \tau_c) = \int_{\tau_c=0}^{\infty} p(\tau_c) \int_{\tau_b=\tau_c}^{\infty} p(\tau_b) d\tau_b d\tau_c \quad , \quad (2.22)$$

where $p(\tau_b)$ is a probability density function (PDF) of τ_b . De Ruiter (1982) gives the following relation for E , assuming only τ_b to have a distribution due to turbulence, and τ_c to be constant:

$$E \propto d \int_{\tau_c}^{\infty} \frac{p(\tau_b)}{T_p(\tau_b)} d\tau_b \quad . \quad (2.23)$$

Here T_p is a function of the occurring shear stress. This gives the opportunity to deal explicitly with a varying turbulence structure. If both τ_c and τ are supposed to be distributed, the following convolution could be used:

$$E \propto d \int_{t=0}^{\infty} p(\tau_c) \int_{\tau_c}^{\infty} \frac{p(\tau_b)}{T_p(\tau_b, \tau_c)} d\tau_b d\tau_c \quad . \quad (2.24)$$

In the probabilistic approaches mentioned above the shear stress is assumed to be (proportional to) the force that dislodges the particle from the bed. If acceleration terms would be shown to be (partly) responsible for the movement of coarse bed material, a similar approach, based on these forces, might also be possible. The same kinds of convolutions could be used with $F = f(u^2, Du/Dt)$ substituted for τ_b .

2.6 Size, shape, position, and orientation of stones

In this section some features which characterise the separate stones are discussed, viz. size, shape, position, and orientation. The distribution of the parameters found in a granular bed, like the grading is also briefly touched upon.

Size. The size of a stone, most often indicated by a ‘diameter’, is an important parameter that determines the stability of a stone. Several typical ‘diameters’ can be used to characterise the size of a stone, like the:

- sieve diameter, d_s (size of smallest sieve opening through which the stone can pass),

- nominal diameter, d_n (edge of a cube with equal volume),
- standard fall diameter (diameter of sphere with equal density and fall velocity).

The characteristic size mainly used for bed protections is the nominal diameter, defined as the edge of a cube with the same volume as the stone:

$$d_n = \sqrt[3]{M/\rho_s} \quad , \quad (2.25)$$

where M is the mass of the stone. Sometimes the characteristic size is defined as the diameter of a sphere with the same volume ($\sqrt[3]{6/\pi} d_n \approx 1.24d_n$).

The diameters of gravel and sand particles are mainly determined by sieving. The ratio d_s/d_n varies with the shape of the stones – d_s is approximately equal to the intermediate of its three principal body axes. For most stones used for bed protections the following ratio can be used (CUR, 1995):

$$d_s/d_n \approx 0.84 \quad . \quad (2.26)$$

The grading of rocks is their size distribution. It usually is quantified by the parameter d_{85}/d_{15} , where m percent of the weight³ of a sample of stone is smaller than d_m . For most applications in protective top-layers the grading is classified as narrow, defined as $d_{85}/d_{15} < 1.5$.

Shape. The shape of a stone can be described by a multitude of factors (Chien & Wan, 1999, give an overview). Many of them are difficult and time consuming to determine.

Several ratios of the lengths of the three principal body axes a , b , c (respectively the shortest, intermediate, and longest) give an idea of the shape. A shape factor often used for classifying the stone shape is defined as:

$$SF = a/\sqrt{bc} \quad . \quad (2.27)$$

It can be regarded as an indication of the flatness of stones. Typically $SF \approx 0.6$ for crushed rock.

The angularity of stones is the factor that describes the sharpness of the edges. It is most easily determined by visual inspection. Measurable parameters are available, like the average radius of the edges on a stone, but their measurement is laborious.

Breusers (1965) found that, when d_n is used in the definition of Ψ , the critical dimensionless shear stress of differently shaped stones is similar. The load under which they start to vibrate is more diverse. Particles shaped like tetrahedrons did

³Sometimes the number of particle is used instead of the weight.

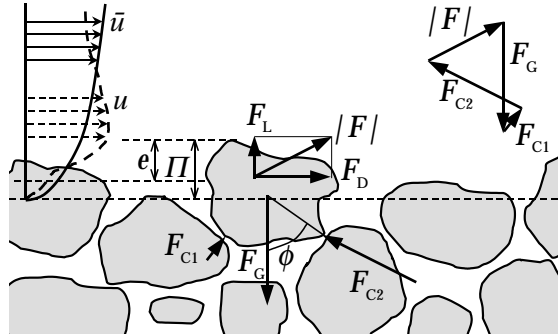


Figure 2.4: Forces on a stone.

move more easily than various other shapes examined. Later research showed that slight differences are present in the critical shear stress.

With crushed rock the points where the flow separates are fixed for the most part by the sharp edges, so a drag crisis does not occur. The angularity of the rocks influences the forces this way. Stones also interlock better when they are more angular. This is shown by De Boer (1998), who found a larger transport rate for rounded stones at low hydraulic loads.

Carling *et al.* (1992) measured the critical shear stress for some single differently shaped stones, placed on beds with varying roughness. For various shapes with the same nominal diameter, the critical shear stress varied by a maximum of approximately 20%.

Position. The position of a stone in a bed can be described by several factors. Three often used parameters which give information about the position of a stone are (Kirchner *et al.*, 1990, see fig. 2.4):

- protrusion, Π : the height of the top of the particle with respect to the mean bed level⁴,
- exposure, e : the height of the top of the particle with respect to the local mean upstream bed level,

⁴The bed level is the average bed elevation, determined by taking the average value of a large number of point measurements of the highest elevation (i.e. not under a stone) at random horizontal positions.

- pivoting angle⁵, ϕ : the maximum angle at which the bed can be tilted without movement of the particle.

These definitions are easy to apply when schematising the problem in two dimensions (see fig. 2.4), but are less clear in three dimensions.

Kalinske (1947) concluded that drag was fully responsible for dislodging particles from the bed. Conversely, around the same time Einstein & El-Samni (1949) assumed that only the lift component was responsible. In later models (Wiberg & Smith, 1987, for example) both force components are included, with the drag force indicated as the largest. Which force component is important is dependent on the position of the particle, which can be described to a large extent by its relative protrusion, Π/d . If $\Pi/d \approx 1$ then the particle is nearly completely exposed and a large drag force will exist. Further, the pivoting angle, ϕ , is then in general such that a drag force gives a large, and the resisting force a small moment around the point of rotation (roughly $\frac{1}{2}F_D d \cos \phi$ and $\frac{1}{2}F_G d \sin \phi$ respectively, see fig. 2.4), making this component very effective in moving the particle. Conversely, if $\Pi/d \ll 1$ then obviously only a lift force can efficiently create large moments.

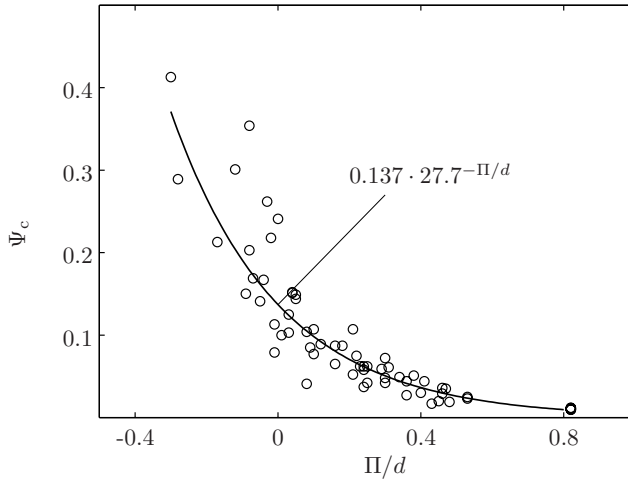


Figure 2.5: Variation of dimensionless critical shear stress Ψ_c with relative protrusion Π/d , after Fenton & Abbot (1977)

Fenton & Abbot (1977) executed experiments in order to determine the effect of the relative protrusion of a particle on Ψ_c . Figure 2.5 shows this influence for hydraulically rough flow. For relative protrusions varying from 0 to 0.8, Ψ_c for a

⁵Unlike the friction angle or angle of repose this is a quantity that refers to a single stone.

single particle varies from 0.15 to 0.01. It is not possible to determine the separate forces acting on the particles from this, as the contributions of the lift and drag force are not known separately as a function of the protrusion.

The protrusion of a stone is not the only factor that influences the forces on it, as the positions of the surrounding stones are also of importance. Still the protrusion can be expected to have a strong influence on the magnitude of the critical force, as it is related to both the resisting force on the particle and the hydrodynamic force. The exposure is more directly related to the hydrodynamic load. On average Π will increase with increasing e . Thus, it may be expected that if the force on a particle is related to the exposure, it will also be related to protrusion, only with more scatter.

The pivoting angles of the different particles in a bed vary. Kirchner *et al.* (1990) determined the probability distributions of Π , e , and ϕ on a gravel bed. The results show that the values are distributed over a wide range.

Orientation. The orientation of a particle is usually quantified by regarding the respective angles of the (longest) body axis to the flow direction and to the bed (azimuth and dip). The shortest body axis of a stone is generally pointing upwards. In research on gravel-bed rivers it is sometimes seen that stones have their longest axis predominantly in the spanwise direction (Nikora *et al.*, 1998). Conversely, De Boer (1998) noted that angular stones in a flume experiment were predominantly orientated with their longest axis in the direction of the flow after water-working.

The above especially holds for natural gravel or dumped stones. In the case of (dry) construction of scour protections or breakwater construction the stones are usually placed with their longest axis vertically to minimize the area that is exposed to the flow or waves. These constructions usually have a limited thickness, so that some movement of the stones by the flow is not allowed.

Carling *et al.* (1992) measured the critical bed shear stress for differently shaped stones on beds of different roughnesses. They found that a difference in orientation could influence the critical Shields parameter for a single stone more than its shape. Stones placed with their long axis perpendicular to the flow moved sooner than when placed parallel. On rougher beds, particles moved at a higher shear stress; apparently they interlocked better with their neighbouring particles. Particles placed parallel to the flow often changed their orientation to perpendicular before moving. On the roughest bed particles were mostly seen to move into a more stable, imbricated position before being entrained by rolling. Once moving, the particles tended to move with their longest axis perpendicular to the flow.

Relative influence. To conclude this section, the possible influence of the above-mentioned characteristics on the stability of stones in a granular bed protection is estimated. The influence of a parameter is defined as the factor with which the

Characteristic	Approximate influence factor	Source(s)
Position ($\Pi/d=0-0.5$)	5	(Fenton & Abbot, 1977)
Orientation	>10	(Carling <i>et al.</i> , 1992)
Size ($d_{85}/d_{15} = 1.5$)	2	(Shields, 1936)
Shape (when d_n is used)	0.2	(Breusers, 1965; Carling <i>et al.</i> , 1992)

Table 2.1: Approximate influence of stone characteristics on stone stability.

overall bed shear stress at which a certain particle on the bed becomes unstable can vary, when this factor is changed within the values typical for a bed protection. We assume that the range of relative protrusions is about 0–0.5 and the grading has a width of 1.5. The corresponding variability of critical shear stresses in a bed is given in table 2.1. The orientation of the individual stones has the largest influence, followed by their protrusion. This reveals a difference between bed protections and gravel-bed rivers. The latter usually have a wider grading where the position of the particles becomes equally important as the orientation, or more.

2.7 Engineering approach

Most design approaches are based on the stability criteria by Shields [eq. (2.14)] or Isbash (1932). The stone size and density should be such that the stability parameter will not surpass a critical value. The main difference between the two stability parameters is that Isbash uses a near-bed velocity⁶ and Shields the shear velocity as the parameter quantifying flow attack. Some later approaches apply a parameter that resembles the Isbash approach where $\langle \bar{u} \rangle_h$ is used to quantify the flow attack, and subsequently apply a friction coefficient for uniform flow, $c_f \equiv u_*^2 / \bar{u}^2$, as a correction factor to the stability parameter for uniform flow. Thus effectively both approaches are the same. As the Shields parameter only applies to uniform flow conditions, several corrections are often applied to the numerator of the Shield factor – which represents the flow attack – to account for non-equilibrium (mean and fluctuating) flow profiles. The way in which this is done is the main difference between the various design approaches.

Pilarczyk (2001) proposes:

$$\Delta d = 0.035 \frac{S}{\Psi_c} \frac{K_T K_h}{K_s} \frac{\langle \bar{u} \rangle_h^2}{2g}, \quad (2.28)$$

⁶The exact position of this velocity is not specified.

where S is an empirical factor accounting for the way the stones are placed, K_T accounts for turbulence, varying from 1.0 for uniform flow to 2.0 at hydraulic jumps and to 3.0–4.0 under ship’s propellers. K_h is equivalent to c_f for uniform flows. However, it is also used for the non-uniform flows. Finally K_s accounts for slopes of the bed protection. The various correction coefficients are rather arbitrary, so the expression can only be used as a rule-of-thumb, or with large safety factors. Especially the turbulence factor, which can vary by a factor 4 – corresponding to a factor 64 in stone weight – is uncertain and has to be chosen according to an ‘engineering judgement’.

Another approach is (Franken *et al.*, 1995; Schiereck, 2001):

$$\Delta d = \frac{c_f(K_v \langle \bar{u} \rangle_h)^2}{K_s g \Psi_c} \quad , \quad (2.29)$$

where K_v is a flow-specific empirical factor for non-uniform flows. K_v has been determined from measurements for many flow types as:

$$K_v = \frac{u_{c,u}}{u_{c,nu}} \quad , \quad (2.30)$$

where $u_{c,u}$ and $u_{c,nu}$ are the critical flow velocity under uniform and non-uniform flow, respectively. The exact place where the flow attack occurs is often not specified using this method, so a large area of bed protection will be dimensioned with the maximum stone diameter. Further, for every construction a physical model test has to be executed in order to determine K_v .

If no model-tests are available, the normalised depth-averaged longitudinal turbulence intensity is sometimes used to characterise the influence of turbulence: $r_0 = \langle \sigma(u) \rangle_h / \langle \bar{u} \rangle_h$ (Hoffmans & Akkerman, 1998). This turbulence intensity is then used in eq. (2.29) by defining:

$$K_v \approx \frac{1 + 3r_{0,nu}}{1 + 3r_{0,u}} \quad , \quad (2.31)$$

where $1 + 3r_{0,nu}$ is an indication of the ratio of the maximum to the mean flow velocity for the non-uniform case, and $1 + 3r_{0,u}$ the same ratio for the uniform case. This approach is roughly based on the approach of Grass (1970). The stability behind a sill or a BFS can be estimated using eq. (2.6) to predict $r_{0,nu}$. This depth-averaged turbulence parameter does not completely describe the flow near the bed, so inaccuracies are generated here, or extra corrections are needed.

Also other parameters are used, for example the turbulence fluctuations averaged over the lower 10% of the water depth (Escarameia & May, 1995). This value is not applicable for shallow flows, where 10% of the water depth can be much smaller than the stone diameter, which makes the determination of the exact value difficult due to the uncertain location of the bed level.

If a model is developed that uses the output of numerical computations for the determination of damage to bed protections, then this would make the use of expensive scale models obsolete. Recently a model has been developed at WL|Delft Hydraulics, based on the following stability parameter (Jongeling *et al.*, 2003):

$$\Psi_{\text{WL}} = \frac{\left\langle (\bar{u} + \alpha\sqrt{k})^2 \right\rangle_{h_m}}{\Delta g d_{n50}}, \quad (2.32)$$

where k is the turbulence kinetic energy, $h_m = 5d_{n50} + 0.2h$, and $\alpha = 6$. In this stability parameter, output of a numerical flow model with a turbulence closure model (\bar{u} and k) is averaged over h_m in order to estimate the flow attack (numerator of Ψ_{WL}). It has been calibrated on measurements and computations of a number of flow configurations. The averaging procedure did not give the same Ψ_{WL} for all critical flow conditions (possibly indicating that other parameters also play a role), and therefore a conservative value of $\Psi_{\text{WL},c} = 8$ was determined.

Most research on bed protection only uses a criterion of ‘damage’ or ‘no damage’ to determine the flow conditions where initial damage occurs. If the entrainment would be measured as a function of flow velocity, this would have two advantages. Firstly, more data would be used, leading to a more accurate determination of the critical conditions. Secondly the designer could specify the required damage level more precisely. At the moment a model based on eq. (2.15) – which uses an instantaneous transport formula – is being developed. A first formulation has been given in Jongeling *et al.* (2003). This would give a more gradual estimation of the damage level.

2.8 Concluding remarks

As there has been much research on stone stability and sediment transport, the above overview is not complete. However, most important aspects are included. From the literature studied some important notions can be obtained.

First of all, it is clear that the turbulence fluctuations in the flow are of importance for the stability of stones. Specifically for non-uniform flows the turbulence has to be taken into account. The exact way in which to do this is not known. However, it is clear that stone entrainment generally takes place during flow events with increased longitudinal velocity. The characteristics of the turbulence near a rough wall are not completely clear either at the moment.

The various parameters that are of importance for the process of particle entrainment can be defined in many ways, which makes comparison of research results difficult. Aspects like the theoretical bed level of a rough bed and the origin of the forces on a bed particle are still subject to discussion. The random nature of the positions and shapes of the separate rocks in a granular bed complicates things further.

The cause of the mean drag force on the bed particles in uniform flow is fairly clear, although the fluctuations cannot be predicted completely from the instantaneous near-bed flow. The determination of a constant instantaneous C_D has not succeeded. The origin of the lift force has more uncertainties. The acceleration terms in the momentum balance might have an influence, in addition to the quasi-steady forces. The velocity at $0.15d$ above the top of a particle seems the best velocity to use when assessing the quasi-steady forces on particles with a varying protrusion. The exact way in which a particle is moved from its place, including the exact change of forces and particle position in time, has not been studied for the present conditions. This is examined further in chapters 5–7.

It seems that for a bed protection with a narrow grading the most important parameter determining the stability of a single stone is its orientation, followed by its vertical position. Most experiments on forces on single particles are done on schematised particle positions, leading to a protrusion of about zero (all particles at the same level) or one (a particle on top of a layer of other particles). It is not known what a characteristic position of an entrained particle is. The orientation and position of the stone under consideration must be representative for a bed protection. Therefore this is examined further in chapter 3, after which the experiments will be treated.

Many concepts about coherent structures from research on smooth-bed flow are used directly for rough-bed flow. This translation cannot be made directly. Some progress has been made in the identification of coherent flow structures in rough-bed flow. Several sources have identified large-scale flow structures with a downward and increased streamwise velocity, which are also connected to the entrainment of coarse bed material. For the areas with a velocity deficit the ‘hairpin vortex packet’ model has been proposed. How these structures are linked to the displacement of stones is the focus of chapter 7.

Several (engineering) models exist for the assessment of stone stability under non-uniform flows. Most of them use the Shields parameter and replace the part for the flow attack (numerator) with an expression including turbulence aspects:

- Some approaches use separate correction factors for the influence of the mean velocity and of the fluctuating velocity (Pilarczyk, 2001).
- Also correction factors are used, which are the ratio of the measured critical velocity for uniform flow to that of the non-uniform flow $K_v = \langle \bar{u}_{c,u} \rangle_h / \langle \bar{u}_{c,nu} \rangle_h$ (Franken *et al.*, 1995).
- Another approach uses the ratio of an estimate of the maximum velocity for the non-uniform flow, compared to that of the uniform flow: $K = (1 + 3r_{0,nu}) / (1 +$

$3r_{0,u}$). r_0 is a depth-averaged quantity, either measured or calculated (Hoffmans & Akkerman, 1998).

- A recent approach uses the results of a numerical flow model with k - ε turbulence closure (Jongeling *et al.*, 2003). It averages $\bar{u} + \alpha\sqrt{k}$ over part of the depth, and uses this in the numerator in the Shields number. Empirical coefficients were calibrated on a large number of flow situations.
- A model was developed with which the turbulence wall pressures influencing stone stability can be calculated from output of a numerical flow model with k - ε turbulence closure. This model has limitations and can only be used as an estimate (Uittenbogaard *et al.*, 1998).

A very novel approach being developed uses the gradient of the sediment transport rate as the cumulative damage to the bed protection (Mosselman *et al.*, 2000; Jongeling *et al.*, 2003).

If the various engineering methods mentioned above – that are used to determine the stability of a bed protection – are to be improved, an increased understanding of the entrainment process is crucial. This research is aimed at this, by regarding the entrainment of a stone on a micro scale. A new model, similar to the third and fourth model mentioned above, and partly based on the notions developed in the other chapters, is presented in chapter 8.

Chapter 3

Stone Positions

3.1 Introduction

How turbulence influences stone stability is not known exactly. Therefore measurements of the pressures on and the movement of a single stone have been performed. These are presented and analysed in chapters 4 to 7. From the literature discussed in the previous chapter it appears that the orientation and position of a stone can significantly influence the way it is entrained. Therefore it is of key importance that the stone that is the focus of the experiments has a characteristic position and orientation. Determining the bed surface characteristics is not the main goal of this thesis, which is to examine the influence of the turbulent flow on stone stability. Still, after examining the existing literature, the conclusion was reached that so little was known about the positions of the stones at the surface of a granular layer that an attempt should be made to gain insight in the positions of the top particles of a granular bed. To this end a simplified model was chosen: a mathematical discrete particle model (DPM) for randomly and sequentially deposited spheres. This model will give a first estimate of the positions of randomly deposited stones on a flat bed. The spherical shape is not very realistic for bed protections, and the orientation of the stones cannot be evaluated. However, the model can be used to illustrate how a bed can reach an equilibrium state in consequence of the attack by the flow, and can give some qualitative information about the structure of a random bed.

First some literature about the use of DPMs for determining granular bed characteristics is mentioned, after which the present model is described. Then the calculations that were executed are presented. Next the implementation of water-working (by erosion) of the bed is explained, which is shown to give statistically similar beds, independent of material properties. The bed for which these parameters are derived

is exactly defined and reproducible, unlike most experimental results. Next the characteristics of this bed are presented. This can help to determine the suitability of certain stone-positions in the experimental set-up.

3.2 Previous use of Discrete Particle Models (DPMS) for determination of bed surface characteristics

A Discrete Particle Model (DPM) can be used to obtain an estimate of the surface characteristics of a granular bed. It is a useful research tool, especially for low mobility and coarse-particle bed load, since the transport of the individual particles is obviously dominated to a large extent by the micro bed structure in this flow regime.

Perhaps the first use of a kind of DPM for obtaining an estimate of the surface characteristics of a fluvial bed was by Kirchner *et al.* (1990). Circular shapes were fitted onto measured longitudinal profiles of the bed elevations, in order to obtain an estimate of the values of certain grain parameters. It was found that the parameters like angle of repose, exposure, and ‘critical shear stress’ varied widely per particle.

McEwan & Heald (2001) used a DPM to describe a bed that is formed by sequentially dropping uniformly sized spheres at random positions. The particles were not removed or redistributed by the flow. The model was therefore used to determine the characteristics of a non water-worked bed. It is known that this bed is completely different from a water-worked bed, as the authors themselves state. The collisions were determined without allowing overlap of the particles. This is a so-called hard-sphere model.

Nikora *et al.* (2001a) determined diffusion characteristics of particles using a DPM. They give the values of several moments of the bed elevations before and after water-working.

Schmeeckle & Nelson (2003) use a hard-sphere model to model bed load transport of a gravel bed, and see that transport by a flow with realistic (measured) velocity fluctuations mainly consists of periods with hardly any transport (low u) and with particles saltating (high u). In the water-worked bed the smaller grains have smaller exposures and higher pivoting angles than the larger grains – albeit with a wide distribution.

All DPM studies mentioned above, except McEwan & Heald (2001), use wide gradings of the stones. They also use a simplified flow model, wherein a velocity – varying in depth and time only – is imposed on the particles, sometimes empirically corrected for the blockage of particles upstream.

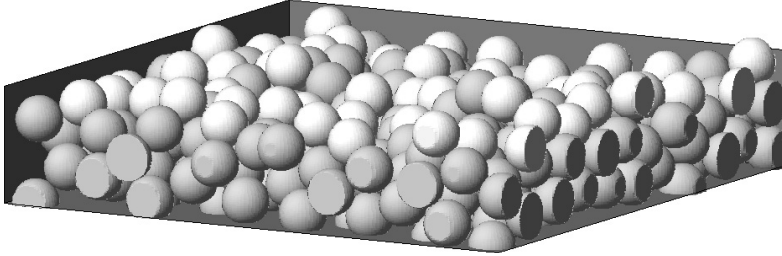


Figure 3.1: A simulated water-worked bed with equally sized spheres. Box size is $12d \times 12d$. The exposed stones have a lighter shading.

3.3 Features of present DPM

A model was developed to simulate the sequential deposition of frictionless spherical stones in a periodic box. It is a soft-sphere model, meaning that the stones are allowed to overlap slightly (about 1‰ of d) during collisions. This overlap determines the contact forces between the stones and the impacts of the stones are calculated by discrete time integration. During deposition simplified hydrodynamic forces act on the spheres. When an initial bed has been deposited, the top stones are removed in order to simulate the water-working process on an eroding bed.

An important characteristic of the model is that the stones are dropped sequentially. This way of depositing stones leads to a bed packing where every stone has a stable position, resting on three others. When stones are deposited in bulk, arches are formed inside the granular medium. With slight vibration they can slowly collapse, leading to values for the porosity in the range of 0.44 (random loose packed) to 0.36 (random close packed). Sequential depositing prevents this possible further compacting of the bed and leads to a single possible value for the porosity of 0.407 (Mehta, 1994). We chose to use a sequentially deposited bed for a number of reasons. First of all, it has a clear description. Secondly the value for the porosity of a sequentially deposited bed coincides with that of a prototype bed protection (Bosma, 2001). Finally many bed protections, especially the ones with large stones, are actually constructed by placing or dumping the rocks sequentially.

The equation of motion for the stone that is solved by the DPM is:

$$\begin{aligned} \vec{a}_p &= \vec{F}_p / M_p \quad , \text{ with} \\ \vec{F}_p &= \vec{F}_D + \vec{F}_G + \vec{F}_{\text{contact}} \quad , \end{aligned} \tag{3.1}$$

where \vec{a}_p , \vec{F}_p , and M_p are the acceleration, force on and mass of the moving stone respectively. The path of a stone is solved by integrating equation (3.1) using a Runge-Kutta scheme. The time step was set such that the collisions were well-resolved (a frontal collision is integrated in about 50 time steps). The various forces are a high Reynolds number drag force $\vec{F}_D = -\frac{1}{2}\rho C_D A |\vec{v}_p| \vec{v}_p$, the gravitational force including buoyancy $\vec{F}_G = (0, 0, -gM_p + gV_p\rho_w)$, and the contact forces due to collisions. The contact force \vec{F}_{contact} has a damping and an elastic component, both working in the line between the centres of the moving stone, \vec{x}_p and of the stone it overlaps, \vec{x}_c :

$$\vec{F}_{\text{contact}} = \begin{cases} \Delta\vec{x} \left[-k \left(\frac{d_p + d_c}{2|\Delta\vec{x}|} - 1 \right) - c \frac{\vec{v}_p \cdot \Delta\vec{x}}{|\Delta\vec{x}|^2} \right] & \forall |\Delta\vec{x}| < \frac{d_p + d_c}{2} \\ 0 & \forall |\Delta\vec{x}| \geq \frac{d_p + d_c}{2} \end{cases} \quad (3.2)$$

in which $\Delta\vec{x} = \vec{x}_c - \vec{x}_p$, k is the spring stiffness and c the damping constant. In this chapter d represents the diameter of the sphere. The notation for the collision force is actually a little more complicated than eq. (3.2) as the periodic boundaries have to be taken into account. In consequence of this, each of the horizontal coordinates can be increased or decreased by the width of the computational domain. From this it follows, that when the distance between two stones is calculated, nine possible combinations of the horizontal coordinates exist. The smallest of the nine distances is used.

Checking all other spheres every time step for collisions becomes computationally expensive for larger domains. Therefore, in order to speed up the computation, the horizontal domain is divided in grid cells with cell widths as large as or larger than the largest possible stone size. The grid cell where a deposited stone comes to rest is stored in a stack. Now only the stones in the same grid cell as the depositing stone and its eight surrounding cells have to be checked for collisions. Especially for wide domains this decreases the computational cost considerably.

3.4 Configurations

The stones used for the simulations had a diameter of $d = 0.1$ m and a spring stiffness for collisions of $k = 10^5$ N/m. A time step of 0.25 ms was used. In total four simulations were executed, see table 3.1. In the first three the damping factor for the stone-stone collisions was varied, which gave rebound velocities v_r for a straight collision of 1%, 50%, and 99% of the incoming velocity v_i , respectively. The ratio of these velocities is called the coefficient of restitution. These computations will be used in the next section to see if the collision characteristics change the bed configuration,

run #	damping coefficient c N/(m/s)	coefficient of restitution v_r/v_i -	width grading d_{85}/d_{15} -	number of stones N -
1	001	0.99	1	10^4
2	125	0.50	1	10^4
3	500	0.01	1	10^4
4	125	0.50	1	10^5

Table 3.1: Calculations executed with the DPM.

and to examine the water-working of the bed. Run 4 was made with more stones, in order to obtain well-converged statistics. The outcome of this run is presented in section 3.6, where the characteristics of a water-worked bed are described.

3.5 Water-working

In this section the difference between the initially deposited beds and the beds after water-working is considered, using runs 1 to 3, see table 3.1.

In figure 3.2.a the average protrusion-distributions of the exposed stones in the initially deposited beds are plotted (actually the distributions of the deviations from the mean protrusion have been plotted). An ‘exposed stone’ is a stone that has no other stones resting on it. It can be seen that the distribution of protrusions for stones with a lower coefficient of restitution (larger c) is wider than the distribution of protrusions for the stones with a higher coefficient of restitution (lower c). This is explained by the fact that stones that bounce a few times before they come to rest at their final position (low c) have a higher chance of ending up in a depression in the bed, from which they cannot leave. Conversely, a stone that drops dead immediately (large c) has a higher probability of coming to rest on top of an elevation of the bed. This means that a higher rebound velocity leads to a flatter bed, which is confirmed in figure 3.2.a.

Now the entrainment process is considered. When flow initiates over a just deposited bed, the most protruding and unstable stones will be removed immediately, even by a flow with low velocity. After that, less protruding stones are removed, and gradually an equilibrium bed forms. In most research on entrainment and transport, flow is applied to the bed for a certain time to let the bed become water-worked, in order to get a good estimate of the critical entrainment (Paintal, 1971, for instance). Evidence of this process is seen in the measurements of Forschelen (1999), who de-

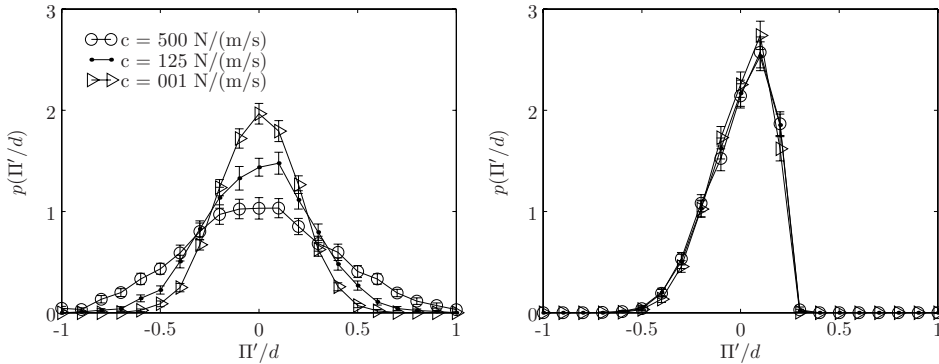


Figure 3.2: a) (left) Initial distribution of protrusions of exposed stones for runs 1–3, with different damping coefficient. b) (right) The distributions of protrusions for the same beds after removing the most protruding stones.

noted the times of all stone movements past a transect under uniform low-mobility flows starting with a non water-worked bed. It can be seen in a plot of his low-mobility experiments with angular stones in figure 3.3 that the initial high transport rate gradually tends towards a constant value. Lammers (1997) measured that a just deposited bed flattened and the hydraulic roughness of the bed decreased in time. After a while the hydraulic roughness did not change noticeably anymore. However, the transport still was reduced somewhat further.

This effect called water-working is modelled in a simple way in the present DPM for uniformly sized stones by simply removing the most protruding exposed stones. The protrusion is very important to the critical force on a stone (Fenton & Abbot, 1977). After one stone has been removed, the exposed stones are determined again, before the next one is removed, as new stones can have been uncovered by removing a stone.

The removed stones are not redeposited on the bed, as information about displacement lengths is limited and uncertain. This means that the model does not simulate water-working under uniform transport. Instead it models water-working of an eroding bed. This is also exactly the condition that is of importance when examining damage to bed protections. The bed level becomes lower, but this is not relevant when searching for a general bed geometry which can be related to any mean level.

Figure 3.2.b shows the protrusion distributions, after several layers of the most protruding exposed stones have been removed. Now the distributions of the different beds are very similar. This implies that, although the initial geometry of the beds was different, the underlying packing is similar or even equal. This leads to the

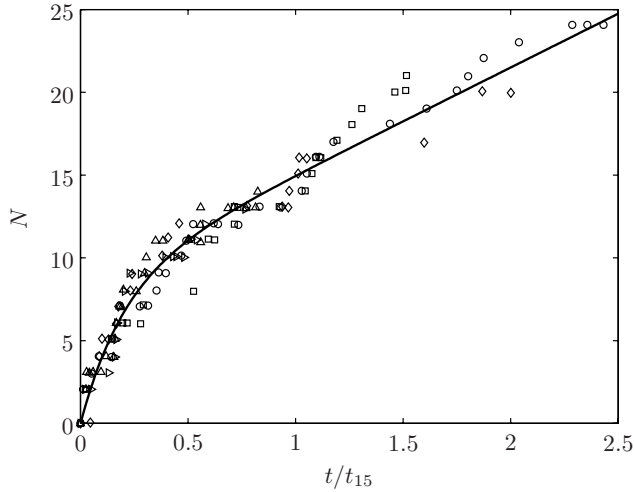


Figure 3.3: Cumulative number of stones N moved per strip under open-channel flow as a function of time for five experiments ($\Psi=0.037-0.048$), based on data by Forschelen (1999). t_{15} is the time at which $N = 15$.

conclusion that if an entrainment model is used, the exact deposition characteristics of the spherical stones do not matter – if dropped sequentially. The surface geometry will of course depend on the entrainment model.

Realistic entrainment processes are more complicated than the entrainment model used presently. Therefore attention should be paid to the kind of entrainment or transport model, instead of the deposition model of the stones. Water-working must be applied to the bed prior to any statistical analysis of critical forces of the various stones in the bed. This holds especially when it is used to compare the modelling results to empirical results such as the Shields curve or a transport formula. This was not done by McEwan & Heald (2001), for instance, so the quantitative values of their comparison to the Shields curve should not be used.

3.6 Characteristics of the modelled water-worked bed

Some quantities characterising the water-worked bed were determined. These can be used to check whether the stones used during the measurements described in the coming chapters have characteristic positions.

Simulation number 4 was made to obtain the statistics of the bed elevations. In

this simulation five beds were deposited with 28800 stones in a $60d \times 40d$ area. From each of these beds initially a large amount of 6000 stones were removed, in order to assure that a fully water-worked bed was formed. Subsequently, four times an extra 2400 stones were removed, resulting in a total of 25 samples of statistically similar water-worked beds on which over 20000 exposed stones were present. The porosity of the bed is 0.7% lower than the theoretical value of 0.407, due to the slight overlapping ($\approx d/1000$) of the spheres.

The bed surface (i.e. the highest elevation at which material is present at a certain horizontal position) was sampled at (infinitesimal small) points with intervals of $d/10$ to determine the parameters describing the bed. These parameters will now be compared to some values from literature.

The bed has a standard deviation of:

$$\frac{\sigma(y_b)}{d} = 0.507 \pm 0.001 \quad .$$

This is between the values obtained from prototype measurements on non-water-worked bed protections, where values of 0.42 and 0.57 were obtained for 40–200 kg and 10–60 kg gradings, respectively (Meulepas *et al.*, 1999, and appendix F). It is somewhat less than what Nikora *et al.* (2001b) calculated for a water-worked bed: 0.58 ± 0.01 . The difference can be explained by the fact that that bed had a range of diameters of 2–8 mm, and that it was not an eroding bed.

The present bed has a negative skewness of

$$S = \frac{\langle y_b^3 \rangle}{\sigma(y_b)^3} = -1.35 \pm 0.01 \quad .$$

This skewness is caused by the fact that the positive tail (i.e. large elevations) of the PDF is cut off by the water-working. On the other hand, large negative elevations occur, as the holes between the stones can occasionally be very deep.

In prototype test (Meulepas *et al.*, 1999, and appendix F) point measurements yielded values for the skewness of -0.26 and -0.33. This is somewhat less than the present computations. Nikora *et al.* (1998) found for various natural gravel beds that the skewness was mostly positive with a mean value of 0.47 in the range of -0.69 to 1.50. As the natural rivers had a grading width of $d_{85}/d_{15} = 3.5$ –5, this can be the cause of the positive skewness. The larger grains have a tendency of protruding more above the average level – giving larger positive bed level fluctuations, while the pores are easily filled by the smaller grains – decreasing the negative bed level fluctuations. The calculation by Nikora *et al.* (2001b) resulted in $S = -0.67 \pm 0.06$, where the skewness was caused by the water-working. The non-water-worked bed had more Gaussian characteristics.

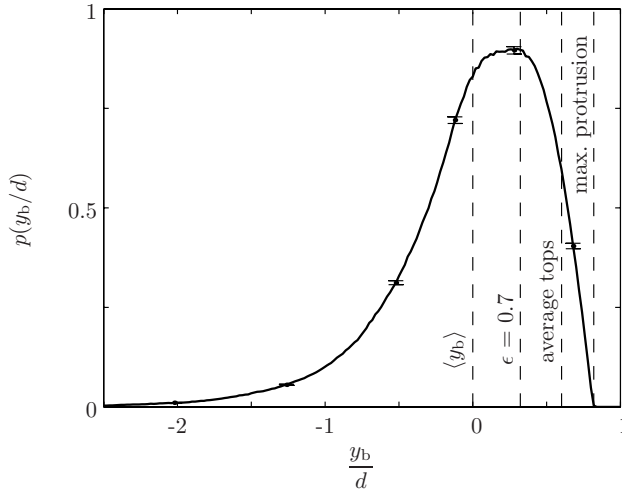


Figure 3.4: Simulated probability density of bed elevations of eroding water-worked bed. Including the position of certain definitions for the bed level.

The present distribution of bed elevations is leptokurtic ($K > 3$) with a kurtosis of

$$K = \frac{\langle y_b'^4 \rangle}{\sigma(y_b)^4} = 6.31 \pm 0.1 \quad .$$

In prototype test (Meulepas *et al.*, 1999, and appendix F) point measurements yielded values for the kurtosis of 3.1 and 3.2, which resembles that of a normal distribution. This is close to the mean value for the kurtosis that Nikora *et al.* (1998) found for natural gravel beds, of: $K = 3.11$. The range was 1.83–5.44. Nikora *et al.* (2001b) calculated $K = 4.25 \pm 0.19$.

The estimated probability density of the bed elevations (not of the protrusions) is presented in figure 3.4. This is a way of visualising the structure of the ideal bed. Several possible definitions of the ‘bed level’ are indicated on it – e.g. the elevation at which the porosity ϵ is 0.7 – so it can be useful to compare the various definitions. The maximum bed level, and hence the maximum protrusion, is $0.22d$ above the mean level of the tops of all exposed stones and $0.82d$ above the mean bed elevation¹. Unfortunately there is no precise information about the exact location of the hydraulic bed level (where the logarithmic velocity profile becomes zero). Often a value of 0.15 to 0.35 under the tops of the roughness elements is mentioned, be it that these are mainly values obtained from regular arrangements of spheres. This would lead to an initial guess of a value to be used in the experiments of $0.4d \pm 0.1d$ above the hydraulic

¹A single sphere on a single layer of densely packed spheres has a protrusion of ≈ 1.06 .

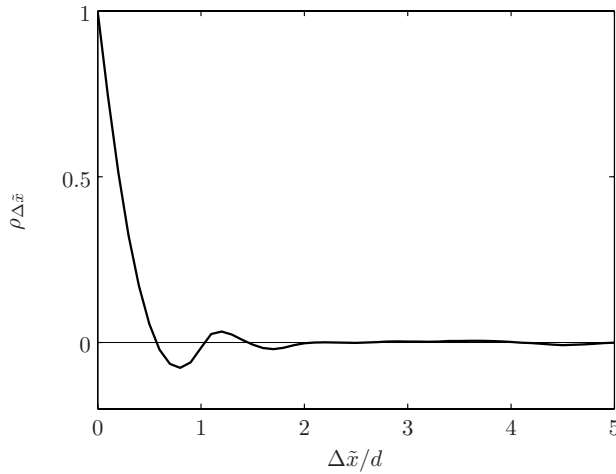


Figure 3.5: Spatial covariance of the bed elevations.

bed level, although the shape of the stone is completely different. If we compare this position with the positions of the particles in the experiments where the forces on these particles were measured, it turns out that this agrees best with the set-up of Chepil (1958). When the size distribution becomes wider, the (average) protrusion of the large particles becomes larger, and that of the small particles will become smaller (Egiazaroff, 1965). Clearly the shape of the particles will be of influence as well.

As we did not include local effects of blockage of the flow, we do not expect large length scales to appear in the horizontal structure of the bed, nor do we expect a direction dependence. These two facts are confirmed when regarding the one-dimensional spatial covariance function² of the bed elevations with respect to an arbitrary horizontal coordinate, \tilde{x} :

$$\rho_{\Delta\tilde{x}} = \frac{\langle y_b(\tilde{x})y_b(\tilde{x} + \Delta\tilde{x}) \rangle}{\sigma(y_b)^2} .$$

This function is plotted in figure 3.5. It is the same for all horizontal directions.

3.6.1 Time dependence

If experiments on stone stability are executed with a non water-worked bed, more stones will move than with a water-worked bed. Therefore the estimated damage will

²Often the related structure function is used to characterise the horizontal structure of the bed (Nikora *et al.*, 1998; Marion *et al.*, 2003). However, the covariance can directly be linked to this function and is better known.

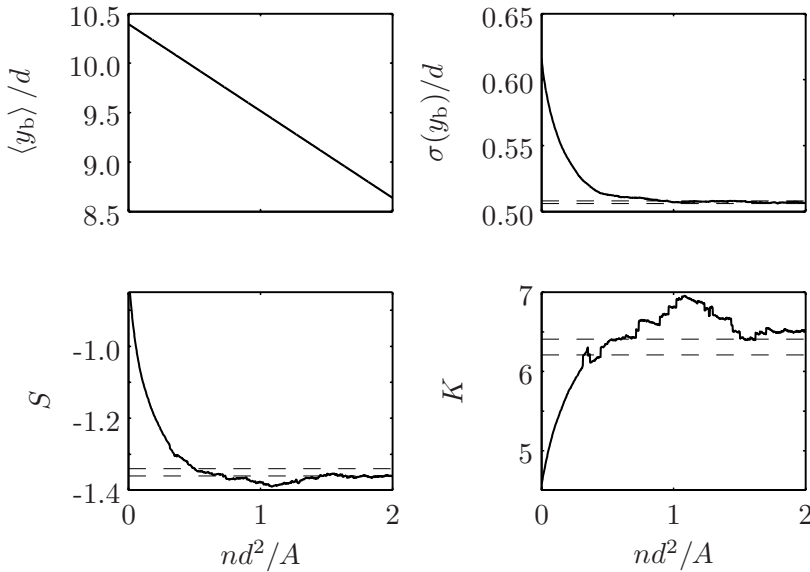


Figure 3.6: Development of the bed structure as a function of the number of entrained stones n (run 4). The equilibrium value lies within the dashed lines.

be too much, which will lead to conservative design rules. Hence it is important to know when a bed is water-worked. To this end we plotted the development of some parameters of the bed topography as a function of the number of removed stones in figure 3.6. At the moment that these parameters reach their equilibrium value, the bed can be regarded to be water-worked. Logically the mean bed level decreases at a constant rate when stones are removed. The standard deviation decreases as well. Even though the standard deviation of the bed level is not the only parameter describing bed roughness, this will probably still be in line with a decreasing hydraulic roughness. The negative skewness increases in absolute value. This can be explained by the fact that the stones that are removed represent the extreme positive excursions of the bed level, whereas the negative excursions are not removed by removing the upper stones. The kurtosis is seen to decrease as well. Some sudden ‘jumps’ in the line (which is an average over five simulations) can be seen. This indicates that the removal of a single stone in this $60d \times 40d$ area can already influence the kurtosis drastically, for instance by uncovering a pore that is a few diameters deep.

The number of stones that have to be removed in order to roughly reach the

equilibrium bed with converged statistics, N_{ww} , is seen to be of the order:

$$N_{\text{ww}} \approx 0.5 \frac{A}{d^2} \quad (3.3)$$

where A is the bed area regarded. This value depends on the initial bed geometry, and this geometry depends on the collision characteristics. Hence this number might vary. However, the value for the coefficient of restitution used is in line with that for natural sediments (Schmeeckle *et al.*, 2001). The number of exposed stones is about $0.38A/d^2$, which is less than N_{ww} . This implies that one has to wait at least until all exposed stones have moved once prior to conducting an experiment on stability. It also implies that a prototype bed protection will only obtain its final strength, after all top stones have moved. This number is very high due to our representation of the effect of water-working. In reality not all the stones are removed from the bed; several end up in a stable position. Moreover, all of the above is only valid for granular layers of several stone diameters thick, otherwise an equilibrium bed will not form in the first place. The orientation of the stones can also alter when the stones are rocking in consequence of the fluctuating hydraulic load. This effect will lead to water-working, without removal of many stones from their pocket.

Above, it was shown that water-working depends on the *number* of stones that have moved. The data of Forschelen (1999) also collapsed when normalised by the time at which a certain *number* of stones had moved. This means that applying a flow to an initial bed for a certain *time* prior to doing stability experiments with different hydraulic loads – which is the normal practise – will result in different initial beds for the experiments. It would be better to start all experiments with beds from which a certain *number* of stones has moved (i.e. a fixed duration at an equal, high load, after which a similar number of stones can be expected to have moved).

3.7 Summary and discussion

It has been shown that sequentially dropped, frictionless, uniformly sized, spherical stones, of which the most protruding stones have been removed, form beds with statistically similar surface characteristics. The exact collision and hydraulic parameters do not significantly influence this bed configuration. This random bed is the most natural bed one can model relatively easily, and which is described precisely. Even though the bed is stochastic in nature, there exists a maximum protrusion of the stones. This maximum protrusion is $0.22d$ from the mean level of the tops of all exposed spheres (the spheres without other spheres resting on them), or $0.82d$ from the average bed level (the mean value of all bed elevations). This is about $0.4d \pm 0.1d$ above the hydraulic bed level (origin of the log-law). The protrusion of the stone used in the experiments should be of the order of this protrusion.

When the first hydraulic load is applied to a just deposited granular layer the most unstable stones reposition and reorientate. This causes the bed surface characteristics to change, the so-called water-working. In this chapter we define a water-worked bed to be a bed from which the most protruding stones are removed. This is a model for an eroding bed, instead of for a bed on which equilibrium transport has taken place. As the least stable stones are repositioned, it can be stated that a water-worked bed obtains its true strength.

These theoretical findings lead to some conclusions regarding bed protections. The random bed especially resembles bed protections made by dumping stones, not by placing stones. Just after construction of a bed protection, or at the first large load on it, some stones are expected to move. This does not mean that the protection layer has failed. The real strength is reached when the surface characteristics do not change after removing a stone.

For the ‘ideal’ bed considered here the number of stones that have to have moved to obtain an equilibrium bed, is as high as $\approx 0.5A/d^2$. As real stones have a distinct shape, the water-working also occurs by reorientating stones, and by the stones that redeposit on the bed. Therefore the number of stones that have to be moved from a real bed to assure that it has been water-worked is lower. The randomness of the bed presented here is only assured for thick layers of rock.

The water-worked bed does have a deterministic critical load that represents the load needed to displace the most unstable stone. However, as this load is dependent on several stone characteristics in reality, and not only on the protrusion, it is difficult to determine.

With most measurement techniques the bed elevations in the pores cannot be resolved. The exponential left tail of the probability density in figure 3.4 represents the bed elevations in the pores. The standard way of measuring bed protections is by a point gauge with a hemisphere on its tip. This means that the pores are not resolved. Therefore the measured mean bed level will be higher than the real mean of all bed elevations. Measurement techniques with a higher resolution will yield a lower bed level. This is also concluded by Meulepas *et al.* (1999).

Conclusions can also be drawn on model tests of bed protections. At the start of a flume test concerning bed stability some loose lying stones will move first that do not determine the real ‘strength’ of a bed protection. Therefore, prior to experiments on bed stability the bed must be water-worked. Otherwise the entrainment of stones will be overestimated, and with that the damage. This will lead to conservative designs of bed protections. The number of stones that have to move before the bed is water-worked is dependent on the initial bed geometry. Therefore a bed is only water-worked when a certain *number* of stones (per unit of area) have moved, not when flow has been applied for a certain *time*.

Chapter 4

Experimental Arrangement

4.1 Introduction

In this chapter the experimental techniques, set-ups and configurations that were employed are described. Two experimental series were conducted. The first focussed on the relation between velocity near and pressure fluctuations on bed material. The second focussed on the relation between flow structures and initial stone movement. To this end, two measurement techniques were developed for the present use. One was the use of miniature pressure sensors, the second was Particle Image Velocimetry (PIV). In the next sections the two measurement techniques are described. This is followed by two sections describing the set-ups of the two experimental series.

4.2 Pressure transducers

During both experimental series pressure sensors were used. The pressure measurements were previously described in Hofland (2001). At the start of the project the following requirements were formulated: the sample frequency had to be at least 100 Hz, the accuracy had to be at least 1 N/m^2 , the measuring area could be $0.5 \text{ cm} \times 0.5 \text{ cm}$ at most and the full range had to be at least 2500 N/m^2 . The sensor had to be water resistant and so small that it could be placed inside an artificial stone. It was not clear yet whether sensors existed, meeting the criteria.

Especially the low range, and corresponding high accuracy, were found to be characteristics rarely available in commercial pressure transducers. Still two suitable sensors were identified from *Druck* and *Honeywell*, see figure 4.1. Both work by a piezo-resistive technique. The piezo-element is a small silicon diaphragm that is subjected to a differential pressure. In the present application one side is connected



Figure 4.1: Selected pressure sensors, *Honeywell* (left) and *Druck* (right) (different scales, approx. 1:1).

to the atmosphere and the other side to the medium in which the pressure has to be measured. The electrical resistance of the diaphragm changes when it is bent by the pressure difference, and this property is used to measure the pressure.

The *Honeywell* transducers (24PCE series) have a full-scale range of 3450 N/m^2 , a response time of $< 1 \text{ ms}$, and a maximum error due to non-repeatability, hysteresis and non-linearity of 0.4% full scale. The size of the measuring diaphragm is $2 \text{ mm} \times 2 \text{ mm}$. The transducers have a rather large temperature dependence.

The *Druck* transducers (PDCR series) have a full-scale range of 7500 N/m^2 and similar accuracy as the *Honeywell* transducers. They are ready-to-use, water-resistant and have a disc of 5 mm diameter as measuring area. They are temperature compensated.

The *Honeywell* sensors were chosen because of the fact that they were the smallest and the measuring range fitted the present application best. The plastic casing of the *Honeywell* sensors could easily be reshaped. The *Druck* sensors were made of steel, and were therefore more difficult to install. With the *Druck* sensors the atmospheric pressure was led through a thin tube such that it took a long time for the dry pressure side to adjust to atmospheric pressure changes. The *Honeywell* sensors were not temperature compensated. However, the temperature of the water did not vary more than 0.1°C during the experiments, so this did not pose a large problem. Considering that the *Druck* sensors were roughly a factor hundred more expensive, and that the results of the *Honeywell* sensors seemed better, the choice was easily made.

An example of pressure measurements using the *Honeywell* sensors is given in figure 4.2. This shows spectra of fluctuating pressures on a bed-mounted cube. It can be seen that the spectra for three different discharges collapse well when normalised with the bulk mean flow velocity, U . This is what is expected with the high Reynolds numbers of these trial experiments.

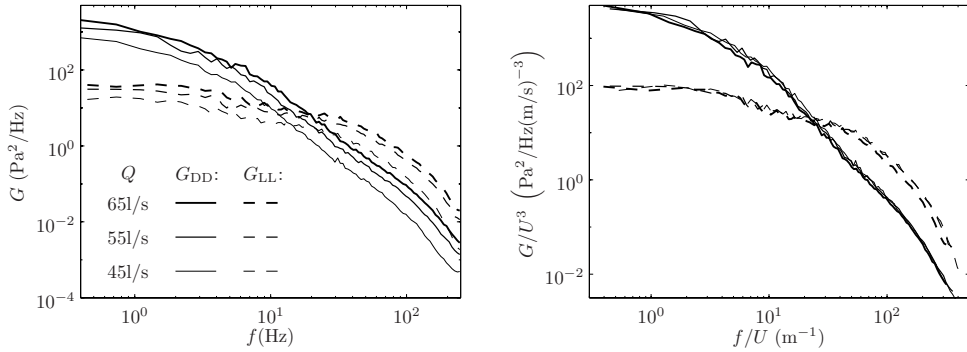


Figure 4.2: Pressure spectra (G_{ii}) on a bed-mounted cube in a granular bed. The right plot depicts normalised pressure spectra. D is the pressure difference between the upstream and downstream face of the cube, L the pressure at the top face.

Especially the flume used in the first experimental series was subject to environmental vibrations that led to spurious pressures. These pressures could partly be filtered out by techniques that are discussed in appendix A.

4.3 Particle Image Velocimetry

In this section the Particle Image Velocimetry (PIV) technique will be described. First the general principle of the technique is briefly described, after which the specifics of the equipment and set-up used are described.

4.3.1 General technique

The PIV technique can be used to measure instantaneous flow fields. This enables examination of the spatial structure of the flow. The PIV method most commonly used at present is double-frame, single-exposure digital PIV. For the 2D implementation of this technique – which was used – two separate images are made of an area in a flow by a CCD camera. The flow is visualised by adding seeding particles to the fluid. These small particles scatter the light and follow the flow well. As the seeding particles are very small, a powerful illumination of the measuring area is needed. A laser is mostly used for this. The coherent light can be shaped to a light sheet that illuminates the required plane in the flow. When one calculates the two-dimensional correlation of the measured light intensity in small parts (windows) of two sequentially recorded images, the maximum correlation is found at the mean displacement of the seeding particles in the flow. This is a direct indication of the velocity at that ‘point’. As the

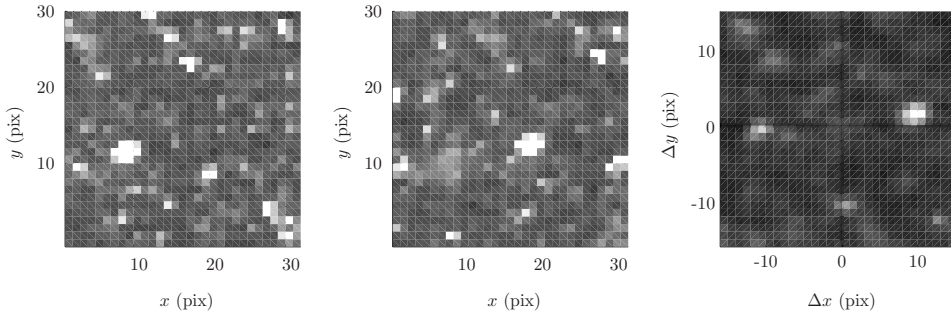


Figure 4.3: Two consecutively recorded 32 by 32 pixels windows and the 2D correlation of the two (right). A lighter shade is a higher value of light intensity or correlation, respectively.

images are made by a CCD camera, all information is digitised from the start of the process. This enables the user to process large amounts of data. A typical camera has 500^2 to 2000^2 pixels, which can be used to obtain a flow field with about 1000 to 60000 vectors. Example plots of two consecutive windows (32 by 32 pixels), and the correlation peak indicating the mean displacement of the particles between the two recordings are shown in figure 4.3. The highest value of the correlation is found at a displacement of about nine pixels to the right and two pixels upward.

4.3.2 Equipment

A standard PIV system (hardware and software of *LaVision*) was used to measure streamwise and vertical 2D velocity fields in the centre of the flume. The dedicated *Kodak* ES1.0 camera (1008×1008 pixels) and 50 mJ double *New-Wave* YAG laser both have a maximum double-frame sampling frequency of 15 Hz. So velocity fields can be obtained with a 15 Hz sampling frequency. The time interval between two images can be set to a very wide range of values, as two separate lasers are used to give the two light pulses. For the flow velocities used in the measurement typically an interval time of 2 ms was used. The flow was seeded with hollow glass spheres of $10 \mu\text{m}$ diameter, which are only available in one size. The optimal situation is obtained when a particle image is as large as two to three pixels, as the position of the particle – and hence the velocity – can then be determined most precisely. Therefore these particles were small for the present purpose (one pixel is $150 \mu\text{m}$ wide, compared to a particle image of around $20 \mu\text{m}$). Still, these were the best particles available. The air inside them gives them good reflective properties and their small size and density

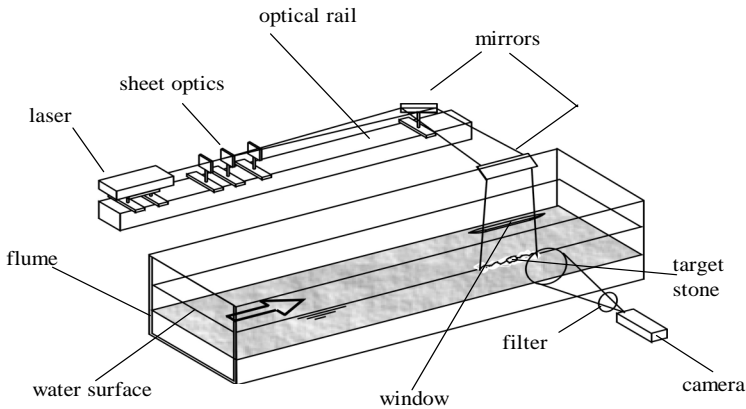


Figure 4.4: Schematised PIV set-up.

of 1100 kg/m^3 lets them follow the flow¹. And actually larger particle images were observed in the recordings (see figure 4.3). This is probably due to the fact that the particles can stick together and that the lens has imperfections. In a test set-up the minimum amount of seeding needed to obtain a good measurement (for a $150 \text{ mm} \times 150 \text{ mm}$ measuring area) was determined at about 20 mg/l . The water has a slightly milky appearance at these concentrations.

The set-up of the PIV system as constructed in the laboratory is depicted in figure 4.4. The distance between light sheet optics and the measuring area was set to about 1.5 m in order to keep the divergence angle of the sheet width limited, yielding a constant light intensity over the height. This distance could become very impractical in the limited space available, therefore the optical rail, on which the optics are mounted, was placed in line with the flume, and the laser sheet was guided towards the measuring area using two mirrors where it was about 150 mm wide. It entered the water surface undistorted through a streamlined and coated window of 20 cm long and 1 cm wide, so that no free water surface was present where the sheet entered the water. This window could be positioned a few mm into the water using micro-positioners. It caused some small waves on its downstream side, but did not affect the flow around the target stone.

¹Using Stokes' law, these particles are predicted to have a fall velocity of $5.4 \mu\text{m/s}$ and an adaptation time (time in which an initial velocity difference decreased by a factor $1/e$) of $6 \mu\text{s}$. This is negligible.

The sheet optics consisted of three lenses. The first lens is a negative spherical lens. The distance from this lens to the measuring area determines the width of the sheet. A positive and a negative cylindrical lens placed just behind this spherical lens determine the thickness of the sheet. The sheet still became slightly thick, so a 1.5 mm slit was placed in the sheet. This resulted in an 1.5–2 mm thick sheet with a rather constant light intensity, see figure 4.5. A thicker sheet would decrease out-of-plane motion of the seeding particles, but the resolution would decrease. With this thickness of the sheet the measuring volumes in which the velocities are determined are almost cubical, so a thicker sheet was not used.

The post processing of the images was done as follows – for an explanation of the terms used see Raffel *et al.* (1998). The velocities were determined using a multi-pass cross-correlation method with discrete window off-set, using window sizes of two times 32×32 pixels and one time 16×16 pixels with a 50% overlap. This gave a vector spacing of 1.2 mm. The final results were checked using a median filter (with the possibility to select the second-highest correlation peak), an absolute allowed vector range, and a minimum ratio of the height of the correlation peak to the highest noise peak of $Q=1.1$. The intermediate vector fields were checked with similar checks ($Q=1.4$) and smoothed with a 3×3 Gaussian filter. The Kolmogorov length scale was not resolved. Therefore the small-scale turbulence (wavelengths smaller than 2.4 mm) will cause noise in the determination of the velocity vectors. Still typically 90% to 95% of all vectors were validated. The unresolved fluctuations will not lead to significant forces on the stone and are therefore not of interest.

4.4 First experimental series

The first set of experiments was performed in order to obtain a data set of pressures on bed material and simultaneous near-bed velocities. The results from these measurements are mainly used to distinguish the different force-generating mechanisms. These are analysed in chapters 5 and 6.

4.4.1 Equipment

The flume that was used had a steel frame and glass sides. It was 14 m long, 0.5 m wide and 0.6 m high. Water was pumped through the flume from a central system in the laboratory. It entered the flume via a stilling basin.

Stones were placed on the floor, one layer thick, from 5 m upstream to 2 m downstream of a cubical model stone with pressure sensors mounted inside. The stones can be classified as being shaped irregularly (CUR, 1995). The stones were angular, i.e. the edges were sharp, like stone used for bed protections. They were sieved with two sieves with openings of respectively 2.5 cm and 4 cm, in order to get

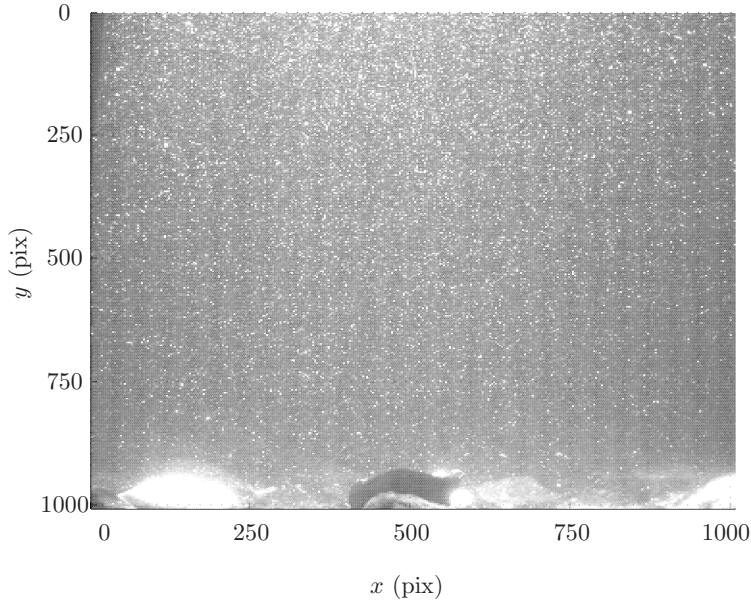


Figure 4.5: Example of a single PIV recording of flow over a rough bed.

a shortest axis (which points upwards) of about 3 cm length, which was the size of the artificial stone used. Extremely elongated or flat stones were removed. Still quite some variation was present in the heights of the stones. The flow velocity during the experiments was too low to displace the stones.

A cubical shape was chosen for the model stone for a number of reasons. It has sharp edges like the crushed stone used for bed protections, it is easy to describe, and the flow around it is fairly easy to analyse. A 30 mm high, hollow cube was made from stainless steel. The cube was placed in the axis of the flume with one face on the bed and two vertical faces parallel to the flow direction. It was possible to move the cube to different vertical positions, enabling different protrusions. The miniature pressure transducers described in section 4.2 were used to capture the fluctuating pressure fluctuations on the cube. They were mounted inside the cube with their diaphragms under pinholes in three faces of the cube, in the centre plane of the flume, see figure 4.6. The electrical wiring and a tube connected to the atmospheric reference pressure were led through the bottom of the flume. A reference pressure sensor was placed in a cavity under the bed to measure spurious pressures generated by environmental vibrations.

A 2-component, 4 mW Laser Doppler Velocimeter (LDV) was applied for the veloc-

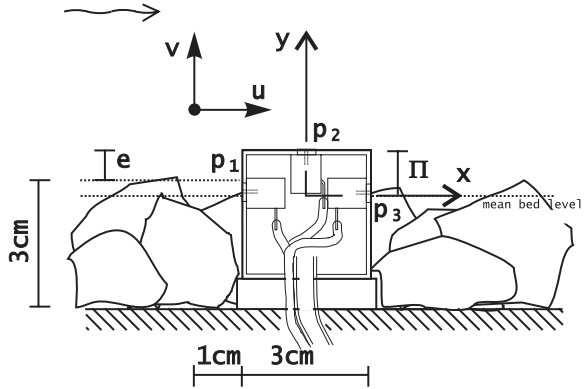


Figure 4.6: Longitudinal section of the instrumented model stone, including three pressure transducers, for $\Pi = 1$ cm.

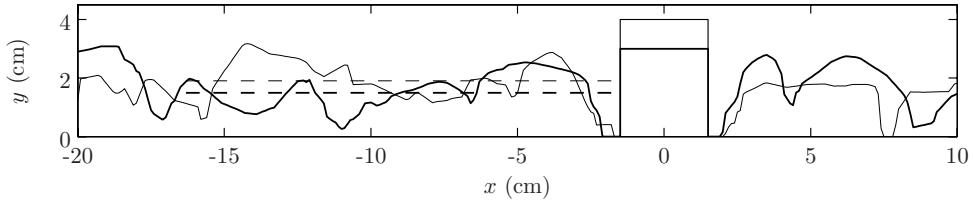


Figure 4.7: Longitudinal bed profiles, averaged over the cube width, for bed 1 (thin line) and bed 2 (thick line). The average local levels upstream of the cube are indicated by the dashed lines (thickness corresponding to the bed profiles). The cube is centred at $x = 0$.

ity measurements. It uses the forward-scatter, reference-beam method. By changing the front lens of the laser the measuring volume can be altered. A 400 mm lens resulted in a measuring volume with dimensions of about 10 mm in spanwise direction, and 1 mm in the other directions. Measurements were done 1 cm upstream of the cube. The laser could be traversed up and down. The sampling frequency was $f_s = 500$ Hz for both the velocity and the pressure measurements. This was enough to resolve the scales that are important for the drag and lift force fluctuations (resolution $\approx U/f_s \approx 1.5$ mm $\ll d_{\text{cube}}$).

All pressure and velocity signals were low-pass filtered with a cut-off at the Nyquist frequency (using the same filter) and recorded simultaneously using a data-acquisition board. Both the tracker of the LDV and the pressure amplifiers have a bandwidth larger than 1 kHz, which ensures that the time delay of the signal is smaller than

the sampling interval of 2 ms. The pressure diaphragm was placed about 3 mm from the outside of the cube giving a flat frequency response under the present Nyquist frequency. These facts ensure that the signals are recorded simultaneously.

Water levels were measured with Pitot tubes at three positions in the flume. The reproducibility of a measurement was within 0.2 mm. The accuracy of one water level measurement is estimated at 0.4 mm. The discharge was measured by an orifice plate in the inflow pipe with an accuracy of about 0.7 l/s.

4.4.2 Configurations

Three flow configurations were considered. A uniform flow (case U), a transition of a smooth bed to a rough bed with developing turbulence (case T) and a backward-facing step (case S). Table 4.1 mentions the flow conditions used for these cases.

The first was a uniform open channel flow (case U). Actually, the flow was not completely in equilibrium, as the bed was horizontal, leading to a slightly accelerating flow, although effects of this are expected to be small. All experiments for case U were repeated once for every combination of discharge and protrusion of the cube with a different bed-layout. Between the two series the stones on the bed were randomly replaced. Each bed was made with the same stones, placed with the same density, so that the mean features of the bed (e.g. roughness) were unaltered. However, the micro-topography around the cube was changed due to the random placement of the stones.

The exposure is defined here as the height of the top of the stone to the local mean upstream bed level. This bed level was determined by averaging the bed elevations, that were measured in three longitudinal sections, over a length of 15 cm upstream of the cube. The measured heights of the stones, including the upstream bed levels as defined here are depicted in figure 4.7. It turned out that the two randomly placed beds had a different upstream level, so that, with two heights of the cube relative to the flat bottom of the flume, four exposures were measured, the values of which are given in table 4.1.

The second configuration was a transition from a smooth bed to a rough bed (case T). To achieve this configuration, all stones more than two water depths upstream of the cube were simply removed from the flume. This enabled measurements at $2h$ downstream of the smooth-rough transition (h is the water depth at the location of the cube). In this configuration the large-scale turbulence has not developed yet, so the relative turbulence intensity near the stone will be less than for case U. The stones near the cube were left in the same positions as during the second series of case U. This enables a fair comparison between the two cases, as the micro-topography was unaltered.

The third configuration was a backward-facing step (case S). Now a 3 metre long

Case	bed #	Π [cm]	e [cm]	Q [$\frac{\text{m}^3}{\text{s}}$]	h [m]	Re [-]	Re_* [-]	τ_b [$\frac{\text{N}}{\text{m}^2}$]
U	1	0	1.1	0.065	0.168	$1.3 \cdot 10^5$	3250	11.3
U	1	1	2.1	0.065	0.166	$1.3 \cdot 10^5$	3250	11.8
U	1	0	1.1	0.055	0.161	$1.1 \cdot 10^5$	2650	7.6
U	1	1	2.1	0.055	0.159	$1.1 \cdot 10^5$	2650	7.5
U	1	0	1.1	0.045	0.157	$0.9 \cdot 10^5$	2200	5.2
U	1	1	2.1	0.045	0.156	$0.9 \cdot 10^5$	2200	5.5
U	2	0	1.5	0.065	0.169	$1.3 \cdot 10^5$	3250	12.1
U	2	1	2.5	0.065	0.167	$1.3 \cdot 10^5$	3250	12.3
U	2	0	1.5	0.055	0.162	$1.1 \cdot 10^5$	2650	10.9
U	2	1	2.5	0.055	0.157	$1.1 \cdot 10^5$	2650	6.9
U	2	0	1.5	0.045	0.156	$0.9 \cdot 10^5$	2200	5.8
U	2	1	2.5	0.045	0.154	$0.9 \cdot 10^5$	2200	4.4
T	2	0	1.5	0.055	0.160	$1.1 \cdot 10^5$	2600*	7.6*
T	2	1	2.5	0.055	0.159	$1.1 \cdot 10^5$	2600*	7.5*
S1	2	0	1.5	0.035	0.201	$0.7 \cdot 10^{5**}$	—*	—*
S1	2	1	2.5	0.035	0.200	$0.7 \cdot 10^{5**}$	—*	—*
S2	2	0	1.5	0.035	0.198	$0.7 \cdot 10^{5**}$	≈ 0	≈ 0
S2	2	1	2.5	0.035	0.198	$0.7 \cdot 10^{5**}$	≈ 0	≈ 0

Table 4.1: Flow conditions for the measurements of the first series. *) τ_b for cases T and S are unreliable, as the water slope is not constant. **) based on local values of h and $\langle \bar{u} \rangle_h$.

and 11 cm high (i.e. 8 cm above the stone layer) step with a smooth surface was placed at two positions upstream of the cubical model stone such that measurements were made at $12h_s$ (case S1) and $8h_s$ (case S2) behind the step (h_s is the step height). The first position is downstream of the reattachment point, the second approximately at the reattachment point. For this configuration the stones surrounding the cube remained at the same positions as for case T and the second series of case U. The Froude number on the step had to be low to prevent the water surface becoming undular, so the water depth was increased, and the discharge was decreased (table 4.1).

The positions of the pressure sensors, giving pressure signals p_i , are shown in figure 4.6. Indicators for the potentially displacing fluctuating drag and lift forces are obtained from the measured pressures by $D = p_1 - p_3$ and $L = -p_2$, respectively.

The pressure sensors used to form D are located at the same height so vibrations are thought to give the same pressures at these locations. Therefore the vibrational noise is cancelled automatically from these signals (see difference filter in appendix A.3). As the bottom of the cube was attached to the floor it was not possible to estimate the lift pressure by measuring a gradient. Therefore only the top pressure was used. The environmental vibration could be filtered from this signal using the reference signal. Further, the measured point pressures have to be translated to forces. In the analysis it will become clear that the fluctuating horizontal pressure difference (D') is created by large-scale / low-frequency flow structures. This means that the pressure measured at a point will be representative for the stagnation pressure. Therefore D' and 'drag force fluctuation' are qualitatively interchangeable. For L' this is more difficult. Due to instrumentation reasons the pressure sensor at the top could not be placed near the leading edge of the cube, where streamline contraction, and the largest Bernoulli lift was present. Nevertheless, the present position of the sensor did enable us to see that the second term in eq. (2.13) does make a contribution to the total force.

The determination of the average pressures was rather imprecise. Because the pressure signal had an unknown offset due to the large amplification of the signal, the mean pressure was determined using the measured mean pressures and water levels before and after stopping the flow. This gave a combination of several error sources, resulting in an error of about $\pm 10\%$.

The bed shear stress was determined with the following equation:

$$\tau_b = \rho(\beta U^2 - gh) \frac{\Delta h}{\Delta x}, \quad \text{where } \beta = \frac{\langle \bar{u}^2 \rangle_h}{\langle \bar{u} \rangle_h^2} \quad (4.1)$$

in which an overbar denotes a time average and pointed brackets a spatial average. The cross-sectional averaged velocity $U=Q/Bh$ (used as an estimate of depth averaged $\langle \bar{u} \rangle_h$), the water depth, h , and the water surface slope $\Delta h/\Delta x$ were measured. The term $\rho\beta U^2 \Delta h/\Delta x$ appears in the momentum balance due to the horizontal bed of the flume. β was determined from a log-fit through a measured velocity profile, resulting in the value 1.06. The side-wall contribution to the total shear stress was neglected because of the large roughness of the bed. As \bar{D} , \bar{L} and τ_b could not be measured with great accuracy, ρU^2 will be used as a scaling variable for the pressures.

4.4.3 Mean flow characteristics

In figure 4.8 the average velocity profiles, Reynolds stress, and turbulence intensities for the various cases are presented, normalised on the basis of the depth-averaged flow velocity $\langle \bar{u} \rangle_h$. The measured turbulence intensity in case U is low compared to the equations given by Nezu & Nakagawa (1993), given in figure 4.8. This is probably caused by the low h/d ratio (Wang *et al.*, 1993).

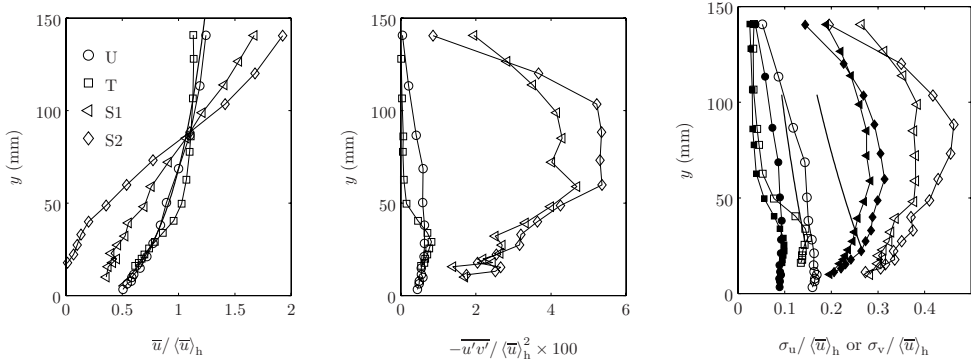


Figure 4.8: Vertical profiles of mean velocity (left), Reynolds stress (middle) and turbulence intensity (right), normalised by depth and time averaged longitudinal velocity $\langle\bar{u}\rangle_h$ for cases U, T, S1 and S2. Turbulence intensities for $\sigma(v)$ have filled markers.

The fluctuating drag and lift indicators D' and L' ($D' = p'_1 - p'_3$ and $L' = -p'_2$) were determined accurately. In figure 4.2, example spectra of both components are depicted for three discharges. As the length scales (depth and stone size) are the same in all cases, the spectra should collapse if the time scale is removed from both axes. So G was divided by U^3 , and f was divided by U . It can be seen that the spectra collapse well, indicating that the flow is fully rough.

4.5 Second experimental series

The second series of experiments was performed in order to see whether certain coherent flow structures are responsible for the entrainment of stones. It has a broader scope than the first measurement series. In the first series only the relation between the flow near a stone and the pressures on it is studied, whereas in the second series the origin of these near-bed velocities is examined, and additionally it is examined when the forces actually cause the displacement of a stone.

The PIV technique as explained in section 4.3 was used to capture the flow field at the time of movement of a stone. We focussed on the movement of a single stone, the target stone. This stone was repositioned at the same position several times. This made it possible to average the flow field at the moment of entrainment and study the average flow field that causes entrainment of the stone, without the variability of the micro bed structure. Additional to the PIV measurements, pressure sensors were placed inside stones surrounding the target stone. De Ruijter (2004) gives more details on the set-up. The measurements are analysed in chapter 7.

4.5.1 Equipment

A flume of 20 m long and 0.495 m wide was used. The water was recirculated in order to preserve the seeding for the PIV. A centrifugal pump powered the flow. The bed protection was modelled with angular stones with a d_{n50} of 1.78 cm, an average shape factor of $SF = 0.57$, and a grading width of $d_{n85}/d_{n15} = 1.27$. They were placed in a layer of about $1.54d_{n50}$ thick. Their size and density were such that they did not move under the flows conditions used. Under this layer concrete slabs were placed first with stones cemented in them which protruded about half their diameter (dotted line in figure 4.9). The spacing of the half-protruding stones was such that no porosity-jump was present near the fixed bed. This procedure also causes a more random placement of the stones on top. Besides the PIV and pressure measurements, a motion sensor was placed under the target stone (see triangle in figure 4.9). This sensor measured whether (a piece of metal under) the target stone was within 1 mm of it. This way it could be monitored when the (moving) target stone was in contact with the bed. The water level was measured at three streamwise positions, and the discharge was measured by determining the pressure drop in the smooth, straight pipes with the return flow.

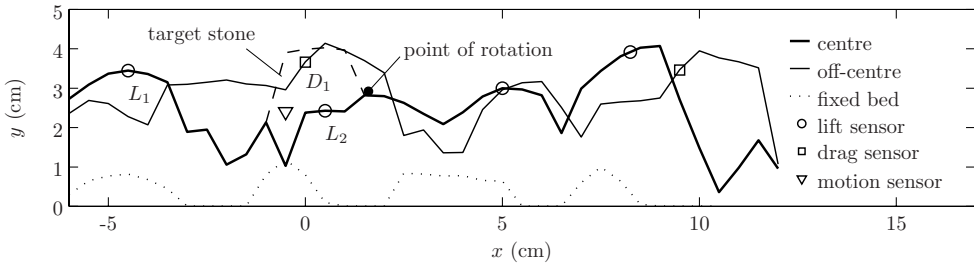


Figure 4.9: Measured longitudinal sections of the bed level near the target stone, indicating positions of pressure sensors. The y -coordinate is different than for the flow results.

4.5.2 Artificial stones

The use of a single moving stone (the target stone) means that all spatial parameters can be kept equal in different experiments, enabling one variable to be changed at a time.

In order to let only a single stone move, it was copied from a real stone using a less dense material, a two-component epoxy resin with $\rho_s \approx 1500 \text{ kg/m}^3$ ('Alabastine houtrotvuller'). The moulds for making the stones were made from latex. By adding

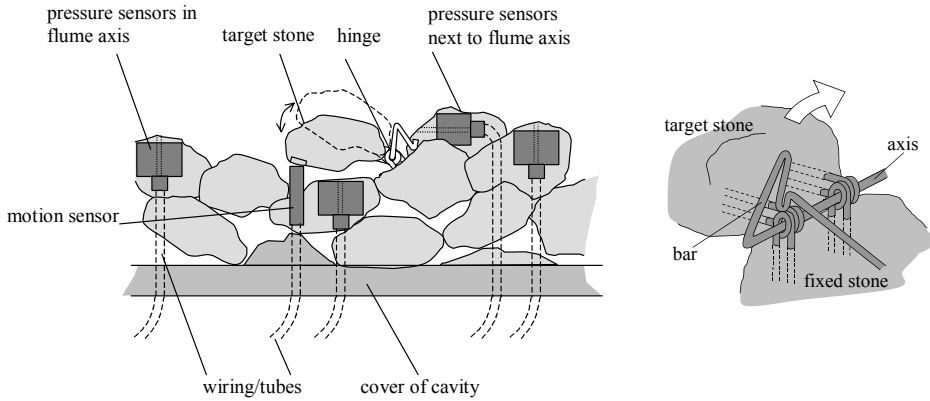


Figure 4.10: Sketch of instrumentation and set-up around target stone, with detail of the hinge (right).

PVC to the epoxy resin, the same stone could be reproduced in different densities. The target stone used most often had a d_n almost equal to d_{n50} , a Δ of 0.3, and a shape factor of 0.62. As the main mode of movement is pivoting or rolling (see appendix B), the stone was hinged in such a way that it could rotate around a point downstream of it (see figure 4.9). Further, the motion of the stone was obstructed by a little bar after pivoting over 10° – 40° . This obstructing bar was part of the axis around which the target stone could rotate, see figure 4.10. During experiments, when the stone reached the bar, the force on the stone was increased, as its exposed area was increased. The allowed angle of rotation was chosen such that the stone, when it reached its maximum rotation possible, would remain pushed against the bar for a noticeable duration before it would fall back with the passage of a negative velocity fluctuation. If the stone was allowed to rotate further, it would not fall back. This means that it would have moved from its position without the bar present.

Six pressure sensors and a motion sensor were installed around the target stone. They were placed in artificial stones. Figure 4.9 shows the measured positions of the sensors, and figures 4.10 and 4.11 show sketches and photographs of the set-up. A piece of granular bed was mimicked with the instrumented and other artificial stones. These stones were glued together to prevent their movement and placed on a 20 cm \times 10 cm plate, which could be placed on a cavity in the bed. These stones had the same grading, layer thickness and porosity as the surrounding bed. There was only place for one pressure sensor per stone, so a direction had to be chosen. As the fluctuating lift forces usually have small length scales, the spatial coherence will be



Figure 4.11: Left: mimicked bed under construction including moulds, wiring, epoxy-resin, etc. Right: mimicked bed in place, with target stone in the centre.

limited. Therefore sensors pointing upwards were put under the laser sheet, in the axis of the flume. The drag force usually has larger length scales, so sensors pointing horizontally upstream were placed off-axis, while the relation between velocity and drag force can still be examined. One sensor was placed in the stone under the target stone, in order to see how the pressure in the pore under the stone changes at the time of movement. A reference pressure sensor was present under the bed, which measured the spurious environmental pressures.

As the light sheet of the PIV system is illuminated from above, the stones on the bed are illuminated by the laser. In order to avoid overexposed recordings by the reflections from the bed, the stones under the sheet were painted with red fluorescent (Rhodamine) paint, and a green band-pass optical filter was placed in front of the camera lens. This way a large part of the reflected light from the stones was red, and was stopped by the optical filter. From trial tests we saw that in this way the amount of light from the laser could become 4 times larger than without the filter – which made the difference between a successful and an unsuccessful measurement – while the movement of the target stone was still visible on the recordings.

4.5.3 Timing

The aim of the experiments was to obtain PIV recordings just prior to, during, and after stone movements. The PIV recording could only be saved to hard disc at a rate of about 2 Hz. Therefore high frequency (15 Hz) recordings could only be made when the recordings were stored in RAM memory. This led to a limited storage capacity of 20 s of measurements. As in some cases the stone moved on average once every hour, the PIV and pressure measurements were only saved when the stone was not in contact with the bed for a certain time, and was thus regarded to have rolled away.

Recording should not start at the moment the stone first moved, as the flow field prior to the stone movement is also of interest. Hence recordings were made continuously and stored in a ring buffer (i.e. the oldest image in memory is replaced by a new recording). A macro was implemented in the PIV software (DaVis) that checked the signal of the motion sensor to determine whether the target stone had moved during the continuous measurements. When this happened, the macro waited for a fixed extra duration, after which the continuous recording was stopped. In this manner measurements from a few seconds before to a few seconds after the entrainment of the stone were stored in the computer memory, which could then be saved to disk. A new recording started automatically when the prior data were saved and the stone was back in its original position. In principle the duration between the detachment of the stone and the first consecutive PIV recording were measured accurately by the motion sensor. This would allow for a precise determination of the position of flow structures that lead to movement of the stone. Due to instrumentation problems, however, it was not possible to use this information.

In order to determine the unconditional flow statistics, additional recordings were made with the stone fixed to the bed, consisting of 300 frames, sampled at 0.5 Hz.

Two modes of motion of the target stone are discerned, rocking and rolling. The target stone is assumed to have rolled (i.e. displaced from its pocket) if it has reached the obstructing bar. When rolling, the entrained number of stones is increased. When merely rocking, the stone stays at the same position, and the entrainment is not influenced. The fact that the stone is sometimes pushed against the bar (i.e. would have rolled away) shows up in the bimodality of the histogram of the durations of the periods that the stone is detached from the motion sensor, ΔT_{up} , in figure 4.12. If the stone is pushed against the bar it takes much longer for it to fall down again. This gives the small second maximum at $\Delta T_{\text{up}} \approx 8$ s. This fact was used to automatically start the recording of the PIV images. The target stone was assumed to have rolled – and therefore recordings were made – when the duration of detachment exceeded the time between the two maxima in the histogram ($\Delta T_{\text{up}}=1$ s). Otherwise the mode of movement was regarded as rocking. The threshold of one second was not strictly dividing both modes of movement, so for determination of the real movements, visual inspection of the recordings was still necessary. For the uniform flow the mean velocity was high, so with a threshold of 1 s, a good division could be made between rocking and rolling. For the BFS this was more difficult, as after the passage of the flow structure that moved the stone, the stone would fall back very quickly.

4.5.4 Configurations

Two flow configurations were studied during the second experimental series, viz. a uniform flow and flow behind a backward-facing step (BFS). See table 4.2 for the

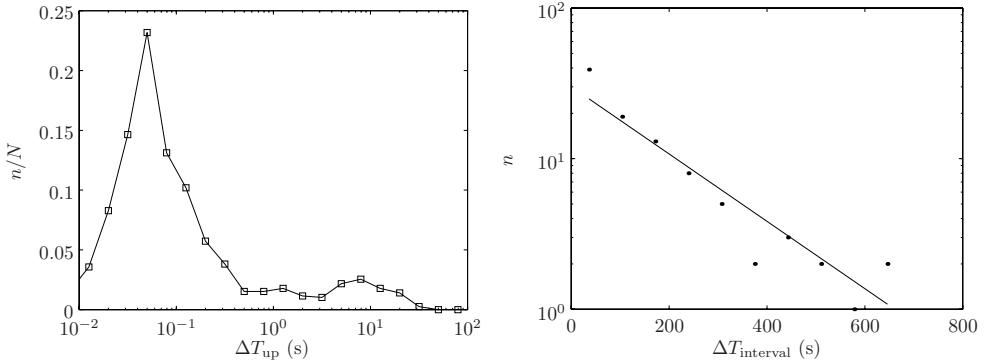


Figure 4.12: Left: histogram of the durations during which the target stone is detached from the bed. Right: histogram of the intervals between events where $\Delta T_{up} > 1$ s.

specific flow conditions.

For the tests with a uniform flow, the flow parameters were kept more or less equal for most tests. The water depth could not be changed too much, as increasing it would give a low B/h ratio, and decreasing it would give a high d/h ratio, both of which will lead to a flow profile that deviates from the standard law-of-the-wall. Fifteen different measurements were made, most of which were trial experiments. In the end five cases were selected with many stone movements, see table 4.2. Case U007 is considered to be the reference case, other measurements have one variation: a larger water depth (U009), a lower mobility, (U005), a larger exposure (U003), or a different target stone (U014). The column presenting the number of events only comprises the events where the stone actually would have rolled from its pocket.

For the BFS case a 5 m long and 12 cm high step was placed upstream of the target stone. Like during the first experimental series, the flow velocity had to be lower than for the uniform case to prevent a wavy water surface. Under these flow conditions the least dense target stone ($\Delta=0.3$) only moved near the reattachment point. So only around that location recordings of a moving stone could be made (cases B006 and B009, see table 4.2). The other recordings were used to determine the development of the flow field behind the step.

4.5.5 Mean flow characteristics

Uniform flow. The Reynolds number was around 10^5 . The turbulence was considered fully developed with the rough bed spanning a length of $66h$ upstream to $28h$ downstream of the target stone. The width/depth ratio of about 3 implies the presence of secondary flow.

Case	stone #	d_n [cm]	f_{mov} [hr ⁻¹]	# events	x_s/h_s [-]	Q [$\frac{\text{m}^3}{\text{s}}$]	h [m]	Re $\cdot 10^4$	Re_* $\cdot 10^3$	u_* [$\frac{\text{cm}}{\text{s}}$]
U003	3	1.8	20.9	34	∞	0.050	0.160	10	-	-
U005	3	1.8	0.6	3	∞	0.043	0.148	8.6	1.07	6.0*
U007	3	1.8	6.5	33	∞	0.051	0.159	10.2	1.14	6.2*
U009	3	1.8	39.3	61	∞	0.058	0.173	11.6	1.19	6.7*
U014	2	1.7	15.3	50	∞	0.042	0.144	8.4	1.07	6.0*
B006	3	1.8	0.8	8	12.1	0.033	0.175	6.7	-	-
B009	3	1.8	0.7	4	14.3	0.033	0.179	6.7	-	-
B007	3	1.8	0	0	8.2	0.033	0.175	6.7	-	-
B008	3	1.8	0	0	10.1	0.033	0.175	6.6	-	-
B010	3	1.8	0	0	0.7	0.032	0.170	6.4	-	-

Table 4.2: Flow conditions of the measurements in the second experimental series. *) The shear velocity was determined from the water-surface slope, the values obtained from a log-fit were about 10% higher.

The bed shear stress was determined from the water level slope using eq. (4.1). For case U007 this gives a Shields factor of $\Psi = 0.073$, using the Δ of the target stone. The low movement frequency of the stone (6.5 hr^{-1}) was expected at a lower Ψ .² It could be that because of the low stone density the added mass is relatively more important – which increases the critical Shields factor – or that the placement of the stone was relatively stable.

According to eq. (2.17) bed load transport increases rapidly with a slight change of the shear stress. This is indeed seen in measurements U005, U007, and U009: while the shear stress increases 25%, the movement frequency becomes 65 times higher.

The bed level was determined by fitting eq. (2.1) through the measured velocity profile, even though $0.2h < 5d$. In the region between $y = 0.006 \text{ m}$ and $y = 0.05 \text{ m}$ the log-law was fitted through three measured profiles. The optimal value for $y=0$ was obtained with the least squares method (based on errors on a log-scale), and the mean value for y_0 was used. With this y_0 the log-law was fitted again. The resulting log-profiles, including the linear profile between the roughness elements (Nikora *et al.*, 2001b) is given in figures 4.13 and 4.14.

The measured streamwise turbulence intensity is also given in figure 4.13 and corresponds reasonably well to eq. (2.2).

²Assuming a constant displacement length of $5d$, a coverage of 33% of the surface by loose stones, and that all these stones have the same chance of movement, the transport parameter, Φ was estimated. Using eqs. (2.17) and (2.18) this leads to $\Psi \approx 0.040$ and $\Psi \approx 0.056$ respectively.

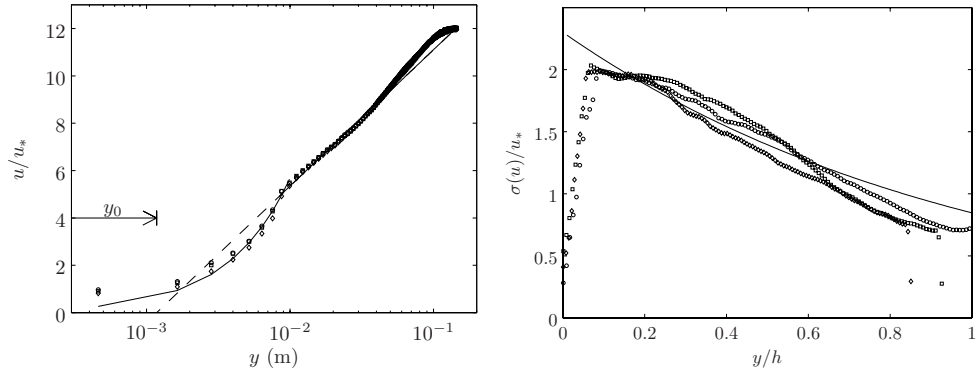


Figure 4.13: Left: streamwise velocity for cases U005, U007 and U009, including a fit of the linear-logarithmic profile. Right: profile of the streamwise turbulence intensity for the same cases and eq. (2.2). The u_* values from table 4.2 were used.

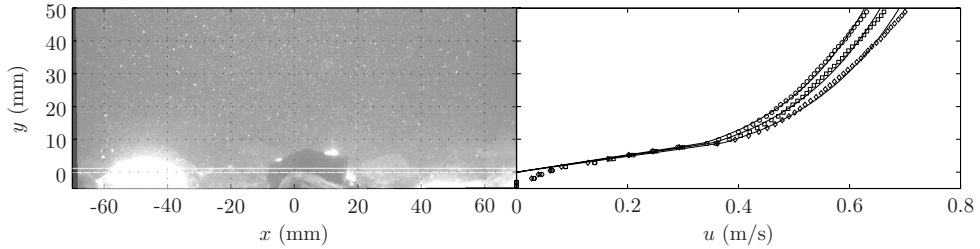


Figure 4.14: Velocity profiles ($Q=43, 51, 58$ l/s) relative to target stone.

Backward-facing step. The $y=0$ position that was found for the uniform flow – see figure 4.14 – was used as reference bed level. Using this level, the step height was determined at $h_s=0.067$ m.

Figure 4.15 shows the mean flow field. The reattachment point can be seen to be situated about 12 step heights from the step. This is quite far compared to Nakagawa & Nezu (1987). Apart from the large reattachment length – this is treated further in the next section – the flow over the BFS seems to correspond to similar flow fields as described in literature, with increased turbulence levels originating in the mixing layer that reach the bed around the reattachment point.

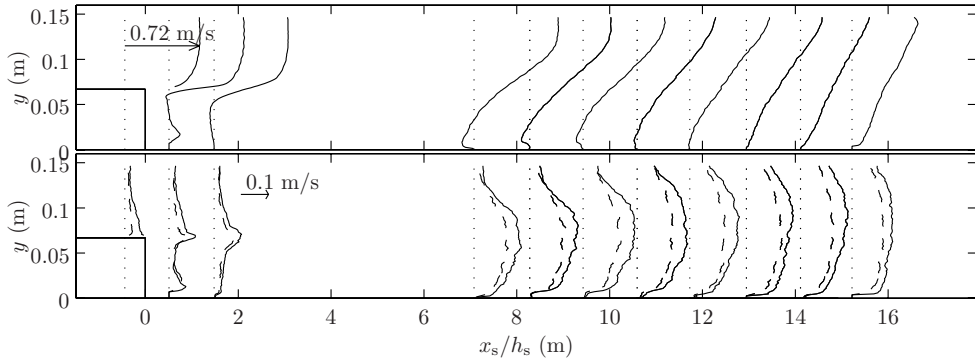


Figure 4.15: Vertical profiles of \bar{u} (top), and $\sigma(u)$ and $\sigma(v)$ (bottom, solid and dashed lines respectively) for BFS.

4.5.6 Position of the target stone

It is important to know whether the target stone represents a realistic stone in a realistic position. It has to be not too stable nor too unstable. Otherwise the flow processes that displace stones in reality will not be found. Due to the random nature of the bed, it is very difficult to determine whether the stone has a characteristic position. A first tool that we can use in order to check the position of the stone is the discrete particle model (DPM).

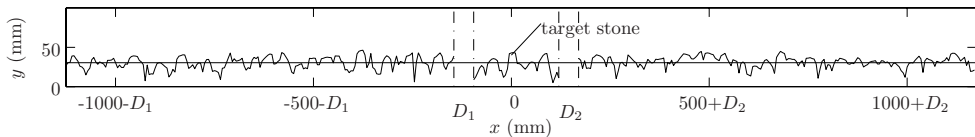


Figure 4.16: Measured streamwise bed profile for second experimental series.

In table 4.3 the characteristics of the elevations of the ideal random bed of spheres (chapter 3), the bed used during the second measurement series, and two prototype beds (Meulepas *et al.*, 1999) are compared. The values for the ideal bed differ from those in chapter 3 as the nominal diameter is used to make the values dimensionless.

The values of $\sigma(y_b)/d$, S , and K for the prototype beds and the bed in the tests are comparable. Only the extreme elevation is much larger for the prototype beds. This is consistent with the fact that no water-working was applied to the prototype beds. Therefore the bed used for the measurements is further compared to the ideal

	$\sigma(y_b)/d_n$	S	K	$\frac{\Pi_{\max}^*}{d_{n50}}$	$\frac{\Pi_{\max}^*}{\sigma(y_b)}$
Spheres	0.63	-1.35	6.3	1.0	1.6
Bed 2	0.44	-0.57	3.1	0.7	1.6
VBKO 40–200 kg	0.42	-0.26	3.1	1.2	2.9
VBKO 10–60 kg	0.57	-0.33	3.2	1.4	2.5

Table 4.3: Comparison between parameters of the elevations of the ideal random bed of spheres, of the bed of the second experimental series, and of two prototype beds (Meulepas *et al.*, 1999, VBKO in table). *) Π_{\max} is the protrusion of the target stone for the real bed.

bed.

A first observation in this comparison is that the standard deviation of the bed elevations of the ideal bed (i.e. the flattest random bed possible for spherical stones) is even higher than the standard deviation of the bed used during the measurements. This is unexpected as the real bed consists of irregularly shaped stones. However, it can be explained by the fact that the real stones will in general have their shortest axis upward, which will decrease the standard deviation of bed elevations.

Further, the bed elevation in the measurements has a negative skewness like the ideal bed, be it less extreme. In this bed, which was about $2d_n$ high, no very deep holes could be present. And if there would be, then they would probably not have been measured due to the resolution restrictions of the measurement. This could also be the reason why the kurtosis of the real bed elevation almost has the exact value of a Gaussian distribution (i.e. 3).

The characteristic of the target stone that is most easy to compare is its vertical extent (protrusion). We can see from table 4.3 that it is comparable to the maximum protrusion of the ideal bed, when normalised by the standard deviation of the bed elevations. However, which kind of structure will eventually move the stone also depends on the orientation and shape of the stone. In chapter 2 it became clear that the orientation of the single stone is the most important factor influencing its stability. The shape of the target stone is typical for bed protections. It has sharp edges, and a normal shape factor. Its smallest axis points upwards. This means that the area on which a lift force can act is usually larger than the vertically exposed area that determines the drag force.

The orientation of the top stones often becomes tilted away from the flow. The quasi-steady drag force is less effective on these stones. The present stone position is therefore probably illustrative for a water-worked bed. The lower the protrusion or the higher the pivoting angle, the more important the TWP forces become. In

order to check whether the TWP are also important for the first movement of a stone with a higher protrusion, a measurement was made with an increased protrusion of the target stone (case U003). For this position, similar flow structures still caused movement of the stone.

4.6 Reattachment length

In both backward-facing step (BFS) configurations, a very large reattachment length downstream of the BFS was measured (10–12 h_s), while in open-channel flows with a smooth bed reattachment lengths of 5–6 h_s are generally found. The main difference between these and the present measurements is the presence of roughness downstream of the step. Besides the possible influence of the roughness, the Froude number and the presence of an adverse pressure gradient have been reported to influence the reattachment length (Nakagawa & Nezu, 1987; Simpson, 1989, respectively). Therefore we plotted the reattachment length x_r against the Froude number at the reattachment point in figure 4.17. Here we see that the reattachment length for the different rough bed measurements is much higher. Moreover, the reattachment length generally increases with Froude number. The influence of the Froude number appears larger for the experiments with rough beds.

Another factor that influences the reattachment length might be the aspect ratio B/h , which was rather low in all three rough bed experiments. This topic deserves further research. The expansion ratio ($h/h_s - 1$) of the experiments reported in literature was similar to that in the present experiments, so this cannot be a reason for the differences.

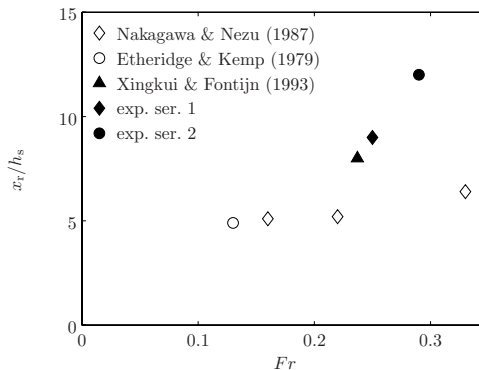


Figure 4.17: Reattachment length against Froude number downstream of BFS. Filled markers represent rough beds, open markers represent smooth beds.

Chapter 5

Quasi-Steady Forces

5.1 Introduction

In this chapter the measurements of fluctuating pressures on and velocities near a fixed bed element made during the first measurement series (see section 4.4) are analysed for the cases with uniform open-channel flow (U) and a roughness transition (T). The analysis focuses on the origin of the fluctuating forces. We will verify certain physical concepts on which conventional models for entrainment of bed material are based. The expressions for the relation between instantaneous near-bed velocity (components) and forces on bed material caused by the quasi-steady mechanism are checked.

It is generally thought that the fluctuating forces on bed material are generated by the same mechanism as the mean forces. Therefore we will refer to them as quasi-steady forces. It is confirmed that the quasi-steady mechanism explains a large part of the forces on bed material. Some deviations will be shown to be present of which some can be explained within the framework of the quasi-steady force and a few can be attributed to the TWP-mechanism. The latter mechanism is treated in the next chapter.

In the first section, the quasi-steady force equations are translated to probability density distributions (PDFs), which are compared to measurements. Then the relation between the exposure of and the forces on the stone is examined. Further analyses comprise a quadrant analysis and spectral analysis. Finally the influence of a low turbulence-intensity due to a smooth-bed-to-rough-bed transition is considered, using spectral analysis and the earlier derived PDF.

The drag and lift force (F_D and F_L) on the bed-mounted cube are assumed to be proportional to force indicators derived from the measured pressures, D and L respectively.

5.2 Probability density function for quasi-steady drag force

In this section the probability density function (PDF) for the forces on bed material is derived, based on the quasi-steady force-generating mechanism. This PDF can be used to check whether the quasi-steady mechanism is responsible for the forces on bed material. If this is the case, it can be used for probabilistic modelling of sediment transport (see section 2.5.2). The turbulence intensity is a parameter in the equation, so the derived distribution can be used to determine the influence of a non-equilibrium turbulence structure on entrainment of bed material.

We use our measurements of pressures on bed material to validate the PDF of drag forces for different turbulence intensities. Before the new relation is treated, the next section deals with the χ^2 -distribution, which Papanicolaou *et al.* (2002) proposed for the PDF for drag forces.

5.2.1 PDF for u_b^2

The drag force on bed material for hydraulically rough flow is often assumed to be proportional to the near-bed velocity squared (Wiberg & Smith, 1987, for example). Another observation is that the near-bed velocity has been seen to be distributed roughly Gaussian (Nikora & Goring, 2000, for example). These two facts enable us to derive the PDF of the drag forces on bed material. The square of a normally distributed variable has a χ^2 -distribution (with one degree of freedom). If the normally distributed variable has a non-zero mean, then the resulting distribution is called non-central. One of the possible expressions for the non-central χ^2 -distribution with one degree of freedom is (Evans *et al.*, 2000):

$$p(x) = \frac{\exp(-\frac{1}{2}x - \frac{1}{2}\delta^2)}{\sqrt{2}} \sum_{j=0}^{\infty} \frac{x^{j-\frac{1}{2}} \delta^{2j}}{\Gamma(j + \frac{1}{2}) 4^j j!} \quad (5.1)$$

where $x = y^2$, and y is normally distributed with a non-zero mean. $\delta = \bar{y}/\sigma(y)$ is the non-centrality parameter. The mean and standard deviation of the χ^2 -distribution are $\mu = \delta^2 + 1$ and $\sigma = \sqrt{4\delta^2 + 2}$, respectively.

The χ^2 -distribution was proposed by Papanicolaou *et al.* (2002) for forces on bed-material. However, they did not test the distribution against direct measurements of forces or pressures. If we choose the drag force F_D to be represented by the stochastic variable, x , and the near-bed velocity, u_b to be used as y – thus assuming that $F_D \propto u_b^2$ – then δ is the reciprocal of the near-bed relative turbulence intensity.

5.2.2 PDF for $u_b|u_b$

A problem that remains to be dealt with is the fact that the drag force actually is proportional to $|u_b|u_b$. This results in a different distribution for cases with a high turbulence intensity (small δ). Therefore we will now derive the PDF for F_D , based on the two notions that a) the near-bed velocity follows the normal distribution:

$$q(u_b) = \frac{1}{\sqrt{2\pi}} e^{-\frac{1}{2}(u_b-\delta)^2} \quad ,$$

where the velocity is normalised by its standard deviation, and b) the drag force is dependent on the near bed velocity as:

$$F_D = \alpha|u_b|u_b \quad ,$$

where α is a constant. Now we can transform the PDF of velocities, $q(u_b)$ to the PDF of drag forces, $p(F_D)$. This is illustrated in figure 5.1. We will first derive the PDF for $u_b > 0$, in which case $|u_b|u_b = u_b^2$.

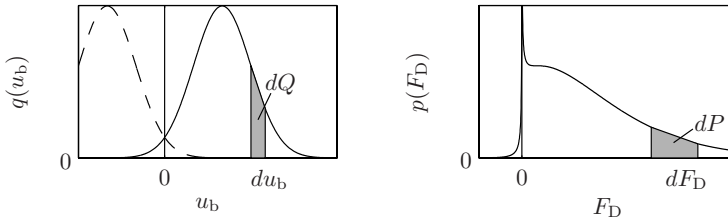


Figure 5.1: Pdf of velocities and derived PDF of drag forces.

We take a small area under the curve of $q(u_b)$, with an infinitesimal small width, du_b , which represents the probability dQ . As F_D increases for increasing u_b , there is a corresponding area under the curve of $p(F_D)$, dP , with infinitesimal small width, dF_D , which has the same probability. Now we can derive the relation between $q(u_b)$ and $p(F_D)$:

$$dQ = dP \Rightarrow p(F_D) = q(u_b) \frac{du_b}{dF_D} = q\left(\sqrt{F_D/\alpha}\right) \frac{1}{2\sqrt{\alpha F_D}} \quad (5.2)$$

We derive the PDF for $F_D < 0$ by mirroring the normal distribution of u_b (dashed line in figure 5.1), performing the same transformation, and mirroring the resulting curve in the y -axis [i.e. $p(F_D, \delta) = p(\alpha(-u_b)^2, -\delta)$ for $F_D < 0$]. The final PDF for F_D becomes:

$$p(F_D) = \frac{1}{2\sqrt{2\pi\alpha|F_D|}} \exp\left[-\frac{1}{2}\left(\sqrt{|F_D|/\alpha} - \text{sign}(F_D)\delta\right)^2\right] \quad . \quad (5.3)$$

This was checked against a Monte Carlo simulation of $p(\alpha|u_b|u_b)$ for 10^6 randomly chosen variables, and the distributions indeed matched. This formulation is easier in use than the χ^2 -distribution, which includes a summation from 0 to infinity. If the part for $F_D < 0$ is mirrored to the positive side, we end up with the χ^2 -distribution.

The mean and standard deviation of the distribution in eq. (5.3) are:

$$\mu = \alpha \left(\sqrt{\frac{2}{\pi}} \delta e^{-\frac{1}{2}\delta^2} + (\delta^2 + 1) A \right) \quad , \quad \text{and}$$

$$\sigma = \alpha \left[(6 - 2A^2)\delta^2 + 3 - A^2 + (1 - A^2)\delta^4 - 2\sqrt{\frac{2}{\pi}} A e^{-\frac{1}{2}\delta^2} (\delta + \delta^3) - \frac{2\delta^2}{\pi} e^{-\delta^2} \right]^{\frac{1}{2}} \quad , \quad (5.4)$$

where A is $\text{erf}(\delta/\sqrt{2})$ and $\text{erf}()$ is the standard error function. For $\delta \rightarrow \infty$ these values go to the values for the χ^2 -distribution ($\mu = \delta^2 + 1$, $\sigma = \sqrt{4\delta^2 + 2}$).

For practical use it is convenient to have explicit expressions for the mean and standard deviation. Hence a simpler function is fitted to the exact values of the mean and standard deviation for the χ^2 -distribution with a correction for the low values of δ :

$$\mu_{\text{fit}} = (\delta^2 + 1) - \exp(-1.63\delta)$$

$$\sigma_{\text{fit}} = \sqrt{4\delta^2 + 2 + e^{-0.55\delta^2}} \quad (5.5)$$

The errors in the parameterisations of μ and σ are less than 3% and 0.1% respectively and go to zero for increasing values of δ .

In figure 5.2 PDFs for $|u_b|u_b$ and u_b^2 (eqs. (5.3) and (5.1) respectively) are plotted for different values of δ . We can see that for $\delta = 0$ the PDF of $u_b|u_b|$ [eq. (5.3)] has a hyperbolic shape. For $\delta > 3$ the distribution has a positively skewed bell shape, getting less skewed when δ becomes larger and it will become Gaussian for $\delta \rightarrow \infty$. For $\delta \approx 2$ there is a transition between a hyperbolic shape and a bell-shaped curve: for values of F_D close to 0 the distribution has a peak and for higher values of F_D it resembles the positive half of a bell-shaped curve. We can see that the $p(|u_b|u_b)$ -distribution is approximated well by the χ^2 -distribution for $\delta > 2$. For $1 < \delta < 2$ only the right tails are still similar, and for $0 < \delta < 1$ they are dissimilar. When $\delta = 0$ it is obvious that the χ^2 -distribution is identical to $2p(|u_b|u_b)$ for $x > 0$, as the negative part of $|u_b|u_b$ is now mirrored to the positive side for u_b^2 . Next we will check whether the PDF [eq. (5.3)] is observed in measurements.

5.2.3 Drag force distribution

The pressure measurements described in 4.4 will now be used to check the influence of the turbulence intensity on the PDF of the drag force. The configurations with the largest exposure are used, as for these cases the drag force is expected to be

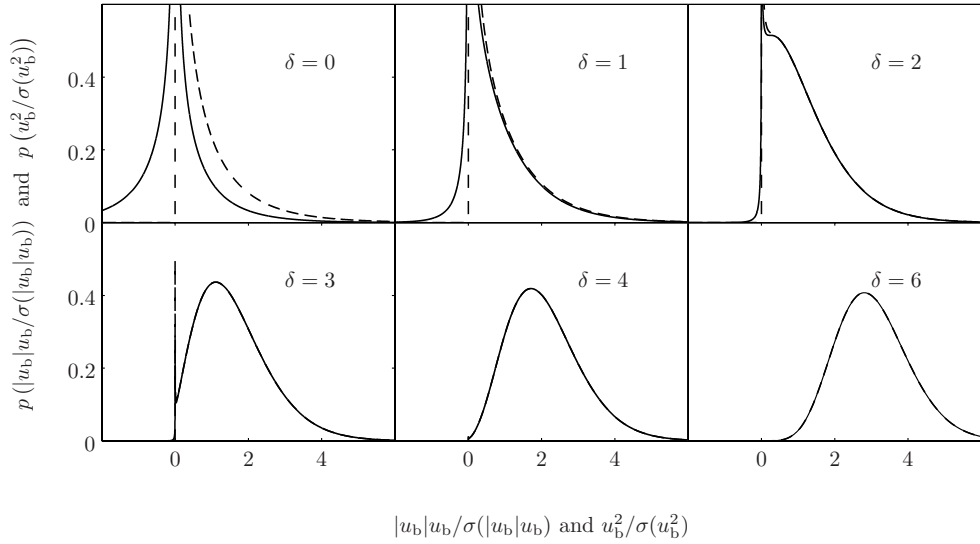


Figure 5.2: PDFs for $u_b|u_b|$ (solid line), and u_b^2 (dashed line), for various values of δ .

determined most by the quasi-steady mechanism. The flow configurations differed in such a manner that a wide range of values for δ – measured at $y = (15 \pm 1.5)$ mm – was obtained, shown in table 5.1. This height is $0.17d$ above the cube, which is close to $0.15d$. This height is optimal for correlating velocity sources and forces, see chapter 2. About 45 minutes of pressure measurements were available for every case, giving well-converged statistics. The PDFs for the measured velocity were not perfectly Gaussian, but could be approximated quite well by such a distribution, see figure 5.3 and the values for the skewness and flatness in table 5.1.

The measured PDFs of the instantaneous horizontal pressure difference, D , for cases U and T can be seen in figure 5.4. Linear scales are used in order to evaluate the shape of the distribution around the mean, and a semi-logarithmic presentation is given to evaluate the shape of the tails. It can be seen that the shape of the PDFs is predicted almost perfectly by eq. (5.3) using a δ determined from the measured velocities. Only the tails are not entirely correct, although the trend with a variation of δ is correct. The turbulence just downstream from the roughness transition is not yet totally developed, yielding a larger δ . This leads to a slightly less asymmetric distribution, which is predicted well by eq. (5.3).

For case S eq. (5.3) does not give a similarly good agreement, see figure 5.5. The theoretical distribution still works well for the (positive) tails of both cases S1 and

case	δ	Re	$\frac{\overline{u_b'^3}}{\sigma(u_b)^3}$	$\frac{\overline{u_b'^4}}{\sigma(u_b)^4}$
U: uniform open-channel flow	4.1	$1.3 \cdot 10^5$	-0.13	2.85
T: smooth-rough transition	5.9	$1.1 \cdot 10^5$	-0.31	2.98
S1: backward-facing step at $12h_s$	1.1	$0.7 \cdot 10^5$	0.58	3.38
S2: backward-facing step at $8h_s$	-0.1	$0.7 \cdot 10^5$	0.36	3.09

Table 5.1: Dimensionless flow parameters for the flow configurations used.

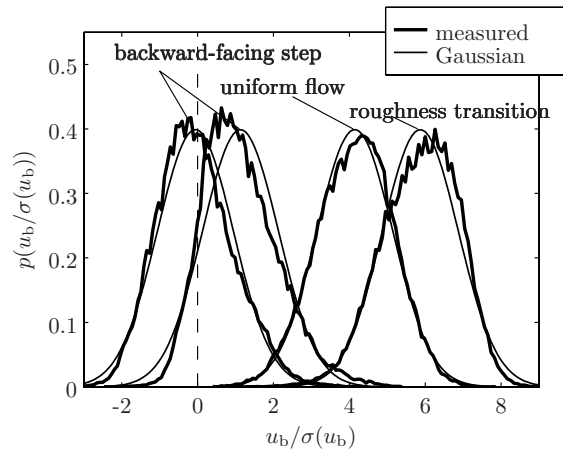


Figure 5.3: PDFs of normalised instantaneous near-bed velocity.

S2, however. When using the PDF for evaluation of sediment entrainment this is the region of interest. The clearly asymmetric shape for case S1, and the more nearly symmetric shape for case S2 are predicted, but the asymptotic behaviour around the mean value is not reproduced. Apparently the $p \propto |u_b|u_b$ law breaks down. Probably TWP cause a large part of the variance in this highly turbulent flow, see chapter 6.

The fact that the shape of the PDF of the drag forces is reproduced well, implies that the drag forces are created by the quasi-steady mechanism. Accordingly, the less perfect agreement for increasing turbulence intensities implies that other mechanisms also play a role.

5.3 Uniform flow

In this section we inspect the pressures on the bed-mounted cube for case U – uniform open-channel flow – in detail.

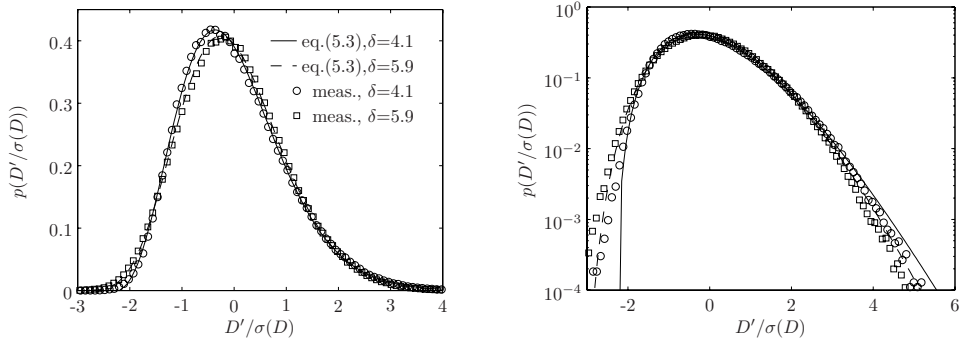


Figure 5.4: PDFs of D' for the uniform flow (U: \circ) and the roughness transition (T: \square).

5.3.1 Influence of exposure

The exposure of the cube is defined here as the distance between the top of the cube and the local upstream bed-level with a length of $5d$ (see the two dashed levels in figure 4.7). This is approximately the distance over which a protruding particle influences the velocity downstream of it (Schmeeckle & Nelson, 2003). In total four exposures have been measured ($e = 1.09$ cm, 1.47 cm, 2.09 cm, 2.47 cm), and three different discharges were applied per exposure. In figure 5.6 it can be seen that the pressures, both mean and fluctuating, indeed increase with exposure, as often assumed (Egiazaroff, 1965, for example). The pressure differentials for different discharges collapse reasonably, when normalised by ρU^2 . Due to the imprecise determination of the mean pressures, the various measurements of $\overline{D}/\rho U^2$ do not collapse very well. For \overline{L} , which was approximately 10% of \overline{D} , the relative error was too large to see whether the points collapsed. Therefore it has not been plotted.

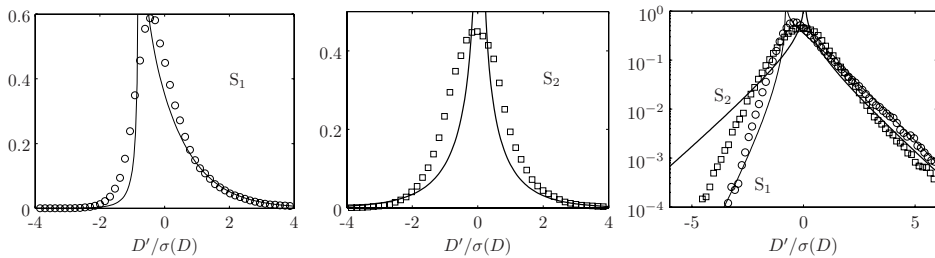
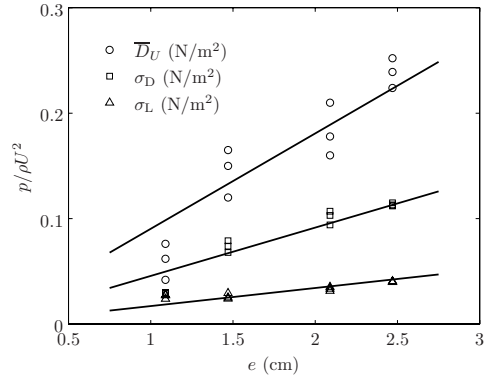


Figure 5.5: PDFs of the measured instantaneous pressure difference for the BFS. Linear (left and middle) and semi-logarithmic plots (right). Eq. (5.3) is plotted for the same values of δ . S1: \circ , and thin line, S2: \square , and thick line.

Figure 5.6: $\overline{D}/\rho U^2$, $\sigma_D/\rho U^2$, and $\sigma_L/\rho U^2$ as a function of e for the uniform flow case. Lines are linear fits through the data points. For each exposure three discharges have been used: 45, 55, and 65 l/s



Quadrant analysis

We will now conduct a quadrant analysis in order to investigate the dependence of the pressures D' and L' on the instantaneous velocity on the basis of figures 5.7 and 5.8. The plots display isolines of the joint probability density of (u_b, v_b) , as well as isolines of the conditionally averaged pressure fluctuations, $\overline{D'}(u_b, v_b)$ and $\overline{L'}(u_b, v_b)$, which show the pressure (difference) averaged over all instances that (u_b, v_b) lies within a certain range (i.e. \vec{u}_b has a certain magnitude and direction). It is defined as:

$$\overline{D'}(u_b, v_b) = \frac{1}{n_i} \sum_{i \in S} D'(i) \quad , \text{ where } S = i : |u(i) - u_b| \leq \frac{1}{2}w \wedge |v(i) - v_b| \leq \frac{1}{2}w \quad (5.6)$$

where i is the sample number, w is the velocity bin width and n_i is the number of measurements within a bin. The definition for $\overline{L'}(u_b, v_b)$ is analogous. This representation of the data shows the influence of the two components on the magnitude of the pressures clearly. If the pressure is highest in a certain quadrant, then it might even be possible to link the pressure fluctuations to certain coherent flow structures.

Q_4 -events ($u_b > 0$, $v_b < 0$) have previously been seen to correspond to transport at higher Re_* (Thorne *et al.*, 1989; Nelson *et al.*, 1995). In figure 5.7 $\overline{D'}(u_b, v_b)$ is depicted for increasing exposure. Except for the lowest exposure, the gradient of $\overline{D'}(u_b, v_b)$ has a fairly constant direction over all (u_b, v_b) combinations, which changes with exposure. For the most exposed particle ($e=2.5$ cm) $\overline{D'}(u_b, v_b)$ is hardly dependent on v_b . A higher u_b simply gives an increased $\overline{D'}(u_b, v_b)$. This will still lead to a situation where most extreme forces occur during Q_4 -events, simply because the events with highest u_b occur in this quadrant. When the exposure decreases it can be seen that $\overline{D'}(u_b, v_b)$ becomes a function of vertical velocity as well. This was not expected at first, but it can be explained by the fact that, when the stone is shielded by upstream stones, a downward flow is necessary to let the flow reach the stone. For

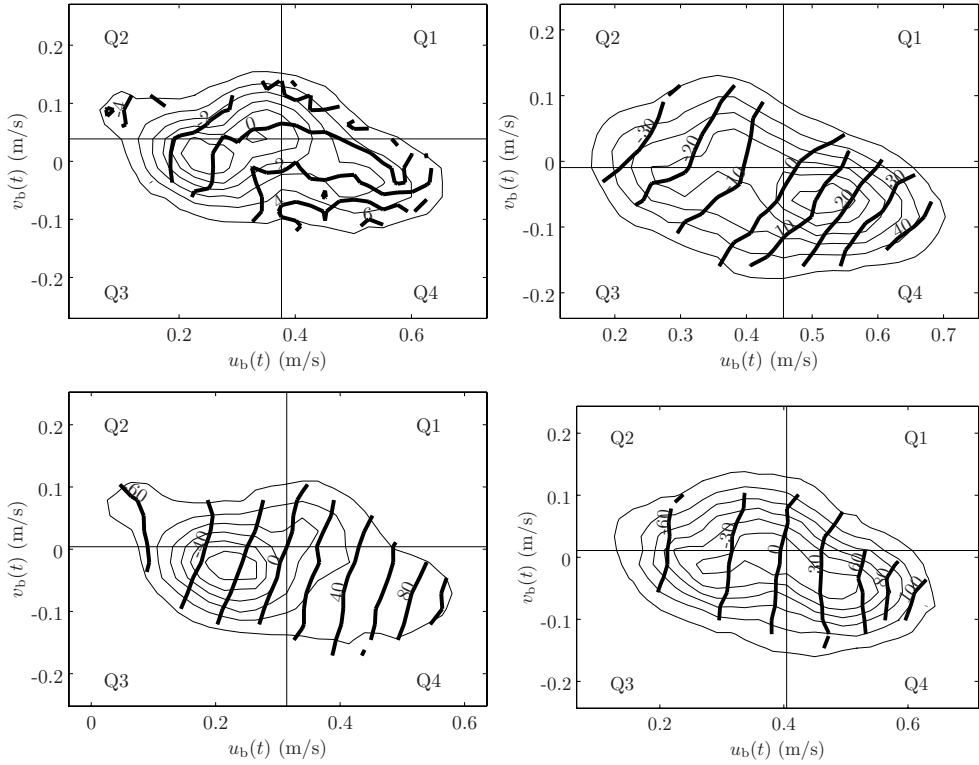


Figure 5.7: Joint PDF of $u_b(t)$ and $v_b(t)$ (thin isolines), and conditionally averaged $\overline{D'(u_b, v_b)}$ (thick isolines, label units: N/m^2) for case U and $e = 1.09$ cm, 1.47 cm, 2.09 cm, and 2.47 cm (from left to right and from top to bottom respectively). The straight solid lines indicate $\overline{u_b}$ and $\overline{v_b}$ respectively.

the smallest exposure, where the cube was almost totally shielded by the upstream stones (see figure 4.7), the dependence of D' on the longitudinal velocity is almost totally gone, and D' is almost totally dependent on vertical velocity. We must keep in mind that we have only measured a point pressure. Therefore for a certain stone this effect will probably be different at various levels on the stone, with the v -dependence highest on the lower, more shielded, levels of the stone. But it does show that Q_4 -events are the source of increased transport not only because large values of u_b occur most frequently in quadrant 4 when a positive shear stress is present (Nelson *et al.*, 1995). A negative v_b directly creates larger drag forces. It can be conceived as that a downward directed flow increases the exposed area of the stone, and hence increases the drag force.

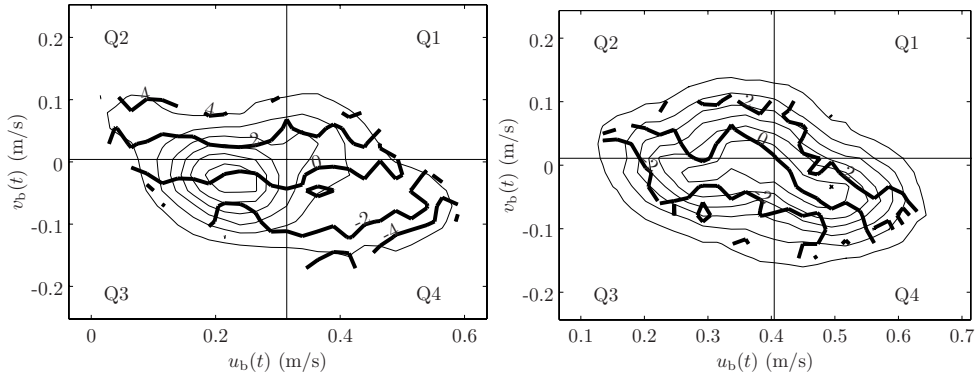


Figure 5.8: Joint probability density function of (u_b, v_b) (thin isolines), and conditionally averaged vertical pressure, $\overline{L'(u_b, v_b)}$ (thick isolines, label units: N/m^2) for uniform flow. $e = 2.1$ cm (left) and $e = 2.5$ (right).

A downward directed flow creates negative (stabilising) lift forces according to the second term on the right hand side of eq. (2.13). This effect is clearly observed in figure 5.8, as $\overline{L'(u_b, v_b)}$ increases with increasing v_b . This effect was present for both configurations and all exposures. A slight influence of u_b on the lift force is present for the higher protrusion (right plot), indicating an influence of the Bernoulli lift [first term on the right hand side of eq. (2.13)]. The $\overline{L'(u_b, v_b)}$ measured was not large; about 5 N/m^2 at maximum. The change of the Bernoulli lift [first term on the right hand side of eq. (2.13)] is probably dominant at the upstream edge of the cube, as the streamlines are contracted most there. However, there were no measurements at this location.

PDFs of D and exposure

The PDF that was derived based on the quasi-steady mechanism was shown to predict the measured distribution of the drag force quite well for the highest exposure of the cube. We will now check how well this correspondence holds for different exposures. In figure 5.9 the measured PDFs of D' are shown. As seen in section 5.2 the PDF for the highest exposure follows our eq. (5.3) very closely. This is probably a consequence of the fact that D' for this exposure is hardly influenced by the vertical velocity which we saw in the quadrant analyses. The PDFs for other exposures deviate to some extent, as the drag force is now also influenced by v . In the semi-logarithmic plot it can be seen that the probabilities for extreme, positive values of D' are described quite well by eq. (5.3) for all exposures. The PDF for the lowest exposure becomes

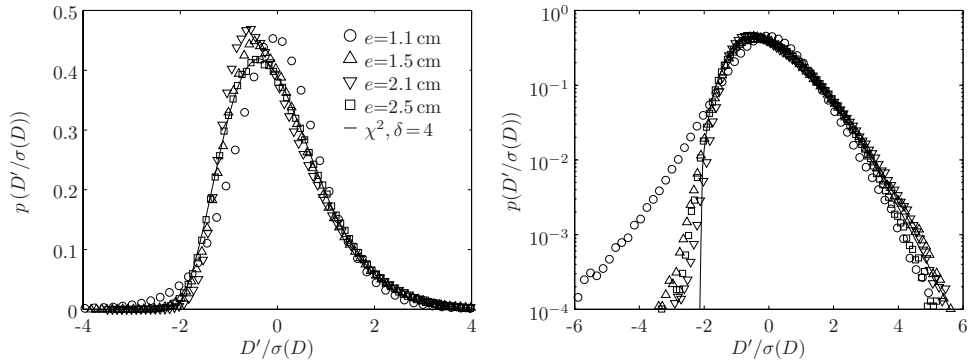


Figure 5.9: Normalised PDF of D' plotted on linear (left) and semi-logarithmic (right) scale for different exposures and uniform flow. Line shows eq. 5.3 with $\delta = 4$.

more symmetric between $\pm 2\sigma(D)$. This is ascribed to the fact that there is no direct influence from the longitudinal velocity anymore, as the stone is shielded too much. The pressures are now probably mainly created by pressure gradients that arise due to passing turbulence eddies. Still, for the positive extreme values, the PDF is again similar to PDFs for the other exposures. For the left side of the PDF eq. (5.3) does not hold.

The PDFs for L' do not correspond to the prediction based on the quasi-steady mechanism and will be treated in the next chapter.

5.3.2 Vortex shedding

Now the origins of force fluctuations by the shedding of vortices from the stone itself, as described by Kalinske (1947) are considered. The time signal of measured pressures on the cube under uniform flow (case U) in figure 5.10 is used for this. The most energetic D -fluctuations have low frequencies of the order of U/h , so these can only be ascribed to large scale flow structures that arise from the main stream (see the indication of the characteristic period T_{large} in figure 5.10). L' is seen to also contain energy at higher frequencies, occurring intermittently ($f \approx U/d$, see the indication of the characteristic period T_{small} in figure 5.10). This was most clear for the most exposed stone position. These fluctuations can be attributed to eddies that are shed from the cube. This is mentioned by Kalinske (1947) as the second origin of force fluctuations. However, Kalinske claims that eddy shedding causes the drag force to fluctuate, and here the vertical pressure (gradient) fluctuates. This is probably very dependent on the exact particle characteristics. In figure 5.10 it can clearly be seen that the low frequency D' follows the low frequency u . At times of increased

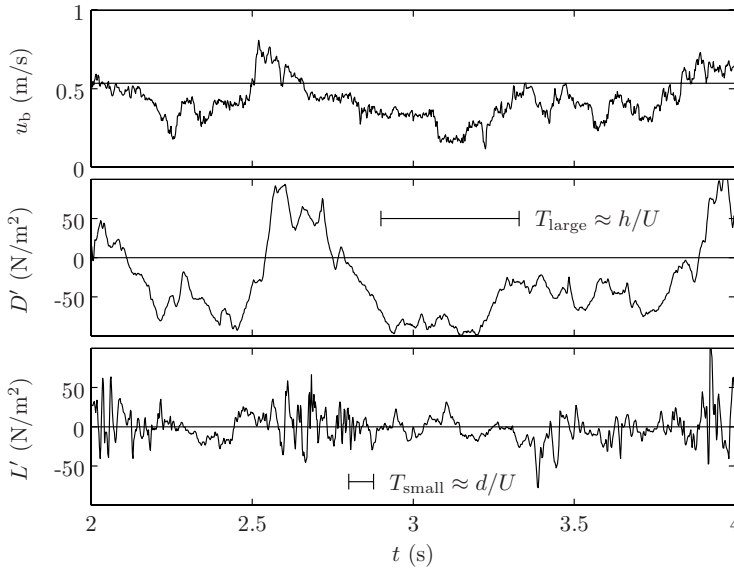


Figure 5.10: Time signal of longitudinal velocity (top), drag force indicator (middle), and lift force indicator (bottom), for $e = 2.5$ cm.

u (the time intervals 2.0–2.1 s, 2.5–2.8 s, and 3.8–4.0 s) there is a clear increase in amplitude of the high frequency L' fluctuations, with an amplitude comparable to the low frequency drag fluctuations. This implies that eddy-shedding mainly takes place during periods when the velocity is high. This behaviour can also be observed in the measurement by Aksoy (1973), although it is not remarked upon by the author himself. The fact that these high-amplitude, intermittent fluctuations only occur part of the time makes them show up less in spectra. Still, with their large magnitude they could give a stone the final push. The intermittent behaviour could also explain why Radecke & Schulz-DuBois (1988) could not determine an adequate gain function between u and F_L , as this function only predicts the transfer from one signal to another at the same frequency, and here a low-frequency fluctuation causes a high-frequency response.

The fact that high-frequency force fluctuations occur during times of low-frequency increased longitudinal velocity, has implications for the possible modelling of entrainment from bed material under non-equilibrium turbulence structure. It implies that only the large scale fluctuations have to be resolved (for instance by large-eddy simulation). The high-frequency fluctuations can subsequently be added as an extra increase in the entrainment as a function of the longitudinal velocity.

5.4 Roughness transition

In the case of the smooth-rough transition (case T) the cube was placed $2h$ downstream of the beginning of the roughness on the bed. The flow at this position can be regarded as a flow with predominantly small-scale turbulence, as the bed roughness has only affected the small-scale near-bed turbulence at the location of the measurement. Large-scale turbulence structures, covering the full depth, require a longer distance to develop (Shvidchenko & Pender, 2001). The large-scale turbulence from the smooth bed still is present, but its intensity is relatively low.

In figure 4.8 the mean velocity, Reynolds stress and standard deviation for cases U and T were presented, amongst others. Near the bed ($y \lesssim 30$ mm) the profiles of the mean velocity are similar. The same holds for the standard deviation. This corresponds to the measurements of Chen & Chiew (2003), who noted that the increased turbulence intensity needs a certain distance to develop. At higher elevations the standard deviation of both velocity components is much less for case T, as the newly developing internal boundary layer has not reached these elevations yet. For case T, \bar{u} has a lower vertical gradient at higher elevations, which reflects the lower shear stress on the smooth part upstream of the transition. The velocity distribution is shifted in such a manner that the discharge is about the same for both configurations. The bed shear stress is also equal for both cases (see table 4.1), which is in agreement with the similar $-\overline{u'v'}$ and \bar{u} profiles for cases U and T near the bed.

Pressure spectra for the two configurations are shown in figure 5.11. These plots show that the low frequency (large scale) pressure fluctuations have not yet developed at the beginning of the bed. Both the D'_T and L'_T spectral levels are lower than those for D'_U and L'_U for $f/U \lesssim 10$ (m^{-1}). Using Taylor's hypothesis, this corresponds to length scales in the order of the water depth. The total variance of the spectrum for case U is roughly 50% higher than for case T.

The PDF of D' (see figure 5.4) is slightly less asymmetrical for case T than it is for case U. This is consistent with the fact that the non-centrality parameter in eq. (5.3) ($\delta = \bar{u}/\sigma(u)$ measured near the bed) is higher for case T than for case U, due to the decrease in $\sigma(u)$. So this can be explained satisfactorily with the quasi-steady mechanism.

5.5 Summary and discussion

In this chapter it was studied whether the quasi-steady mechanism can account for the forces on bed material, using the measured pressures on the bed-mounted cube of the first experimental series. This mechanism was shown to hold very well for the drag force on a protruding particle under uniform flow. Also the influence of developing turbulence downstream a sudden increase of bed roughness was explained well by it.

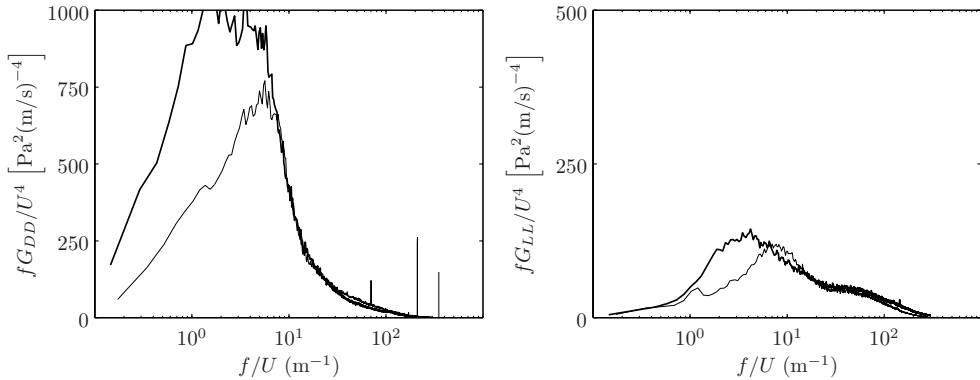


Figure 5.11: Premultiplied pressure spectra for configurations U (thick line) and T (thin line). $e=1.5$ cm. Left: D , right: L .

For shielded particles and the flow behind a backward-facing step the quasi-steady mechanism could not explain all fluctuations anymore.

An expression for the PDF of the instantaneous drag force on rough bed material has been derived. This distribution is solely based on the quasi-steady mechanism. The shape of the distribution is determined entirely by the value of the near-bed relative turbulence intensity, without any fit parameters. This model predicted the measured PDF of pressures on the most exposed cube under a uniform flow perfectly. For a large range of turbulence intensities, the PDFs of the drag forces (especially the positive extreme values) were predicted reasonably well. The differences between the theoretical quasi-steady PDF and the measured distribution around $F_D=0$ imply that these small forces are generated by a different mechanism.

As the bed shear stress is composed of the various drag forces on the bed material, and the largest drag force is exerted on the most protruding particle, the shear stress on a rough bed can be expected to be well described by the distribution proposed herein. This is treated in appendix C.

The good agreement between the PDFs implies that most of the skewness of the drag force PDFs can be attributed to the fact that $F_D \propto |u|u$ in combination with a Gaussian distribution of u , instead of to the intermittency of the turbulence, which is sometimes done (Obi *et al.*, 1996; Mosselman & Akkerman, 1998).

The magnitudes of the mean and fluctuating drag forces on the cube seem to be correlated to the exposure of the particle regardless of the micro bed-topography. The shapes of the PDFs were slightly changing for decreasing exposures, but still resembled eq. (5.3). Only for the lowest exposure the shape of the PDF was distinctly different. The magnitude of the measured fluctuating pressures on top of the cube

was correlated to the exposure as well.

Drag, caused by longitudinal velocity fluctuations, is probably the source for the largest (most important) force fluctuations for the most exposed stones. The extreme, positive excursions of u generally coincide with a negative v (Q_4 -events). The Q_4 -events cause the longitudinal velocity to penetrate deeper into the bed and therefore the exposed area of the stone (for the drag force) increases. This makes the (fluctuating) drag force a function of the vertical velocity as well, which was not expected. Conversely, the negative vertical velocity gives a negative (stabilising) contribution to the lift force. Whether the u dependence (lift increases during Q_4 -events) or the $-v$ dependence (lift decreases during Q_4 -events) of the lift force was dominant is not certain. Concluding, it can be said that both F_D and F_L are a function of the two velocity components, such that at the moment of occurrence of the extreme values of u , the drag forces gets an additional increase, and the lift forces an additional decrease due to the vertical velocity component.

The notion of Kalinske (1947) that eddy-shedding also contributes to the fluctuating forces was seen directly in the measurements. High frequency fluctuations in L' were seen to coincide with the low-frequency extreme values of the longitudinal velocity. These lift force fluctuations are attributed to vortex-shedding.

More generally, it can be stated that the instantaneous flow field causing the extreme forces on a bed particle is not simply an extension of the mean flow field. Therefore it is not realistic to model the extreme forces on a particle simply as an extension of the mechanism that creates the average forces.

The low-frequency turbulence above the cube placed just downstream from a smooth-rough transition was not completely developed. The large-scale velocity fluctuations were very weak. Therefore the extreme values of D' were much lower. From this it cannot be concluded with certainty that the bed material is more stable at the beginning of a rough bed than under developed turbulent flow. The mean shear stress might be increased the very first part of the rough bed, leading to a larger instability of the stones, see section 2.2.3. As the large-scale fluctuations need a length of twenty to thirty times the water depth to adjust to the local circumstances, the effects of roughness transitions on bed stability are not local.

Chapter 6

Turbulence Wall Pressures

6.1 Introduction

In this chapter a second force-generating mechanism is discussed – assumed to act in addition to the quasi-steady forces. This mechanism is based on the pressure gradients that are directly induced by the turbulent flow.

The quasi-steady forces are caused by pressure differences due to the streamline curvature of the flow passing a protruding stone. The presence of the stone forces this streamline curvature (hence the name ‘form drag’). In a turbulent flow, however, acceleration of water parcels and streamline curvature are always present, also without an obstructing stone present. Therefore, turbulence near a wall creates fluctuating pressures on the bed, even when it is smooth. These turbulence wall pressure fluctuations (TWP), when integrated over a stone, will result in net forces on the stone and therefore contribute to the fluctuating forces on a stone. Whether – and if so: for which conditions – the TWP can give a significant contribution to the extreme forces on the bed-particles, and consequently to their entrainment, is examined in this chapter.

First, the possible contribution of the TWP on the fluctuating forces on stones is explored theoretically. From this theory the possible behaviour of the forces can be deduced, as well as some ways in which to show their existence from measurements. It is also used to estimate the possible contribution to the variance of the fluctuating forces. After this the experimental results of the first experimental series are analysed further. The measured pressures on a cube placed under a uniform flow and downstream of a backward-facing step (BFS) of the first experimental series are used for this purpose. The origins of the pressure fluctuations are examined by inspection of their cross correlations, PDFs, and spectra.

6.2 Theoretical considerations

6.2.1 Mechanisms

To examine the relation between the near-bed velocities and the TWP-induced forces, a Reynolds decomposition eq. (2.8) is made for a fixed stone in a bed. For the horizontal force component this yields:

$$F_{D,TWP} \approx \rho V(1 + C_m) \left(\frac{\partial u'}{\partial t} + \bar{u} \frac{\partial u'}{\partial x} + v' \frac{\partial \bar{u}}{\partial y} \right) \quad (6.1)$$

The last term at the right hand side indicates an influence of the vertical velocity on the TWP-induced forces. A similar derivation for the vertical force component does not yield a similar term including the mean shear. Unfortunately the material derivative [first two terms in eq. (6.1)] could not be measured in either of the two set-ups. In the first set-up only a point measurement of velocity was made, so $\partial u/\partial x$ could not be measured. Conversely, in the second series the temporal resolution was not high enough to evaluate $\partial u/\partial t$. Still eq. (6.1) indicates that the vertical velocities are linked to the TWP-induced forces.

6.2.2 Model vortex

In order to illustrate what the direct influence of the TWP on stone stability can be, we regard a rectilinear model vortex in a uniform potential flow over a wall, as described by Doligalski *et al.* (1994). This flow field can be seen as a rough approximation of a vortex in a turbulent flow. For example the flow field due to the head of a horseshoe vortex or a 2D roller originating from a mixing layer behind a BFS. From this simple model we can infer a few characteristics of the wall pressures induced by this vortex. With this model we can make it plausible that the pressures caused by the rotational flow around a vortex have an effect on the fluctuating forces on a stone – as argued before by Müller *et al.* (1971).

A point vortex with strength (circulation) κ is placed in a uniform flow with velocity U_0 , inducing a velocity κ/r at distance r from the vortex. By adding a mirrored vortex, the wall is modelled. As the flow induced by the mirrored vortex moves the original vortex, and vice versa, the convection rate of the vortex is $U_c = U_0 - \frac{1}{2}\kappa/a$, where a is the distance of the vortex to the wall. In figure 6.1 the streamlines of the flow field are depicted. In a frame of reference moving with the vortex, the resulting flow field is stationary, and the pressure on the wall can be determined using Bernoulli's law, $p = \frac{1}{2}\rho u^2$, yielding:

$$p' = \rho \frac{\kappa^2}{a^2} \frac{X^2 - 1}{(X^2 + 1)^2} \quad , \quad (6.2)$$

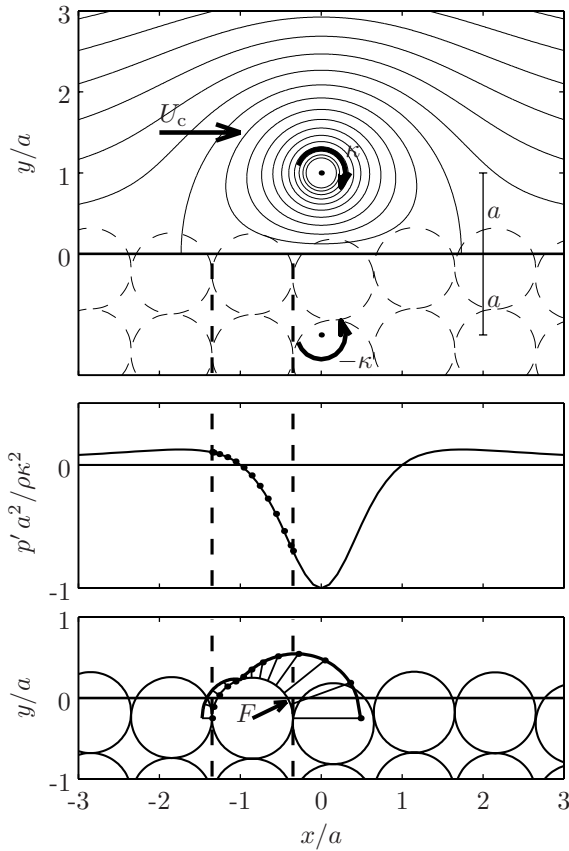


Figure 6.1

Top: streamlines of a 2D potential flow around a point vortex near a wall, in a frame of reference moving with the vortex. Middle: the resulting TWP. Bottom: the pressure field around a stone, assuming a vertically constant pressure, and the resulting net force.

where x is the distance along the wall and $X=x/a$. This pressure field is shown in figure 6.1 as well. If a porous granular bed is present, this pressure gradient will penetrate further into the bed than the longitudinal velocity, which will be blocked by the surrounding stones. This pressure gradient can create a net force on a stone placed in the bed. The pressure on the stone between the dashed lines is higher on the upstream side (left) than on the downstream side, creating an increased horizontal force component (lowest plot in figure 6.1). Note that this counteracts the quasi-steady mechanism, as at this moment u is decreased under the vortex. The added mass term also gives a positive contribution to the horizontal force component at this moment. A vortex rotating in the opposite direction (less common in wall flow) might create larger forces on a stone, as the quasi-steady drag, the added mass and the pressure gradient then all work in the same direction.

Also lift forces are predicted by this model. If we regard a vortex exactly above the

stone, then the pressure on the sides, and therefore also under the stone, is high, while the pressure on the top of the stone is low. This could result in a lift force. The most intense forces are expected to be created by large gradients, which are proportional to $\sim a^{-3}$. Therefore most intense forces are expected to be created by vortices close to the bed. However, for vortices closer than a distance $\approx d/2$ to the bed the integrated force decreases again as the pressure dip is not wide enough anymore. Following this line of thought, the expected duration of a large force created by a near-wall vortex is short, as the small vortex will have passed quickly. However, the convection velocity of the vortex decreases if its strength increases, causing a longer duration of the force. Therefore especially the extreme forces created by intense vortices (rotating clockwise) could have a longer duration.

6.2.3 Transfer functions

In the previous section an example was shown of a possible way in which a single vortex can induce TWP-forces. Now we will examine whether the TWP that are inherent to a fully turbulent flow field could, in principle, lead to significant forces on a stone. To this end we integrate a one dimensional pressure field – varying in the streamwise direction only – over simplified stone shapes, and determine magnitudes of the drag and lift force fluctuations that may result from it. First we deduce the transfer functions from the pressure field to the forces on the stone. Then we translate a TWP spectrum from literature to a force spectrum and from this we determine the standard deviation of the force fluctuations.

Drag force. A stone in a stationary, turbulent wall flow is considered. The mean forces are not taken into account. The effect of a convecting, ‘frozen’ sinusoidal pressure field is determined. The pressure field is given by:

$$p' = \hat{p} \sin(kx - U_c kt) \quad , \quad (6.3)$$

where \hat{p} is the amplitude of the pressure field, k is the wave number, and U_c is the convection velocity.

First we treat a spherical stone, with its centre at $x = 0$. If we assume that the pressure is not changed by the stone, the TWP-induced drag force becomes:

$$F'_{D,TWP} = \int_{-R}^R p' \frac{dA}{dx} dx \quad , \quad (6.4)$$

where

$$A = \pi(R^2 - x^2) \quad \text{for } |x| \leq R \quad ,$$

$R = d/2$, and A is the cross-sectional area of the stone.

After substitution and solving the integral in eq. (6.4), the force becomes:

$$F'_{\text{D,TWP}} = -K_{\text{D}}\hat{p} \cos(U_c k t) \quad , \quad (6.5)$$

where

$$K_{\text{D}} = 4\pi R^2 \left(\frac{\sin \tilde{k}}{\tilde{k}^2} - \frac{\cos \tilde{k}}{\tilde{k}} \right) \quad ,$$

and \tilde{k} is kR . $|K_{\text{D}}|$ is the gain function between \hat{p} and \hat{F} . The drag force on a cylinder has the same temporal behaviour as that on a sphere, given in eq. (6.5) – only with a different K_{D} , which cannot be evaluated analytically. The (squared) gain functions are shown in figure 6.2.

Lift force. A similar derivation can be made for the TWP-induced lift force. In order to enable analytical integration we first consider a 2D case (cylinder) for the lift force. The pressure field acts on the stone, eq. (6.3). Modelling the pressure field under the stone is not trivial. Two simplified models are tried. We start by assuming that the pressure on the lower half of the rod is constant in time and space. The fluctuating lift force on a rod with radius R and width R is then given by:

$$F'_{\text{L,TWP},1} = -R \int_{-R}^R p' dx = K_{\text{L},1} \hat{p} \sin(U_c k t) \quad , \quad (6.6)$$

where

$$K_{\text{L},1} = 2R^2 \frac{\sin \tilde{k}}{\tilde{k}} \quad .$$

This can be compared to the case where the pores are small or filled with finer material. If the pressure is assumed to be linearly changing with x under the lower half of the cylinder, as in an open granular structure, then the lift force becomes:

$$F'_{\text{L,TWP},2} = -R \int_{-R}^R p' dx + R^2 (p'(-R) + p'(R)) = K_{\text{L},2} \hat{p} \sin(U_c k t) \quad , \quad (6.7)$$

with

$$K_{\text{L},2} = 2R^2 \left(\frac{\sin \tilde{k}}{\tilde{k}} - \cos \tilde{k} \right) \quad .$$

In contrast to the drag force, K_{L} cannot be evaluated analytically in the case of a spherical stone.

Figure 6.2 depicts the various gain functions. The gain function for the drag on a cylinder is obtained via numerical integration. The figure shows that especially the pressure fluctuations with wavelengths of the same order of magnitude as the diameter of the stone ($\lambda = 2\pi/k \approx 1.5 d$) contribute to the forces on the stones and will hence

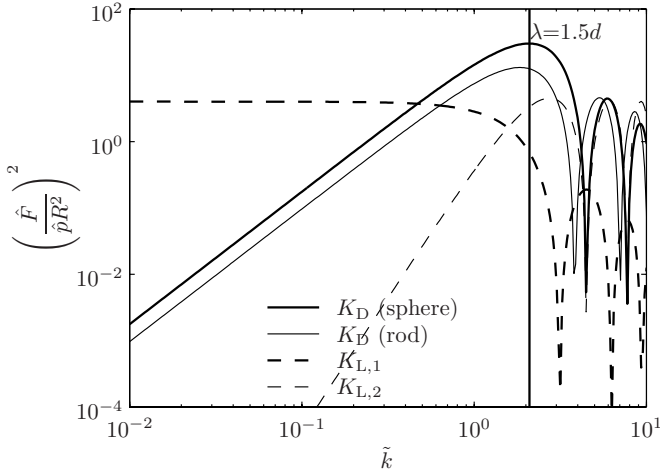


Figure 6.2: Dimensionless, squared gain functions for drag and lift force.

be important for the determination of the stability of the stones (see vertical line in figs. 6.3 and 6.2). This agrees with the notion of Booij (1998).

A distinct difference is present between K_L evaluated with and without the pressure penetrating in the pores under the stone – eqs. (6.7) and (6.6) respectively. At low wavenumbers $K_{L,1}$ remains constant, while $K_{L,2}$ goes to zero for decreasing wavenumbers.

It is clear that for very low wave numbers the function will have to tend to zero, as the pressure will penetrate under the stone, but whether the slope at low frequencies is as steep as for $|K_{L,2}|^2$ is not sure. The gain functions for the drag force on the sphere and the rod both rise $\sim k^2$ in the low frequency range, which is the relation between pressure spectra and pressure gradient spectra (George *et al.*, 1984, for example). The fall-off at high frequencies differs between the two.

6.2.4 Estimation of magnitude of TWP-forces

Subsequently an estimate of the variance of the forces caused by TWP can be obtained by using a TWP spectrum as a starting point and multiplying it by $|K_D|^2$. As an example an ‘open-channel flow’ is chosen with parameters: $\langle \bar{u} \rangle_h = 2$ m/s, $h = 4$ m, $\rho_s = 2650$ kg/m³, $y_0 = d/15$. We assume incipient bed material motion, using $\Psi = 0.04$, which yields $d = 2$ cm.

Figure 6.3 shows the rough wall TWP spectrum and the estimated force spectra. The TWP spectrum is obtained from windtunnel measurements of Blake (1970).

Although an open-channel flow has different turbulence characteristics than an equilibrium boundary layer flow, the TWP characteristics for the mid- and high-frequency ranges – which scale with d and u_* – are expected to be similar, as they are generated by near-bed flow processes. For the low frequencies however, the spectra are expected to differ, as the free surface influences the pressures. Therefore we only use the high frequency TWP part of the spectrum. This is scaled to prototype size to represent the flow parameters for the present case, and the spectrum is extrapolated to the lower frequencies by a f^{-1} trend (dotted line). This spectral slope is predicted for the mid frequency range (Farabee & Casarella, 1991). The spectrum is cut off at a frequency of $f = \langle \bar{u} \rangle_h / h$. For the transformation of the spectrum from ω to k , the relation $k = \omega / 0.5 \langle \bar{u} \rangle_h$ is used.

The variance of the TWP-induced drag and lift forces is subsequently obtained by integrating the estimated force spectra. This yields a first estimate of the force magnitudes of the TWP. In stability models three to five times the standard deviation is often given as the maximum occurring force fluctuation. Extreme wall pressures of four times the standard deviation have been reported (Schewe, 1983). As the flow is critical ($\Psi = 0.04$), the maximum occurring forces are of the order of the submerged gravitational force on the stone. Therefore we normalise the ‘maximum’ TWP-force with the submerged weight of the stones. Hence in table 6.1 the values for $4\sigma(F)/F_G$ are presented.

In the present example four times the estimated standard deviation of the drag force on a sphere is equal to over 70% of the (submerged) gravitational force. This means that the extreme values of the fluctuating forces calculated by the model are of the same order of magnitude as the total maximum force on the stone. Further, the difference between the drag fluctuations on the sphere and the cylinder indicates that the shape of a stone can have a large influence on the effectiveness of the TWP force. For flat stones (small vertical dimension) the ratio lift force / stone weight is expected to increase. Moreover, the pattern of wall pressure penetration under the stone is seen to be very important for the magnitude of the lift forces. The TWP-induced lift force is 4 times larger if the pressures do not penetrate under the stone.

	$\sigma(F)$ (N)	$4\sigma(F)/F_G$ (%)
F_D sphere	0.0115	71
F_D cylinder	0.0081	33
F_L cylinder, filled	0.0104	43
F_L cylinder, pores	0.0025	10

Table 6.1: Estimated standard deviations of TWP-induced forces.

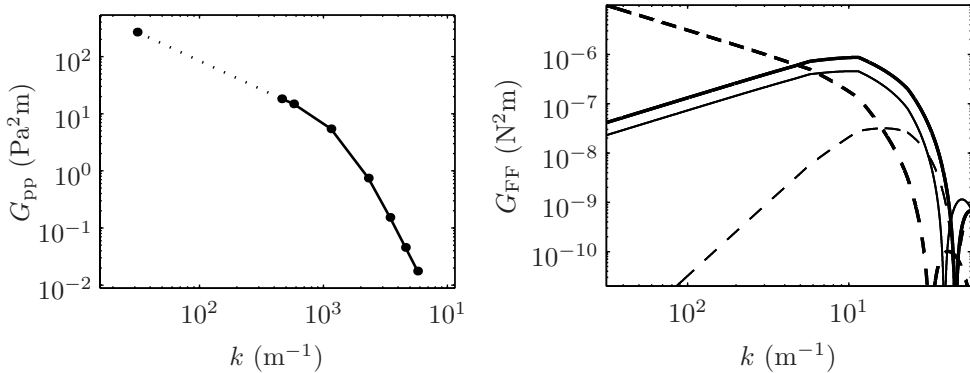


Figure 6.3: Spectrum of pressures on rough bed (left) and the estimated spectra of the drag and lift forces. For the legend see figure 6.2.

The model is highly idealised. The main idealisation is that the effect of the stone on the pressure field is not taken into account. Experiments must show to which extent this is a valid assumption. Even so, the model indicates that the TWP could give a significant contribution to the forces on coarse stones, in addition to the (quasi-) steady forces.

6.2.5 Behaviour of TWP forces in time

Now we regard the behaviour in time of the resultant force if a frozen pressure field is advected over a stone. This behaviour will be shown to decrease the stability of the stones. It can also be used to predict the shape of the normalised cross-covariance function between F_D and F_L , which can be compared to measurements.

The factors K_D , $K_{L,1}$ and $K_{L,2}$ are all positive for $0 < \tilde{k} < \pi$, which means that for wavelengths larger than the stone diameter the force vector will rotate clockwise¹ in time, along an ellipsoidal path, with semi-axes equal to $\hat{p}K_D$ and $\hat{p}K_L$. This time variation of the TWP-force is illustrated in figure 6.4. This behaviour is increasing the efficiency in which this force can dislodge a stone. First of all, the force vector covers all directions, including the direction where it generates the largest moment around the rotation point of the stone, i.e. when the force acts perpendicular to the line between the centre of gravity of the stone and the contact point. Secondly, if the stone rolls away, the angle of repose (ϕ , see figure 2.4) becomes smaller, which rotates the optimal angle for creating the largest moment around the point of contact in the same direction as the fluctuating force is rotating. This increases the duration of a large moment around the pivoting point when the stone starts moving.

¹When the flow is from left to right.

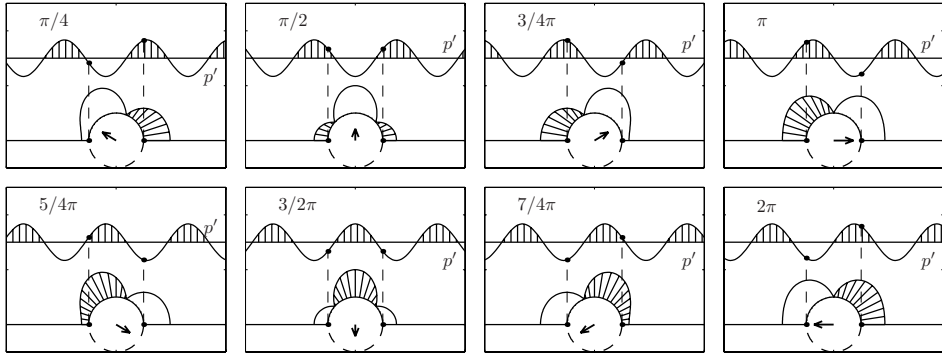


Figure 6.4: Change of the integrated force on a stone (2D, semi-circular cylinder) due to a convected frozen pressure field for $\lambda/d=1.5$. The vectors represent the resulting net force acting on the stone.

In order to see whether the temporal behaviour of the force vector is observed in our measurements we will compare the theoretical shape of the normalised cross covariance function between drag and lift, $\rho_{DL,TWP} = -\sin \omega \tau$ (τ is the time lag), to the measured function, ρ_{DL} . The turbulence field is obviously not a sine as used for the derivation of the force-functions. Therefore we multiply $\rho_{DL,TWP}$ by the loss of correlation of the wall pressures. When the autocorrelation function of wall pressures, γ , is assumed to be exponential, it yields: $\gamma^{|x|k/2\pi}$. If we further substitute $U_c \tau$ for x we obtain:

$$\rho_{DL,TWP}(\tau) = -\sin(U_c k \tau) \gamma^{U_c k |\tau|/2\pi} \quad (6.8)$$

It can be seen that the values of K_D and K_L do not appear in this formulation, which makes it easier to compare this shape to measurements.

6.3 Analysis of measurements

A number of analyses of the measurements will be presented, from which the significance of the TWP-induced pressures for the forces on bed material will be inferred.

6.3.1 Cross-correlation drag and lift

The first thing we will check is whether the expected shape of the normalised cross-covariance function between drag and lift force – the damped sine given by eq. (6.8) – is recognisable in the measurements. The measured correlation functions (ρ_{DL}) are shown in figure 6.5 for the various cases. The correlation functions are plotted as a

function of $\tau \langle \bar{u} \rangle_h$ as in eq. (6.8) it is a function of τU_c , and the convection velocity of the dominant eddies is assumed to be proportional to the mean flow velocity. It can be seen that ρ_{DL} for all cases resembles the typical shape with a local maximum for negative time lags and a minimum for positive time lags. This is a signature of a ‘frozen’ pressure field being convected over the stone. The correlation at $\tau=0$ is not zero for all cases, which is not in agreement with eq. (6.8).

For the highest exposure ρ_{DL} is positive at $\tau=0$. This means that on average drag and lift have the same sign at the same moment. This is probably due to the quasi-steady mechanism, where the streamwise velocity creates drag forces (stagnation pressure) and lift forces (streamline contraction) simultaneously.

For the other exposures – except the lowest – ρ_{DL} is negative at $\tau=0$. This means that both force components have the opposite sign at the same moment. This can be explained by the mechanism whereby during Q_4 -events ($u>0, v<0$) the stagnation pressure – which now partly acts on the top of the cube – creates a negative lift force on the stone [see eq. (2.13)], and the opposite occurs during Q_2 -events ($u<0, v>0$), see eq. (2.13).

For the case with the lowest exposure ρ_{DL} is zero at $\tau=0$. Also eq. (6.8) could be fitted through the measured curve with realistic values for the parameters. The wavelength ($k/2\pi$) was 0.12 m. This is 4 times the stone diameter, and somewhat smaller than the waterdepth of 0.16 m. The convection velocity is 0.2 m/s, which is about a quarter of the mean velocity. Further, the fitted value of γ_λ was 0.005. This means that the correlation is 0.5 after the characteristic eddy has travelled 0.13 wavelength. This value seems rather small. The fit is added in figure 6.5. The resemblance indicates that the pressures on the cube with the lowest exposure can be attributed to the TWP.

The normalised covariance functions for cases S1 and S2 are also plotted in figure 6.5. The wavelength of the damped sine is longer, indicating a larger size or lower convection velocity of the dominant eddies. The damped sine of $\rho_{DL,TWP}$ has a negative offset however, giving a negative ρ_{DL} at $\tau=0$. The sign of this offset corresponds to the uniform flow case with the same bed and a low exposure, and differs from the case with the highest exposure, where ρ_{DL} is positive at $\tau=0$.

Concluding, it can be said that only the measured ρ_{DL} for the lowest exposure follows the theoretical curve well and that the resemblance deteriorates with increased exposure. This confirms that the TWP become more important for decreasing exposure. An increased turbulence intensity is of influence as well. It appears that the characteristic eddies causing the TWP behind a backward-facing step are larger and/or slower than in a uniform flow.

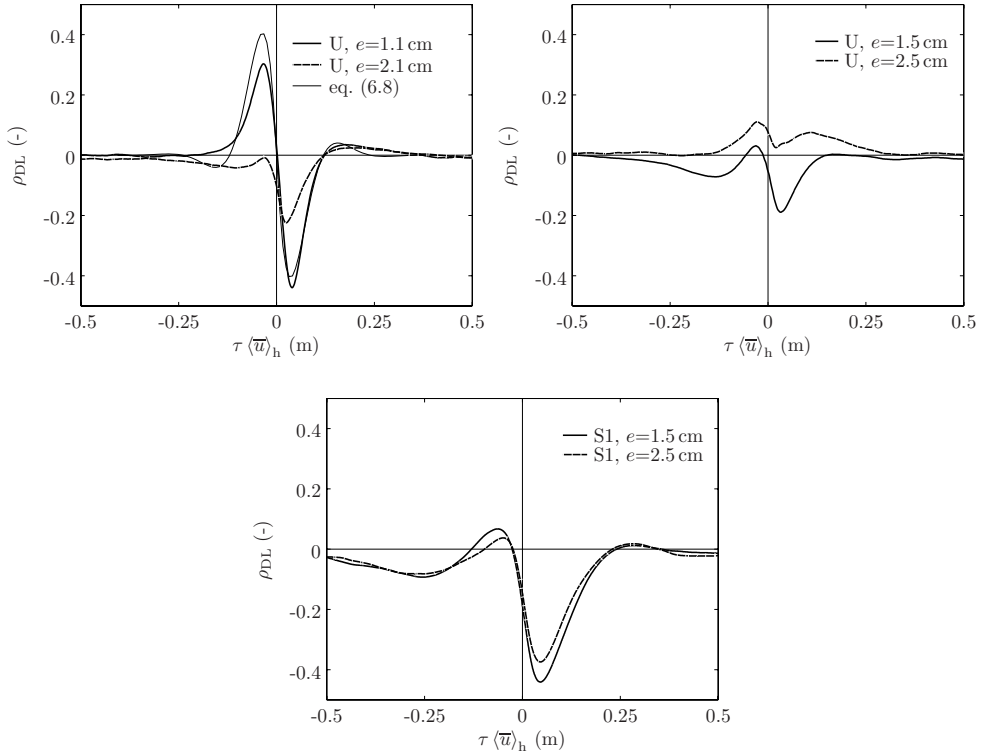


Figure 6.5: Measured correlations ρ_{DL} for configurations U and S1.

6.3.2 Probability density of lift force

In the previous chapter (section 5.2) only the PDFs for the drag forces were examined, as they resembled the distribution based on the quasi-steady mechanisms well. For the stone with the highest exposure under uniform flow the agreement with eq. (5.3) was excellent, strongly supporting the fact that the quasi-steady mechanism is the cause of most force-fluctuations for this case. However, for decreasing exposure (figure 5.9) and increasing turbulence intensity (figure 5.5) the similarity between quasi-steady theory and experiment broke down, especially around the mean value of the force. This could indicate an increased importance of the TWPs. The extreme values, however, still coincided with the theoretical quasi-steady PDF for most cases – except the lowest exposure that was measured ($e=1.1$ cm). Here the correspondence between measurements and eq. (5.3) breaks down completely. This PDF is quite symmetrical, so it could well be caused by TWP, as a convecting pressure field is expected to give

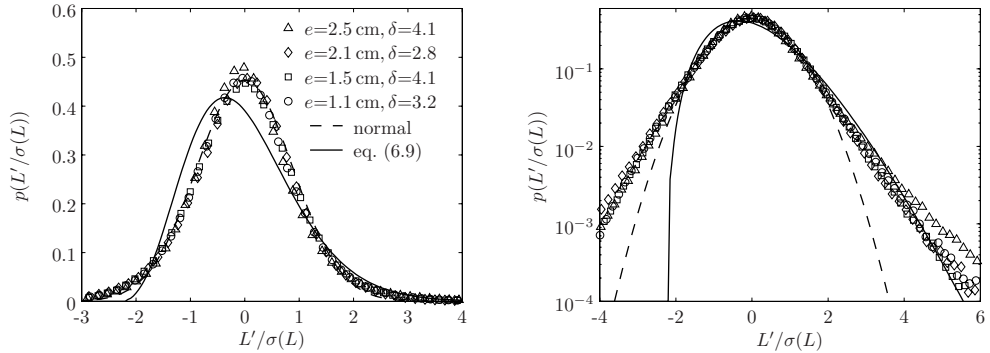


Figure 6.6: Measured PDFs of L' for case U and various exposures on a linear (left) a semi-logarithmic (right) scale.

similar pressure statistics at both sides of the stone and hence a symmetrical PDF.

According to the quasi-steady mechanism the lift force, F_L is proportional to u^2 , so the PDF of this force component would be equal to the χ^2 -distribution. This distribution can be derived from eq. (5.3) by mirroring the left side to the positive side, yielding:

$$p(L) = \frac{1}{\sqrt{8\pi\alpha L}} \left(e^{-\frac{1}{2}(\sqrt{L/\alpha}-\delta)^2} + e^{-\frac{1}{2}(\sqrt{L/\alpha}+\delta)^2} \right), \quad (6.9)$$

which is the same as eq. (5.1).

The PDFs of the measured lift force for case U (L'), presented in figure 6.6, clearly do not follow eq. (6.9). They are almost distributed normally for most exposures. Only values outside $\pm 2\sigma(L)$ deviate. So the flatness of the distribution is higher than for a normal distribution. A normal distribution of the lift force was observed by Einstein & El-Samni (1949) between $\pm 2\sigma(L)$, but their apparatus was not able to measure beyond that. Also Xingkui & Fontijn (1993) measured a normal distribution of the lift force between $\pm 2\sigma(L)$, and they found a positive deviation beyond that. All this corresponds to the present measurements, as the shape of a normal distribution can be fitted through the measured PDF of L' in the middle section (due to the deviation outside $\pm 2\sigma(L)$ the area under this curve is not equal to one). The correspondence between the PDFs of our lift force indicator and those of integrated lift forces, indicates that the top pressures are representative for the integrated lift forces. The particle used by Einstein & El-Samni was a hemisphere within a densely packed bed of hemispheres. Such a hemisphere has an exposure, according to the present definition, equal to $(\frac{1}{2} - \frac{1}{18}\pi\sqrt{3})d \approx 0.20d$, which would be 0.6 cm for $d=3$ cm. This is lower than the lowest exposure used in the present measurements. The exposure of the angular stone used by Xinkui & Fontijn was also very low. The lift

forces for the BFS flow had the same PDFs as those for the uniform flow.

The fact that the known measured PDFs of lift clearly do not follow eq. (6.9) indicates that another mechanism is involved in the fluctuating lift forces on bed material. In the present measurements the lift PDF only slightly deviates from a Gaussian distribution. It only has an increased flatness and skewness for the highest exposure. This could mean that quasi-steady lift forces begin to act on the stone for higher protrusions, as the quasi-steady forces yield a skewed distribution according to eq. (6.9).

6.3.3 Pressure spectra

Now the present measurements of pressures on a rough bed behind a BFS (cases S1 and S2) will be compared to measured TWP on a smooth bed in a wind tunnel (Lee & Sung, 2002) in order to evaluate the presence of TWP-induced forces on rough-bed material.

The top of the cube with $e=1.5$ cm in the present rough-bed measurements is approximately located at the level of the bed, therefore the pressure sensor on top of the cube for $e=1.5$ cm is placed at about the same vertical position as the pressure sensor used in the smooth wall windtunnel experiments where the pressure sensor was placed flush in the bed. A comparison between the two is possible when x (zero at the step), p , and f are made dimensionless by h_s , ρu_0^2 and $u_0 h_s^{-1}$ respectively, where h_s is the step height and u_0 is the depth and time averaged velocity on the step.

The fact that the wall in the windtunnel experiments was smooth, and that the wall in the present experiments is very rough, gives us the possibility to distinguish between the origins of the forces on the cube. If the forces are generated by the pressure gradients generated by the turbulence of the outer flow (TWP-induced forces) then the pressure spectra will be similar, and if the interaction between the protruding bed material and the flow is important (quasi-steady forces or maybe an influence of the added mass) then the spectra are expected to differ. Furthermore, a $f^{-7/3}$ slope in the TWP spectrum is attributed to the turbulence-turbulence term in homogeneous turbulence in a free shear flow (George *et al.*, 1984), and will also be an indication that TWP create the forces on the bed material.

The normalised smooth wall windtunnel spectra overlap the present rough wall spectra for the high frequency range in most cases (figures 6.7 and 6.8). Especially the overlap in figure 6.7 is remarkable. This implies that the source for the high-frequency fluctuating pressures is indeed the turbulence generated by the outer flow, as the flow near the bed (smooth wall vs. very rough wall) is completely different. Moreover, the pressure sources must be situated in the mixing layer, as the flow above the mixing layer is completely different as well (developing boundary layer vs. free surface flow). The added mass term is not important, as this is the result of the alteration of the

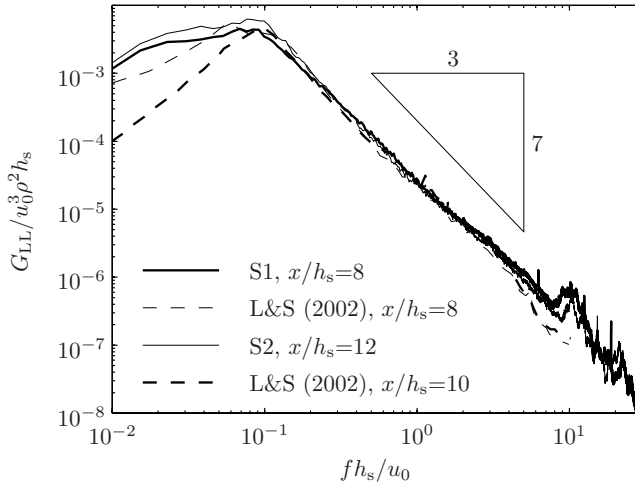


Figure 6.7: Comparison of spectra of pressures on a cube (L) behind a BFS with $e=1.5$ cm to TWP spectra from a smooth wall windtunnel experiment (Lee & Sung, 2002).

flow by the bed material, like the quasi-steady drag force. The $f^{-7/3}$ slope also seems to be present in the rough-bed data for the lowest exposure (figure 6.7).

The low-frequency part of the spectra that were measured do have different characteristics. This is probably due to the fact that the windtunnel experiments have an irrotational outer flow above the boundary layer, and the present open-channel measurements have a water-air interface. In the present measurements waves could also produce part of the low-frequency fluctuations. The irregular shape of the spectrum around $fh_s/u_0 \approx 10$ is ascribed to environmental vibrations of the flume.

Now it will be inspected which parameters influence the possible resemblance between the smooth-bed and rough-bed spectra. Hereto the lift spectra are compared to the smooth-bed (windtunnel) spectra (right plots in figure 6.8). The resemblance is very reasonable and the exposure does not seem to influence the lift spectra significantly. The spectral densities for case S2 ($x/h_s=8$) are consistently higher than for case S1 ($x/h_s=12$).

The spectra of the drag forces are depicted in the left plots in figure 6.8. The high-frequency spikes in the spectra are caused by electronic noise. For case S2, even the drag force can be seen to have a similar spectrum as the lift force, indicating that the TWP indeed penetrate the granular bed and cause a net drag force. This is especially true for case S2, where the cube is situated near the reattachment point. Here the quasi-steady force fluctuations, which will increase the spectral levels, and are dependent on the average longitudinal flow velocity [see eq. 2.11], are small. There-

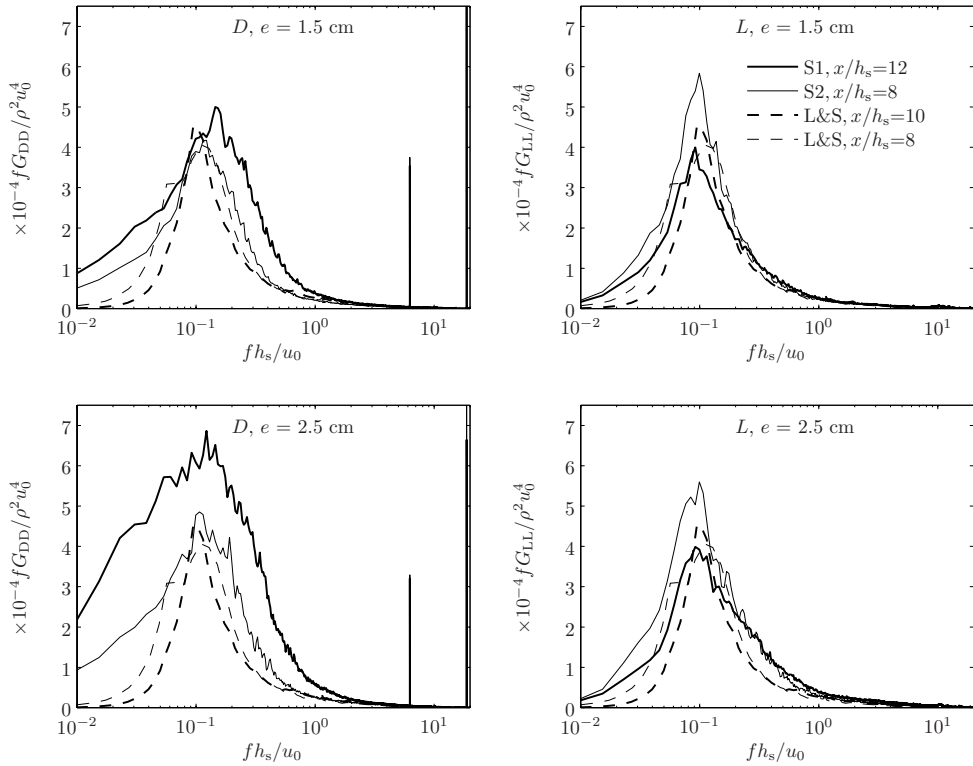


Figure 6.8: Comparison of spectra of the pressures on a rough-wall element (D and L) to TWP on a smooth wall (Lee & Sung, 2002), both behind a BFS, for $e=1.5$ cm and 2.5 cm.

fore the TWP become more dominant at this location. For the higher exposure, the spectral levels of the drag force fluctuations become clearly higher than those of the smooth wall pressures, especially for case S1. This is consistent with the fact that the stone is subject to higher flow velocities, increasing the relative contribution of the quasi-steady mechanism to the total variance. Yet, if it is assumed that the contribution of the TWP to the total variance remains equal to the value in the windtunnel experiments, the contribution of the TWP to the total variance is still significant.

6.4 Summary and discussion

In chapter 5 it was concluded that the quasi-steady drag force fluctuations are dominant for stones with a high exposure. However, for low protrusions and high tur-

bulence intensities deviations between quasi-steady theory and measurements were noticeable, possibly caused by the TWP. This was investigated further in this chapter.

First this is investigated analytically, and a crude estimate of the magnitude of the force fluctuations resulting from TWP indicates that they might well give a significant contribution to the force fluctuations on coarse granular bed elements.

Analysing the present experimental results, we find evidence that TWP play a role. First of all, the cross-covariance of drag and lift has the shape predicted on the basis of convecting TWP, especially for the lowest exposure. Further, the spectra of the pressures on top of the cube (lift) downstream of a BFS coincide with smooth wall pressure data, which clearly illustrates that the quasi-steady mechanism is not applicable here. The spectra of the drag force coincide with the smooth wall pressure data as well, especially for the low exposure and high relative turbulence levels. The maximum drag forces still seem to be created by the quasi-steady mechanism at higher turbulence levels, as seen from the PDFs.

From the findings above we can conclude that TWP are of importance for the entrainment of granular material, especially for stones that are shielded by other stones. In a granular bed that has been water-worked this would be the smaller stones, as they generally have small exposures (Egiazaroff, 1965). Additionally, for higher exposures the relative influence of the TWP seems larger on the lift force than on the drag force.

A passing vortex will induce a resultant force on the stone via the TWP-mechanism that rotates in time, increasing the effectiveness in dislodging a stone from a bed. Especially TWP with wavelengths of roughly $1.5d$ are expected to have a large influence on the fluctuating forces. If these are caused by vortices, then the vortices will be situated at about $1d$ from the stone.

The symmetrical PDF with an increased flatness of the lift force as measured by Xingkui & Fontijn (1993) and Einstein & El-Samni (1949) was confirmed by the present measurements for stones with a small exposure. For the largest exposure measured a deviation was present. An increasing deviation is expected for even larger exposures, for which the Bernoulli pressure will become more important.

Chapter 7

Flow Structures and Stone Movement

7.1 Introduction

In this chapter the results of the second experimental series are presented and analysed. Mainly the PIV results are discussed. The actual movement of a stone was used as a trigger to identify the velocity fields leading to stone entrainment, allowing conditional sampling and averaging. This is a step further than the examination of the pressures in the previous two chapters, as stone displacement not only depends on the magnitude of the pressures, but also on their location and duration. The flow structures that are present during the entrainment of the stone are visualised. They are determined from the measurements by conditionally averaging the flow fields recorded during stone movement. These structures are linked to the force-generating mechanisms that were presented in chapters 5 and 6.

The flow structures that are present during stone movement are determined both for uniform flow and backward-facing step (BFS) flow. They are compared to each other, and to structures reported in literature. It is determined whether certain flow structures can be detected in the measurements repeatedly; whether they are rarely occurring or are a common feature with an unusually high magnitude; or whether it is a rare combination of several kinds of flow structures.

7.2 Data processing

7.2.1 Inspection of vector plots

It is difficult to distinguish the structural features of an instantaneous turbulent flow field when large velocity gradients are present or when the flow structures have a wide range of scales. Both these complicating factors are present in the flows being examined. To overcome these problems the flow field is often decomposed in various spatial or temporal scales. Adrian *et al.* (2000a) give an overview of several possibilities for decomposing velocity fields. A limited number of techniques were used. These are discussed briefly next.

It is convenient to inspect the instantaneous flow fields first using a Reynolds decomposition, because only one image results from this decomposition. In this decomposition the local time-averaged flow field is subtracted from the instantaneous flow field. In 2D this yields: $u'(x, y, t) = u(x, y, t) - \overline{u(x, y, t)}$, where the overbar indicates time averaging. Inspection of a flow field using this decomposition can give direct information on the presence of an increased quasi-steady force, as this coincides with an increased streamwise velocity, or positive u' .

For closer inspection we use the Galilean transform. Here a single velocity is subtracted from the whole field. Usually this velocity is determined as a fraction of the spatially averaged bulk velocity, so: $u'(x, y, t)_{\text{GT}} = u(x, y, t) - \alpha U$. This decomposition does not alter the gradients (i.e. pressure sources) in the flow field, contrary to the Reynolds decomposition. In this chapter it is denoted for example as ' $\vec{u} - 0.6\vec{U}$ ', if 60% of the bulk mean velocity ($\vec{U} = (U, 0)$) is subtracted.

For evaluating the presence of vortices we use plots of the swirling strength, λ_{ci} . The swirling strength is a measure of the intensity of the local rotation in a flow field. It is capable of pinpointing separate vortices accurately – also in shear flows. The swirling strength is the imaginary part of the complex eigenvalues of the shear tensor. This quantity has a zero value if the shear is dominant over the rotation. We use a definition where it is positive with a vortex present:

$$\lambda_{\text{ci}}^2 = \max \left[0, -4 \frac{\partial u}{\partial y} \frac{\partial v}{\partial x} + 2 \frac{\partial u}{\partial x} \frac{\partial v}{\partial y} - \frac{\partial u^2}{\partial x} - \frac{\partial v^2}{\partial y} \right]. \quad (7.1)$$

A number of other quantities exist that reveal the presence of a rotational motion (Jeong & Hussain, 1995). Most of these are equivalent for incompressible 2D flows. λ_{ci}^2 is proportional to the source term in the Poisson equation for fluctuating pressures. This indicates the connection between the presence of a vortex and the presence of pressure gradients. As the present interest is the force-generating potential, the squared values of λ_{ci} are depicted.

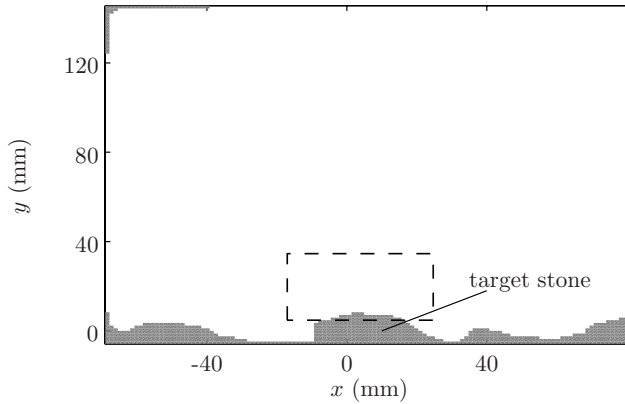


Figure 7.1: Area used for determining force indicators.

7.2.2 Indicators for force mechanisms

It could be that several types of flow structure are responsible for the entrainment of stones and that they vary in size. Therefore knowledge from previous chapters will be used to distinguish between different flow structures that cause movement of the stone. We will check whether it is possible to divide the flow fields for all events into two classes, corresponding to the two previously identified force generating mechanisms, quasi-steady force fluctuations (QSF, chapter 5) and turbulence wall pressure fluctuations (TWP, chapter 6). These two mechanisms are related to different velocity components and length scales. Therefore they should be recognisable in the flow field and could help to distinguish between different flow structures that cause entrainment.

The QSF depend on the near-bed streamwise velocity. To quantify the relative influence of this force generating mechanism from a PIV measurement, we will average the u -velocity field of the individual recordings in an area A near the stone. This yields the time varying $\langle u \rangle_A$, and we will assume that the following quantity:

$$F_A = |\langle u \rangle_A| \langle u \rangle_A \quad , \quad (7.2)$$

should be proportional to the quasi-steady forces on the particle. The extent of the area (42.9 mm wide and 31.0 mm high) is depicted in figure 7.1. This area roughly has the size of the stone. The horizontal dimension is larger in order to capture the flow structures, that move horizontally.

The TWP can also lead to significant forces on bed material. The origin of TWP can be small-scale vortices. As TWP with a length scale of the order of the stone

diameter d are most effective in generating forces on a stone, a vortex centre at $0.5-2d$ above the target stone will probably induce the largest (lift) forces. It was also seen that a fluctuating vertical velocity of any sort is a source of fluctuating forces [see eq. (6.1)]. To identify the presence of this force-generating mechanism we will therefore consider the instantaneous spatial variance of v in the same area A near the target stone,

$$\sigma(v)_A^2 = \frac{1}{n_i} \sum_{i=1..n_i} (v_i - \langle v \rangle_A)^2 \quad , \quad (7.3)$$

where v_i represents the vertical velocities at positions i in area A. This value becomes large when a vortex is present, and is not very sensitive to the exact position of the vortex. Not only vortices, but small-scale wall-normal fluctuations of any kind are indicated by this quantity.

7.2.3 Splicing

The field of view of the PIV recordings was limited to one water depth ($1h$) in stream-wise direction, while the large-scale flow structures can – at least in uniform flow – have dimensions of many water depths. In order to observe the large-scale flow structures a hybrid technique was used to merge a sequential series of PIV recordings. This technique will be called splicing here, after the technique used for joining pieces of rope by interweaving strands. First it has to be determined how far the flow structure moves from one recording to the next. To this end the correlation of the upstream part of the outer u' field of the first image, $u'_{1,overlap+}$ to an equally sized downstream part of the outer u' field of the second image $u'_{2,overlap-}$ is determined as a function of the overlap length, $L_{overlap}$:

$$\rho(L_{overlap})_{12} = \frac{\langle u'_{1,overlap+} u'_{2,overlap-} \rangle_{overlap}}{\sqrt{\langle u'_{1,overlap+} \rangle_{overlap}} \sqrt{\langle u'_{2,overlap-} \rangle_{overlap}}} \quad (7.4)$$

The overlap at which this function is maximal is taken as the distance that the total flow structure has been advected. Subsequently a new flow field is created by averaging the velocities of the overlapping part of the two images, and adding the other parts on both sides.

Using the spliced image of the first two images and the third image, the process can be repeated, and so on for all recordings during the measurement of a single event. It is depicted for the first two steps in figure 7.2. An example of 20 original images and the spliced result is given in figure 7.3.

The process is similar to transforming a point measurement into a spatial measurement based on Taylor's hypothesis of frozen turbulence. Differences are that: the vertical structure is measured instantaneously, each velocity value is averaged over

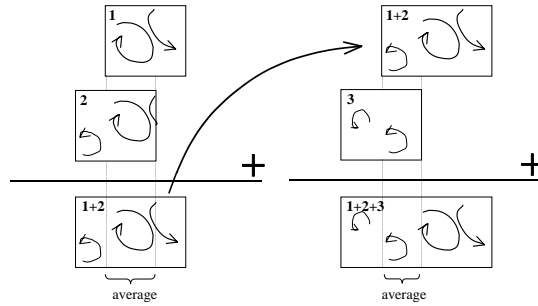


Figure 7.2: Principle of splicing technique applied to three sequentially measured flow fields.

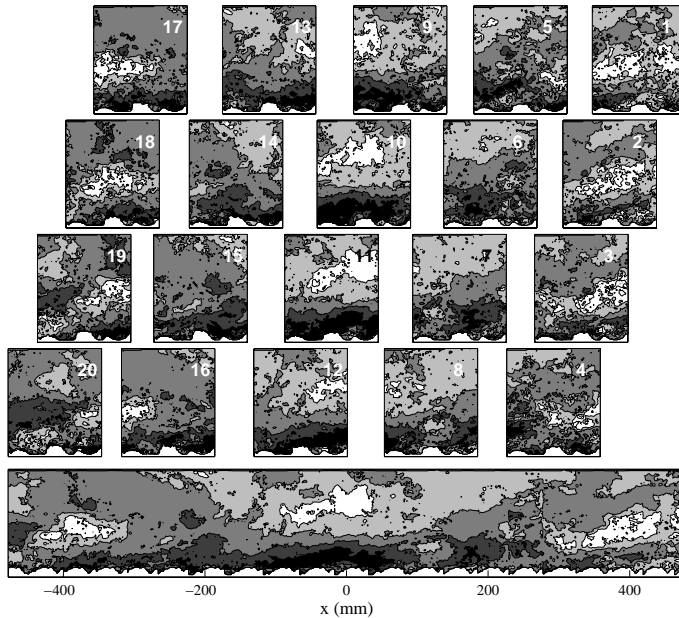


Figure 7.3: Twenty separate recordings of $u(x, y)$ during stone movement event #1 of U007, together with the spliced image obtained from them (bottom). The horizontal positions of neighbouring images correspond to the overlap with the highest correlation.

a few measurements (here the average is based on roughly three vector fields as the structure moves about a third of the whole field per recording), and the convection velocity of the flow structure is determined for every image separately.

The aim of the technique is to determine the large-scale flow structure. Therefore an area that spans the whole recorded field above the target stone is used to determine the correlation. Using this large area, the convection velocity is mainly determined by the large velocities high up in the flow. As the convection velocity increases with y , a large overlap length (or convection velocity) is obtained.

A spliced flow field can be interpreted to represent the shape of an advected flow structure, or the temporal development of the flow field at a fixed (horizontal) position. The plots that are presented later in this chapter are given in spatial coordinates. As the flow structures move downstream, a second recording will be placed left of the first, see figure 7.3. Hence, if the plots are interpreted as the time evolution of the flow field at a fixed position, the time increases from right to left. In the plots that present the flow field during a stone movement, the stone movement starts at $x = 0$. The stone movement has a certain duration which generally lasts 4 or 5 frames at 15 Hz, in the case of the uniform flow. In the spliced plots this is equivalent to 250 mm to 400 mm left of $x = 0$. After that (in the plots: left of that) the stone has reached the obstructing bar, and the stone is assumed to be so unstable that it would have continued its rolling motion without the bar.

The spliced flow fields of the streamwise and vertical velocity have been spatially filtered by a 4×4 vector moving average (after splicing) in order to enable interpretation. The spliced plots of the swirling strength have been filtered by a weighted average with a 16×16 vectors Gaussian kernel.

7.3 Uniform flow

First the results for the uniform flow are presented. The measured mean velocities and turbulence intensity were presented in chapter 4. Here the focus is on the flow structures that cause stone movement. The reference case U007 is treated mainly. In total 33 stone movements were measured, so the flow structures causing stone movement can be obtained with confidence from this case. After that cases U003, U005 and U014 are inspected to determine whether the flow structure is the same for a different stone (position) or movement frequency of the stone.

7.3.1 Classification

It is expected that the indicators F_A and/or $\sigma(v)_A^2$ will have high values if the respective quasi-steady or TWP forces are large. The values of these indicators at the moment of first stone movement will be compared to the values at a random instance.

If the values for an indicator are increased at the time of stone movement then it is an indication that the corresponding force mechanism aids in the stone entrainment. Figure 7.4 depicts the combinations of F_A and $\sigma(v)_A^2$ for the flow fields just before movement (at maximum $\frac{1}{15}$ s) and for a measurement with a fixed stone for reference. It is clear that the values of the indicators for the flow fields just before movement are among the maximum values of the reference measurement. This confirms that both force generating mechanisms play a role in the entrainment process. The values of F_A and $\sigma(v)_A^2$ just before entrainment seem slightly negatively correlated. This indicates that both forces act together on the stone and that the sum of them should surpass a certain critical threshold for the stone to move.

The circles representing stone movements and the dots representing normal, unconditional flow do not form two separated groups. This indicates that the chosen indicators cannot entirely predict stone movement. The facts that only one plane in the transverse direction is considered, that the transverse velocity is not taken into account, and that the indicators are only considered at one moment, can be reasons for this.

The circles representing stone movements also cannot be divided in clear groups, so probably not two distinctly different types of flow structure are responsible for the movement of the stone. In this regard a strict classification of all events according to the force-generating mechanism is not possible. Nonetheless we will call events with large F_A QSF events, and with large $\sigma(v)_A^2$ TWP-events. The dashed lines in the figure indicate the arbitrary limits of this classification.

F_A is larger than average for almost all movement events, and the streamwise velocity is above average for all entrainment events (as $\bar{u}^2 < \overline{u^2}$). This indicates that an increased streamwise velocity is a prerequisite for the entrainment of a stone, which is in line with previous research (Nelson *et al.*, 1995; Drake *et al.*, 1988; Thorne *et al.*, 1989, for example), and with chapter 5.

The dependence on the fluctuation of the vertical velocity was also noted by some researchers, but less clearly (Nelson *et al.*, 1995, for example). This could be caused by the fact that most previous measurements were point measurements, and small-scale fluctuations of the v velocity will give a zero average if the position in the structure where the velocity is measured varies. The spatial standard deviation used presently is hardly influenced by this ‘phase jitter’.

7.3.2 Conditional averages

Now the flow structure present at the time of entrainment will be presented and linked to the force mechanisms. Before inspecting the individual flow fields, the smoother conditionally averaged flow fields will be inspected. Afterwards it will be checked whether the structures present in these fields can be recognised in the individual

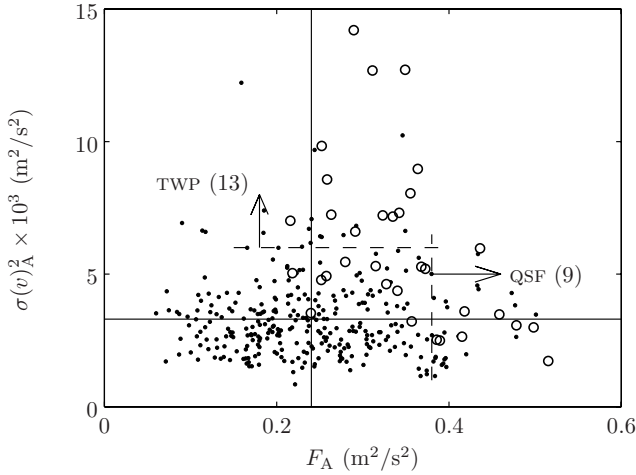


Figure 7.4: Classification of events. F_A and $\sigma(v)_A^2$ indicate QSF and TWP-forces respectively. Dots are the values of a reference measurement with a fixed stone (10 min. duration at 0.5 Hz). The circles are the values just before stone movement. The solid lines represent the average values of the indicators, the dashed lines are arbitrary limits for QSF and TWP events.

fields as well. Whereas the fully turbulent flow field at initial stone movement exhibits many flow structures at different scales – of which it is not clear whether they are responsible for the stone movement – the conditionally averaged flow field shows the persistent flow features during stone movement.

The conditionally averaged spliced plot of all 33 movements of case U007 are presented in figure 7.5. It is clear that distinct features are present at the time of stone movement ($x=0$). This indicates that a certain structure indeed exists, that causes stone movement. The streamwise velocity, shown in the top panel, is clearly increased around the time of movement. It is part of a large-scale structure spanning about $5h$ in streamwise direction (about the whole plot). Of course this size might have been increased due to the smearing caused by the averaging procedure. This large-scale structure also has a predominant downward velocity near the bed for $x = -400$ mm to 100 mm, so it can be classified as a Q_4 or sweep event ($u' > 0, v' < 0$). This structure roughly resembles the large wedge-shaped structures with increased u that were measured by Buffin-Bélanger *et al.* (2000) in a gravel bed river. These events were reported to be responsible for most bed load transport at higher transport rates (Drake *et al.*, 1988).

It is remarkable that the streamwise velocity just at the beginning of movement

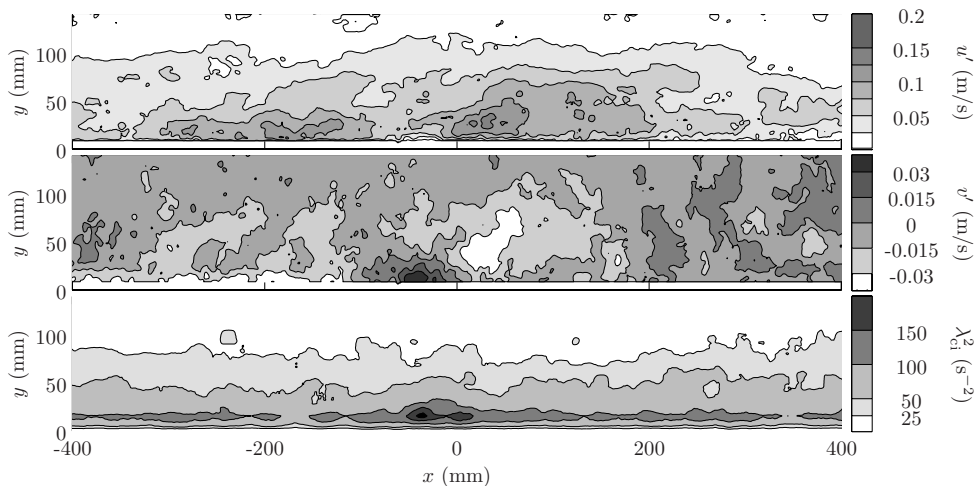


Figure 7.5: Contour plots of spliced and conditionally averaged recording for all events of case U007. The stone moves at $x = 0$.

of the stone (just left of $x=0$) is much lower than during the rest of the large-scale motion. If only the QSF were responsible for the entrainment of the stone, one would expect the maximum velocity to be present at $x=0$. This small patch of relatively decreased u' seems to be connected to a small-scale v' fluctuation. In the middle panel clear patches of upward and downward flow are discernible. The increased value of the near-bed λ_{ci}^2 in the lower panel further indicates that the vortical motion is above average at the time of movement. The small-scale fluctuating velocities seem to be related to that. It thus seems that a small-scale structure causing TWP is nested inside a large-scale structure causing QSF. This combination of structures could be caused by distinctly different flow structures, that do not occur together in reality, as all events were averaged. Therefore the conditional averages of the events that were classified as TWP and QSF events will now be treated separately.

The conditionally averaged sequences of QSF events and those of TWP events (not shown) have similar features as the conditional average for all events. Both show a similar large-scale sweep and small-scale v fluctuation. However, the sweep in the QSF-events is larger and has a slightly higher magnitude than the conditional average of all events. Conversely, the TWP-events exhibit a smaller sweep and the small-scale patches with up- and downward motion – together with the values of λ_{ci}^2 – are more intense. This seems to corroborate that the large-scale sweep is connected to the magnitude of the QSF, and the small-scale fluctuation of the vertical velocity is connected to the TWP-forces. Note however, that both force-sources are present in both situations.

7.3.3 Small-scale instantaneous flow structure

We will now investigate the small-scale flow structure present at the moment of first movement of the target stone in more detail. Just after the initial movement of the target stone (i.e. left of $x=0$ in the spliced figures) a small patch of fluid with decreased near-bed u is often present. This decrease is relative to the surrounding flow, which usually has an increased velocity. Not all events that were classified as QSF events exhibit a small-scale structure, though.

The observed decrease of the near-bed u , together with the up- and downward flow around it, as well as the increased values of λ_{ci}^2 , all correspond to the presence of clockwise-rotating spanwise vortices. Vector plots were regarded in order to see whether vortical flow is present. As only vortices at a distance of about the stone size are expected to create considerable forces, only part of the measured flow field was inspected. Indeed, one or more intense spanwise vortices were present near the stone (upstream of the stone on the image before, and downstream of the stone on the image after first movement) in 24 out of the 33 events. See figure 7.6 for two examples. Almost all flow fields that are classified as TWP fields in figure 7.4 are among these (12 out of 13).

One kind of flow structure that can be discerned is a single vortex rotating in the clockwise direction. In the top panel of figure 7.6 an example of such a vortex is depicted. Around the area with high λ_{ci}^2 a rotational flow field is indeed visible if the proper convection velocity is subtracted. See the figure captions for the exact velocities that were used. The value of λ_{ci}^2 has several maxima, but a noisy image can be expected in such a turbulent flow. This flow can be responsible for lifting the stone, as the vortex causes a low pressure under its core – compare to figure 6.1. Similar flow fields were found at 7 out of the 33 events. The centre of the vortex is typically located 10–30 mm above the top of the stone. Tomkins (2001) observed that intense vortices of the scale of the roughness size occurred more frequently than other sizes. This would mean that the vortices capable of moving stones are relatively frequently present in uniform flows.

Regularly a vortex is accompanied by a Q_2 event or ejection ($u' < 0, v' > 0$) upstream of it. These two structures together are thought to represent the cross-section of a hairpin vortex, and are hence called a hairpin vortex signature (Adrian *et al.*, 2000b, and section 2.2.1). See the left panel of figure 7.7 for an example. Here a vortex is present at (0,20) mm and the Q_2 event around (-5,15) mm.

Another flow structure that could regularly be discerned at the time of first movement was a small hairpin-vortex package (HVP), where several small hairpin vortex signatures are aligned in a straight line of increasing elevation in downstream direction. These vortices span a wedge-shaped area with retarded and upward velocity (Q_2 event) relative to the large-scale flow – not to the mean flow. A clear HVP was

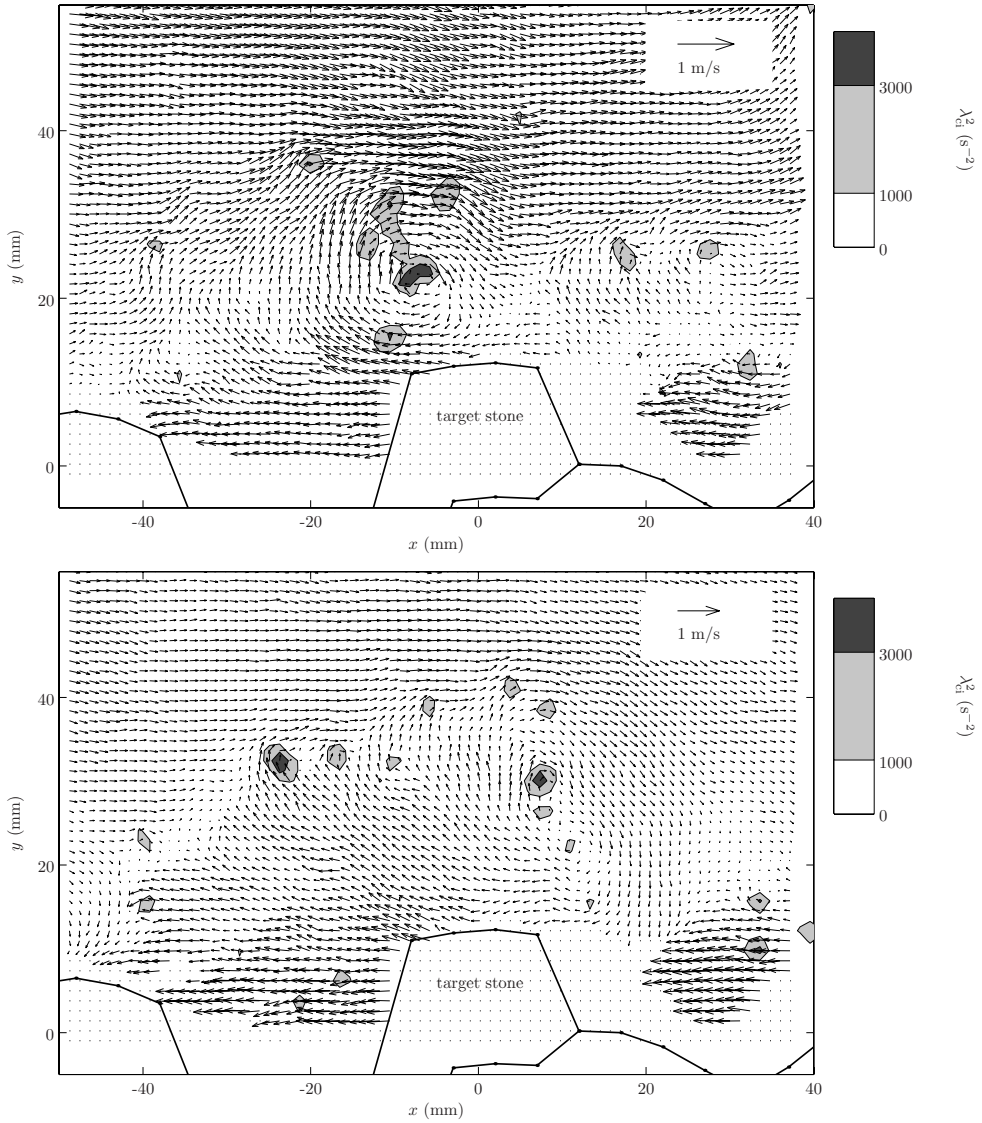


Figure 7.6: Detail of instantaneous field just before movement of the target stone. Top: event #5, $\vec{u} = 0.65\vec{U}$, bottom: event #28, $\vec{u} = 1.0\vec{U}$.

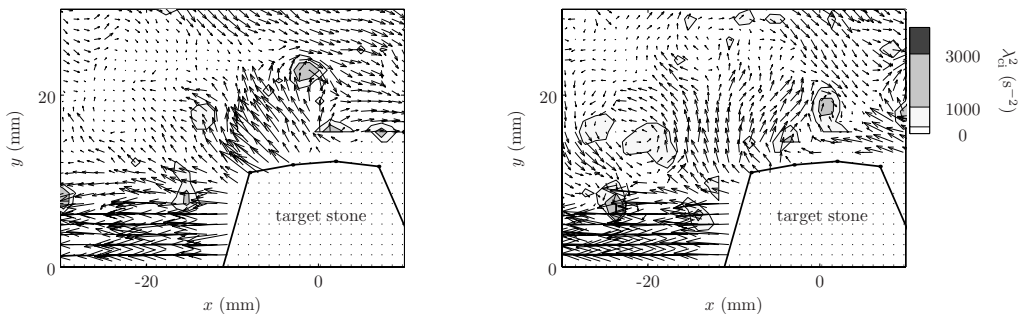


Figure 7.7: Left: Event #29, just after first movement of the stone, $\vec{u} - 0.70\vec{U}$. Right: Event #23, just before movement, $\vec{u} - 0.85\vec{U}$.

visible at 9 out of the 33 events. An example is depicted in the bottom panel of figure 7.6. As the HVP is embedded in a large-scale Q_4 event, an increased u velocity follows right after the Q_2 event has (slightly) lifted the stone from the ground.

A vortex that rotates anti-clockwise creates an increased quasi-steady drag and TWP-lift simultaneously. Hence this flow structure could be very efficient in dislodging a stone from the bed. On the other hand, the consecutive occurrence of lift and drag – which is implied by the conditionally averaged flow field – increases the total duration of the forces on the stone, which gives the stone time to accelerate. Anti-clockwise vortices can be seen in 5 out of the 33 movement events, be it with a low intensity. Therefore it is not conclusive whether these vortices aid in the entrainment of the stone. See the right panel of figure 7.7 for an example of such a vortex at (-25,15) mm. Note that the intensity of the vortex is low. Further note the high convection velocity of the vortex of $0.85U$ (the velocity in the centre of the vortex).

7.3.4 Large-scale flow structure during individual movements

The sweep event in the conditionally averaged plot had a length of about $5h$. This size may have been somewhat increased by the averaging procedure. The length scale of the sweep events is difficult to define objectively. A visual inspection of the length of the sweep events (maximum extent of regions where $u' > 0.1$ m/s) indicates that most sweep events present at the time of initial stone movement are $2-4h$ in length. This size is the usual size of large-scale structures in open-channel flow (Nezu & Nakagawa, 1993). No clear sweep is present at the time of initial stone movement in only 3 out of the 33 cases. In these cases the stone moves at the moment that an intense, large-scale Q_2 event arrives at the stone. Furthermore, the gradients of the velocities are larger in the individual spliced plots, which is also due to the fact that velocities are

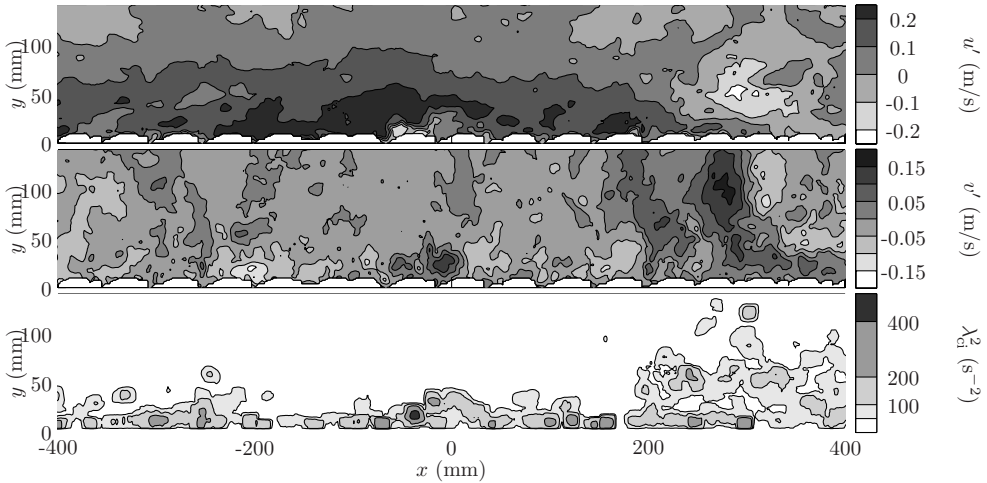


Figure 7.8: Large-scale spliced flow field of event #28.

not smeared out by the averaging procedure.

The presence of the two flow structures in the conditional average is not an artefact of the averaging procedure. An example of this is event #28 (figure 7.8), which resembles the conditional average remarkably well. There is a small-scale upward velocity at $x = 0$, which was seen to belong to a small hairpin vortex package (HVP) in the previous section. This HVP is embedded in a Q_4 event of about $4h$ length.

Not every event has this embedded structure, however. A good example is event #5. The intense vortex of event #5, already shown in figure 7.6, seems to be part of a HVP as well (see figure 7.9). This HVP is larger and is not embedded in a Q_4 event as is the case for event #28. Instead a Q_4 event of a size comparable to the Q_2 event follows it (i.e. is situated left of it). The HVP can be recognised from the inclined line of vortices (large λ_{ci}^2) extending from $x = -100$ mm to 100 mm which separates a Q_2 event and a Q_4 event. The angle of the line of vortices to the bed is roughly 16 degrees, which is in the range of 10° – 20° found by Tomkins (2001) for HVPs. Several equally sized HVPs seem to be present in this flow field.

7.3.5 Sensitivity of results

It is laborious to change the many parameters that govern the probability of movement of the target stone, like the size, shape, position, and orientation of the stone, the surrounding topography, and the strength or depth of the flow. Only a few changes were made. The results of these are discussed next, mainly to see whether the findings of case U007 also hold for other configurations.

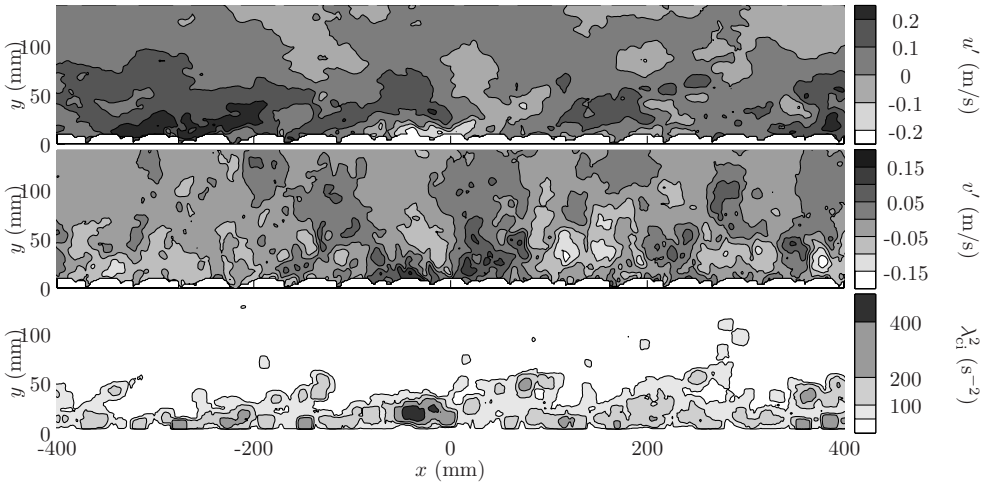


Figure 7.9: Spliced flow field of large-scale event #5.

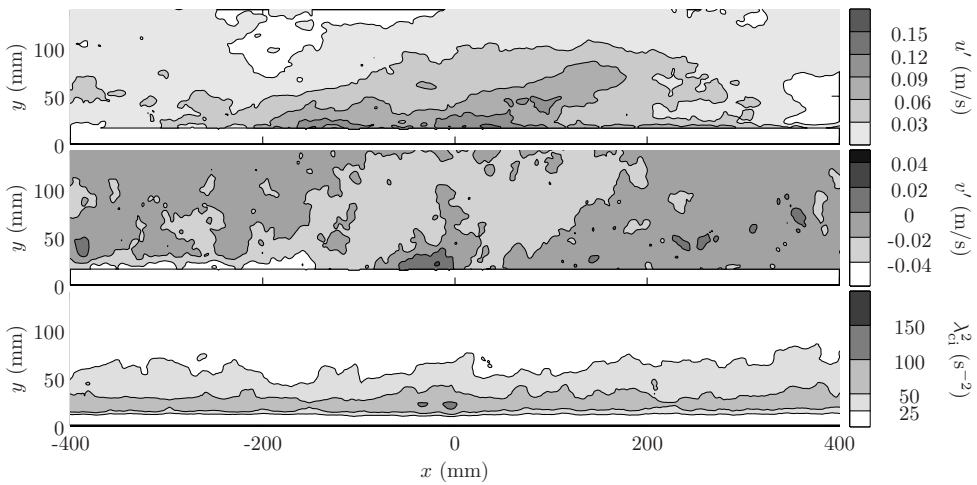


Figure 7.10: Large-scale conditionally averaged flow structure for stone with slightly increased protrusion (U003).

Exposure

One variation was the increase of the exposure of the original target stone by about 3 mm (U003). This clearly effected the mobility of the stone: the movement frequency increased from 6.5 hr^{-1} to 20.1 hr^{-1} , while the shear stress was even slightly decreased. The increased exposure was accomplished by placing the leading part of the stone on a small support. The conditionally averaged flow over the 34 recorded movement events is shown in figure 7.10. It can be seen that the flow structure that is necessary to move the stone is similar to that during the reference measurement. Both the large-scale sweep, as well as the small-scale embedded fluctuation can be seen.

Other stone

Also a measurement with a different target stone was undertaken (U014). This stone was smaller than in the reference case U007. The conditionally averaged flow over the 50 recorded movement events is shown in figure 7.11. In this case the sweep event is more intense than for U007. A small-scale structure is still present in the image of the vertical velocity, but not in the streamwise velocity.

When regarding a classification plot similar to that of U007 (figure 7.12), we can see that the QSF are more frequently important for movement in this configuration, as most events have a large F_A -value (QSF-indicator). When regarding the individual spliced plots for the movement events we see that flow structures with embedded

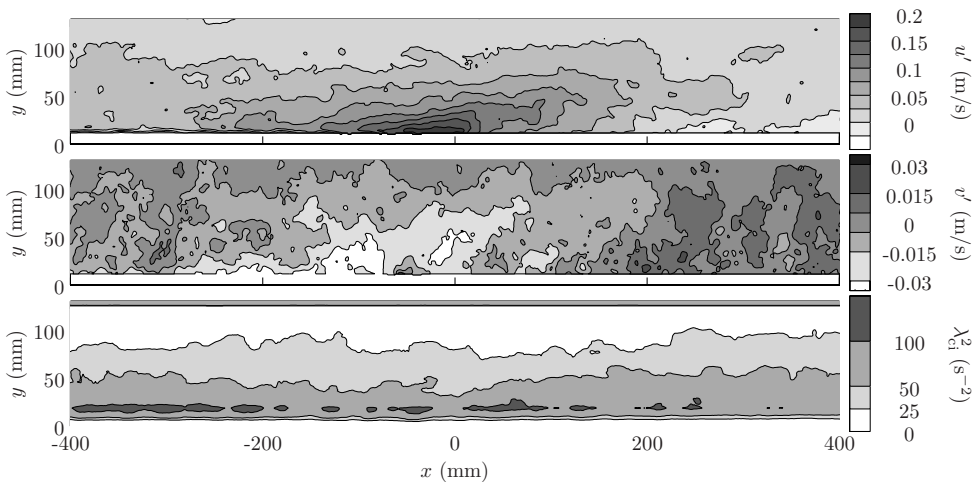


Figure 7.11: Large-scale flow structure for different stone (U014).

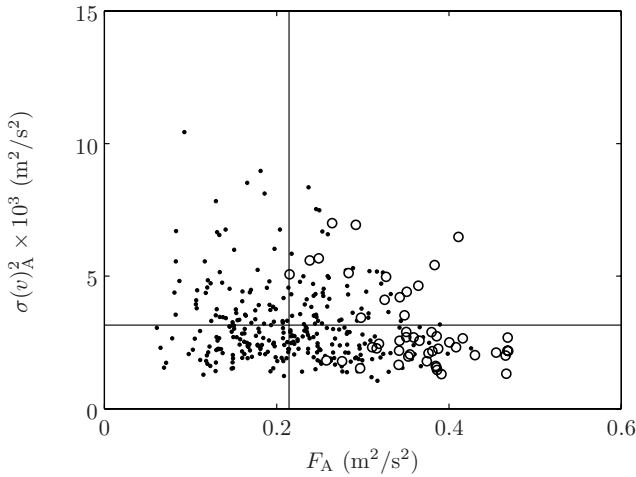


Figure 7.12: Classification of events for different stone (U014). Dots are the values of a reference measurement with a fixed stone (10 min. duration & 0.5 Hz). The circles are the values just before stone movement. The solid lines represent the average values of the indicators.

small-scale v -fluctuations still occur at the time of first movement, be it less often. It seems that the TWP-induced forces are required less for stone movement in this case of the smaller stone than for case U007.

Low mobility

One experiment was made with a very low mobility flow (U005). The measured shear stress was not much lower than in the reference case U007, but the stone only moved 3 times in one day of measurements. This can be expected when regarding the steep slope of the transport curve of Paintal (1969). The force indicators for these three events indeed have extreme values as well. Two have a very large $\sigma(v)_A^2$, and one has a very large F_A . Therefore it is concluded that the flow structures that entrain stones do not change when the mobility is varied in the low-mobility range.

7.4 Backward-facing step

A similar analysis as undertaken for the uniform flow is made for the backward-facing step (BFS) flow. Mainly case B006 is treated which was measured at the reattachment point at $12h_s$ from the step. First we see which force mechanisms are present in the

flow at the time of first movement, and after that we present the conditionally averaged flow structures. These are checked against some instantaneous flow fields. The BFS flow has often been studied, be it mainly in ducts (i.e. with a rigid lid) and with a smooth bed. Here some flow structures were identified that occur with a certain periodicity. We check whether and how these are connected to the entrainment of the target stone.

A comprehensive presentation of the results presented in this section can be found in De Ruijter (2004).

7.4.1 Classification

The classification plot of the force indicators for the movement events of the BFS experiment B006 is presented in figure 7.13. The dots, which represent a 10 minutes experiment with a fixed stone, have a different distribution than in case of the uniform flow. The large number of dots representing a value of the QSF-indicator near zero can be explained by the quadratic nature of the QSF and the fact that the mean flow velocity near the bed is very low – it is predicted by the probability distribution of $u|u|$ in eq. (5.3). For this case it is very clear – more than for the uniform flow – that the movement events (circles) are characterised by values of $\sigma(v)_A^2$ and F_A

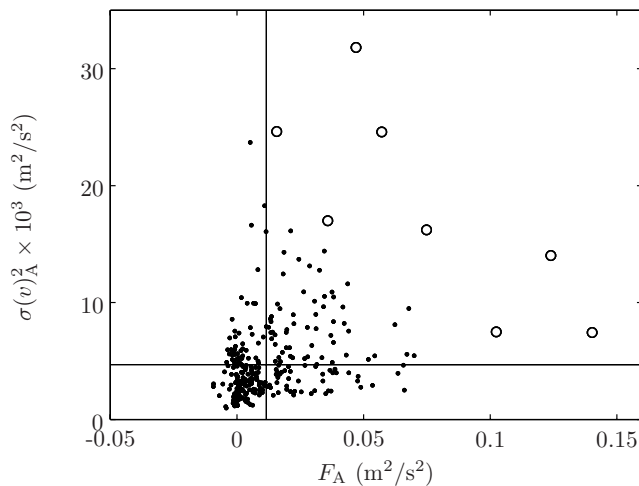


Figure 7.13: Force indicators of flow fields just before stone movement at reattachment point (B006). Dots are the values of a reference measurement with a fixed stone (10 min. duration at 0.5 Hz). The circles are the values just before stone movement. The solid lines represent the average values of the indicators.

that are both above average. Also the fact that the combination of the two forces has to be large enough to dislodge the stone is much clearer. The lower envelope of the points indicating the movement events clearly forms a line with a negative slope. The fact that the classification plot is much clearer for the BFS flow might be due to the fact that the duration of a stone movement is generally much shorter in this configuration. This makes the probability that both force-indicators are large in the same image – and do not occur sequentially – larger than for the uniform flow case. Another possibility is that in the uniform cases different mechanisms that cannot be measured, like a fluctuating spanwise velocity, affect the stability of the target stone.

7.4.2 Conditionally averaged flow structure

The conditionally averaged flow structure around the time of movement of the target stone is shown in figure 7.14. It has not been spliced as the mean flow has a larger vertical gradient (with negative velocities near the bed). Therefore the validity of the splicing procedure becomes doubtful. From the Reynolds decomposed plots of the streamwise velocity it can be seen that fluid with high velocity is transported from the upper layers to the bed. At the same time a structure with high vertical velocity is coming to the bed. From the vector plots (right panels in figure 7.14) this is seen to be part of a spanwise vortex. This vortex is located above the stone at the time of first movement of the stone (between $t=-33$ ms and $+33$ ms).

Other position

Similar measurements were executed at $14h_s$ from the step. The same kind of flow structure was seen to be responsible for stone movement at this location. This has not been investigated further.

7.4.3 Quasi-periodic structures

In literature a number of quasi-periodic structures occurring in BFS flow are mentioned. The main features are the shedding of large vortices from the step and a low-frequency flapping motion of the mixing layer. An oscillation of the reattachment point is also reported, which is probably directly linked to the shedding of the large-scale vortices. Table 7.1 denotes the frequency of occurrence of certain flow features mentioned in literature. We will inspect whether the frequency of occurrence of the conditionally averaged flow structure at first stone movement is comparable to the frequencies reported in literature for one of these features. The frequencies have to be made dimensionless in order to be able to compare them. The step height h_s and the reattachment length x_r are sometimes chosen, for the length scale. As the ratio of these length scales is rather constant in the low-Reynolds number duct flows

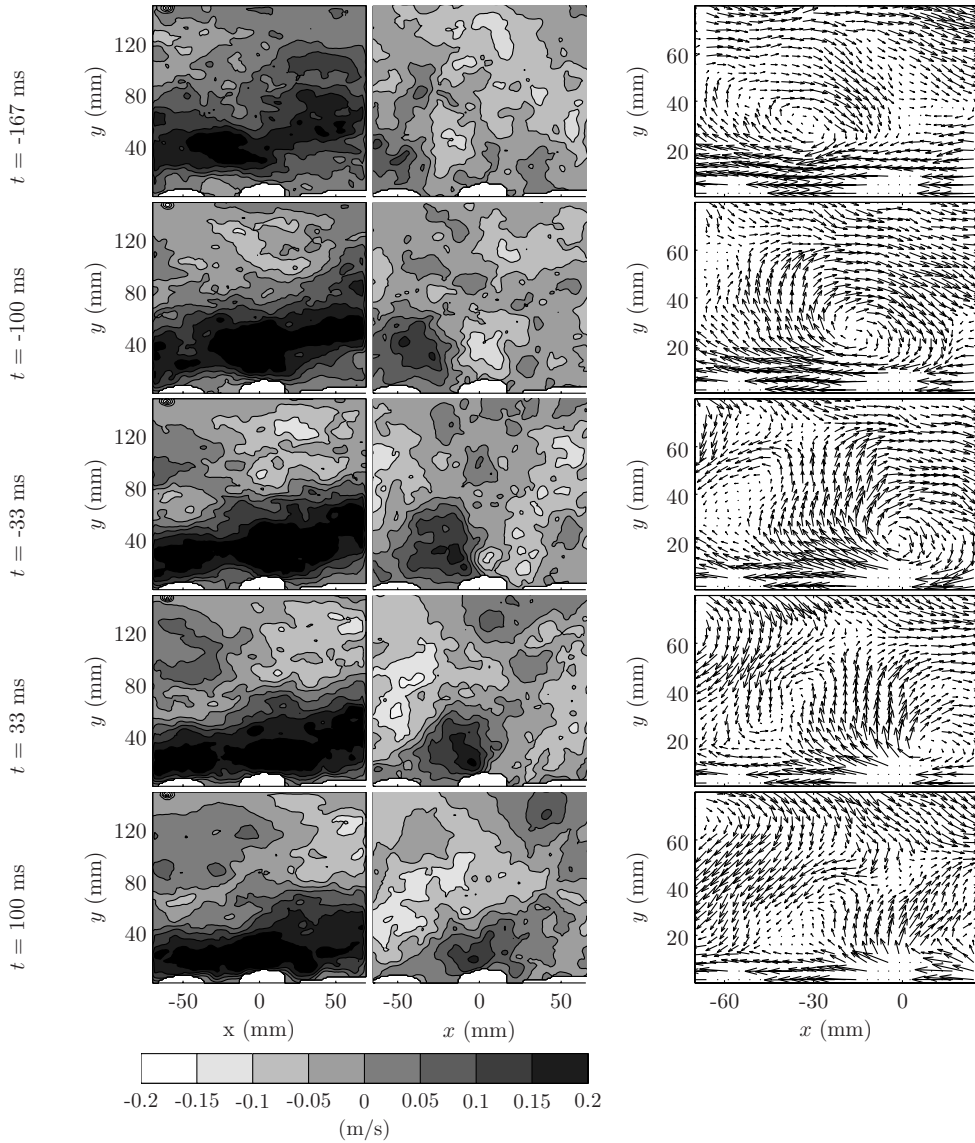


Figure 7.14: Conditionally averaged flow structure around the time of movement ($t=0$) for case B006. The target stone is situated at the reattachment point, $(x,y)=(0,0)$. Left: u' , middle: v' , right: $\vec{u} - 0.8\vec{U}$, detail with every second vector plotted.

Mechanism	Source	$\frac{f h_s}{U_0}$	f [Hz]
Shedding of large vortices	Lee & Sung (2002)	0.065	0.7
Oscillation of reattachment length	Simpson (1989)	0.09–0.15*	1.0–1.7
Flapping of shear layer	Lee & Sung (2002) Simpson (1989)	0.0136 < 0.02*	0.15 < 0.22

Table 7.1: Quasi-periodic phenomena in BFS flow and their frequency. The right column represent the frequency expected in the present set-up, when the measured U_0 and h_s are used. *) These frequencies were scaled by x_r , and have been recalculated assuming $x_r/h_s=5.5-6.5$.

treated in literature, both can be interchanged rather easily. The present set-up has a reattachment length of $12h_s$, which is about twice that in most cases treated in literature (see also chapter 4), so one of the two has to be chosen. In chapter 6 it was shown that the wall pressure spectrum of the rough bed measurements resembles that of the smooth beds very well when made dimensionless with the step height. This is confirmed for the pressure measurements of the second experimental series where also some pressure sensors were installed. Therefore h_s is used as the representative length scale.

To inspect whether the flow structure that initiates stone movement is a normal flow structure, the correlation between the conditionally averaged u' field just before movement (third plot from the top in figure 7.14) to a time-series of u' recordings that was recorded with 15 Hz for 20 seconds is determined:

$$\rho(t)_{uCA} = \frac{\langle \overline{u'}_{CA}(x, y) u'(x, y, t) \rangle_A}{\sqrt{\langle \overline{u'}_{CA}(x, y)^2 \rangle_A \langle u'(x, y, t)^2 \rangle_A}} \quad , \quad (7.5)$$

where $\overline{u'}_{CA}(x, y)$ is the conditionally averaged flow field at first stone movement, and $\langle \dots \rangle_A$ is a spatial average over the recording area A.

The result is plotted in figure 7.15. Regularly the correlation coefficient has maximum values which are rather high (about 0.7). Apparently a u' field very similar to the conditionally averaged field is present regularly. The maxima in the correlation are highlighted by circles in figure 7.15. These are found by determining the points that are maximum in a 1.25 s surrounding window. As every peak consists of a few points, it means that the correlation function is time-resolved. The frequency of oc-

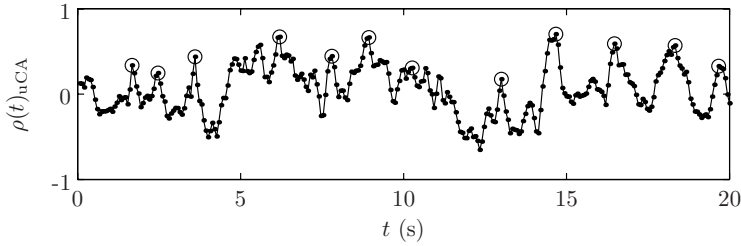


Figure 7.15: Coherence between conditionally averaged field of streamwise velocity just before stone movement (\bar{u}_{CA}) and a recording with a fixed target stone.

currence of these maxima is about 0.6 Hz (12 peaks divided by 20 s). A similar peak frequency of 0.7 Hz is obtained from spectral analysis. This is very close to the value reported for the shedding of large-scale eddies from the step, mentioned in table 7.1.

When applying a similar correlation using the v field we obtain a signal resembling white noise (not shown). This means that this structure probably occurs with a higher frequency than the Nyquist frequency of 7.5 Hz. This raises the question whether the conditionally averaged v field at the time of stone movement is comparable to the v field corresponding to the maxima of the correlation of the u' fields. This can be seen in figure 7.16. Here the average flow field at all the instants of the maxima indicated in figure 7.15 is depicted to the left of the conditionally averaged flow structure just before stone movement. It can be seen that the u' fields are very similar. This is to be expected, as this is the flow structure that was searched for by the correlation procedure. Surprisingly, the v fields are completely different. The vertical velocities in both plots are of opposite sign. The ‘normal’ flow structure has a negative vertical velocity, which is connected to the downward transport of the high streamwise velocity, whereas the intense small vortex that is transported towards the stone just before stone movement causes an upward velocity.

The observed frequency of occurrence of the u' flow field of roughly 0.6 Hz yields a dimensionless frequency of occurrence, fh_s/U_0 , of roughly 0.06. This is comparable to the dimensionless frequency of 0.065 that is linked to the shedding of large vortices from the step (Lee & Sung, 2002). Therefore it is likely that the large-scale streamwise flow structure at the time of stone movement is connected to the normal shedding of large vortices. These vortices (see figure 14 in Lee & Sung (2002)) are created by the merging of several smaller vortices (Lee & Sung, 2002). It might be that occasionally one of these is not completely merged with the others and causes the small-scale v fluctuation which causes the initial stone movement.

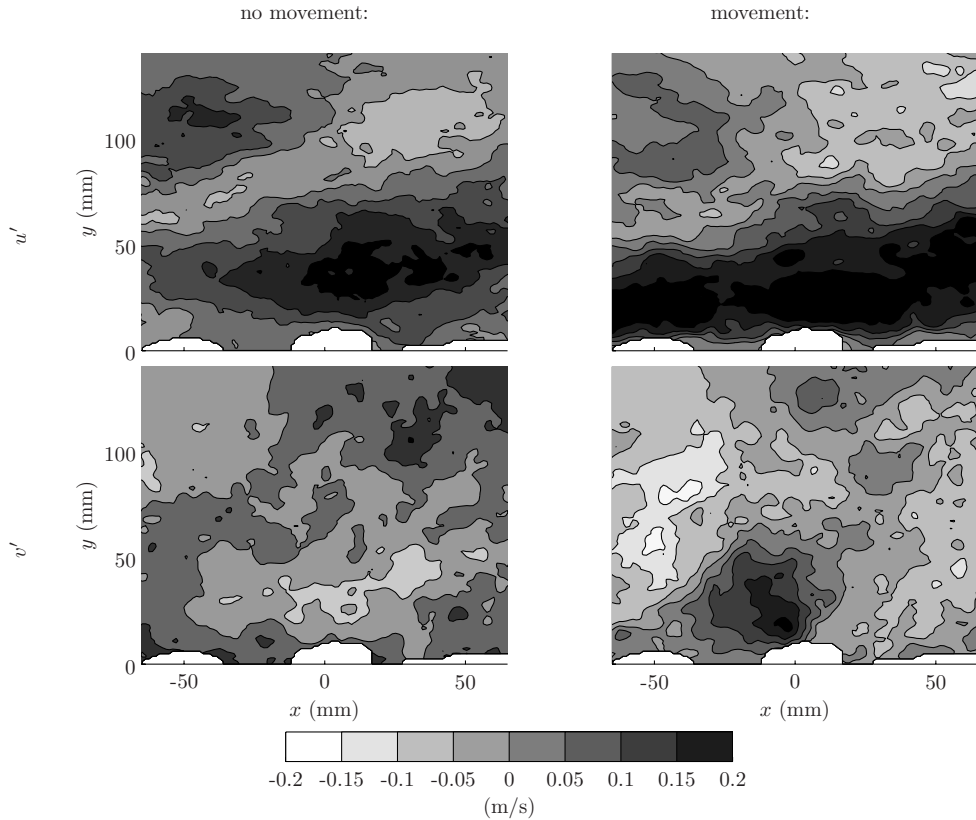


Figure 7.16: Left: ‘normal’ flow, i.e. conditionally averaged flow structure during maximum correlation with the $\overline{u'_{CA}}$ field (circles in figure 7.15) (top: u' , bottom: v'). Right: flow field just before stone movement ($\overline{u'_{CA}}$ and $\overline{v'_{CA}}$).

7.5 Evaluation of quadrant analysis

The combination of a large-scale Q_4 event and a small-scale Q_2 event is optimal for moving material from a bed. This combination occurred during initial stone movement, both for uniform flow and BFS flow. A Q_4 event causes an increased drag and lift force due to the enlarged streamwise velocity. However, the corresponding negative v' decreases the lift [eq. (2.13)]. For the initial movement of the stone, the lift force is often important as the vertical exposed area of the stone is still small and the moment created by the drag force is not yet very large due to the large pivoting angle. Therefore an increased lift force of short duration is necessary to dislodge the stone. Once the stone is raised, the drag force alone is capable to move it further over

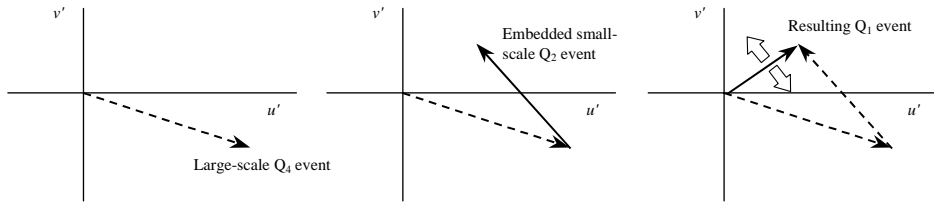


Figure 7.17: Illustration of a Q_4 event (sweep) and an advected Q_2 event (ejection), together creating a Q_1 event (outward interaction).

its point of rotation. A small Q_2 event can create the lift force needed for this first movement. Adding an advected small-scale Q_2 event to a Q_4 event can result in a Q_1 event ($u' > 0, v' > 0$), as depicted in figure 7.17. The large-scale Q_4 event has a longer duration than the Q_2 event, so the resulting force vector fluctuates as indicated by the block arrows. This causes the force direction to rotate in the same direction as the stone, such that the moment remains large for a longer time. A quadrant analysis which only regards the instantaneous values of u' and v' at a single point does not capture this sequence of flow structures that is needed to move the stone.

7.6 Pressures

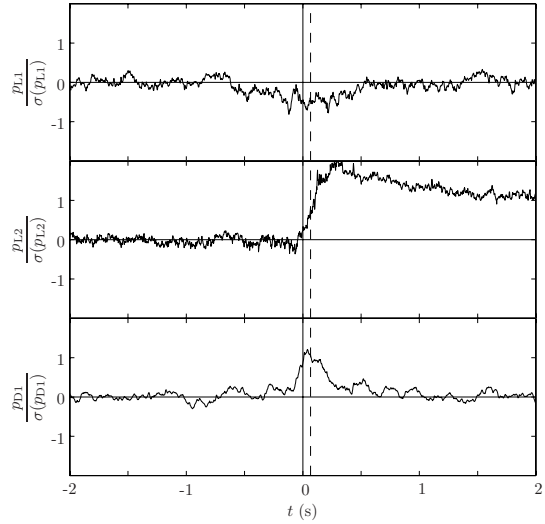
Before concluding this chapter a brief analysis is presented of the pressures that were measured around the target stone during the second measurement series. These corroborate certain findings and assumptions presented earlier.

The measured pressures, conditionally averaged over all stone movements for the uniform flow case U007, are depicted in figure 7.18. The positions of the various sensors are given in figure 4.9. The pressure on the lift sensor L_1 , upstream of the target stone, decreases when the target stone moves, indicating lift. It is reasonable to conclude that the target stone experiences this lift as well. Therefore the quasi-steady lift does seem to be present.

The pressure under the target stone (L_2) increases when the stone begins to move. This is explained by the increasing exposure of the stone, which leads to a stagnation pressure under the target stone. This is in line with the statement that once the stone is only slightly lifted (possibly by the TWP), a much lower streamwise velocity is necessary for the stone to rotate further.

The drag pressure sensor besides the target stone, D_1 , shows an increased drag around the moment of movement. This is in line with the presence of a large sweep

Figure 7.18: Conditionally averaged pressures near target stone during entrainment at $t=0$. Top: lift sensor upstream of stone, middle: sensor under stone, bottom: drag sensor next to stone. The dashed line indicates the latest possible time that the first PIV recording after movement is made.



that causes increased QSF. The sensor was placed 4 cm besides the target stone, implying that the sweeps have a width of at least 8 cm, which is roughly $h/2$.

The pressure spectra of the various sensors are depicted in figure 7.19. These are compared to a spectrum of Lee & Sung (2002), as was done for the bed-mounted cube in chapter 6. It can be seen that the dimensionless peak frequency of all spectra is 0.1. Moreover, the spectral slope at higher frequencies for the present measurement as well as for the Lee & Sung spectrum is about $-7/3$. The low-frequency part of the spectrum is higher than the Lee & Sung spectrum, like the spectra of the first measurement

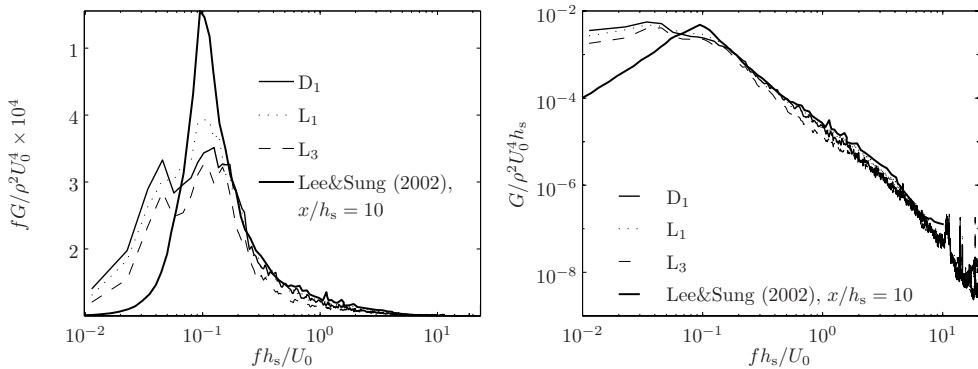


Figure 7.19: Spectra of pressures on stones surrounding target stone.

series. This implies that the conclusions that were drawn for the bed-mounted cube are also valid for stones with more realistic shapes. The fact that the spectrum of D_1 is similar to the spectra for the lift sensors indicates that for the realistic position of the stones in the second measurement series, the drag is influenced to a large extent by the TWP.

Some differences can be observed between the presently measured spectra and the spectrum of Lee & Sung (2002). The peak in the spectrum at $fh_s/U_0 \approx 0.1$ is lower and an extra low-frequency peak is present at $fh_s/U_0 \approx 0.045$. It is not clear what the origin of these differences is.

7.7 Conclusions

The conclusions derived here apply to a few single stones with their specific position, orientation, shape, size, and density. Still, as some crucial parameters were changed and the results remained comparable, we believe that the results are representative for the entrainment process of coarse, sharp-edged bed material in bed protections.

The flow structure that leads to stone movement is very similar in uniform flow and in backward-facing step (BFS) flow. The stone is entrained during the presence of large-scale areas with increased streamwise and downward velocity (Q_4 event). Often it gets an initial lift (or rotation) by an intense, small-scale fluctuation of vertical velocity. Here the streamwise velocity is locally decreased (Q_2 event). This is usually connected to the presence of a spanwise, clockwise rotating vortex (probably a cross-section of a hairpin vortex). However, differently oriented vortices might also be responsible for the initial movement of the stone. The initial lift of short duration increases the exposed area and angle of repose such that the stone is moved more easily by the increased streamwise velocity reaching the stone after the fluctuation in vertical velocity. The intensities of the two flow structures (i.e. the large Q_4 and the small Q_2 event) at initiation of movement appear to be negatively correlated. This can be explained by the fact that if one is more intense, the other can be less intense for the total force to overcome the critical force and vice versa.

In the uniform-flow case the increased longitudinal velocity is part of a large-scale Q_4 motion. The size of these sweeps is typically about $2-4h$ in streamwise direction and $\frac{2}{3}h$ in the vertical direction, but lengths of $\approx 6h$ were also observed. These sweep events resemble the structures normally occurring in open-channel flow (Nezu & Nakagawa, 1993; Buffin-Bélanger *et al.*, 2000). They cause increased quasi-steady forces on the stone.

In uniform flow, the fluctuating vertical velocity is often caused by single vortices or vortex packets close to the stone (typically $0.5-2d$) which cause turbulence wall pressures. Most often this small-scale structure is embedded in the large-scale

sweep. Some strong Q_4 events without the increased small-scale vertical fluctuations were observed, but the streamwise velocity was always above its mean value during stone movement. In other cases a Q_2 event and a Q_4 event of comparable size occur sequentially without the nesting of a small structure inside the larger Q_4 event.

In the BFS flow the pattern of increased streamwise velocity occurs with a dimensionless frequency, fh_s/U_0 , of about 0.06. This flow structure is probably caused by the periodic shedding of large vortical structures, which are described in literature as having a dimensionless frequency of 0.065. These large-scale vortical structures can be regarded to be the downstream part of the recirculation area that sheds from the main recirculation area and has a size larger than the step height. The direction of the vertical velocity near the stone at initial movement is opposite to the direction present during the normal occurrence of this flow field. This is due to an extra small vortex, which creates the initial lift force on the stone. This vortex originates from the mixing layer, instead of the bed, as was the case for the uniform flow.

One can state that in general the stone is moved by an exceptional combination of two normal structures, at least one of which has an exceptionally high magnitude.

Chapter 8

Modelling Damage to Bed Protections

8.1 Introduction

Bed protections are usually built near hydraulic structures like groins, weirs, sluices, etc. These structures cause the flow to be non-uniform. However, the stability parameter of Shields (1936), which is the basis of most design formulae, is meant for uniform flows. Therefore physical modelling is still necessary for the design of bed protections in new configurations. Otherwise large safety factors have to be used. Contrary to this lack of knowledge, the computation of the hydrodynamics has increased immensely during the last decades. In this chapter we try to make the link between the output of such computer models and the stability of bed protections. Hereto a new methodology for designing bed protections is developed, which is partly based on the approaches developed by Hoffmans & Akkerman (1998), Mosselman *et al.* (2000), and Jongeling *et al.* (2003). This model is meant in first instance for stationary, non-uniform flows, but an extension to waves is thought to be possible.

In section 8.2 the general form of the stability model is described. The flow attack is assessed in a Shields-like parameter, of which a general form is given. The bed response (i.e. damage) is described by the (dimensionless) entrainment of bed material. The aim is to find a stability parameter that can predict the entrainment rate for various flow conditions.

Next, in section 8.3 the numerical method that is to be used to calculate the flow attack is assessed. The use of Large Eddy Simulation – where the large-scale turbulence is resolved – is discussed briefly. However, the method that will be used is a 3D, Reynolds-averaged Navier-Stokes (RANS) model with k - ε turbulence closure. The

turbulence intensity is also output of such a model, and is needed for the estimation of damage to bed protections.

In section 8.4 the formulation of the stability parameter is determined. The parameter explicitly models the quasi-steady forces only. It weights the velocity sources in the water column above the bed using a turbulence length scale. Then, in section 8.5 the relation between the new stability parameter and the entrainment rate is calibrated. To this end existing measurements are reanalysed.

In section 8.6 it is evaluated how (already available) computations with a RANS model can predict the entrainment. The chapter ends with conclusions.

8.2 Governing parameters

8.2.1 Shields parameter including Quasi-Steady and TWP forces

The Shields parameter describes the ratio of the mean quasi-steady forces (bed shear stress) on the bed material to the resisting forces. A similar parameter can be defined where the numerator consists of both quasi-steady forces as well as forces due to accelerations (TWP). Both can have a mean and a fluctuating part, as in:

$$\Psi_{\text{tot}} \equiv \frac{(C_B(\bar{u} + \tilde{u}')^2 + C_m(\bar{a} + \tilde{a}')d)_{\text{max}}}{\Delta g d}, \quad (8.1)$$

where a is the acceleration of the flow and the tilde means the projection of the velocity on the bed (e.g. $\tilde{u}^2 = u^2 + w^2$ for a horizontal bed). C_B is a combined drag and lift coefficient, and C_m is the added mass coefficient. Note that the two forces scale differently with d . The fluctuations (of both u and a) can be due to waves and turbulence, but we focus on the turbulence part here.

The subscript ‘max’ means that the entrainment will mainly be governed by an extreme value of the occurring forces (for simplicity designated as the ‘maximum’ force). For this a term like $F_{\text{max}} \propto (\bar{u} + \alpha\sigma(u))^2$ has been used, see e.g. eq. (2.32). As this ‘maximum force’ only incorporates the velocity explicitly, it is an estimate of the quasi-steady forces only. Sometimes probabilistic methods are used, where the probability of $P(F > F_c)$ is evaluated.

However, the acceleration can have an additional and significant influence on the forces on the particles, with both a mean and a fluctuating part. The stationary acceleration can be due to e.g. steep water-surface slopes or jet flow deflected on a bed (Dessens, 2004; Schokking, 2002). The fluctuating acceleration can be due to turbulence (chapter 6) or waves (Tromp, 2004, who found $C_m \approx 7C_B$). Simply taking the sum of the two forces is often referred to as the Morison approach (usually applied to calculate wave forces on piles).

The exact formulation of Ψ_{tot} used in the present study is given in section 8.4.4.

8.2.2 Damage criterion: Entrainment

The parameter Ψ_{tot} is a measure of the flow attack on the bed. If the mechanisms causing stone displacement are correctly represented in Ψ_{tot} , with properly calibrated coefficients, then the value of Ψ_{tot} should determine the bed response for a variety of flow conditions – uniform and non-uniform. To check whether this is the case, or to which extent, a clearly defined and quantified measure of the bed response is required. This quantity should be dependent on the local hydrodynamic conditions, and should represent ‘damage’ to bed protections. For reasons mentioned below, we will use the entrainment rate (E) as this quantity.

No clearly defined measure of damage is available at present. In physical model tests an arbitrary number of stones moving from an arbitrarily sized area of the bed protection is usually chosen as the initiation of damage. Also a time dependence should be added. Damage to a bed protection under a steady flow increases in time as due to turbulence fluctuations a stone is moved sporadically. The quantity that represents the volume (or the number) of stones that is picked up from a bed protection per unit of bed area and time is the entrainment rate of stones, E . This is a clearly defined quantity, which can be compared between different investigations in its dimensionless form:

$$\Phi_E \equiv E/\sqrt{\Delta g d_{n50}} \quad . \quad (8.2)$$

The entrainment rate has the advantage that it is completely dependent on the local hydrodynamic parameters. Conversely, the transport and the deposition of bed material are dependent on hydraulic loads upstream; all the stones passing a certain cross section (transport) have been entrained upstream of this cross section. This means that it is fundamentally impossible to make a transport or deposition formula for non-uniform flow based on the local hydrodynamic forces only.

To clarify this we can regard the sediment continuity equation (2.15) – which was used by Mosselman *et al.* (2000) to estimate the evolution of damage in time. It can be rewritten as:

$$\frac{\partial y_b}{\partial t} = -\frac{1}{1-\epsilon} (E - D) \quad , \quad (8.3)$$

Here D is the deposition rate. Per definition $D \geq 0$ and $E \geq 0$. It can be expected that at places with maximum damage (high hydraulic loads), the deposition rate will be small. Therefore, if the non-local parameter D is omitted, the following time-dependent damage indicator is obtained:

$$\Delta y_b(t_1)_{\text{max}} = \frac{1}{1-\epsilon} \int_0^{t_1} E dt \quad , \quad (8.4)$$

where the bed protection was constructed at $t=0$, and $\Delta y_b(t_1)_{\text{max}}$ is the maximum lowering of the bed at $t=t_1$, which is per definition larger than or equal to the real

lowering of the bed. In reality the bed will not lower gradually. Still $\Delta y_b(t_1)_{\max}$ is a measure of the probability that holes will appear in the cover layer. For a single layer protection $\Delta y_b(t_1)_{\max}$ will probably have to be less than a few percent of the stone diameter. By neglecting the deposition of the stones a conservative (safe) estimate of the damage level is obtained. It was already mentioned that at places with maximum damage the deposition is expected to be small. Therefore $\Delta y_b(t_1)_{\max}$ will be close to the real lowering of the bed, $\Delta y_b(t_1)$.

Using eq. (2.15) or (8.3) to estimate damage could also lead to a false sense of safety. For example, if we imagine a stretch of bed protection with large and equal entrainment and deposition rates, giving $dq_s/dx=0$ on average, we would not expect any damage according to eq. (2.15). Still many stones are picked up and deposited over time, increasing the chance that holes will develop in the bed protection, which could lead to failure of the protection layer.

Also when a more classical critical-value stability approach is adopted, a low threshold value of the dimensionless entrainment parameter Φ_E can be used as the mobility of the bed that is regarded as ‘initiation of motion’. The stability parameter corresponding to that $\Phi_{E,c}$ can subsequently be determined. This critical stability parameter can then be used for designing bed protections.

8.2.3 Aim

The aim of this chapter is to find a damage predictor for non-uniform flows. From the preceding it follows that this can be accomplished if an expression for Ψ_{tot} is found, that includes the quasi-steady and TWP-induced forces in a representative way. The expression for Ψ_{tot} should govern the bed response, expressed by the (dimensionless) entrainment rate. Hence there should be a unique relation:

$$\Phi_E = f(\Psi_{\text{tot}}) \quad . \quad (8.5)$$

It must be determined which flow parameters can be used in the numerator of Ψ_{tot} and how they can be obtained from a numerical calculation. Measured entrainment-flow combinations for a range of non-uniform flows can be used to find the formulation of Ψ_{tot} that gives a relation with the least scatter. If calibrated and verified, this relation can be the basis for a method of designing bed protections using numerical flow calculations.

8.3 Assessment of possible modelling approaches

8.3.1 (Very) Large Eddy Simulation

In chapter 5 it was mentioned that low-frequency ($f \approx \langle \bar{u} \rangle_h / h$) drag fluctuations most probably cause the largest forces (and moments) on stones. In addition, the total force caused by the low-frequency drag force fluctuations can (at least for some stones) be increased temporarily by high-frequency ($f \approx \langle \bar{u} \rangle_h / d$) TWP – sometimes caused by vortex shedding from the stone – giving higher extreme forces. Changes in geometry of a flow (steps, roughness transitions, etc.) have a non-local influence on damage, as the large-scale turbulence level takes a length of tens of water depths to change. Large Eddy Simulation (LES) CFD models might be used to resolve the large-scale flow structures (which cause the low-frequency velocity variations). Bed-protections have a limited spatial extent, so that the computational domain need not be too large. This gives the possibility to use more advanced three-dimensional calculations. Therefore, at first glance LES seems feasible for the design of bed protections. It would directly yield the probability distribution of the near-bed velocity, and hence QSF, which can be used to predict damage. The effect of the computed turbulence on the probability distribution of forces could be estimated by using eq. (5.3).

Foreseeable problems of the use of LES in practice are that the computational time might become too large – despite the limited spatial dimensions – as a substantial time span has to be simulated to obtain reasonable statistics of the turbulent fluctuations in the flow. In order to keep the computational time limited, one would have to use a coarse grid and a short simulation time. This would lead to large errors in the computed flow field. Further, the probability of occurrence of extreme values of the velocity – required for the probability of occurrence of extreme forces – would not be determined accurately. Therefore the shape of the tails of the probability distribution would still have to be estimated. A possible influence of TWP cannot be calculated directly, so a sub-grid model should be used for this. For these reasons, combined with the fact that the use of LES for wall flow is disputed and it is not widely used in practise yet, this way of modelling damage is not pursued further here.

8.3.2 RANS simulation with k - ε turbulence closure

LES computations are rather expensive, as flow during a long time has to be modelled, so the use of a Reynolds-averaged Navier-Stokes (RANS) model is preferred. These models directly compute the mean flow field, but need a closure to determine the turbulence viscosity. The k - ε model is widely used for this in the civil engineering practise, which makes it a logical choice to use. The k - ε model is a semi-empirical model with some fundamental shortcomings. The major one is that k - ε models give one turbulence length scale per point, so one cannot distinguish between different

scales of turbulence at one position, e.g. scales connected to bottom turbulence and free turbulence. Still, in certain cases it can give a fair estimate of the mean flow and turbulence properties. However, assuming that the model gives the exact values for \bar{u} , k , ε and p , still some problems remain. These problems are also present if the required parameters are measured precisely, and the stability of the bed on prototype scale has to be examined. A first problem is that when knowing k , the ratios $\sigma(u)^2 : \sigma(v)^2 : \sigma(w)^2$ are still unknown. Secondly, the exact shape of the probability distribution – and in particular its tails – and therewith the probability of occurrence of extreme forces, is not known (as k only describes the second-order moment of the velocity fluctuations). Thirdly, the usual boundary value for the near-bed value of k is: $k \propto u_*^2$. So using this k in a stability parameter will effectively yield the classical Shields parameter without turbulence effects. And this is what we wanted to avoid in the first place, as damage will be underestimated at places with a high turbulence intensity. The latter problem can be solved by using velocity sources from higher up in the flow (Jongeling *et al.*, 2003, use this method). The problem with using velocity sources away from the bed, however, is that the main (quasi-steady) forces are determined by the flow velocity very close to the stones, so it appears that velocities from higher levels in the water column cannot be used.

Given the above, there seem to be many problems with using the RANS output. However, when trying to find a rationale for using velocity sources away from the bed, which would solve the third problem, one also finds that the second problem mentioned above is addressed, making the use of a RANS model seem possible. This rationale is given next.

Why use non-local parameters?

Only near-bed velocities cause the quasi-steady forces on bed material. Therefore it does not seem correct to use velocities from higher up in the flow. However, it has just been mentioned that using k obtained from a k - ε model at the grid point nearest to the bed will give a trivial answer that does not solve the problem of explicitly modelling the effect of turbulent fluctuations. But if we regard another previously mentioned ‘problem’ – that k only represents the second-order moments of the velocity components – it becomes possible to justify the use of values of k and \bar{u} from other positions in the vertical. The velocities at higher levels in the flow, where the length scale of the turbulence usually is of the order of the water depth, can determine the higher-order moments of the near-bed velocity fluctuations. A large length scale at a certain elevation implies that the turbulence structures from that elevation will have a larger chance of reaching the bed sporadically, bringing velocities of the order of magnitude of the velocity at that depth to the bed. These fluctuations may be rare and intermittent, and therefore hardly alter the intensity (i.e. second order moment of

u') of the turbulence near the bed, while the probability of extreme forces is increased. This makes it plausible that parameters at different depths can – or rather should – be used to determine the extreme values of u near the bed.

In light of the above it was decided to develop a stability model that is based on the output of a hydrodynamic RANS model with a k - ε turbulence closure. This model is developed in the next section.

8.4 New model for using RANS output

In this section possible ways to use the computed turbulence parameters in the estimation of damage are discussed. A new model is developed which estimates a representative ‘maximum velocity’ near the bed, and hence the ‘maximum’ quasi-steady force on the bed. An important new element is that the relative importance of velocity sources above the bed is determined using the relative length scale of the turbulence.

8.4.1 Incorporating the length-scale of the turbulence

A simple physical argument is used to determine a way to incorporate the turbulence length scale in the stability parameter. In chapter 7 it is shown that both in uniform flows and in BFS flows large-scale structures with increased u with a vertical size of the order of the water depth are present at the time of entrainment of the stone. This is a rationale for using velocity sources from the whole water column for estimating the quasi-steady forces. Figure 8.1 shows a simplified flow structure. This is used to obtain a relation between the computed parameters at a certain elevation and the (extreme) velocities that are subsequently caused near the bed.

If we assume that the large-scale vertical velocity fluctuation at height y above the bed is proportional to \sqrt{k} , and has a certain horizontal length scale, L_H , and we further assume that this is part of a large rolling structure with a vertical size equal to $2y$, then conservation of mass ($yu'_b \approx \frac{1}{2}L_H v'$) leads to the approximate relation:

$$u'_b \propto \frac{L_H}{y} \sqrt{k} \quad . \quad (8.6)$$

As the structure also transports the mean momentum to the bed, we pose that the following velocity estimate could be used in a stability parameter:

$$u_b \propto \frac{L_H}{y} (\bar{u} + \alpha \sqrt{k}) \quad . \quad (8.7)$$

Here $\bar{u} + \alpha \sqrt{k}$ is an estimate of the temporal ‘maximum’ of the local velocity, consisting of the mean velocity plus a few times the standard deviation, as expressed in the term

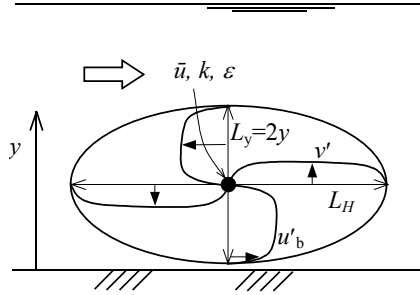


Figure 8.1: Model of large-scale eddy that causes damage.

$\alpha\sqrt{k}$, in which α is a calibration factor (see 8.4.3). As these ‘maximum’ velocities only sporadically reach the bed (they do not influence k near the bed), the spatial maximum over the depth of this temporal ‘maximum’ is taken to represent the extreme velocity near the bed governing the low-mobility entrainment:

$$u_{b,\max} \propto \max \left[\frac{L_H}{y} \left(\bar{u} + \alpha\sqrt{k} \right) \right] . \quad (8.8)$$

The horizontal length scale is dependent on the kind of turbulence that is present.

In addition it is necessary to estimate the intensity of the *large-scale* fluctuations, as only these fluctuations will reach the bed. For instance, it is not likely that a beginning mixing layer – that gives an intense small peak in the turbulence intensity – influences the stability of the bed. This situation is present at the first measurement location at the gate configuration (described in the next section, figure 8.5). In case we use a k - ϵ model, we do not obtain information in the spectral domain, but we do obtain spatial information. We can argue that if a large-scale structure exists at a certain height, it will influence the turbulence intensities at all places surrounding this height that are not more than half its length-scale away from this point. Therefore, for the estimate of the large-scale intensity at height y we take the mean value of the turbulence intensities over a height between $y \pm L_H/2$ to be the turbulence sources from that height that influence bed stability. In other words: the vertical turbulence intensity profile will be filtered by taking the moving average over the (variable) width of L_H , written as $\langle \dots \rangle_{L_H}$.

After this filtering operation we multiply the resulting ‘maximum velocity’ with L_H/y in order to obtain the influence of the turbulence at height y on the bed. As a final step the velocity source causing the largest ‘maximum velocity’ near the bed is taken as the velocity that governs the damage to the bed. Therefore the

(vertical spatial) maximum of the (temporal) ‘maximum velocity’ $(\bar{u} + \alpha\sqrt{k_u})L_H/y$ above the bed is chosen as the velocity to be used in the numerator of the new stability parameter:

$$\Psi_{LH} = \frac{\max \left[\left\langle \bar{u} + \alpha\sqrt{k} \right\rangle_{LH} \frac{L_H}{y} \right]^2}{\Delta g d} \quad (8.9)$$

Next we need an expression for L_H .

8.4.2 Determination of the length scale

Two methods were tried to obtain the appropriate length scale of the turbulence, L_H . These are described next.

Using the dissipation length, L_ε

From the calculated parameters k and ε , the dissipation length scale:

$$L_\varepsilon = \frac{k^{\frac{3}{2}}}{\varepsilon} \quad , \quad (8.10)$$

can be obtained. This length scale might be used as L_H in eq. (8.9). It is calculated by the flow model, so it is potentially a good length scale to use. In order to check whether this length scale can be used, it will be compared to a measured length scale. We will check if it can be connected to the measured integral streamwise length scale, which is defined as (Nezu & Nakagawa, 1993):

$$L_x = u_c \int_0^\infty \rho_{uu}(\tau) d\tau \quad , \quad (8.11)$$

where $\rho_{uu}(\tau)$ is the auto covariance of u , τ is the time lag, and u_c the convection velocity of the flow structures. This can be determined from measurements. If an inertial subrange applies, the large-scale L_x and small-scale L_ε are related by (Nezu & Nakagawa, 1993):

$$\frac{L_x}{L_\varepsilon} = K \frac{\sigma(u)}{\sqrt{k}} \quad , \quad (8.12)$$

where $K \approx 0.691 + 3.98/\sqrt{Re_L}$, and $Re_L = \sigma(u)L_x/\nu$. With use of the relations for $\sigma(u_i)$ in eq. (2.2) and the further assumption that $Re_L \rightarrow \infty$ for prototype flows, the relation becomes $L_x/L_\varepsilon \approx 0.73$. This would enable us to compare the measured and calculated length scales of turbulence fluctuations. However, L_x as defined in eq. (8.11) is not always easy to determine from measurements. Sometimes the autocorrelation does not go to zero for longer time lags, and the spectrum at the low-frequency range – which can also be used to determine ρ_{uu} – is very noisy. A second inaccuracy is the

use of Taylor's hypothesis for the conversion of the temporal autocorrelation to the spatial autocorrelation, which is not precise for the large-scale motion. Therefore we will use the following rough approximation:

$$L_x \approx u_c \tau_{\rho_{uu}=0.5} \quad , \quad (8.13)$$

where the length scale is determined from the measurements by taking the time lowest lag where $\rho_{uu} = 0.5$, and we assume that this length scale is proportional to the length scale obtained using (8.11).

According to the above, L_ε and L_x are proportional to each other. This only holds if an inertial subrange applies, which is not always true in non-uniform flows. Therefore these will be compared in section 8.5.2, after the measurements and calculations are presented. This comparison will lead to the conclusion that the calculated L_ε does not resemble L_x at all. The use of the calculated length scale is therefore abandoned, and the use of another length is discussed next.

Using the Bakhmetev mixing length, L_m

As the use of the calculated length scale L_ε is aborted, another length scale is used. This is the mixing length according to the Bakhmetev distribution, which is not dependent on the calculated turbulence field. This distribution is derived for a uniform open-channel flow but will be used for all flows. It reads:

$$L_m = \kappa h \gamma \sqrt{1 - \gamma} \quad , \quad (8.14)$$

where $\gamma = y/h$. As we use this length scale distribution for non-uniform flows, it is more an estimate of the largest possible structure due to the geometrical constraints of the bed and the free surface than an exact relation for the (integral) length scale. If we make this length scale dimensionless with the height according to eq. (8.6) we obtain the simple relation:

$$\frac{L_m}{y} = \kappa \sqrt{1 - \gamma} \quad . \quad (8.15)$$

This has a maximum near the bed, so when this is used in eq. (8.9) it corresponds to fully taking into account the velocity sources near the bed, with a decay towards the free surface. Intuitively this seems a very reasonable weighting function for the velocity sources.

8.4.3 Inclusion of Turbulence Wall Pressures

The present new stability model still does not explicitly incorporate the TWP forces [the contribution of the acceleration a' in eq. (8.1)]. However, the value of α in eq. (8.9) of 6, as found by Jongeling *et al.* (2003) (which will hereafter turn out to be

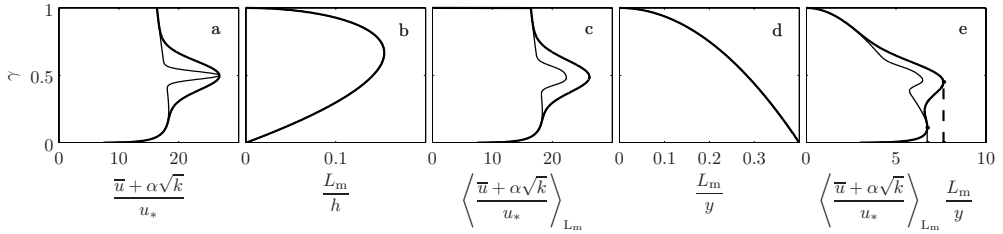


Figure 8.2: a) Vertical ‘maximum velocity’ distribution according to eqs. (2.1) and (2.2) with a Gaussian bump of two sizes, b) Bakhmetev mixing length. c) Estimate of the large-scale ‘maximum’ velocity. d) Relative influence of velocity at a certain elevation. e) The estimated influence of the large-scale turbulence on the bed. The vertical lines indicate the two maximum values.

the optimal value in the present model as well) is very high. This might be due to the fact that the model implicitly incorporates the effect of TWP. As the TWP are only efficient if they have a spatial dimension of the order of the stone diameter, only velocity sources close to the bed will lead to large TWP forces. Therefore only turbulence sources near the bed should be used. A model like the one of Uittenbogaard *et al.* (1998, see chapter 2) could be used to incorporate the effect of TWP explicitly, in addition to a model for the quasi-steady forces. On the other hand, it was observed that the high-intensity high-frequency pressure fluctuations can coincide with the (low-frequency) events with high longitudinal velocity (figure 5.10). This leads to an indirect dependence of TWP on velocity sources over the whole water column, increasing the erosive capacity of a sweep with a certain velocity. So for now the TWP are indirectly accounted for by an increased value of α in the stability parameter.

The additional force due to a stationary acceleration in the flow in the numerator of Ψ_{tot} is not investigated in this chapter, as the available measurement data do not exhibit large stationary accelerations, so they cannot be used to test the approach.

8.4.4 The new stability parameter

As the Bakhmetev mixing length is chosen as the length scale to use, the new stability parameter is formulated as:

$$\Psi_{L_m} = \frac{\max \left[\left\langle \bar{u} + \alpha \sqrt{k} \right\rangle_{L_m} \frac{L_m}{y} \right]^2}{\Delta g d} . \quad (8.16)$$

The different steps in finding the dominant velocity near the bed using this model are illustrated in figure 8.2 for a uniform flow with an extra turbulence source at mid depth ($\gamma=0.5$).

8.5 Performance of the methods

Two methods for the description and prediction of flow attack on bed protections (i.e. the numerator of Ψ_{tot}) are checked against measurements in the following sections. These are:

- An existing parameter Ψ_{WL} : this uses $\bar{u} + \alpha\sqrt{k}$, averaged over a certain interval above the bed, eq. (2.32) (Jongeling *et al.*, 2003).
- The present parameter Ψ_{LM} : this uses the maximum over the depth of the local values of $(\bar{u} + \alpha\sqrt{k_u})$ weighted with the relative distance L_m/y [eq. (8.16)].

The classical stability parameter Ψ , which assumes that the turbulence velocity fluctuations are proportional to the shear velocity, eq. (2.14) (Shields, 1936) was not originally meant for non-uniform flows, but it is used as reference.

In the measurements presented in this thesis the flow field and its influence on a few single stones were studied. As all stones have different characteristics, measurements of bulk entrainment are needed in order to find a quantitatively valid relation between a flow parameter and the stone entrainment rate; preferably for a range of flow configurations with a large range of relative turbulence intensities and types of turbulence.

8.5.1 Data used

In order to check the possible approaches for predicting damage outlined above, data are used of measured entrainment and velocities at WL|Delft Hydraulics (Jongeling *et al.*, 2003, next: WL) – of a number of different configurations – and measurements by De Gunst (1999, next: DG) of a backward-facing step (BFS). All configurations have no variations in the transversal direction, which corresponds to the way the entrainment rate is measured. Furthermore, both free turbulence and wall turbulence are present with various values of the relative turbulence intensity. The following nine configurations are used (see also figure 8.3):

- 1–3: Uniform flow, $h=0.25, 0.375$ and 0.50 m (WL).
- 4: Long sill, 1:3 lee-side, $h= 0.375$ m (WL).
- 5–6: Increased large-scale turbulence, $Q=83.4$ and 68.4 l/s (WL).
- 7: Short sill, 1:8 lee-side (WL).
- 8: Gate (WL).
- 9: Backward-facing step (DG).

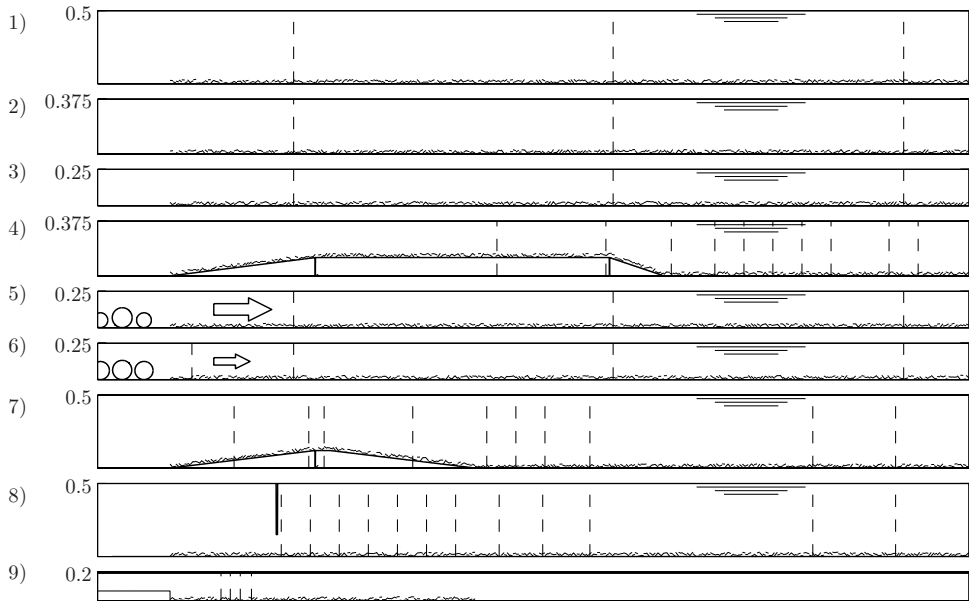


Figure 8.3: Longitudinal sections of the geometries used. Dashed lines are velocity-measurement locations

Velocity profiles (mean and fluctuating), as well as stone entrainment were measured for these configurations. The bed had a low mobility.

As Jongeling *et al.* (2003) calculated the flow characteristics of some of these configurations with a numerical model (CFX) using the k - ϵ turbulence model, the suitability of using a RANS model for determining stone stability can be evaluated.

Next we briefly describe the data of the different measurements and calculations.

Velocity data

WL. The u and v velocities were measured using a two-component (x, y), forward scatter, 6 mW laser-doppler velocimeter (LDV). An electro-magnetic flow meter (EMF) was placed above the small measuring volume of the LDV, giving the x and z velocity components. As the measuring volume of the EMF is larger, the fluctuating velocities were underestimated. Therefore $\sigma(w)$ was corrected using the ratio between $\sigma(u)$ measured by the LDV and the EMF. The sampling frequency was 100 Hz.

The velocities were calculated using the commercial CFX 4 package. This uses a collocated grid and combined Cartesian and σ grid cells. The free surface option was used for all computations, except for the gate where it did not give stable results.

The long sill was 5 mm too low, compared to the measurements. In appendix E the configurations are briefly explained. The ways in which the measurements were processed or corrected for the present use are briefly described as well. Jongeling *et al.* (2003) describe the measurements elaborately.

De Gunst. A rigid lid was put on the water surface. Only the u and v velocity components were measured, using an LDV similar to the one used by Jongeling *et al.* The sampling frequency was 100 Hz. The data were obtained from the graphs in the report. The velocity was measured at a lower discharge (Q_{meas}) than the discharge at which the entrainment was measured (Q_E). Therefore the mean velocities were multiplied by the correction factor Q_E/Q_{meas} and the turbulence kinetic energy by Q_E^2/Q_{meas}^2 .

Stone data

The specifications of the stones that were used during the WL and DG experiments are given in table 8.1.

The determination of the entrainment rates from the measurements is described next. First the general approach is discussed, then the peculiarities that were dealt with for both measurement series.

Research	d_{n50} [mm]	d_{n85}/d_{n15} [-]	Δ [-]	strip width [mm]
WL	6.2	1.51	1.72	100
DG	10.8	1.32	1.70	100

Table 8.1: Stone characteristics of experiments.

Determination of E

In physical models damage to bed protections is usually measured by applying the stones in the protection layer in transversely oriented strips with uniformly coloured stones. The stones of a certain colour that leave their strip of origin during a certain time-span stand out on the differently coloured background and can easily be counted. A first estimate of the average entrainment rate in a strip, E_{meas} , is obtained by:

$$E_{\text{meas}} = \frac{nd^3}{AT} \quad , \quad (8.17)$$

where n is the number of stones that have been removed from the strip, A is the area of the strip, and T is the duration of the measurement.

These kinds of measurements can be used to obtain the required relation between the stability parameter Ψ_{tot} and the entrainment parameter Φ_E . As the mobility of the bed and the hydrodynamic load both change in the flow direction, one configuration with several strips thus yields several measurements of the required relation.

However, the local entrainment rate is not determined exactly from these measurements, as some entrained stones will deposit in their strip of origin. This will lead to an underestimation – that turns out to be significant – of the entrainment rate. This underestimation should be corrected for in order to end up with a quantity that can be compared between different investigations. In appendix D a method is derived which can be used for this. Input to the method is the probability distribution of the displacement lengths of the stones. Using this method for the DG data, where also the displacement lengths were measured, a corrected entrainment of $E_{\text{tot}} = 1.93E_{\text{meas}}$ is found for the DG data. Assuming that the displacement lengths scale with d gives a correction for the WL data – where the strips were wider compared to the stone diameter – of $E_{\text{tot}} = 2.83E_{\text{meas}}$. These corrected entrainment rates are used in this chapter. At places where the entrainment rate was low the entrainment rate was averaged over a number of adjacent strips in order to reduce the measurement error. See appendix E for more details of the measurements.

WL. For the cases (see figure 8.3) of the gate (8), increased turbulence (5–6), and uniform flow configurations (1–3) the total number of entrained stones was measured at several times. The entrainment in the first period was a few times larger than in the periods afterwards. This indicates that water-working occurred in this period (see chapter 3). The real ‘strength’ of the bed protection can only be evaluated after water-working. Therefore the data of the first period were not used in the cases where water-working was observed. For the other configurations the total number of entrained stones was measured only once. Here this total is simply used.

The number of displaced stones was measured three times for the gate configuration (8). At certain strips, the total amount of entrained stones had decreased significantly compared to the previous periods. This can be explained by the way that E was determined. The strips with stones had seven different colours that were repeated. The entrainment was determined by attributing the displaced stones of a certain colour to the first strip upstream of that colour. This means that if stones pass the following strip with the same colour, this can lead to a decrease in the observed number of stones that has been entrained from the original strip. Therefore the last measurement for the gate configuration was omitted.

Also the difference $E-D$ was measured (denoted as the number of stones per strip per measurement) for all configurations. As every stone that is entrained must deposit somewhere, the integral $\int_0^\infty (E-D) dx$ must become zero. For an unknown reason this was not the case for the long sill, the number of deposited stones was roughly

6% higher than the number of entrained stones. As the results did seem realistic otherwise, the measured E was used nevertheless.

De Gunst. Although the report is not very clear on this, DG probably tabulated the number of stones that arrived in a strip. Therefore the entrainment rate had to be estimated by assuming a fixed displacement length distribution for the displaced stones, viz. 80% of the stones displaces over a distance of one strip and 20% over a distance of two strips, based on the observed displacement lengths.

8.5.2 Comparing measured and calculated flow fields

Some of the calculated flow fields are compared to the measurements.

The uniform-flow field was calculated well by the CFX program. The vertical profiles of both the measured \bar{u} and k , eqs. (2.1) and (2.2), and the calculated values were very similar (not shown). Some deviations are present in the measured profiles due to the side-wall influence. We now focus on the ability of the model to calculate the non-uniform flow fields.

Figures 8.4 to 8.6 depict the calculated and measured profiles of \bar{u} and k for the long sill (case 4), gate (case 8), and short sill (case 7) as examples of the results of the k - ε model. Also the calculated length scales L_ε are compared to two estimates of the integral length scale L_x from measurements [see eq. (8.13)]: one uses $u_c = \bar{u}(y)$ (third panel in the figures), and one uses $u_c = \langle \bar{u} \rangle_h$ (bottom panels).

Long sill: Figure 8.4 shows the flow profiles for the long sill. The mean flow is calculated well, the turbulence intensity is reproduced reasonably. The turbulence intensity in the mixing layer is underestimated, and the maximum is situated too low. This leads to errors of the local ‘maximum’ velocity, $\bar{u} + 6\sqrt{k}$, of roughly $\pm 30\%$, see figure 8.7. A value of $\alpha=6$ is used, obtained from Jongeling *et al.* (2003). The circles in this figure denote the positions of the measurements 1 m downstream of the sill and below the level of the sill crest. The diamonds show a comparison of the maximum values per longitudinal location, in order to see whether, besides a shift of the maximum value, also the magnitude of the vertical maximum is underpredicted by the calculation. It can be seen that the underestimation of the values cannot be explained completely by the shift of the maximum, but the underestimation of the maximum is less than when the velocity is compared at fixed locations.

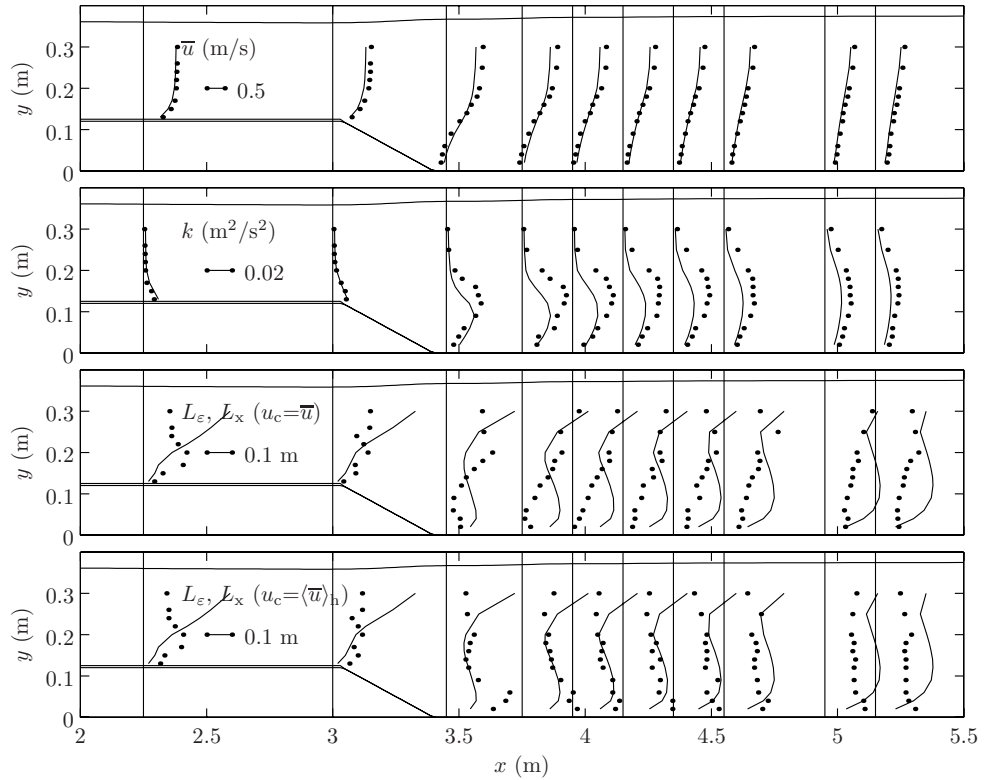


Figure 8.4: Profiles of calculated (lines) and measured (dots) flow parameters over the long sill. The lower two panels show the length scales determined from the calculations (L_ε , dots) and from the measurements (L_x , lines).

Gate: Figure 8.5 shows the flow profiles for the gate configuration. The mean flow is simulated reasonably, although the mixing layer widens more quickly than measured. The turbulence intensity is not calculated very well. The origin of this error lies just upstream of the gate (not visible in figure 8.5). This is an acceleration area with almost potential-flow-like behaviour, so no turbulence production is expected here. However, in the acceleration area a high production of turbulence is calculated. Therefore, at the first measurement transect the turbulence profile is already completely wrong. This leads to an overestimation of the local ‘maximum’ velocity by more than 100%, see figure 8.7. This problem might be solved by applying a different grid upstream of the gate. The circles in figure 8.7 denote the measurement locations at positions where $y < 0.15$ m and $x < 1.3$ m. The diamonds denote the measurement locations where $y > 0.15$ m and $x < 2$ m.

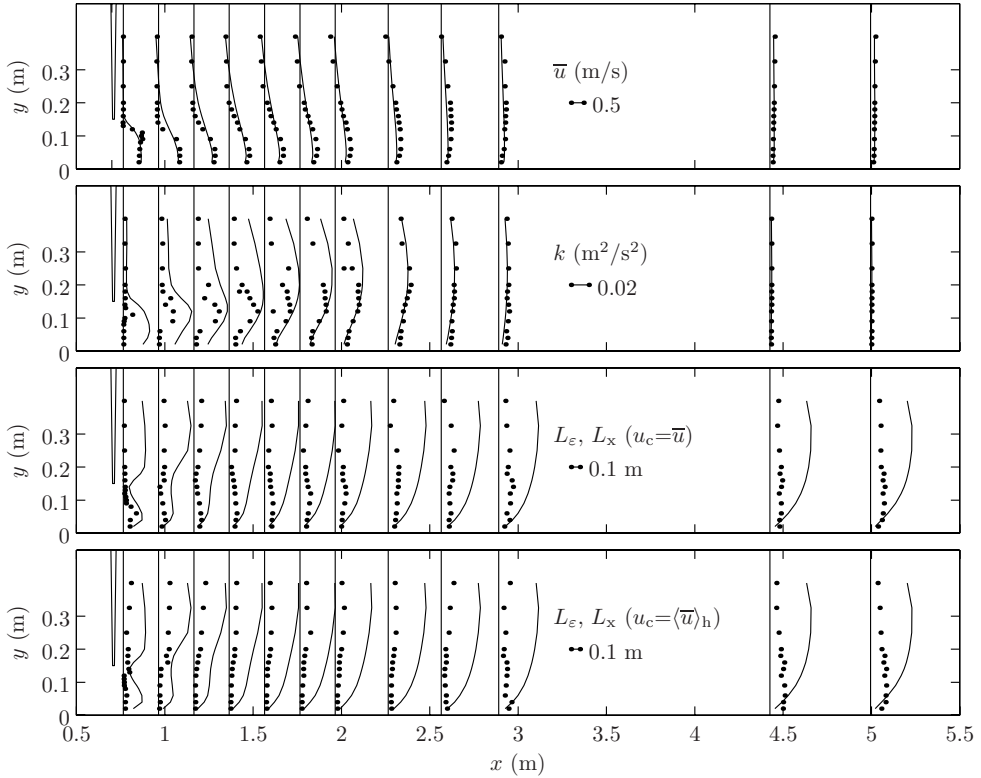


Figure 8.5: Profiles of calculated (lines) and measured (dots) flow parameters at gate. The lower two panels show the length scales determined from the calculations (L_ε , dots) and from the measurements (L_x , lines).

Short sill: This simulation gives very good results (figure 8.6), both of the mean flow and of the turbulence intensity. This leads to values of the local ‘maximum’ velocity with an error within $\pm 10\%$, see figure 8.7. The overestimated values with the circles are the lowest points of the transects on the sill, and are probably caused by the boundary condition. The underestimated values with the squares are in the deceleration area downstream of the sill.

Length scales: The calculated (L_ε) and measured (L_x) length scales are presented in the lower two panels of figures 8.4 to 8.6. The calculated length scale is equal in both panels, the measured length scale is determined in two manners, as indicated on the graphs (see section 8.4.2). The measured and calculated length scales do not coincide well for all configurations. The two length scales should be proportional to

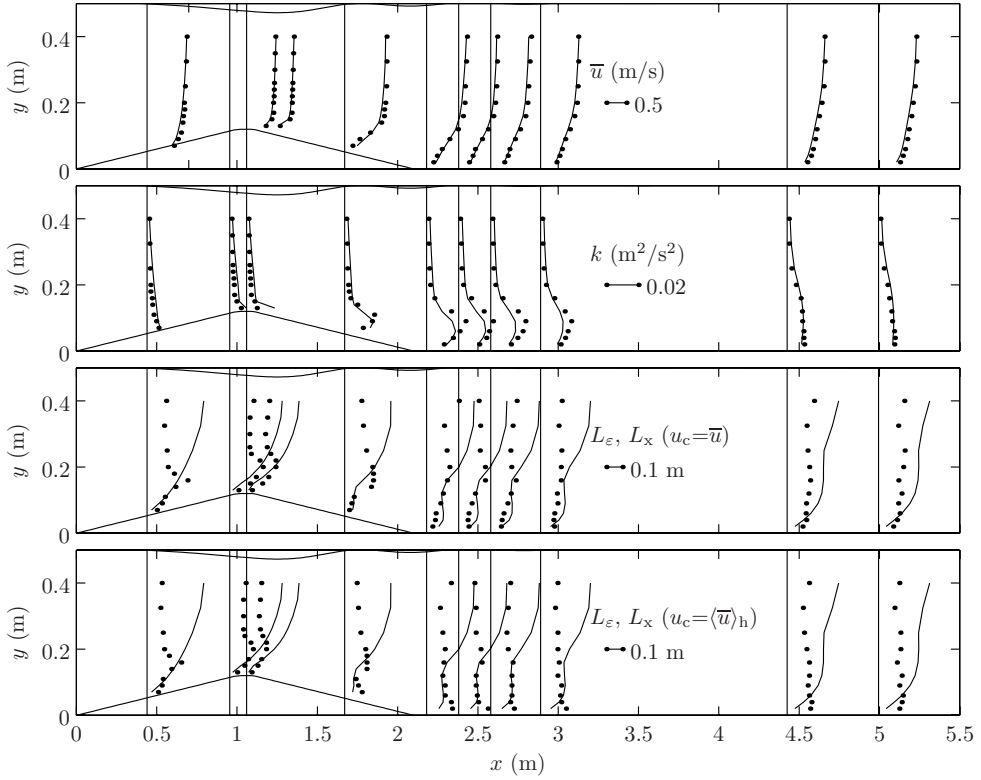


Figure 8.6: Profiles of calculated (lines) and measured (dots) flow parameters over the short sill. The lower two panels show the length scales determined from the calculations (L_ε , dots) and from the measurements (L_x , lines).

each other, but the vertical profiles do not have the same shape. The measured and calculated length scales agree reasonably only for the long sill, when using the depth-averaged velocity as the convection velocity in eq. 8.13 (see lowest panel in figure 8.4). Hence L_ε is not used in the formulation of the new stability parameter.

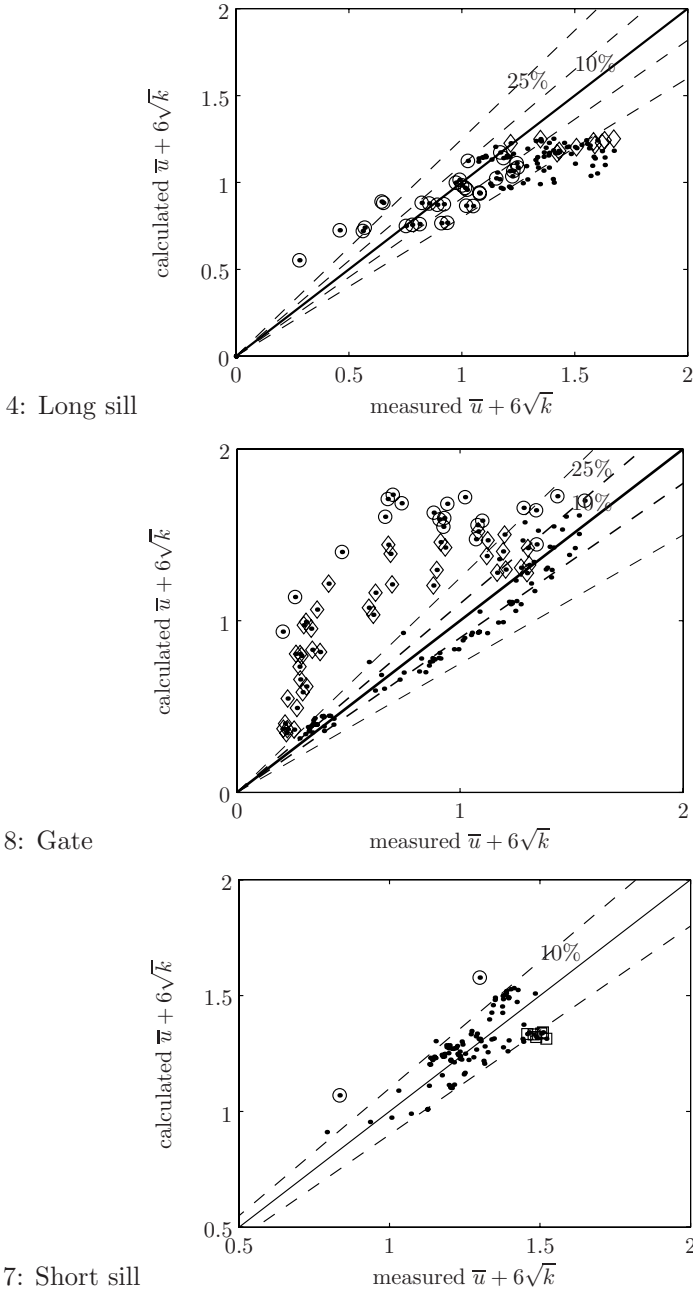


Figure 8.7: Comparison of measured and calculated local $\bar{u} + 6\sqrt{k}$ for long sill, gate and short sill.

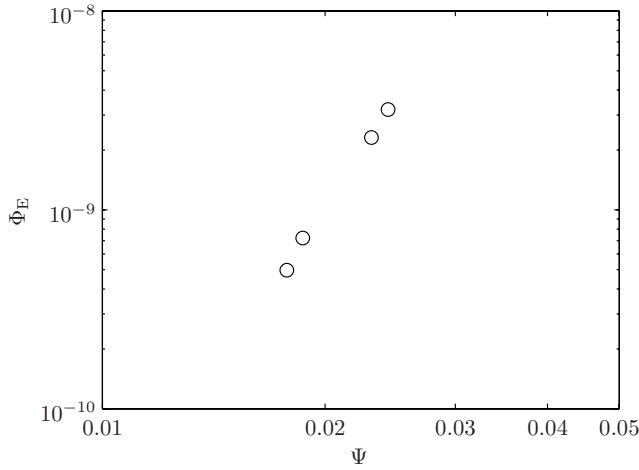


Figure 8.8: Measured entrainment under uniform flow (WL) as a function of Ψ .

8.5.3 Entrainment under uniform flow

First the entrainment curve from the uniform flow experiments (WL) will be established. The entrainment rate E was determined for all strips as explained previously and corrected following appendix D. In order to get a reliable estimate of E all these rates had to be averaged over a number of strips (this is possible as the flow is nearly uniform). For the experiment with $h=25$ cm the average entrainment was determined over the first and the last 28 strips. For the other two uniform-flow experiments E was averaged over all 56 strips, as E was lower. The shear stresses¹ for the first experiment were obtained from the CFX calculations. The shear stresses for the other two measurements were obtained from the integrated log-law – eq. (2.1) – and the measured Q . The resulting E – shown in its dimensionless form in figure 8.8 – has a strong dependence on Ψ , comparable to the Paintal curve, eq. (2.18), for the sediment transport rate.

In figure 8.9 the entrainment parameter is evaluated against the measured values of the various stability parameters Ψ , Ψ_{WL} , and Ψ_{Lm} . The position at the downstream end of the long sill is added in the comparison, as the flow there is nearly uniform as well. The shear stress (needed to evaluate Ψ) was determined using the point closest to the bed and the law-of-the-wall. It can be seen that the entrainment parameter is correlated to all three stability parameters in a similar way for uniform flow. Only the

¹The flow velocity is slightly increasing due to the horizontal bed, therefore multiple ‘measurements’ can be obtained from one uniform flow configuration.

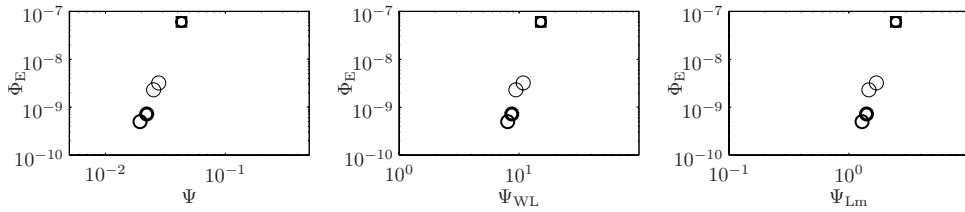


Figure 8.9: Measured entrainment under uniform flow (WL, cases 1–3) as a function of Ψ , Ψ_{WL} , and Ψ_{Lm} . A thicker circle denotes a larger h . The square marker indicates the flow on the long sill (case 4).

absolute value of the parameters is different due to the different implementation of the velocities in the different stability parameters. It appears that all stability parameters describe entrainment (and hence damage) of stones well for uniform flow – at least for the present range of the relative depth, h/d that was used. An examination of the influence of h/d is given next.

8.5.4 Entrainment under non-uniform flow

As the calculated velocity and turbulence kinetic energy are only accurate for some cases, and are not available for all cases, we will use the Ψ_{WL} or Ψ_{Lm} based on *measured* flow properties for comparison to observed values of Φ_E for the various (non-uniform) flows. This will show which stability parameter is suited best for the prediction of entrainment of bed material, and hence damage to bed protections.

First, for reference, the plot of the Shields parameter, Ψ , against the entrainment parameter for all cases is shown in figure 8.10. The shear stress was evaluated using the first velocity point near the bed and the law-of-the-wall. Note the wide range of Ψ values, down to extremely low values (10^{-5}) for which no motion would be expected in uniform flow. It is clear that no correlation exists between the two parameters. As the points with a high turbulence intensity give a large entrainment, but have a low mean shear stress, we can see a large number of points with a high Φ_E and a low Ψ . Clearly there is no sensible relation between Ψ and Φ_E for this variety of flow conditions.

Next we consider the possible relation between Ψ_{WL} and Φ_E , the top plot in figure 8.11. These variables are correlated, although still a large amount of scatter is present. The points with markers which have a (partly) circular shape can be regarded to represent rather uniform flow cases (i.e. the flow on the long sill and far away from the disturbance is regarded as almost uniform), although some cases are still slightly non-uniform. It is clear that these points give a reasonable power law. The points of

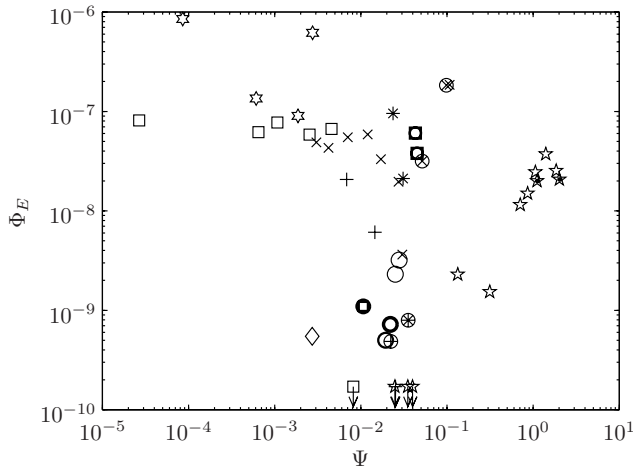


Figure 8.10: Measured Φ_E versus the measured Ψ for a variety of flow conditions. For legend see next figure. The markers with arrows have $\Phi_E=0$.

the flow downstream of the long sill and just downstream of the large stones in the increased turbulence case are still on the high side of the curve. In these cases the entrainment increases for decreasing Ψ_{WL} . This indicates that the turbulence is still not incorporated very well.

Finally the outcome of the new method is shown in the bottom panel of figure 8.11. A few values for α were tried, but $\alpha=6$ yielded the best collapse of data. Note that no further fit coefficients are used in the determination of the maximum velocity used to predict the damage. It can be seen that the points with high turbulence intensity that were relatively far on the left side of the data cloud in the top panel are now situated more in the neighbourhood of the other points, although the scatter is still considerable.

It seems that the new way of determining the QSF is slightly better than the WL-method. It also turns out that the DG data (BFS, case 9), which were also meant to be representative of ‘initiation of movement’, actually had a larger entrainment parameter. This shows that using a subjective definition of initiation of movement will not yield consistent design criteria. As the correction of the entrainment rate is derived for uniform flow, the estimated entrainment rate might be slightly different. However, without correction the relative difference between the DG and WL entrainment rates would even be larger.

A tentative power law has been drawn more or less as an upper envelope of the

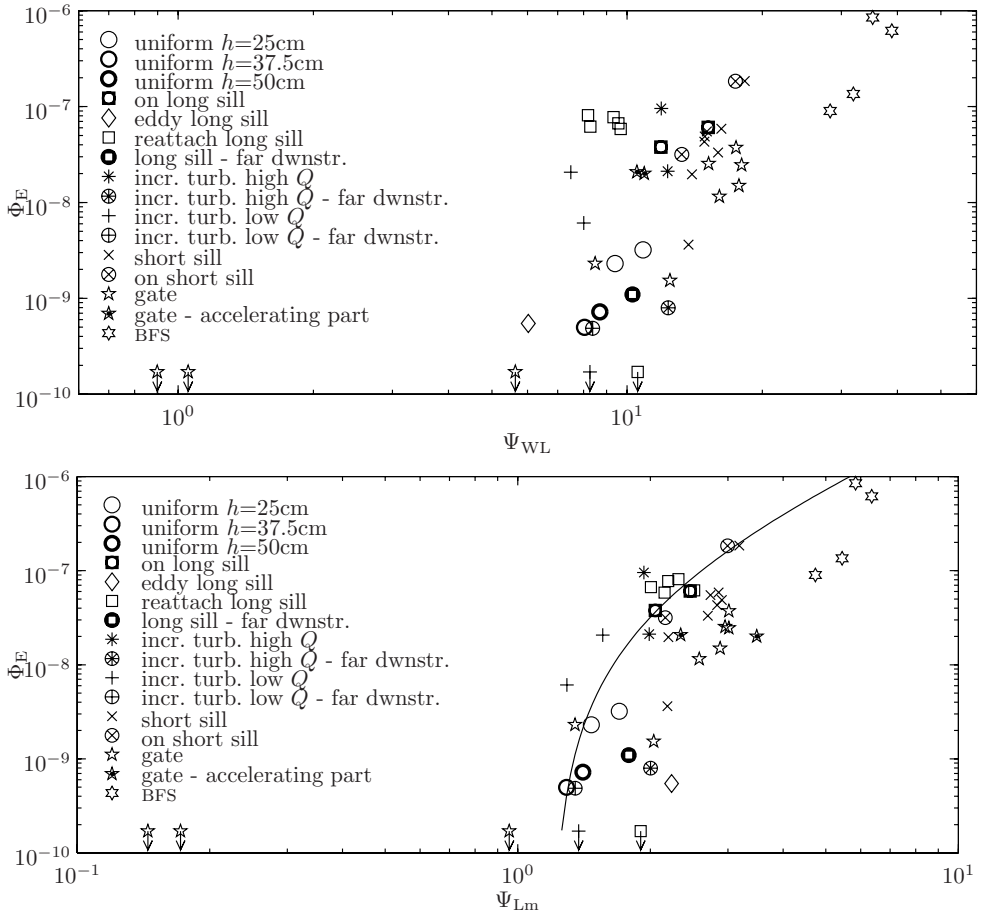


Figure 8.11: Top: measured Φ_E versus the measured Ψ_{WL} for a variety of flow conditions. Bottom: measured Φ_E versus the measured Ψ_{Lm} for the same flow conditions.

data points for the new stability parameter in figure 8.11:

$$\Phi_E = \Phi_{E,0} (\Psi_{Lm} - \Psi_{Lm,c})^p, \text{ for } \Psi_{Lm,c} < \Psi_{Lm} < 7 \quad , \quad (8.18)$$

with

$$\Phi_{E,0} \approx 5 \cdot 10^{-8} \quad ,$$

$$\Psi_{Lm,c} \approx 1.2 \quad ,$$

$$p \approx 2 \quad .$$

The coefficient $\Phi_{E,0}$, the threshold value $\Psi_{Lm,c}$, and the exponent p represent a conservative fit through the present data. As they have no clear physical meaning they cannot be used outside the present range of Ψ_{Lm} . Still this gives the required relation between a stability parameter (including turbulence effects) and the entrainment rate. This can be used for the (preliminary) design of bed protections. Further validation of the technique and the values is still advised.

8.6 Evaluation of new approach

The *measured* values of Ψ_{Lm} and Φ_E show a clear correlation, although the scatter is still large.

A plot of the *calculated* Ψ_{Lm} and the measured Φ_E is given in figure 8.12. It shows that the calculated values of Ψ_{Lm} are still correlated to Φ_E . The scatter has obviously increased compared to figure 8.11 (bottom plot) and is larger than the range of Ψ_{Lm} over which Φ_E rises.

In section 8.5.2 some calculations of the ‘maximum velocity’ $\bar{u} + \alpha\sqrt{k}$ were evaluated. The best computation gave local ‘maximum velocities’ that differed less than ten percent from the measured ones. This means that – with inclusions of the uncertainty in the ratio $\sigma(u)/\sqrt{k}$ – the best model results will yield results with an accuracy of roughly 15%. This is equivalent to an accuracy in the stability parameter of about 30%.

Despite the enhanced scatter in the relation between Ψ_{Lm} and Φ_E in figure 8.12, due to shortcomings of the applied computational models, it is believed that the calculations – if properly executed – can be used to obtain a fair estimate of the stability of a bed protection. This stability can for instance be plotted as the safety factor $\Psi_{Lm,c}/\Psi_{Lm}(x, y)$, which will have to be sufficiently larger than one at all positions on the bed protection. It will thus be possible to obtain an estimate of the location, size and shape of possibly damaged areas. The exact location cannot be determined, as the size of a mixing layer is not always predicted well.

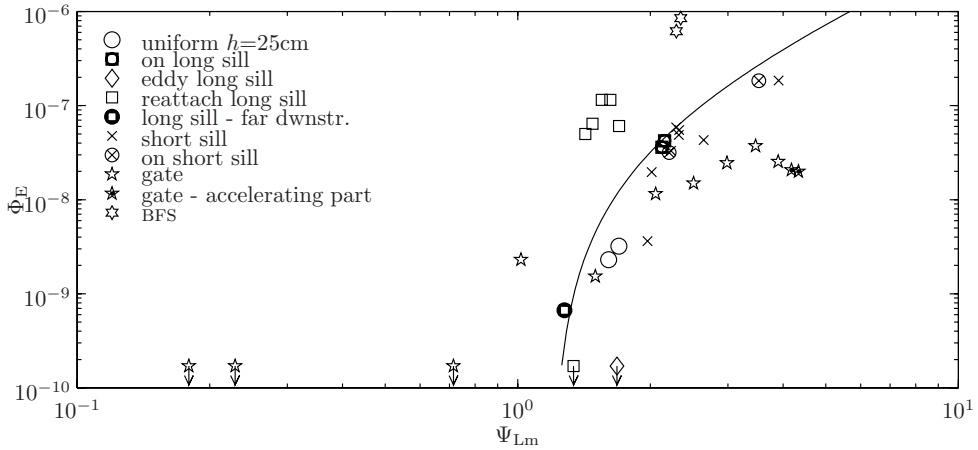


Figure 8.12: Measured Φ_E versus the *calculated* Ψ_{Lm} for a range of flow conditions.

This kind of information can also be used to predict a stone size that will be stable, d_{optimum} , using a safety factor γ .

$$d_{\text{optimum}} = \gamma \frac{\Psi_{Lm}}{\Psi_{Lm,c}} d_{\text{design}}$$

where d_{design} is the diameter of the top layer of stone in the (preliminary) design. Based on the accuracy of the computational models, the safety factor has to be at least about 1.5. Note that if the stone size is changed, the calculation should be executed again, as a new stone diameter will also change the flow pattern. Jongeling *et al.* (2003) state that one iteration is sufficient.

When we further regard the steep slope of the entrainment curve then we must come to the conclusion that the ‘gradual damage’ approach using eq. (8.4) is not yet feasible. The approach using the transport rate of the stones in eq. (2.15) will be even less feasible, as it incorporates the displacement of the stones, which introduces even more uncertainty in the process.

If the calculation accuracy increases, however, the gradual stability approach can be applied with increasing reliability. Care must be taken with the implementation of the grid and the boundary values of the computational model.

8.6.1 Influence of the relative depth

For uniform flows, the present model and the WL model give different results than the Shields approach for a changing relative depth. This is discussed in this section.

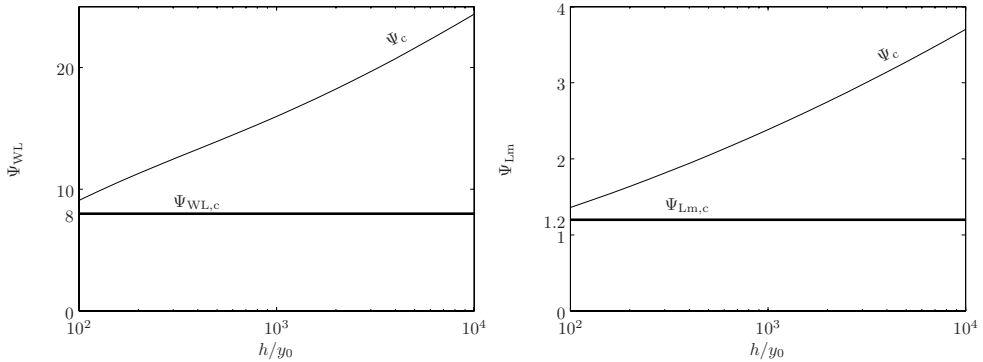


Figure 8.13: Ψ_{WL} (left) and Ψ_{Lm} (right) for uniform flow at critical conditions ($\Psi_c=0.03$, $\Psi_{WL,c}=8$, $\Psi_{Lm,c}=1.2$), as a function of h/y_0 .

The WL parameter Ψ_{WL} can be evaluated analytically. Standard expressions for \bar{u} and $\sigma(u)$ [eqs. (2.1) and (2.2)] are substituted in the expression for Ψ_{WL} , eq. (2.32), using $y_0=d/15$. When switching the order of averaging and squaring² the following ratio for the WL parameter and the Shields parameter can be obtained:

$$\frac{\Psi_{WL}}{\Psi} \approx \left(\frac{1}{\kappa} \left[\ln \left(0.2 \frac{h}{y_0} + 75 \right) - 1 \right] - 2.2\alpha \frac{1}{0.2 + 75 \frac{y_0}{h}} \left[e^{-(0.2 + 75 \frac{y_0}{h})} - 1 \right] \right)^2. \quad (8.19)$$

It turns out that this ratio is a function of the relative depth, h/y_0 . For a realistic range of values of $h/y_0=10^2-10^4$, it increases by a factor of about 2.5. Using eq. (8.19) it is possible to see which value of the WL stability parameter corresponds to the critical value of the Shields parameter, as a function of h/y_0 . This is plotted in figure 8.13 for a value of Ψ_c of 0.03. It can be seen that Ψ_{WL} corresponding to Ψ_c is higher than the critical limit of $\Psi_{WL,c}=8$, proposed by WL. This means that the WL method offers a conservative approach for uniform flow, especially for large water depths (low relative roughness).

The ratio of the newly proposed stability parameter Ψ_{Lm} to the Shields parameter was analysed as well, be it numerically. This ratio shows a very similar trend as the ratio Ψ_{WL}/Ψ , see figure 8.13. So in this respect the WL approach and the present approach are comparable.

It is generally accepted that the critical Shields parameter remains constant for particle Reynolds numbers, Re_* , that are larger than a certain value (≈ 500). However, the present (and WL) model predicts an influence of the relative depth h/d on the critical shear stress for $Re_* \gg 500$. Therefore it seems that the stability

²This gives a negligible difference for the uniform-flow case and enables analytical integration.

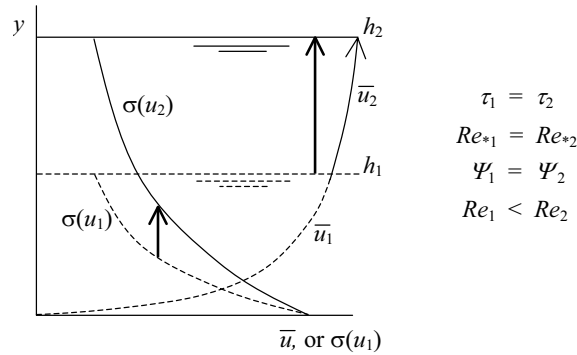


Figure 8.14: Influence of relative depth or global Reynolds number on near-bed turbulence intensity.

parameters are not correct for uniform flows. Note however that the usual assumption that the critical Shields parameter is constant for very high Re_* has not been proven empirically yet. Empirical evidence of these quantities is scarce and imprecise (Buffington & Montgomery, 1997). Furthermore, the critical Shields parameter is notoriously difficult to determine and its value is influenced by the method of determination (Buffington & Montgomery, 1997).

The influence of the relative depth on the new models can be explained as follows. We regard a uniform flow. We slowly increase the water depth, maintaining a constant shear stress by increasing the discharge. In this situation the Shields parameter is constant. As the shear stress remains equal, the velocity profile near the bed remains the same (law of the wall). However, the profile is extended towards the new water surface. This means that the maximum and bulk mean velocity of the flow increase, see figure 8.14. When fluid with high velocity originating from near the water surface is transported to the bed by large-scale turbulence, then the maximum occurring velocity magnitudes near the bed might increase.

The effect of the relative depth is caused by the fact that the value of the turbulence intensity is scaled by the relative depth according to eq. (2.2) (see figure 8.14). Hence at a fixed relative distance from the bed (scaled by d) the magnitude of the fluctuating velocity increases for increasing depth. There is empirical evidence corroborating the above. Examinations of smooth wall flows show an increasing near-bed streamwise turbulence intensity with an increasing global Reynolds number Re (DeGraaff & Eaton, 2000; Jiménez *et al.*, 2004), which is due to extra large-scale velocity modes that appear in the flow. Note that $Re = Re_* \frac{h}{d} \frac{U}{u_*}$ and that $\frac{U}{u_*}$ is an increasing function of $\frac{h}{d}$. Therefore an increasing $\frac{h}{d}$ is equivalent to an increasing Re at a fixed Re_* .

The above is valid when the flow and the turbulence have adjusted to the roughness of the bed protection (i.e. developed turbulence). This occurs after a length of at least 30 water depths. Consequently this will hardly ever be the case for real bed protections, which usually have limited dimensions. Here usually the case of a roughness transition occurs. However, many prototype applications do have a relative depth that is much larger than the largest relative depth that can be realised in a flume. For instance, typical dimensions of an estuary are a velocity of 1 m/s and a depth of 20 m. When gravel of about 5 cm would be applied here, this yields $h/d=400$, compared to a typical $h/d=40$ for flume situations. Therefore, although the uniform flow problem as described above is not expected to occur in reality, an influence of the relative depth could occur. Whether the newly proposed model is correct should therefore be checked at prototype scale as well.

8.7 Conclusions

A method for evaluating the stability of bed protections under non-uniform flows (i.e. near structures) based on output of a 3D RANS model has been formulated. The profiles of the mean velocity and turbulence kinetic energy in the water column above the bed are used to formulate a local stability parameter [eq. (8.16)], which basically is a Shields parameter, adapted to account for turbulence of varying relative intensity.

The entrainment rate is used as a measure of damage. The entrainment can be made dimensionless in an entrainment parameter [eq. (2.20)] which can be used to compare different investigations. It can be determined from conventional measurements (using coloured strips) when a correction is made for the transport within a strip (a method for this is presented in appendix D), and the increased entrainment rate during the initial water-working of the bed is not incorporated in the measurement.

The measured values of the new stability parameter are correlated to the entrainment parameter. This indicates that the stability represents the flow attack to the bed. A tentative relation between the stability parameter and the entrainment parameter is given by eq. (8.18). The existing stability parameter Ψ_{WL} was also correlated to the entrainment parameter with slightly more scatter, while the conventional Shields parameter could not predict the entrainment rate at all.

The stability parameter was calculated reasonably well by the CFX model for some configurations, but care must be taken when using output of the model. The implementation of aspects like the grid and boundary value set-up is very important.

The relatively large influence of the turbulence (high value of α) in the stability parameter – which is based on the quasi-steady force mechanism – indicates that a different force generating mechanism (turbulence wall pressures) may be aiding in the entrainment of stones.

Chapter 9

Conclusions and Recommendations

Turbulent stationary flows over granular bed protections are considered. These bed protections are defined as hydraulically rough granular beds under non-uniform flow with a low mobility of the stones in the bed. Turbulence is a key factor in this flow regime, as in this regime only turbulence-generated extreme forces can dislodge stones from the bed. The physical concepts that are generally used for the evaluation of the influence of turbulence on stability of bed material, derived for uniform flows, are often only qualitatively or partially true if applied to non-uniform flows. A number of frequently used concepts is examined regarding the origin of the fluctuating forces on the stones and the manner in which the stones are entrained. To this end two measurement series were carried out, and calculations were executed with a numerical discrete particle model. Additionally, existing measurements of stone displacements under various non-uniform flows were analysed, and used to calibrate a new stability model.

9.1 Conclusions

Stone positions

From a comparison of several sources in literature it can be concluded that of the geometric factors that determine the stability of an individual stone – given the typical characteristics of a bed protection – the orientation of the stone influences its stability the most. The orientation has a larger influence on the stability of the individual stone than its vertical position, size, or shape.

When large flow velocities are applied for the first time to a bed protection some loose stones will always move. Other stones rock until they have a more stable orientation. Most displacing stones roll from their pocket in a pivoting motion, some slide from their place. This process is called water-working. It can be stated that a water-worked bed obtains its intrinsic strength.

From calculations with a Discrete Particle Model (DPM) we can conclude that the way in which the stones were dumped – if random – together with the collision and hydraulic parameters do not significantly influence the bed configuration of the water-worked bed. Furthermore, even in a randomly deposited bed there exists a fixed value of the critical hydraulic load for the most unstable stone. For the ideal bed formed with equally sized spheres, the maximum protrusion of a stone is $0.82d$ above the mean of all bed elevations.

Force origins

The model that is most widely used for predicting the forces on the stones on the bed is that the (drag and lift) forces on a stone are proportional to the near-bed streamwise velocity squared. These are called quasi-steady forces (QSF), as the instantaneous forces are generated by the same mechanism as in a steady flow. From literature it follows that ‘near-bed’ is best represented by $0.15d$ above the top of the stone under consideration. The quasi-steady drag force on a shielded stone is also dependent on the vertical velocity. This can be understood by the fact that a changed angle of attack changes the exposed area of the stone.

A second mechanism that was identified was the influence of turbulence wall pressures (TWP). Whereas the QSF are a consequence of the streamline curvature that is induced by the protruding particle itself, the TWP are also present on smooth walls. These fluctuating pressures are caused by the streamline curvature induced by the turbulence (vortices). The difference between the two force mechanisms is illustrated by the fact that if a spanwise vortex (with vorticity of the same sign as the mean shear) is advected over a stone, the TWP-induced drag and lift force can be increased, while the near-bed velocity is decreased.

The drag force on very exposed stones is predicted very well by the quasi-steady mechanism. The intensity of these quasi-steady drag forces is mainly governed by large-scale flow structures. The probability density of the instantaneous values of these quasi-steady drag forces is well schematised by eq. (5.3) for any value of the relative turbulence intensity.

When the exposure of the stone decreases, the drag force fluctuations cannot be explained solely by the quasi-steady forces anymore. The TWP begin to influence the variance of the force.

The value of the ‘instantaneous Reynolds stress’ near the bed, $-u'v'(t)$, has not

been seen to have any direct importance to the stability of the stones or the value of the instantaneous bed shear stress.

The instantaneous lift force is not predicted well by the quasi-steady mechanism for any of the exposures measured. Lift force fluctuations generally have higher frequencies than those of the drag force. They can have several origins: the influence of turbulence wall pressures that are caused by passing vortices, vortex shedding from the stone itself, and the quasi-steady mechanism.

The lift force is also influenced considerably by the spatially varying flow direction near the rough bed (Schmeeckle & Nelson, 2003). This influence was not investigated in the present set-up.

Near the reattachment point downstream of a backward-facing step the main source of (the variance of the) fluctuating forces on the stones – both drag and lift – are the TWP. The extreme positive drag forces, however, are probably still caused by the quasi-steady mechanism.

Flow structures and stone movement

PIV measurements were used to obtain the characteristics of the flow structures that move a stone. For both flow conditions measured (a uniform flow and flow at the reattachment point of a backward-facing step) the stone was most often moved by an exceptional combination of two normal flow structures, at least one of which had an exceptionally high magnitude. The first structure is a large-scale sweep motion, the second is an intense vortex or vortex package. The latter structure was sometimes embedded in the former. Although both the shape of the large-scale sweep and the origin of the small-scale vortex differ between the two flow conditions, this kind of combination is observed in both configurations (uniform and BFS flow).

The large-scale areas with increased streamwise velocity generally have a downward velocity (i.e. sweeps or Q_4 events). They cause increased (drag) forces via the QSF mechanism. In the uniform-flow case these areas extend vertically over about two thirds of the water depth, are typically $2h$ to $4h$ long and have a width exceeding $0.5h$. Near the reattachment point behind the BFS these sweeps are smaller and occur quasi-periodically due to the separation of large-scale eddies from the recirculation region. The small-scale vortices cause a lift force via the TWP mechanism. In the uniform flow case the small-scale vortices probably originate from the bed elements upstream, while in the BFS flow they probably originate from the mixing layer that is present between the recirculation region and the main flow.

A lift force caused by TWP and a quasi-steady drag force can cooperate to dislodge the stone from the bed. Initially the stone does not protrude far into the flow, so the QSF are still weak. Hence the lift force is often important for the initial movement of the particle. Even if the lift force has a short duration, the exposed area of the

particle can have increased, and its angle of repose can have decreased. An increased streamwise velocity following this lift force is therefore more likely to roll the stone out of its pocket.

When regarding the individual movement events for different stones, the increased streamwise velocity at the time of movement is present more often than the small-scale cause of TWP. Therefore the QSF can be considered as more important. However they do not completely govern the entrainment of a stone.

Stability model of bed protections in practical applications

A stability parameter has been formulated that can be used to obtain an estimate of the flow attack on a bed protection [eq. (8.16)], using output of a Reynolds-averaged flow model (that yields \bar{u} and k). The entrainment was chosen as a suitable indicator of the local bed response to the flow attack. The stability parameter is correlated to the entrainment parameter for various non-uniform flows. Therefore it describes the hydraulic load. The (dimensionless) entrainment as a function of this stability parameter is given in eq. (8.18).

The influence of the turbulence in the new stability parameter is high, compared to the influence of the mean flow. This indicates that the TWP are indirectly taken into account.

The entrainment is an objective criterion for damage level that can be compared between investigations.

The model is meant for bed protections that are attacked by flow. It is not suited for waves. It can be used to evaluate the stability of (designs of) bed protections under complex flows, like foundations of caissons, pipeline covers, bed protections downstream of weirs, etc. Besides determining the stability of a design, the model can be used to obtain an estimate of the optimal stone size to be used as a function of the horizontal position on the bed protection. To this end the optimum stone size then has to be determined iteratively.

9.2 Recommendations

In this section recommendations are given for further experimental work, more advanced modelling of bed stability, and the design of bed protections.

9.2.1 Experimental research

- Stability of bed protections should also be examined at prototype scales. There are indications that aspects like a large relative depth or Re_* influence the stability.

- The $\Psi_{Lm}-\Phi_E$ curve, eq. (8.18), should be validated using other measurements with different flow conditions, stone sizes, and strip widths.
- Useful new areas for in-depth (i.e. stone-scale) experiments are the stability of stones under turbulent jets caused by ship's propellers, and of stones under waves.
- PIV measurements in different planes ($x-z$, or $z-y$) will help in visualising the flow structures that move stones. If recordings are made in the $x-z$ plane just above the bed, it is possible to obtain the movement of the bed material from the PIV recordings, besides the flow field.
- The following recommendations can be made regarding the execution of experiments on (bulk) stone stability.
 - A bed should be water-worked prior to the real test to remove the loose stones, that do not determine the strength of the bed. A bed is water-worked when a certain *number* of stones (per unit of bed area) have moved, not when flow has been applied for a certain *time*.
 - If the entrainment rate is measured by using coloured strips with stones, and counting the number of stones of a certain colour downstream of their strip of origin, then the entrainment rate should be corrected using a technique such as the one presented in appendix D.
 - The strip width determines the resolution of the stone stability measurement. If the flow varies rapidly in space then the resolution of the bed stability measurement should be increased by decreasing the strip width. If not enough stones move in this case, then it automatically follows that the experiment has to be repeated more often to get the same accuracy for the ensemble-averaged results.

9.2.2 Modelling

- The pressure gradients associated with a stationary acceleration of the flow and the acceleration due to waves should ultimately be used as extra forces in the stability parameter. These accelerations were not significant in the data set used presently (in chapter 8).
- The effects of the fluctuating accelerations (TWP) should be added in the stability parameter as an extra force. To this end a good model should be found for the small-scale pressures on the bed. These are governed by the near-bed k , ε , and $d\bar{u}/dy$.

- A probabilistic approach should be used to obtain a better description of damage to bed protections. Some aspects, like the PDF of the quasi-steady forces [eq. (5.3)] and the protrusion distribution of the ideal bed (figure 3.4) can be used in an entrainment formulation like eq. (2.24). More information, like an estimate of the time-scale of the turbulence fluctuations is also required for this.
- If the precision of the entrainment function will be increased by further calibration, it should also be used to estimate the cumulative damage over time. If the temporal development of damage over time can be described with a higher accuracy than presently possible, this will help with making decisions regarding maintenance frequency and lifetime analysis of hydraulic structures.
- The use of the bed-load transport of stones in a gradual stability approach is in principle possible, but should not be pursued until an accurate prediction of the entrainment rate – the first step of the transport process – is possible.

9.2.3 Design of bed protections in practice

- The approach developed in chapter 8 can be used to obtain estimates of the stability of bed protections and the expected size of the area with a large hydraulic attack (large Ψ_{Lm}). The stability parameter Ψ_{Lm} can be determined in a postprocessing step of a numerical calculation with a 3D, non-hydrostatic Reynolds-averaged Navier-Stokes flow model (e.g. with $k-\varepsilon$ closure). Examples of such computational models are Fluent, Phoenix, CFX, or Delft-3D with a non-hydrostatic flow correction.
- When designing a bed protection a low value of the entrainment parameter can be subjectively chosen to be ‘critical’, and this can be translated to a critical value for Ψ_{Lm} using eq. (8.18).
- Care must be taken when using the CFD models. Items like grid set-up and boundary conditions are crucial to a reasonable outcome.
- Some stones will always be lost from dumped bed protections after an initial load on the stone layer.

Acknowledgements

In order to gain knowledge of the process of damage to bed protections, the Road and Hydraulic Engineering Section (DWW) of Rijkswaterstaat decided to fund the present Ph.D.-research. Maarten van der Wal has put in a large effort to realise this. The research was co-funded by Delft Cluster. Boskalis and Van Oord made it possible for me to write the modelling chapter. Their aid is much appreciated.

My guidance committee was very important: Jurjen Battjes, Kees d'Angremond, Rob Booij, Harry Fontijn, and Henk Jan Verhagen. I especially want to thank Rob Booij, my daily supervisor, for the good guidance. I also really enjoyed the experiments with the basketballs and the walks over the Vesuvius and through the forbidden city. And I thank Jurjen Battjes, who could always improve and structure my writings. I further want to thank my other daily supervisors Harry Fontijn and Wim Uijttewaal who I could always bother with small and large problems.

Luckily there were many skilled people who helped me building the required contraptions in the laboratory: Karel de Bruin, Fred van der Brugge, Jaap van Duin, Kadir Baldemir, Hans Tas, and Arie den Toom. I would have been lost during the measurements without Paul Vermeulen, Michiel van der Meer, and Frank Kalkman.

I thank all members of my promotion committee, who took the effort to critically go through my thesis.

Rohnen de Ruijter put in an enormous effort in the PIV measurements. He executed the measurements with a lot perseverance, dedication, and cleverness. I appreciate this very much.

The bimonthly discussions with the people from Aero & Hydro: Wim Paul Breugem, Rob Uittenbogaard, Bendiks Jan Boersma were inspiring.

During the last part of the project I was aided by people from WL|Delft Hydraulics: Tom Jongeling, Henk Verheij, and Bert Jagers.

I was blessed to have fun roommates. First Marcela Busnelli, who was followed by David Ham. And I want to thank all the other AIOs who made my 4 to 5 year stay at the laboratory very pleasant, like Lucas, Ankie, Bram, Petra, Federico, Elmar, Gerben, Alexander, and all the AIOs from the second floor.

Thanks to my father for getting the thesis printed and to Stijn and Gwen for being my paranimphen.

And I could never have finished my thesis while starting a new job and becoming a father without the support and love of Elisabeth.

List of symbols

Roman symbols

a	acceleration, or distance of vortex from wall (chapter 6)
A	area
B	width (of flume)
c	damping coefficient
c_f	friction factor $\equiv u_*^2 / \langle u \rangle_h^2$
C_B	bulk quasi-steady force coefficient
C_D	drag coefficient
$C_{D,*}$	C_D based on shear velocity
$C_{D,0.15}$	C_D based on velocity $0.15d$ above stone
$C_{D,0}$	C_D based on velocity at the height of the stone centre
C_L	lift coefficient
C_m	added mass coefficient
d	particle, stone or sphere diameter
d_n	nominal stone diameter $\equiv \sqrt[3]{V}$
d_{n50}	nominal diameter exceeded by 50% of stones (weight)
D	drag force indicator ($\equiv p_1 - p_3$), or deposition rate (chapter 8)
e	exposure (stone height compared to local upstream bed level)
E	entrainment rate
E_{meas}	measured entrainment rate, without correction
f_{mov}	movement frequency
F_A	force indicator obtained from PIV image
F_D	drag force
F_{contact}	contact force during collisions

F_G	gravitational force
F_L	lift force
F_{\max}	(estimate of) maximum occurring force
Fr	Froude number $\equiv U/\sqrt{gh}$
g	gravitational acceleration
G_{ii}	power spectral density of signal i
G_{ij}	cross spectral density of signals i and j
h_s	step height
h	water depth
k	spring constant, or turbulence kinetic energy, or wave number
K	kurtosis, or transfer function
$ K $	gain function
L	lift force indicator ($\equiv -p_2$), or displacement length
L_H	horizontal length scale of large-scale turbulence
L_m	Bakhmetev mixing length
L_x	turbulence length scale determined from autocorrelation
L_y	vertical turbulence length scale
L_ε	dissipation length scale
n	an integer number
N	an integer number
p	pressure, or probability density
p_1	pressure signal measured on the upstream face of cube
p_2	pressure signal measured on the top face of cube
p_3	pressure signal measured on the downstream face of cube
P	probability
q_s	sediment transport rate
Q	discharge
R	radius
Re	Reynolds number $\equiv Uh/\nu$ (or $U\delta/\nu$, or $\equiv Ud/\nu$)
Re_*	particle Reynolds number $\equiv u_*d_n/\nu$

S	skewness
t	time
T	period, time-scale or duration
T_p	pick-up duration
u	streamwise velocity
u_0	average velocity on step
u_*	shear velocity $\equiv \sqrt{\tau_b/\rho}$
u_b	near-bed streamwise velocity
$u_{b,\max}$	(estimate of) maximum near-bed streamwise velocity
u_c	convection velocity
U	cross-sectional average of streamwise velocity
v	upward velocity
v_b	near-bed upward velocity
v_p	velocity of stone/particle
V	volume (of stone)
w	transverse velocity
x	coordinate in direction of flow or, stochastic variable with a χ^2 -distribution
x_r	reattachment length
y	vertical coordinate a normally distributed stochastic variable
y_0	roughness length
y_b	bed elevation
z	transverse coordinate

Greek symbols

α	empirical constant (various uses)
γ	relative distance from bed y/h , or safety factor
γ_{ij}^2	coherence between signals i and j
Γ	standard gamma function
δ	non-centrality parameter ($\equiv \bar{u}/\sigma(u)$), or boundary layer thickness
Δ	specific submerged density of stone ($\equiv \rho_s/\rho - 1$)
ϵ	porosity
ε	turbulence dissipation
θ	phase shift or, angle

κ	Von Karman constant
λ	wave length
λ_{ci}^2	swirling strength
ν	kinematic viscosity
Π	protrusion of particle above mean bed level
ρ	density of water
ρ_s	density of stone
ρ_{DL}	correlation between drag and lift (indicators)
$\rho_{\Delta x}$	normalised covariance of bed elevations
$\rho_{12}(L_{\text{overlap}})$	area-based correlation between 2 PIV recordings
ρ_{12}	area-based correlation between PIV recording and splice
$\sigma(x)$	standard deviation of x
τ	shear stress, or time lag
τ_b	bed shear stress
τ_c	critical bed shear stress
ϕ	pivoting angle
Φ	transport parameter
Φ_E	entrainment parameter
Ψ	Shields parameter ($\equiv u_*^2/\Delta gd$)
Ψ_c	critical Shields parameter
$\Psi_{Lm,c}$	threshold value for Ψ_{Lm}
Ψ_{Lm}	stability parameter using Bakhmetev mixing length
Ψ_{tot}	general form of stability parameter
Ψ_{WL}	stability parameter developed at WL Delft Hydraulics
$\Psi_{WL,c}$	critical value of Ψ_{WL}
ω	angular frequency

Mathematics

$ x $	absolute value of
\vec{x}	x is a vector
$\min(x)$	minimal value of all elements of x
$\max(x)$	maximal value of all elements of x
\bar{x}	temporal average of x
$\langle x \rangle$	spatial average of x
x'	fluctuating part of x around \bar{x}
\hat{x}	amplitude
\tilde{x}	dimensionless form, or

	horizontal projection (ch. 8)
\equiv	defined as
\propto	proportional to
\approx	approximately equal to
$\frac{D}{Dt}$	material derivative
$\frac{\partial}{\partial}$	partial derivative
$\frac{d}{d}$	derivative
\int	integral
\pm	plus or minus
$f(x)$	unspecified function of x
Δx	difference between two values of x

Abbreviations

2D	two-dimensional
3D	three-dimensional
BFS	backward-facing step
CCD	charge-coupled device
CFD	computational fluid dynamics
DNS	direct numerical simulation
DPM	discrete particle model
EMF	electro-magnetical flow meter
HVP	hairpin-vortex package
HVS	hairpin-vortex signature
LES	large eddy simulation
LDV	laser-doppler velocimeter
PDF	probability density function
PIV	particle image velocimetry
RANS	Reynolds-averaged Navier-Stokes
TWP	turbulence wall pressures

List of Figures

1.1	Left: laboratory model of a granular bed protection (present tests). Right: trial bed protection with 10-60 kg rock (Meulepas <i>et al.</i> , 1999).	2
2.1	Model of HVP, viewed from the side. Flow is from left to right.	13
2.2	Original Shields curve (1936). The hatched area depicts the critical shear stress as a function of the particle Reynolds number.	26
2.3	Dimensionless transport for low Ψ values after Paintal (large particles only).	28
2.4	Forces on a stone.	32
2.5	Variation of dimensionless critical shear stress Ψ_c with relative protrusion Π/d , after Fenton & Abbot (1977)	33
3.1	A simulated water-worked bed with equally sized spheres. Box size is $12d \times 12d$. The exposed stones have a lighter shading.	43
3.2	a) (left) Initial distribution of protrusions of exposed stones for runs 1–3, with different damping coefficient. b) (right) The distributions of protrusions for the same beds after removing the most protruding stones.	46
3.3	Cumulative number of stones N moved per strip under open-channel flow as a function of time for five experiments ($\Psi=0.037-0.048$), based on data by Forschelen (1999). t_{15} is the time at which $N = 15$	47
3.4	Simulated probability density of bed elevations of eroding water-worked bed. Including the position of certain definitions for the bed level. . .	49
3.5	Spatial covariance of the bed elevations.	50
3.6	Development of the bed structure as a function of the number of entrained stones n (run 4). The equilibrium value lies within the dashed lines.	51
4.1	Selected pressure sensors, <i>Honeywell</i> (left) and <i>Druck</i> (right) (different scales, approx. 1:1).	56

4.2	Pressure spectra (G_{ii}) on a bed-mounted cube in a granular bed. The right plot depicts normalised pressure spectra. D is the pressure difference between the upstream and downstream face of the cube, L the pressure at the top face.	57
4.3	Two consecutively recorded 32 by 32 pixels windows and the 2D correlation of the two (right). A lighter shade is a higher value of light intensity or correlation, respectively.	58
4.4	Schematised PIV set-up.	59
4.5	Example of a single PIV recording of flow over a rough bed.	61
4.6	Longitudinal section of the instrumented model stone, including three pressure transducers, for $\Pi = 1$ cm.	62
4.7	Longitudinal bed profiles, averaged over the cube width, for bed 1 (thin line) and bed 2 (thick line). The average local levels upstream of the cube are indicated by the dashed lines (thickness corresponding to the bed profiles). The cube is centred at $x = 0$	62
4.8	Vertical profiles of mean velocity (left), Reynolds stress (middle) and turbulence intensity (right), normalised by depth and time averaged longitudinal velocity $\langle \bar{u} \rangle_h$ for cases U, T, S1 and S2. Turbulence intensities for $\sigma(v)$ have filled markers.	66
4.9	Measured longitudinal sections of the bed level near the target stone, indicating positions of pressure sensors. The y -coordinate is different than for the flow results.	67
4.10	Sketch of instrumentation and set-up around target stone, with detail of the hinge (right).	68
4.11	Left: mimicked bed under construction including moulds, wiring, epoxy-resin, etc. Right: mimicked bed in place, with target stone in the centre.	69
4.12	Left: histogram of the durations during which the target stone is detached from the bed. Right: histogram of the intervals between events where $\Delta T_{up} > 1$ s.	71
4.13	Left: streamwise velocity for cases U005, U007 and U009, including a fit of the linear-logarithmic profile. Right: profile of the streamwise turbulence intensity for the same cases and eq. (2.2). The u_* values from table 4.2 were used.	73
4.14	Velocity profiles ($Q=43, 51, 58$ l/s) relative to target stone.	73
4.15	Vertical profiles of \bar{u} (top), and $\sigma(u)$ and $\sigma(v)$ (bottom, solid and dashed lines respectively) for BFS.	74
4.16	Measured streamwise bed profile for second experimental series.	74
4.17	Reattachment length against Froude number downstream of BFS. Filled markers represent rough beds, open markers represent smooth beds.	76

5.1	Pdf of velocities and derived PDF of drag forces.	79
5.2	PDFs for $u_b u_b $ (solid line), and u_b^2 (dashed line), for various values of δ	81
5.3	PDFs of normalised instantaneous near-bed velocity.	82
5.4	PDFs of D' for the uniform flow (U: \circ) and the roughness transition (T: \square).	83
5.5	PDFs of the measured instantaneous pressure difference for the BFS. Linear (left and middle) and semi-logarithmic plots (right). Eq. (5.3) is plotted for the same values of δ . S1: \circ , and thin line, S2: \square , and thick line.	83
5.6	$\overline{D}/\rho U^2$, $\sigma_D/\rho U^2$, and $\sigma_L/\rho U^2$ as a function of e for the uniform flow case. Lines are linear fits through the data points. For each exposure three discharges have been used: 45, 55, and 65 l/s	84
5.7	Joint PDF of $u_b(t)$ and $v_b(t)$ (thin isolines), and conditionally averaged $\overline{D'(u_b, v_b)}$ (thick isolines, label units: N/m^2) for case U and $e = 1.09$ cm, 1.47 cm, 2.09 cm, and 2.47 cm (from left to right and from top to bottom respectively). The straight solid lines indicate $\overline{u_b}$ and $\overline{v_b}$ respectively.	85
5.8	Joint probability density function of (u_b, v_b) (thin isolines), and conditionally averaged vertical pressure, $\overline{L'(u_b, v_b)}$ (thick isolines, label units: N/m^2) for uniform flow. $e = 2.1$ cm (left) and $e = 2.5$ (right).	86
5.9	Normalised PDF of D' plotted on linear (left) and semi-logarithmic (right) scale for different exposures and uniform flow. Line shows eq. 5.3 with $\delta = 4$	87
5.10	Time signal of longitudinal velocity (top), drag force indicator (middle), and lift force indicator (bottom), for $e = 2.5$ cm.	88
5.11	Premultiplied pressure spectra for configurations U (thick line) and T (thin line). $e=1.5$ cm. Left: D , right: L	90
6.1	Top: streamlines of a 2D potential flow around a point vortex near a wall, in a frame of reference moving with the vortex. Middle: the resulting TWP. Bottom: the pressure field around a stone, assuming a vertically constant pressure, and the resulting net force.	95
6.2	Dimensionless, squared gain functions for drag and lift force.	98
6.3	Spectrum of pressures on rough bed (left) and the estimated spectra of the drag and lift forces. For the legend see figure 6.2.	100
6.4	Change of the integrated force on a stone (2D, semi-circular cylinder) due to a convected frozen pressure field for $\lambda/d=1.5$. The vectors represent the resulting net force acting on the stone.	101
6.5	Measured correlations ρ_{DL} for configurations U and S1.	103

6.6	Measured PDFs of L' for case U and various exposures on a linear (left) a semi-logarithmic (right) scale.	104
6.7	Comparison of spectra of pressures on a cube (L) behind a BFS with $e=1.5$ cm to TWP spectra from a smooth wall windtunnel experiment (Lee & Sung, 2002).	106
6.8	Comparison of spectra of the pressures on a rough-wall element (D and L) to TWP on a smooth wall (Lee & Sung, 2002), both behind a BFS, for $e=1.5$ cm and 2.5 cm.	107
7.1	Area used for determining force indicators.	111
7.2	Principle of splicing technique applied to three sequentially measured flow fields.	113
7.3	Twenty separate recordings of $u(x, y)$ during stone movement event #1 of U007, together with the spliced image obtained from them (bottom). The horizontal positions of neighbouring images correspond to the overlap with the highest correlation.	113
7.4	Classification of events. F_A and $\sigma(v)_A^2$ indicate QSF and TWP-forces respectively. Dots are the values of a reference measurement with a fixed stone (10 min. duration at 0.5 Hz). The circles are the values just before stone movement. The solid lines represent the average values of the indicators, the dashed lines are arbitrary limits for QSF and TWP events.	116
7.5	Contour plots of spliced and conditionally averaged recording for all events of case U007. The stone moves at $x = 0$	117
7.6	Detail of instantaneous field just before movement of the target stone. Top: event #5, $\vec{u} - 0.65\vec{U}$, bottom: event #28, $\vec{u} - 1.0\vec{U}$	119
7.7	Left: Event #29, just after first movement of the stone, $\vec{u} - 0.70\vec{U}$. Right: Event #23, just before movement, $\vec{u} - 0.85\vec{U}$	120
7.8	Large-scale spliced flow field of event #28.	121
7.9	Spliced flow field of large-scale event #5.	122
7.10	Large-scale conditionally averaged flow structure for stone with slightly increased protrusion (U003).	122
7.11	Large-scale flow structure for different stone (U014).	123
7.12	Classification of events for different stone (U014). Dots are the values of a reference measurement with a fixed stone (10 min. duration & 0.5 Hz). The circles are the values just before stone movement. The solid lines represent the average values of the indicators.	124

7.13 Force indicators of flow fields just before stone movement at reattachment point (B006). Dots are the values of a reference measurement with a fixed stone (10 min. duration at 0.5 Hz). The circles are the values just before stone movement. The solid lines represent the average values of the indicators. 125

7.14 Conditionally averaged flow structure around the time of movement ($t=0$) for case B006. The target stone is situated at the reattachment point, $(x,y)=(0,0)$. Left: u' , middle: v' , right: $\vec{u} - 0.8\vec{U}$, detail with every second vector plotted. 127

7.15 Coherence between conditionally averaged field of streamwise velocity just before stone movement ($\overline{u'}_{CA}$) and a recording with a fixed target stone. 129

7.16 Left: ‘normal’ flow, i.e. conditionally averaged flow structure during maximum correlation with the $\overline{u'}_{CA}$ field (circles in figure 7.15) (top: u' , bottom: v'). Right: flow field just before stone movement ($\overline{u'}_{CA}$ and $\overline{v'}_{CA}$). 130

7.17 Illustration of a Q_4 event (sweep) and an advected Q_2 event (ejection), together creating a Q_1 event (outward interaction). 131

7.18 Conditionally averaged pressures near target stone during entrainment at $t=0$. Top: lift sensor upstream of stone, middle: sensor under stone, bottom: drag sensor next to stone. The dashed line indicates the latest possible time that the first PIV recording after movement is made. . . 132

7.19 Spectra of pressures on stones surrounding target stone. 132

8.1 Model of large-scale eddy that causes damage. 142

8.2 a) Vertical ‘maximum velocity’ distribution according to eqs. (2.1) and (2.2) with a Gaussian bump of two sizes, b) Bakhmetev mixing length. c) Estimate of the large-scale ‘maximum’ velocity. d) Relative influence of velocity at a certain elevation. e) The estimated influence of the large-scale turbulence on the bed. The vertical lines indicate the two maximum values. 145

8.3 Longitudinal sections of the geometries used. Dashed lines are velocity-measurement locations 147

8.4 Profiles of calculated (lines) and measured (dots) flow parameters over the long sill. The lower two panels show the length scales determined from the calculations (L_ε , dots) and from the measurements (L_x , lines). 151

8.5 Profiles of calculated (lines) and measured (dots) flow parameters at gate. The lower two panels show the length scales determined from the calculations (L_ε , dots) and from the measurements (L_x , lines). 152

8.6	Profiles of calculated (lines) and measured (dots) flow parameters over the short sill. The lower two panels show the length scales determined from the calculations (L_ε , dots) and from the measurements (L_x , lines).	153
8.7	Comparison of measured and calculated local $\bar{u}+6\sqrt{k}$ for long sill, gate and short sill.	154
8.8	Measured entrainment under uniform flow (WL) as a function of Ψ	155
8.9	Measured entrainment under uniform flow (WL, cases 1–3) as a function of Ψ , Ψ_{WL} , and Ψ_{Lm} . A thicker circle denotes a larger h . The square marker indicates the flow on the long sill (case 4).	156
8.10	Measured Φ_E versus the measured Ψ for a variety of flow conditions. For legend see next figure. The markers with arrows have $\Phi_E=0$	157
8.11	Top: measured Φ_E versus the measured Ψ_{WL} for a variety of flow conditions. Bottom: measured Φ_E versus the measured Ψ_{Lm} for the same flow conditions.	158
8.12	Measured Φ_E versus the <i>calculated</i> Ψ_{Lm} for a range of flow conditions.	160
8.13	Ψ_{WL} (left) and Ψ_{Lm} (right) for uniform flow at critical conditions ($\Psi_c=0.03$, $\Psi_{WL,c}=8$, $\Psi_{Lm,c}=1.2$), as a function of h/y_0	161
8.14	Influence of relative depth or global Reynolds number on near-bed turbulence intensity.	162
A.1	Premultiplied spectrum of measured open-channel, smooth-wall wall pressures.	198
A.2	A power density spectrum of wall pressures, both unfiltered and filtered.	199
A.3	Schematised set-up of reference pressure sensor.	202
B.1	Sequences of recordings by digital camera of initial movements of individual stones ($\Delta = 0.4$) from a granular bed under uniform flow. Each column depicts another stone movement. Left: the stone sits idle in pocket. It sometimes rocks a little. The stone is lifted at its upstream side and slowly slides to a stable position with a higher exposure, until it lies stable for a while. Until the upstream side of the stone is lifted up again and the stone rolls away. Right: the stone sits motionless in its pocket, sometimes its side lifts up, but the stone remains at its position; until it rolls downstream.	204
C.1	Pdf of shear stresses in equilibrium boundary layer. Measured and χ^2 -distribution.	208
D.1	Stone moving from strip 0 to strip n : definitions.	210
D.2	Probability of a stone displacing from strip 0 to strip i , as a function of \tilde{L}	211

D.3	The fraction of stones depositing in the n^{th} strip downstream of the strip of origin (DG), the fitted eq. (D.4), and the estimate of the number of stones deposited in the strip of origin, as a fraction of the measured number of deposited stones.	213
F.1	Left: point gauge measurement at Verolme Dock in progress (Meulepas <i>et al.</i> , 1999). Right: result of a scan with a multi-beam echosounder. .	220
F.2	From left to right, respectively the following measurements: 40–200 kg point gauge, 40–200 kg multibeam, 10–60 kg point gauge, 10–60 kg multibeam.	220

References

- Adrian, R.J., Christensen, K.T. & Z.C., Liu. 2000a. Analysis and interpretation of instantaneous turbulent velocity fields. *Experiments in Fluids*, **29**, 275–290.
- Adrian, R.J., Meinhart, C.D. & Tomkins, C.D. 2000b. Vortex organisation in the outer layer of the turbulent boundary layer. *Journal of Fluid Mechanics*, **422**, 1–54.
- Aksoy, S. 1973. Fluid Force Acting on a Sphere near a Solid Boundary. *In: XV IAHR Congress*, vol. 1.
- Andrews, E.D. & Smith, J.D. 1992. A Theoretical Model for Calculating Marginal Bedload Transport Rates of Gravel. *In: (Billi et al., 1992)*.
- Arcalar, M.S. & Smith, C.R. 1987. A study of hairpin vortices in a laminar boundary layer. Part 1. Hairpin vortices generated by a hemisphere protuberance. *Journal of Fluid Mechanics*, **175**, 1–41.
- Auton, T.R. 1987. The lift force on a spherical body in a rotational flow. *Journal of Fluid Mechanics*, **183**, 199–218.
- Bendat, J.S. & Piersol, A.G. 1971. *Random Data: analysis and measurement procedures*. Wiley-Interscience.
- Bendat, J.S. & Piersol, A.G. 1980. *Engineering applications of correlation and spectral analysis*. Wiley-Interscience.
- Benedict, B.A. & Christensen, B.A. 1972. Hydrodynamic lift on a stream bed. *In: Shen, Hsieh Wen (ed), Sedimentation, Symposium to Honor prof. H.A.Einstein*.
- Billi, P. Hey, C.R. Thorne, C.R. & Tacconi, P. (eds). 1992. *3rd int. workshop on dynamics of gravel-bed rivers*. New York: John Wiley & Sons.
- Blake, W.K. 1970. Turbulent boundary-layer wall-pressure fluctuations on smooth and rough walls. *Journal of Fluid Mechanics*, **44**(4), 637–660.

- Booij, R. 1998. *Erosion under a geometrically open filter*. Tech. rept. 2-98. Delft University of Technology. In Dutch.
- Bosma, C. 2001. *Porosity in crushed-stone constructions*. M.Sc. thesis, Delft University of Technology, Delft. In Dutch.
- Breusers, H.N.C. 1965. *Gradual closure VI, influence of shape and grading on the stability of riprap*. Tech. rept. M731. WL|Delft Hydraulics, Delft. In Dutch.
- Breusers, H.N.C. & Schukking, W.H.P. 1971. *Beginning of movement of bed material*. Tech. rept. S159-1. WL|Delft Hydraulics, Delft. In Dutch.
- Bridge, J.S. & Bennet, S.J. 1992. A model for the entrainment and transport of sediment grains of mixed sizes, shapes, and densities. *Water Resources Research*, **28**(2), 337–363.
- Buffin-Bélanger, T., Roy, A.G. & A.D., Kirkbride. 2000. On large-scale flow structures in a gravel-bed river. *Geomorphology*, **32**, 417–435.
- Buffington, J.M. & Montgomery, D.R. 1997. A systematic analysis of eight decades of incipient motion studies, with special reference to gravel-bed rivers. *Water Resources Research*, **33**(8), 1993–2029.
- Carling, P.A. Kelsey, A. & Glaister, M.S. 1992. Effect of Bed Roughness, Particle Shape and Orientation on Initial Motion Criteria. *In: (Billi et al., 1992)*.
- Chang, P.A., Piomelli, U. & Blake, W.K. 1999. Relationship between wall-pressures and velocity-field sources. *Physics of Fluids A*, **11**(11), 3434–3448.
- Chen, X. & Chiew, Y.M. 2003. Response of Velocity and Turbulence to Sudden Change of Bed Roughness in Open-Channel Flow. *Journal of Hydraulic Engineering*, **129**(1), 35–43.
- Cheng, E.D.H. & Clyde, C.G. 1972. Instantaneous hydrodynamic lift and drag forces on large roughness elements in turbulent open channel flow. *In: Shen, Hsieh Wen (ed), Sedimentation, Symposium to Honor prof. H.A. Einstein*.
- Chepil, W.S. 1958. The use of evenly spaced hemispheres to evaluate aerodynamic forces on a soil surface. *Transactions, American Geophysical Union*, **39**(3), 397–404.
- Chepil, W.S. 1959. Equilibrium of soil grains at the threshold of movement by wind. *Soil Science Society of America*, **23**, 422–428.
- Chien, N. & Wan, Z. 1999. *Mechanics of Sediment Transport*. ASCE Press.

- Coleman, N.L. 1967. A theoretical and experimental study of drag and lift forces acting on a sphere resting on a hypothetical streambed. *In: Proc. 12th IAHR Congress.*
- Coleman, N.L. 1972. The drag coefficient of a stationary sphere on a boundary of similar spheres. *La Houille Blanche*, 17–21.
- CUR. 1995. *Manual on the use of rock in hydraulic engineering.* Tech. rept. 169. Centre for Civil Engineering Research and Codes, Gouda, The Netherlands.
- De Boer, G.M. 1998. *Transport of stones on a granular bed-protection.* M.Sc. thesis, Delft University of Technology, Delft. In Dutch.
- De Gunst, M. 1999. *Stone stability in a turbulent flow behind a step.* M.Sc. thesis, Delft University of Technology, Delft. In Dutch.
- De Ruijter, R. 2004. *Turbulence structures affecting stone stability in backward-facing step flow. Experiments by means of PIV.* M.Sc. thesis, Delft University of Technology.
- De Ruiter, J. 1982. The mechanism of sediment transport on bedforms. *Pages 137–142 of: Sumer, B. & Muller, A. (eds), Euromech 156: Mechanics of sediment transport.* Istanbul: A.A. Balkeman, Rotterdam.
- Defina, A. 1999. Transverse spacing of low-speed streaks in turbulent flow over smooth and rough boundary. *Excerpta*, **13**, 181–202.
- DeGraaff, D.B., & Eaton, J.K. 2000. Reynolds-number scaling of the flat-plate turbulent boundary layer. *Journal of Fluid Mechanics*, **422**, 319–346.
- Dessens, M. 2004. *The influence of an accelerating flow on the stability of stones.* M.Sc. thesis, Delft University of Technology. www.waterbouw.tudelft.nl.
- Doligalski, T.L., Smith, C.R. & Walker, J.D.A. 1994. Vortex interactions with walls. *Annual Review of Fluid Mechanics*, **26**, 573–616.
- Drake, T.G., Shreve, R.L., Dietrich, W.E., Whiting, P.J. & Leopold, L.B. 1988. Bed-load transport of fine gravel observed by motion-picture photography. *Journal of Fluid Mechanics*, **192**, 193–217.
- Egiazaroff, I.V. 1965. Calculation of nonuniform sediment concentrations. *Journal of the Hydraulics Division, Proceedings of ASCE.*, **91**(HY4), 225–247.
- Einstein, H.A. 1942. Formulas for the transportation of bed load. *Transactions ASCE*, **107**, 561–597.

- Einstein, H.A. 1950. *Bed load function for sediment transportation in open channel flows*. Tech. rept. 1026. U.S. Dept. of Agriculture, Soil Conservation Service, Washington D.C.
- Einstein, H.A. & El-Samni, E.A. 1949. Hydrodynamic forces on a rough wall. *Reviews of Modern Physics*, **21**(3), 520–524.
- Escarameia, M. & May, R.W.P. 1995. Stability of riprap and concrete blocks in highly turbulent flows. *Proc. Instn Civ. Engrs Wat. Marit. & Energy*, **112**, 227–237.
- Etheridge, & Kemp. 1979. Velocity measurements downstream of a rearward-facing step, with reference to bed instability. *Journal of Hydraulic Research*, **17**(2), 107–119.
- Evans, M., Hastings, N.A.J. & Peacock, J.B. 2000. *Statistical distributions*. New York: Wiley. The Wiley series in probability and statistics.
- Farabee, T.M. & Casarella, M.J. 1991. Spectral features of wall pressure fluctuations beneath turbulent boundary layers. *Physics of Fluids A*, **3**(10), 2410–2420.
- Fenton, J.D. & Abbot, J.E. 1977. Initial movement of grains in a stream bed: the effect of relative protrusion. *Proceedings of the Royal Society of London, Series A*, **352**, 523–537.
- Forschelen, P. 1999. *Transport of granular bed material*. M.Sc. thesis, Delft University of Technology, Fac. Civ. Eng. , Hydr. Eng. section. In Dutch.
- Franken, A., Ariëns, E. & Klatter, H. 1995. *Manual for the design of bed protections behind two-dimensional outflow constructions*. Tech. rept. BOD-R-95002. Bouwdienst Rijkswaterstaat. In Dutch.
- George, W.K., Beuther, P.D. & Arndt, R.E.A. 1984. Pressure spectra in turbulent free shear flows. *Journal of Fluid Mechanics*, **148**, 148–191.
- Grass, A.J. 1970. Initial instability of fine bed sands. *Journal of the Hydraulics Division, Proceedings of ASCE.*, **96**(HY3), 619–632.
- Grass, A.J. 1971. Structural features of turbulent flow over smooth and rough boundaries. *Journal of Fluid Mechanics*, **50**(2), 233–255.
- Grass, A.J. & Mansour-Tehrani, M. 1996. Generalized scaling of coherent structures in the near-wall region of turbulent flow over smooth and rough boundaries. *Pages 41–61 of: Ashworth, P.J. Bennet, S.J. Best, J.L. & McLelland, S.J. (eds), Coherent flow structures in open channels*. John Wiley & Sons.

- Gravante, S.P., Naguib, A.M., Wark, C.E. & Nagib, H.M. 1998. Characterization of the pressure fluctuations under a fully developed turbulent boundary layer. *AIAA Journal*, **36**(10).
- Gyr, A. & Schmid, A. 1997. Turbulent flows over smooth erodible sand beds in flumes. *Journal of Hydraulic Research*, **35**(4), 525–544.
- Hoffmans, G.J.C.M. & Akkerman, G. 1998. Influence of turbulence on stone stability. *In: 7th international conference on River Sedimentation*.
- Hofland, B. 2000. *Stability of stones in the top layer of a granular filter – literature survey*. Tech. rept. 07-00. Delft University of Technology.
- Hofland, B. 2001. *Pressure Sensors and Filtering Techniques for Stone Stability Assessment*. Tech. rept. 04-01. Delft University of Technology.
- Hommema, S.E. & Adrian, R.J. 2003. Packet structure of surface eddies in the atmospheric boundary layer. *Boundary-Layer Meteorology*, **106**, 147–170.
- Isbash, S. 1932. *Construction of dams by dumping stones into flowing water*. Tech. rept. Leningrad. Translated by A. Dovjikov for the War Department of the US Engineer office, Engineering division, Eastport Maine.
- Jeong, J., & Hussain, F. 1995. On the identification of a vortex. *Journal of Fluid Mechanics*, **285**, 69–94.
- Jiménez, J., Del Alamo, J.C. & Flores, O. 2004. The large-scale dynamics of near-wall turbulence. *Journal of Fluid Mechanics*, **505**, 179–199.
- Jongeling, T.H.G., Blom, A., Jagers, H.R.A., Stolker, C. & Verheij, H.J. 2003 (December). *Design method granular protections*. Tech. rept. Q2933 / Q3018. WL|Delft Hydraulics. In Dutch.
- Kalinske, A.A. 1947. Movement of sediments as bed load in rivers. *Trans. Am. Geophys. Union*, **28**(4), 615–621.
- Kim, J., Moin, P. & Moser, R. 1987. Turbulence statistics in fully developed channel flow at low Reynolds number. *Journal of Fluid Mechanics*, **177**.
- Kim, K.C. & Adrian, R.J. 1999. Very large-scale motion in the outer layer. *Physics of Fluids*, **11**(2), 417–422.
- Kirchner, J.W., Dietrich, W.E., Iseya, F. & Ikeda, H. 1990. The variability of critical shear stress, friction angle, and grain protrusion in water-worked sediments. *Sedimentology*, **37**, 647–672.

- Kleinhans, M.G. & Van Rijn, L.C. 2002. Stochastic Prediction of Sediment Transport in Sand-Gravel Bed Rivers. *Journal of Hydraulic Engineering*, **128**(4), 412–424.
- Kostas, J., Soria, J. & Chong, M.S. 2002. Particle Image Velocimetry measurements of a backward-facing step flow. *Experiments in Fluids*, **33**, 838–853.
- Lammers, J.C. 1997. *Using Shields in Practise*. M.Sc. thesis, Delft University of Technology. In Dutch.
- Lee, I. & Sung, H.J. 2002. Multiple-arrayed pressure measurement for investigation of the unsteady flow structure of a reattaching shear layer. *Journal of Fluid Mechanics*, **463**, 377–402.
- Ling, C.H. 1995. Criteria for Incipient Motion of Spherical Sediment Particles. *Journal of Hydraulic Engineering*, **121**(6).
- Marion, A., Tait, S.J. & McEwan, I.K. 2003. Analysis of small-scale gravel bed topography during armoring. *Water Resources Research*, **39**(12).
- Maxey, M.R. & Riley, J.J. 1983. Equation of motion for a small rigid sphere in a nonuniform flow. *Physics of Fluids*, **26**(4), 203–207.
- McEwan, I. & Heald, J. 2001. Discrete Particle Modeling of Entrainment from Flat Uniformly Sized Sediment Beds. *Journal of Hydraulic Engineering*, **127**(7), 588–597.
- McEwan, I., Sorensen, M., Heald, J., Tait, S., Cunningham, G., Goring, D. & Willets, B. 2003. Probabilistic modelling of bed-load composition. *Journal of Hydraulic Engineering*, **130**(2), 129–139.
- McLean, S.R., Nelson, J.M. & Wolfe, S.R. 1994. Turbulence structure over two-dimensional bed forms: implications for sediment transport. *Journal of Geophysical Research*, **99**(C6), 12,729–12,747.
- Mehta, A. 1994. *Granular matter; an interdisciplinary approach*. New York: Springer. ISBN: 0-387-94065-0.
- Meulepas, G.-J., Van Reenen, J., & Van der Burg, P. 1999. *Een onderzoek naar hoogteligging breuksteen met multi- en singlebeam echosounders*. Research report. Gemeentewerken Rotterdam, Port of Rotterdam, Boskalis bv, Rijkswaterstaat, VBKO. In Dutch.
- Miyagi, M., Kimura, M., Shoji, H., Saima, A., Ho, C., Tung, S. & Tai, Y. 2000. Statistical analysis on wall shear stress of turbulent boundary layer in a channel flow using a micro-shear stress imager. *Int. Journ. of Heat and Fluid Flow*, **21**(5), 576–581.

- Moraga, F.J., Bonetto, F.J. & Lahey, R.T. 1999. Lateral forces on spheres in turbulent uniform shear flow. *Int. Journ. of Multiphase Flow*, **25**, 1321–1372.
- Mosselman, E. & Akkerman, G.J. 1998. *Low-mobility transport of coarse-grained material*. Tech. rept. Q2395.40. WL|Delft Hydraulics, Delft.
- Mosselman, E., Akkerman, G.J., Verheij, H. Hoffmans, G. Jongeling, T. & Petit, H. 2000. *Stone stability, progress report*. Tech. rept. Q2539. WL|Delft Hydraulics.
- Müller, A., Gyr, A. & Dracos, T. 1971. Interaction of rotating elements of the boundary layer with grains of a bed; a contribution to the problem of the threshold of sediment transportation. *Journal of Hydraulic Research*, **9**(3), 373–411.
- Naguib, A.M., Gravante, S.P. & Wark, C.E. 1996. Extraction of turbulent wall-pressure time-series using an optimal filtering scheme. *Experiments in Fluids*, **22**, 14–22.
- Nakagawa, H. & Nezu, I. 1987. Experimental investigation on turbulent structure of backward-facing step flow in an open channel. *Journal of Hydraulic Research*, **25**(1), 67–88.
- Nakagawa, H. & Tsujimoto, T. 1980. A stochastic model for bed load transport and its applications to alluvial phenomena. *In: Shen, H.W., & Kikkawa, H. (eds), Application of stochastic processes in sediment transport*. Littleton, Colorado: Water resources publications. Chapter 11.
- Nelson, J.M., Shreve, R.L., McLean, S.R. & Drake, T.G. 1995. Role of near-bed turbulence structure in bed load transport and bed form mechanics. *Water Resources Research*, **31**(8), 2071–2086.
- Nezu, I. & Nakagawa, H. 1993. *Turbulence in Open-Channel Flows*. Rotterdam: Balkema.
- Nezu, I. & Tominaga, A. 1994. Response of velocity to abrupt changes from smooth to rough beds in open-channel flow. *Pages 195–204 of: Proc. Symposium on fundamentals and advancements in hydraulic measurements and experimentation*.
- Niño, Y., & Garcia, M.H. 1996. Experiments on particle-turbulence interactions in the near-wall region of an open-channel flow: implications for sediment transport. *Journal of Fluid Mechanics*, **326**, 285–319.
- Nikora, V.I., & Goring, D.G. 2000. Flow turbulence over fixed and weakly mobile gravel beds. *Journal of Hydraulic Engineering*, **126**(9), 679–690.

- Nikora, V.I., Goring, D.G. & Biggs, B.J.F. 1998. On gravel-bed roughness characterization. *Water Resources Research*, **34**(3), 517–527.
- Nikora, V.I., Heald, J., Goring, D. & McEwan, I. 2001a. Diffusion of saltating particles in unidirectional water flow over a rough granular bed. *J. Phys. A: Math. Gen.*, **34**, L743–L749.
- Nikora, V.I., Goring, D., McEwan, I. & Griffiths, G. 2001b. Spatially averaged open-channel flow over rough bed. *Journal of Hydraulic Engineering*, **127**(2), 123–133.
- Nikora, V.I., Koll, K., Mclean, S., Dittrich, A. & Aberle, J. 2002. Zero-plane displacement for rough-bed open-channel flows. *In: River Flow 2002, Louvain-la-Neuve*.
- Nikuradse, J. 1933. Strömungsgesetze in rauhen Röhren. *Verein Deutscher Ingenieure, Forschungsheft*, **361**.
- Obi, S., Inoue, K., Furukawa, T. & Masuda, S. 1996. Experimental study on the statistics of wall shear stress in turbulent channel flows. *Int. Journ. of Heat and Fluid Flow*, **17**(3), 187–192.
- Paintal, A.S. 1969. *The probabilistic characteristics of bed load transport in alluvial channels*. Ph.D. thesis, University of Minnesota.
- Paintal, A.S. 1971. Concept of critical shear stress in loose boundary open channels. *Journal of Hydraulic Research*, **9**(1), 91–113.
- Papanicolaou, A.N., Diplas, P., Evaggelopoulos, N. & Fotopoulos, S. 2002. Stochastic Incipient Motion Criterion for Spheres under Various Packing Conditions. *Journal of Hydraulic Engineering*, **128**(4), 369–379.
- Patnaik, P.C., Vittal, N. & Pande, P.K. 1992. Drag coefficient of a stationary sphere in gradient flow. *Journal of Hydraulic Research*, **30**(2), 389–402.
- Patnaik, P.C., Vittal, N. & Pande, P.K. 1994. Lift coefficient of a stationary sphere in gradient flow. *Journal of Hydraulic Research*, **32**(3), 471–480.
- Pilarczyk, K.W. 2001 (September). Unification of stability formulae for revetments. *In: Proc. XXIX IAHR congress*.
- Radecke, H. van & Schulz-DuBois, E.O. 1988 (July). Linear Response of Fluctuating Forces to Turbulent Velocity Components. *In: Applications of Laser Anemometry to Fluid Mechanics*.
- Raffel, M., Willert, C.E. & Kompenhans, J. 1998. *Particle Image Velocimetry – A Practical Guide*. Experimental Fluid Mechanics. Springer-Verlag. ISBN: 3-540-63683-8.

- Raupach, R.M. 1981. Conditional statistics of Reynolds stress in rough-wall and smooth-wall turbulent boundary layers. *Journal of Fluid Mechanics*, **108**, 363–382.
- Robinson, S.K. 1991. Coherent motions in the turbulent boundary layer. *Annual Review of Fluid Mechanics*, **23**, 601–639.
- Schewe, G. 1983. On the structure and resolution of wall-pressure fluctuations associated with turbulent boundary-layer flow. *Journal of Fluid Mechanics*, **134**, 311–328.
- Schiereck, G.J. 2001. *Introduction to bed, bank and shore protection*. First edn. Delft: Delft University Press. ISBN: 90-407-1683-8.
- Schmeeckle, M.W. & Nelson, J.M. 2003. Direct numerical simulation of bedload transport using a local, dynamic boundary condition. *Sedimentology*, **50**, 279–301.
- Schmeeckle, M.W., Nelson, J.M., Pitlick, J. & Bennet, J.P. 2001. Interparticle collision of natural sediment grains in water. *Water Resources Research*, **37**(9), 2377–2391.
- Schokking, L.A. 2002. *Bowthruster-induced Damage*. M.Sc. thesis, Delft University of Technology. www.waterbouw.tudelft.nl.
- Shields, A. 1936. Anwendung der Aehnlichkeitsmechanik und der Turbulenzforschung auf die Geschiebebetrieb. *Mitteilungen der Preussischen Versuchsanstalt fur Wasserbau und Schiffbau*, **Heft 26**.
- Shvidchenko, A.B. & Pender, G. 2001. Macroturbulent structure of open-channel flow over gravel beds. *Water Resources Research*, **37**(3), 709–719.
- Simpson, R.L. 1989. Turbulent boundary-layer separation. *Annual Review of Fluid Mechanics*, **21**, 205–234.
- Sutherland, A.J. 1967. Proposed Mechanism for Sediment Entrainment by Turbulent Flows. *Journal of Geophysical Research*, **72**(24), 6183–6194.
- Tamburrino, A. & Gulliver, J.S. 1999. Large flow structures in a turbulent open channel flow. *Journal of Hydraulic Research*, **37**(3), 363–380.
- Thorne, P.D., Williams, J.J. & Heathershaw, A.D. 1989. In situ measurements of marine gravel threshold and transport. *Sedimentology*, **36**, 61–74.
- Tomkins, C.D. 2001. *The structure of turbulence over smooth and rough boundaries*. Ph.D. thesis, University of Illinois at Urbana Champaign, Urbana, Illinois.

- Tromp, M. 2004. *The influence that fluid accelerations have on the threshold of motion*. M.Sc. thesis, Delft University of Technology. www.waterbouw.tudelft.nl.
- Uittenbogaard, R., Hoffmans, G. & Akkerman, G.J. 1998. *Turbulence schematization for stone stability assessment*. Tech. rept. Q2395.30. WL|Delft Hydraulics, Delft.
- Van Rijn, L. 1993. *Principles of sediment transport in river, estuaries and coastal seas*. Amsterdam: Aqua Publications.
- VBKO. 2000. *Maak- en meetnauwkeurigheden bij de uitvoering van baggerwerken en steenbestortingen*. Tech. rept. VBKO, Gemeentewerken Rotterdam, Port of Rotterdam. In Dutch.
- Wang, & Shen. 1985. Incipient Motion and Riprap Design. *Journal of Hydraulic Engineering*, **111**(3), 520–538.
- Wang, J., Dong, Z., Chen, C. & Xia, Z. 1993. The effects of bed roughness on the distribution of turbulent intensities in open-channel flow. *Journal of Hydraulic Research*, **31**(1), 89–98.
- Watters, G.Z. & Rao, M.V.P. 1971. Hydrodynamic effects of seepage on bed particles. *Journal of the Hydraulics Division, Proceedings of ASCE.*, **97**(HY3), 421–439.
- White, C.M. 1940. The equilibrium of grains on the bed of a stream. *Proceedings of the Royal Society of London, Series A*, **174**, 322–338.
- Wiberg, P.L. & Smith, D. 1987. Calculations of the critical shear stress for motion of uniform and heterogeneous sediments. *Water Resources Research*, **23**(8), 1471–1480.
- Wiberg, P.L. & Smith, J.D. 1985. A theoretical model for saltating grains in water. *Journal of Geophysical Research*, **90**(C4), 7341–7354.
- Willems, B.B. & Murray, C.G. 1981. Lift exerted on stationary spheres in turbulent flow. *Journal of Fluid Mechanics*, **105**, 487–505.
- Xingkui, W. & Fontijn, H.L. 1993. Experimental study of the hydrodynamic forces on a bed element in an open channel with a backward-facing step. *Journal of Fluids and Structures*, **7**, 299–318.
- Zhou, J., Adrian, R.J., Balachandar, S. & Kendall, T.M. 1999. Mechanisms for generating coherent packets of hairpin vortices in channel flow. *Journal of Fluid Mechanics*, **387**(May), 353–396.

Appendix A

Techniques for Filtering Spurious Pressures

A.1 Introduction

The signal of measured turbulence pressures is wide-band and resembles noise. This makes it difficult to distinguish it from real noise. Therefore a thorough inventory was made of possible noise sources prior to measuring turbulence pressures, described in Hofland (2001). The main noise sources are environmental sound and vibration. Three possible filtering techniques are described here. Furthermore, the application of the filters is checked against measurements as well as on an artificially generated signal. One filter is also analysed analytically, as its description in literature was not entirely correct. The notation of Bendat & Piersol (1971) is mainly used for the analysis of the filters

A.2 High-pass filtering

A simple way of eliminating noise is to ensure that possible noise is present in another frequency range than the signal of interest. When the peaks are in a lower-frequency range a high-pass filter can simply be used to remove the noise peak. Conversely, a low-frequency filter can be used when high-frequency noise is present. It is also possible to obtain a signal in the time domain this way. Figure A.1 presents the premultiplied (variance preserving) spectrum of a wall pressure measurement on a smooth-wall open-channel flow. The wall pressure fluctuations are smaller for this flow than for the case with the bed-mounted cube, so the noise sources are more clear. The variance in the measured signal is distributed over two separate frequency ranges (0.1–

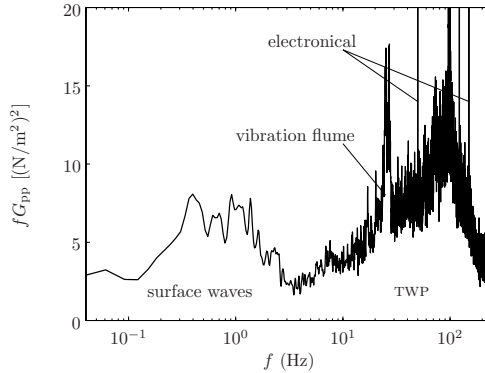


Figure A.1: Premultiplied spectrum of measured open-channel, smooth-wall wall pressures.

3 Hz and 3–250 Hz). The high-frequency fluctuations are caused by the turbulence wall pressures, and the low-frequency fluctuations probably by slightly instationary standing waves (Hofland, 2001). In this case the low-frequency energy can be cut off from the signal by a high-pass filter without loss of much of the turbulence signal. However, some of the signal is lost, so this procedure is not perfect. Especially for turbulence signals, which are wide band signals, this approach is often not possible.

A.3 Difference filter

A filter that is often used in measurements of wall pressures is the difference technique. It is suited for removing spurious pressures caused by structural and acoustical vibrations. An experimental set-up with two pressure sensors, mounted flush with the wall, having the same longitudinal position (in the direction of the flow) and a spacing in the lateral direction is used. For this technique it is required that the pressure signals, s_i , consist of a turbulent part, c_i , and a vibrational / acoustical part, v_i :

$$\begin{aligned} s_1(t) &= v_1(t) + c_1(t) \\ s_2(t) &= v_2(t) + c_2(t) \end{aligned} \tag{A.1}$$

The filter is based on the fact that structural and acoustical pressure disturbances are uniform over relatively large areas, compared to the turbulence pressures. If the distance between two pressure sensors in a flume is large enough (at least the water depth), the turbulence pressures will be uncorrelated, while the vibrational / acoustical pressures can still be approximately equal ($v_1(t) \approx v_2(t)$). When these

conditions are fulfilled, the two signals can simply be subtracted. This gives:

$$\Delta s(t) = s_2(t) - s_1(t) \approx c_2(t) - c_1(t) \Rightarrow G_{\Delta s \Delta s} \approx G_{c_1 c_1}(f) + G_{c_2 c_2}(f) \quad (\text{A.2})$$

where G_{ii} is the autospectral density of the signal i .

This result can be used as a filter that is able to determine the spectral characteristics if the two turbulence signals are statistically equal, i.e. measured at a similar position in the flume. In this case it simply follows that $\frac{1}{2}G_{\Delta s \Delta s}$ is equal to the autospectral density of one turbulence signal. The time trace is only obtained of the difference in pressures. The time trace of a pressure difference can also directly be used for examining stone stability, as only a pressure gradient can cause a net force on a stone.

A problem could occur when using the difference filter for pressure measurements around a stone. If pressure sensors are placed at various locations around a stone, instead of at a fixed depth, it is questionable whether a fixed vibration gives the same pressures at the different sensors, because the water height (\propto accelerated mass \propto pressure) above the various sensors varies. This will make the difference filter not totally effective.

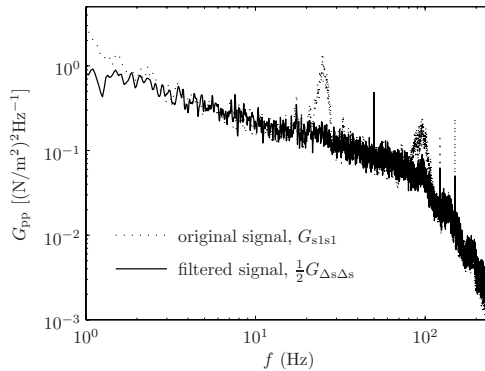


Figure A.2: A power density spectrum of wall pressures, both unfiltered and filtered.

A.3.1 Performance of the filter

The difference filter was shown to be functioning very well for the wall pressures that were measured. At lower velocities still some wide vibrational / acoustical noise peaks remained in the spectrum. A sample plot for a measurement with a medium noise-content is given in figure A.2. The few wide peaks created by vibrational / acoustical

noise that were visible in the spectrum (around 23 Hz and 95 Hz) can be seen to be completely attenuated. Also the electrical peaks at 50 and 150 Hz were partly attenuated. The low frequency noise due to surface waves is also reduced.

A.4 Optimal filter

The optimal filter was described by Naguib *et al.* (1996). It is based on the same set-up as the difference filter. Now we call one of the signals the measured signal s , and the second the reference signal r :

$$\begin{aligned} s(t) &= v_s(t) + c_s(t) \\ r(t) &= v_r(t) + c_r(t) \end{aligned} \quad (\text{A.3})$$

In order for the filter to work, the noise at both pressure sensors does not have to be exactly the same, like with the difference filter. It does have to be correlated via a linear system. In short: $\gamma_{\text{vsr}}^2 = 1$, where γ_{ij}^2 is the coherence function between signals i and j . The turbulence still has to be uncorrelated: $\gamma_{\text{cscr}}^2 = 0$, but does not need to have the same spectral density anymore. The filter determines the correlated part of the two signals, which can be subtracted from the original signal. The method was reported to be working very well by Naguib *et al.* (1996), who used a convolution method in the time domain for calculating the filtered signal. Although this is possible, it requires greatly increasing computing times for increasing filter lengths. It is also possible to execute the filter in the frequency domain, which significantly decreases the computational time required. The filter function in the frequency domain reads:

$$c'_s(t) = s(t) - \int_{-\infty}^{\infty} F'_{\text{vs}} e^{2\pi f t i} df \quad , \text{ with } \quad F'_{\text{vs}} = H_{\text{rs}} F_{\text{r}} \quad (\text{A.4})$$

where $c'_s(t)$ is the filtered turbulence signal, F'_{vs} is the Fourier transform of the estimated noise component, H_{rs} is the frequency response function of the two signals, and F_{r} is the Fourier transform of reference signal. The power spectrum can also be filtered directly in the following way:

$$G'_{\text{cs,cs}} = (1 - \gamma_{\text{sr}}^2) G_{\text{ss}} \quad , \quad (\text{A.5})$$

where G'_{ii} is the power spectral density of the turbulence signal i and γ_{ij}^2 is the coherence function of signals i and j .

A.4.1 Performance of the filter

Equations (A.5) and (A.4) are taken from Bendat & Piersol (1971). The term ‘optimal’ is presented by them, as it is shown by a least-squares procedure that this gives

the optimal estimation of the signal, in the sense that the integrated square difference between the real and the filtered signal is minimal. The filter is derived for systems with two linearly correlated signals with random noise at the output. However, for our application the correlated part, which is called the ‘signal’ by Bendat & Piersol (1971), is defined as the (vibrational) noise, and conversely their uncorrelated ‘noise’ part is the turbulence signal we need. Further, there is also uncorrelated turbulence signal added to the input of the linearly correlated noise. In consequence of this the filtered turbulence signal c'_s is not completely equal to the original signal c_s . Below it is shown that even for a perfect measurement set-up the optimal filter is not perfect. If we assume the following in order to simplify the analysis of the filter:

$$G_{cscs} = G_{crcr} = G_{cc}, \quad \text{and} \quad v_s = v_r \quad ,$$

equation (A.5) can be rewritten as (Bendat & Piersol, 1980; Naguib *et al.*, 1996):

$$\frac{G'_{cc}}{G_{cc}} = 1 + \frac{1}{1 + SNR} \quad (\text{A.6})$$

where SNR is the energy-based signal to noise ratio, G_{cc}/G_{vsvs} . This equation shows that there is always a part of the noise left, and that the noise on the signal cannot be totally attenuated after filtering. Naguib *et al.* (1996) argue that for decreasing SNR the relative attenuation of the noise goes to 100%. This is true. However, although the percentage of noise that is reduced tends to 100% in the limit of $SNR \rightarrow 0$, the overestimation of the turbulence signal also goes to 100%, which is 0.3 decades on a log scale. Therefore a large noise peak in the original signal will remain present in the filtered spectrum as a distinct peak. Surprisingly this was not mentioned in the paper.

The filter described in eq. A.4 was tested on both measurements of wall pressures and artificial signals, confirming eq. (A.6). Several options are possible to improve the method. One is to repeat the filter operation on the filtered signal. This increased its performance after the first repetition. Further repetitions did not cause an improvement, however.

The filter does not work well in consequence of the turbulence at the reference sensor. Therefore a better estimate of the noise at the reference sensor has to be obtained. This can be accomplished by averaging n surrounding signals to obtain a reference signal. Now the non-correlated turbulence part added to the measured noise will be suppressed. This gives the following estimation of the turbulence signal if the spectral densities of the turbulence and vibrational parts of all signals are assumed equal:

$$\frac{G'_{cc}}{G_{cc}} = 1 + \frac{1}{n + SNR} \quad (\text{A.7})$$

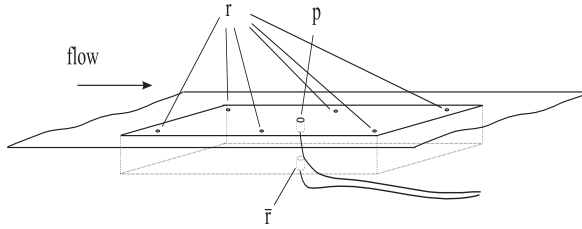


Figure A.3: Schematised set-up of reference pressure sensor.

This shows that an increase in the number of reference pressure sensors will improve the performance of the filter. However, a large number of reference pressure sensors would have to be used.

A.4.2 Implementation

For the present application we found that the best improvement was possible by inspecting the sources of the noise. We concluded that the main source of spurious pressures was environmental vibration rather than sound waves. Therefore the pressure sensor did not have to be placed in the flow itself. One sensor was placed in a cavity filled with water under the bed. Now the reference sensor mainly measured the vibration, so a complete prediction of the turbulence part of the other sensor –in principle– be obtained. The cavity was connected to the main flow by several small holes in the bed. These holes allowed sound waves and pressures due to long free-surface waves to reach the pressure sensor, so also these distortions could be filtered from the signal, although it is not clear how well these pressures reached the sensor. Possible turbulence-induced pressures that might reach the reference sensor from the different holes will be diminished as predicted by equation (A.7), where n now is the number of holes. The set-up is illustrated in figure A.3.

Appendix B

Rolling Stones

This appendix deals with the way in which the target stone had to be placed during the experiments. The idea was that the stone would be placed on a hinge, thereby fixing the centre of rotation. This obviously restricts the way in which the stone can move, but is very convenient for the execution of the experiments. Therefore it had to be proven that the hinge does not limit the movement of the stone in an unnatural way.

Three modes of initial movement are found in literature: rolling or pivoting, sliding and lifting. The critical shear stress for the initiation of rolling is always lower than that for lifting (Ling, 1995, for instance). Most models based on a balance of forces or moments on micro scale use the rolling threshold. Carling *et al.* (1992) investigated the movement of particles of different shapes and sizes on different roughnesses. They found that most particles rotated from their pocket on all roughness sizes. Extreme shapes like a rod and a disc sometimes showed a different behaviour, mostly sliding. On the roughest bed, some particles were seen to first move to an imbricated position (like roof-tiles), before being entrained by rolling. On the smallest roughness a cuboid slid away. However, the bed was unrealistically flat, as even for the roughest bed used – where the roughness elements were of the same size as the element that moved – the roughness elements were all placed on a flat plate, giving an unnatural flat bed.

De Gunst (1999) examined the stability of stones downstream of a backward-facing step and for an equilibrium flow, using video-analysis, and also saw the stones rolling away. She did notice that, prior to rolling, the stones were lifted slightly from their pockets. She does not mention at which point this lifting changes into a rotation. The difference between a slight rotation and a slight lifting is also difficult to notice.

We made some observations of moving stones with $\Delta = 0.4$. Two typical sequences of pictures are shown in figure B.1.

We observe the following: First, before movement the stone is sometimes seen

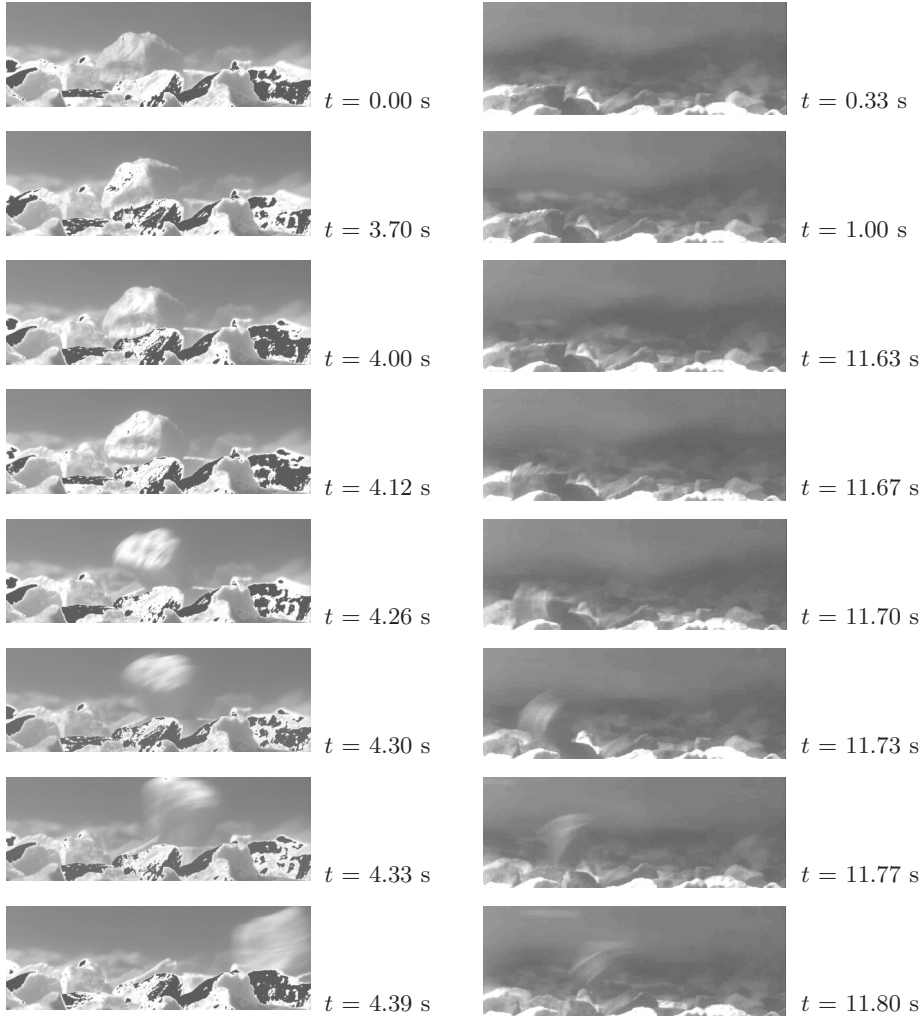


Figure B.1: Sequences of recordings by digital camera of initial movements of individual stones ($\Delta = 0.4$) from a granular bed under uniform flow. Each column depicts another stone movement. Left: the stone sits idle in pocket. It sometimes rocks a little. The stone is lifted at its upstream side and slowly slides to a stable position with a higher exposure, until it lies stable for a while. Until the upstream side of the stone is lifted up again and the stone rolls away. Right: the stone sits motionless in its pocket, sometimes its side lifts up, but the stone remains at its position; until it rolls downstream.

to either slide to an imbricated position or tilt in a direction perpendicular to the stream. This is seen in the first two pictures at the top left of figure B.1. This was also noted by Carling *et al.* (1992). Second, the main mode of movement whereby the stone is displaced from its pocket is rolling over the stone downstream, which agrees with the accepted notion in literature that this is the mode of movement. Only when the rotation in streamwise direction has commenced some rotation over another of the stone's axes is sometimes observed.

As most stones are observed to move in a rolling fashion, a hinge with a horizontal axis perpendicular to the flow will allow the stone to move realistically for the first part of the rolling motion.

Appendix C

PDF of bed shear stress

The instantaneous bed shear stress has been used in the past for modelling the transport of sediments (Grass, 1970; Paintal, 1971; De Ruiter, 1982; Bridge & Bennet, 1992; Van Rijn, 1993; Kleinhans & Van Rijn, 2002). In these models the amount of sediment transported is hypothesised to be linked to the amount of time that the shear stress surpasses a critical value. For a rough bed the shear stress consists of the combined drag forces on the particles in the bed. The PDF for the drag forces can therefore also be used to describe the probability density of the bed shear stress.

In recent probabilistic sediment transport models a Gaussian shape has been chosen for the instantaneous shear stress distribution (Kleinhans & Van Rijn, 2002, for example), although a log-normal distribution also has been used in order to include the observed skewness (Bridge & Bennet, 1992), and other distributions have been tried (Mosselman *et al.*, 2000). However, it can be expected that the bed shear stress has the same PDF as the drag forces, which was given by eq. (5.3). This can be explained by the fact that the shear stress can be regarded as a low-pass filtered drag force:

$$\tau_b = \sum_{i \in A} \frac{F_{D,i}}{A}, \text{ where } d \ll \sqrt{A} \ll h, \quad ,$$

where $F_{D,i}$ is the drag force on stone i , and A is the area over which the shear stress is determined. Further, the largest drag forces are created by large-scale flow variations and forces on the most protruding particles are largest. Hence eq. (5.3) is expected to represent the PDF of the bed shear stress for a range of relative turbulence intensities. Moreover, for hydraulically smooth beds the shear stress is proportional to $u|u|$ as well, as given by the log-law. Therefore we will check eq. (5.3) against shear stress data from literature.

Direct measurements of shear stresses under smooth-bed channel flow are available for Reynolds numbers (based on channel width and centreline velocity) of 5,600-6,600

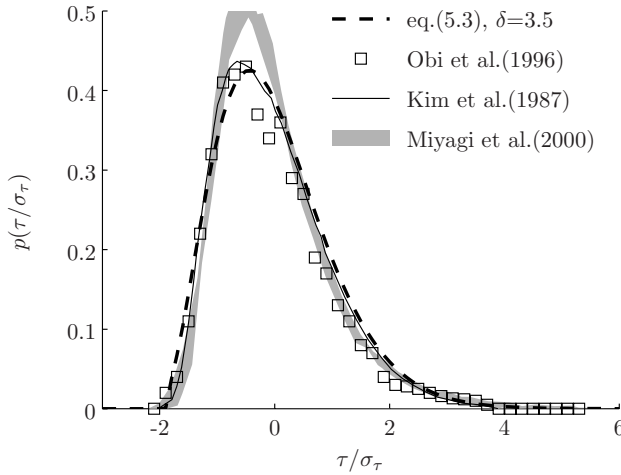


Figure C.1: Pdf of shear stresses in equilibrium boundary layer. Measured and χ^2 -distribution.

(Obi *et al.*, 1996; Kim *et al.*, 1987) and 17,400-35,000 (Miyagi *et al.*, 2000). These measurements are plotted in figure C.1. The PDF of the DNS computations of Kim *et al.* (1987) as taken from Obi *et al.* (1996) is plotted in the figure as well. Also eq. (5.3) is depicted. The near-bed σ_u is larger for smooth beds than for rough beds (Nezu & Nakagawa, 1993), which would imply that δ will have a lower value. This is why a value of $\delta = 3.5$ is chosen instead of the $\delta = 4.1$ that we saw in our rough bed measurements. It can be seen that eq. (5.3) for $\delta = 3.5$ follows the measured points quite well. The skewed distribution has previously been ascribed to the intermittent nature of turbulence near the viscous sublayer (Obi *et al.*, 1996). It is clear from the analysis presented herein that this is not necessarily true. The shear stress distribution can very well be explained by a normally distributed near-bed u -velocity.

Appendix D

Estimating entrainment from conventional stone stability measurements

D.1 Introduction

The usual way of measuring damage to bed protections is by counting the numbers of stones that are removed from strips with similarly coloured stones that are oriented perpendicular to the flow. It is not clear which physical quantity is exactly measured by this technique. As some stones leave their position and end up within the same strip, it is not a pure measurement of entrainment. However, as also stones from other strips pass this strip, it is also not a pure measurement of transport. Normally an arbitrary number of stones leaving a strip is chosen as ‘beginning of movement’ or ‘damage’. When different (relative) strip sizes are used for different investigations comparison of these investigations becomes difficult.

When all stones that passed the end of a strip – also the ones with a different colour – are summed, we obtain a measurement of transport, however, no method is available yet to obtain a good estimate of the total entrainment. In this appendix a method is developed for obtaining an estimate of the total entrainment from a certain strip. For this method the numbers of stones originating from this strip that arrived in the strips downstream of the strip are needed.

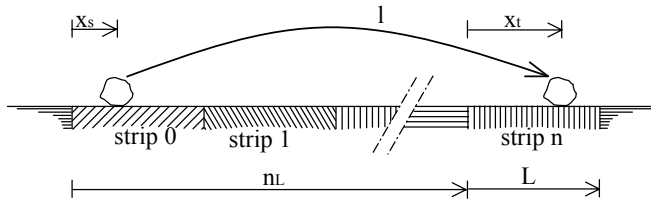


Figure D.1: Stone moving from strip 0 to strip n : definitions.

D.2 Definitions and assumptions

The following assumptions are the basis of the method:

- The probability of a certain displacement length, $p(l)$, is distributed according to a negative exponential distribution:

$$p(l) = \frac{1}{\Lambda} e^{-l/\Lambda}$$
 where $\Lambda = \bar{l}$. This implies that l is unaltered by the local flow conditions. This distribution was proposed by Nakagawa & Tsujimoto (1980). From the measurements of De Boer (1998) and De Gunst (1999) a similar distribution can be observed.
- $\Lambda \propto d$, i.e. Λ is mainly dependent on the micro-topography of the bed.
- The probability of a certain stone originating from a certain position within a strip is uniformly distributed.
- Usually a certain number of colours is used repeatedly for the strips. This causes that stones that displace this number of strips or more are attributed to the wrong strip. For simplicity we now assume that this effect is negligible. Otherwise the method will have to be extended.

In figure D.1 the definitions and nomenclature used in the following derivation are denoted. First we evaluate the chance that a stone originating from strip 0 will end up in strip n . For this we have to integrate the probability density of the displacement length, $p(l)$, from $l = nL - x_s + x_t$ to $l = (n + 1)L - x_s + x_t$. We then average the resulting probability over all possible x_s . This leads to the following double integral:

$$P(0 \rightarrow n) = \frac{1}{L} \int_0^L \int_0^L \frac{1}{\Lambda} e^{-\frac{nL - x_s + x_t}{\Lambda}} dx_t dx_s ,$$

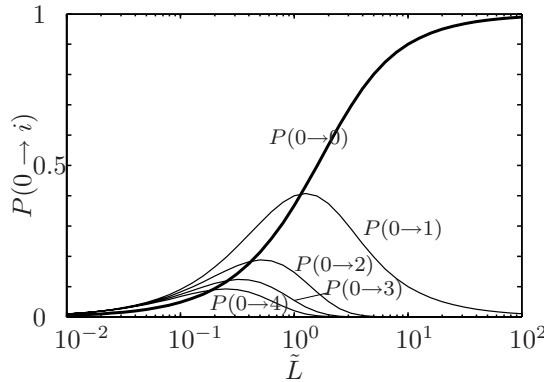


Figure D.2: Probability of a stone displacing from strip 0 to strip i , as a function of \tilde{L} .

which can readily be evaluated:

$$P(0 \rightarrow n) = \frac{2}{\tilde{L}} e^{-n\tilde{L}} \left(\cosh \tilde{L} - 1 \right), \text{ with } \tilde{L} = \frac{L}{\Lambda}. \quad (\text{D.1})$$

A similar integral can be formulated for the chance that a stone will remain in strip 0:

$$\begin{aligned} P(0 \rightarrow 0) &= \frac{1}{\tilde{L}} \int_0^L \int_{x_s}^L \frac{1}{\Lambda} e^{-\frac{x_t - x_s}{\Lambda}} dx_t dx_s \\ &= 1 - \frac{1}{\tilde{L}} + \frac{1}{\tilde{L}} e^{-\tilde{L}}. \end{aligned} \quad (\text{D.2})$$

The chance that a stone will be removed from strip 0 – to any other strip – can simply be stated as:

$$P(0 \rightarrow 1, 2, \dots) = 1 - P(0 \rightarrow 0). \quad (\text{D.3})$$

Figure D.2 shows the probabilities of eqs. (D.1) and (D.2). It can be seen that all probabilities tend to zero as the relative strip width \tilde{L} becomes small. In this case the stones travel very far and will have a fairly uniform chance of ending up in any downstream strip. This does not conform to the assumption of low mobility anymore. For very large values of \tilde{L} all probabilities become very small again, except $P(0 \rightarrow 0)$. This is understandable, because now the displacement length becomes so small that hardly any stones will travel a full strip width. Most stones will end up in strip 0 again. In this area the ratio between $P(0 \rightarrow 1)$ and $P(0 \rightarrow 2)$ will become very large. So all the stones that do leave strip 0, will only go to strip 1, and no stones from strip -1 will end up in strip 1. Therefore with a large strip width we will only be

able to have a sediment transport rate measurement instead of an entrainment rate measurement.

For a large number of entrained stones, the above theoretical probabilities of a stone reaching a certain strip n are proportional to the measured number of stones in strips n , which we denote as m_n , divided by the total entrained number of stones $E_{tot} = \sum_0^\infty m_i$. As m_0 was not measured, only the sum of all stones that were observed to have moved, $E_{meas} = \sum_1^\infty m_i$, can be measured. So we can state:

$$\frac{m_n}{E_{meas}} \approx \frac{P(0 \rightarrow n)}{P(0 \rightarrow 1, 2, \dots)} = \frac{2e^{-n\tilde{L}}}{1 - e^{-\tilde{L}}} (\cosh \tilde{L} - 1) \quad (\text{D.4})$$

The left hand side of eq. (D.4) is measured by the standard counting technique. Therefore we can fit the right hand side to these measured data for a certain strip and determine \tilde{L} . Subsequently the total entrainment can be estimated by:

$$E_{tot} = \frac{E_{meas}}{P(0 \rightarrow 1, 2, \dots)} = \frac{\tilde{L}}{1 - e^{-\tilde{L}}} E_{meas} \quad (\text{D.5})$$

This is the required correction factor to be applied to the measured entrainment rate. This method was checked against a Monte-Carlo simulation and the results indeed were the same.

D.3 Using the technique

De Gunst (1999) gives the average measured displacement lengths during the BFS measurements. These displacement lengths will be used to get an estimate of the correction factor E_{tot}/E_{meas} . De Gunst has a strip width of $L=9.2d$. She only presents the average distributions of displacement lengths for stones originating from all strips. These average distributions are given for various times in the measurement where the discharge is increased in steps. Only the last two steps are used, as here the number of stones moved becomes large enough for the relative error to be small. The measured displacement lengths (in strips) are depicted in figure D.3. From the fit we conclude that \tilde{L} is 1.51, which leads to an estimate of $E_{tot} = 1.93E_{meas}$. If we consequently use the assumption that $\Lambda \propto d$ we obtain for the WL data – where $L/d=16.1$ – the estimate of $E_{tot} = 2.83E_{meas}$.

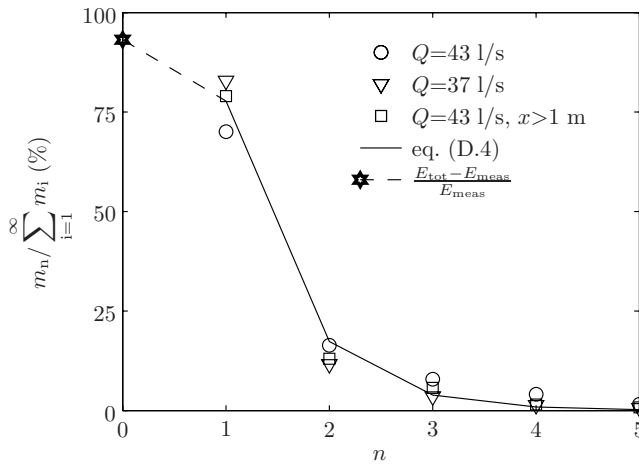


Figure D.3: The fraction of stones depositing in the n^{th} strip downstream of the strip of origin (DG), the fitted eq. (D.4), and the estimate of the number of stones deposited in the strip of origin, as a fraction of the measured number of deposited stones.

Appendix E

Measurements used for evaluation of modelling approach

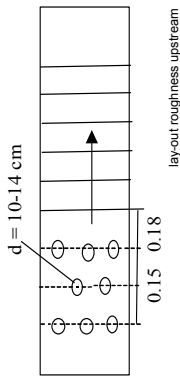
Measurements WL (Q2933 / Q3018) and De Gunst
Extra analysis

stones	0.0082
d_{160}	1.716
Δ	0.45
d_{nB4}	0.0076
d_{n16}	0.0051
d_{d85}	0.00765
d_{n15}	0.00506
W_n	1.51

Strip width	=
0.1 m	
16.1 d	

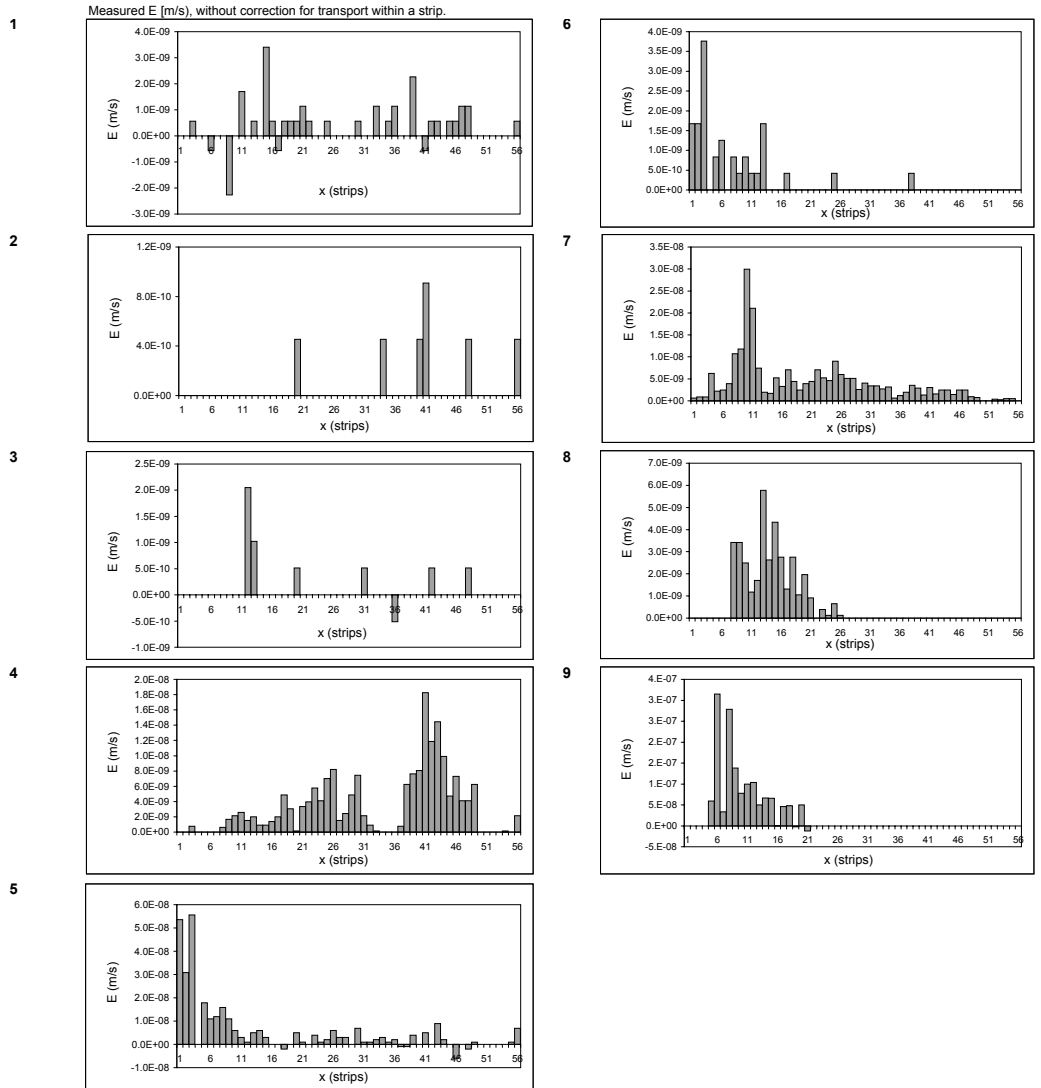
correction $dn16 \Rightarrow dn15$ en $dn84 \Rightarrow dn85$
 $(1-F)dn50+Fdn64$
 $(1-F)dn50+Fdn16$
 $F = (dn85-dn50) / (dn84-d50) / (dn50-dn15) / (dn50-d16)$
 $= 1.036$

Other parameters	
ρ	1000 kg/m ³
g	9.81 m/s ²



numb. report	numb. WL	computation # (W/L)	Q (l/s)	h (m)	T (min.)	#Etot* (stems/min)	Configuration	check $q_{L, tot} = 0?$	X measurements (m)	Strip numbers used for determination E
1	1	13	83	0.25 (0.23)**	45 185	0.0250 X 0.0040 used	Uniform flow	no (-12)	0.85 3.05 5.05	0.85 3.05 5.05
2	4	AnalYT	117.4	0.375	175	0.0007 used	Uniform flow	fairly	0.85 3.05 5.05	0.85 3.05 5.05
3	5	AnalYT	168.4	0.5	50 205	0.0043 X 0.0010 used	Uniform flow	fairly	0.85 3.05 5.05	0.85 3.05 5.05
4	11	17h	96.7	0.375	522	0.0410	Sill 1:3 lee-side	no (-83)	2.30 3.00 3.50 3.78 3.98 4.20 4.41 4.59 4.99 5.32	18-29 29-31 35-36 38-39 40-41 42-43 44-45 46-47 50-51 53-54
5	2	X	83.4	0.25	51 101	0.1373 X 0.0618 used	Roughness upstream, high Q	fairly	0.85 3.05 5.05	08-10 28-34 46-56
6	3	X	68.4	0.25	60 250	0.0140 X 0.0034 used	Roughness upstream, low Q	yes	0.15 0.85 3.05 5.05	01-03 08-10 25-39 46-56
7	10	15h	188.0 (200)	0.5	652	0.0505	Sill 1:8 lee-side	yes		
8	7	20	39.3	0.5	425 605 875	0.0089 used 0.0069 used -0.0018 X	Gate	yes	0.44 0.86 1.06 1.67 2.18 2.38 2.58 2.89 4.43 5.00	04-06 09-11 11-11 16-18 21-23 23-25 25-27 28-31 43-47 48-52
9	--	VOP(2000)	59	0.2	40	---	Backward-facing step	--	0.35 0.41 0.48 0.55	03-05 04-05 05-06 05-07

* entrainment total of all strips, only over the last period
 ** brackets denote the values used in the computation
 *** the values of the velocity measurements have been interpolated to obtain the stability parameter at the center of the area where E is evaluated



Appendix F

Geometrical characteristics of prototype bed protections

In 1999 tests were executed in a dock in the Rotterdam harbour to evaluate the difference between measurements with multibeam and with singlebeam echosounders. To this end two stretches of layers of standard gradings of rock were built. The elevations of these two bed protection were measured using measurements with a point gauge (the ‘real’ elevations, see figure F.1) and with a point gauge with a hemisphere with a diameter of $d_{n50}/2$ on its tip. Later the dock was inundated, and several multi- and singlebeam echosounders were used to measure the elevations of the two stretches of bed protection. These tests are reported by Meulepas *et al.* (1999), and used in VBKO (2000).

These tests had as aim to compare the measurements of a singlebeam and multi-beam echosounders to the measurement using the point gauge with a hemisphere, which is the standard measurement in hydraulic engineering. The present interest is to obtain the real statistics of the bed elevations, which are related to the point measurements. Therefore the measurements were reanalysed. Although the protections were inundated, no flow velocities were applied to the beds, therefore they cannot be regarded as water-worked. Still, they were manually flattened. Therefore they will also resemble a random flat bed.

Two beds were made using different gradings. Bed A had a grading of 40–200 kg, and bed B of 10–60 kg. In figure F.2 the measured elevations of both beds of the point measurements and multi-beam measurements (of one system) are shown. The stretches in the white dotted borders are used to obtain statistics of the bed elevations, as the bed is rather flat there. Still a small slope is present in the z -direction (not vertical in the present definition), which is corrected for. The moments of the bed

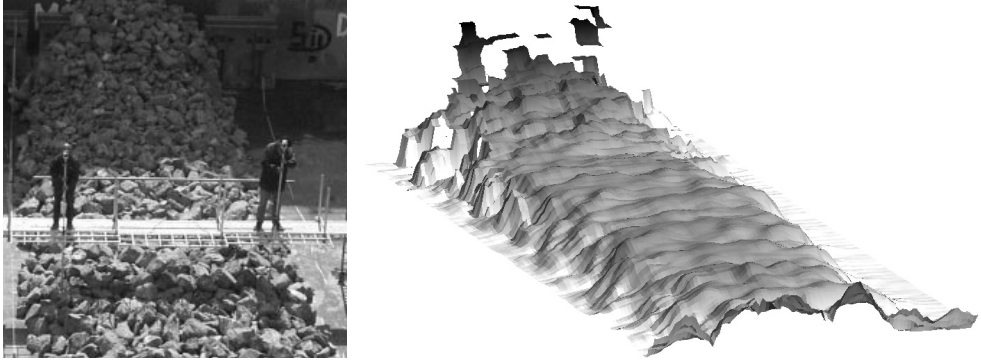


Figure F.1: Left: point gauge measurement at Verolme Dock in progress (Meulepas *et al.*, 1999). Right: result of a scan with a multi-beam echosounder.

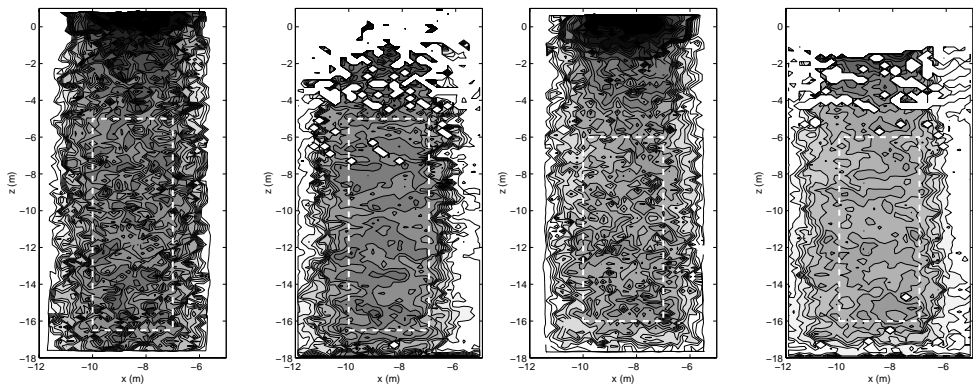


Figure F.2: From left to right, respectively the following measurements: 40–200 kg point gauge, 40–200 kg multibeam, 10–60 kg point gauge, 10–60 kg multibeam.

measurement	σ	σ/d	S	K
A: 40–200 kg, point gauge	0.153	0.420	-0.263	3.116
A: 40–200 kg, multibeam	0.127	0.349	-0.690	7.647
B: 10–60 kg, point gauge	0.137	0.572	-0.330	3.279
B: 10–60 kg, multibeam	0.091	0.380	0.220	3.330

Table F.1: Standard deviation and higher order moments determined for both bed protections by two techniques.

elevations are determined relative to the trendline in the z -direction.

The resulting bed characteristics are tabulated in table F.1. Also other multibeam systems were used. All these systems gave a linear relation between the measured standard deviation of the bed elevations and the stone grading. This is less clear for the point gauge measurements. However, the fact that the higher order moments of the multibeam measurements differ so much between the two measurements, makes that the point gauge measurements are deemed more accurate. The fact that the higher order moments are more extreme for the 40–200 kg gradation could be because the multibeam system can resolve the pores between the rocks in that case, while it cannot for the 10–60 grading.

Curriculum vitae

Bas Hofland was born on 9 December 1974. He graduated in 1993 at the Christelijk Lyceum in Alphen aan den Rijn. After that he studied Civil Engineering at the Delft University of Technology. In 1999 he graduated with the specialization of Hydraulic Engineering and an extra certificate for Civil Engineering in Developing Countries. During the study a 2 month project on river training in Bangladesh and a 3 month traineeship at the Ennore Coal Port project were carried out. Additionally he was tutor in Physics and Mathematics for high school students and student assistant for the modelling assignments of two computer courses at Civil Engineering. His graduating thesis dealt with the effects of a Current Deflecting Wall on the water exchange between a tidal river and a harbour basin. For this study he cooperated in a team of international scientists to perform experiments in the Tidal Flume at WL|Delft Hydraulics. From April 2000 to August 2004 he conducted the PhD research that led to this thesis. Currently Bas Hofland is employed at the Marine, Coastal & Industrial Infrastructure department at WL|Delft Hydraulics.